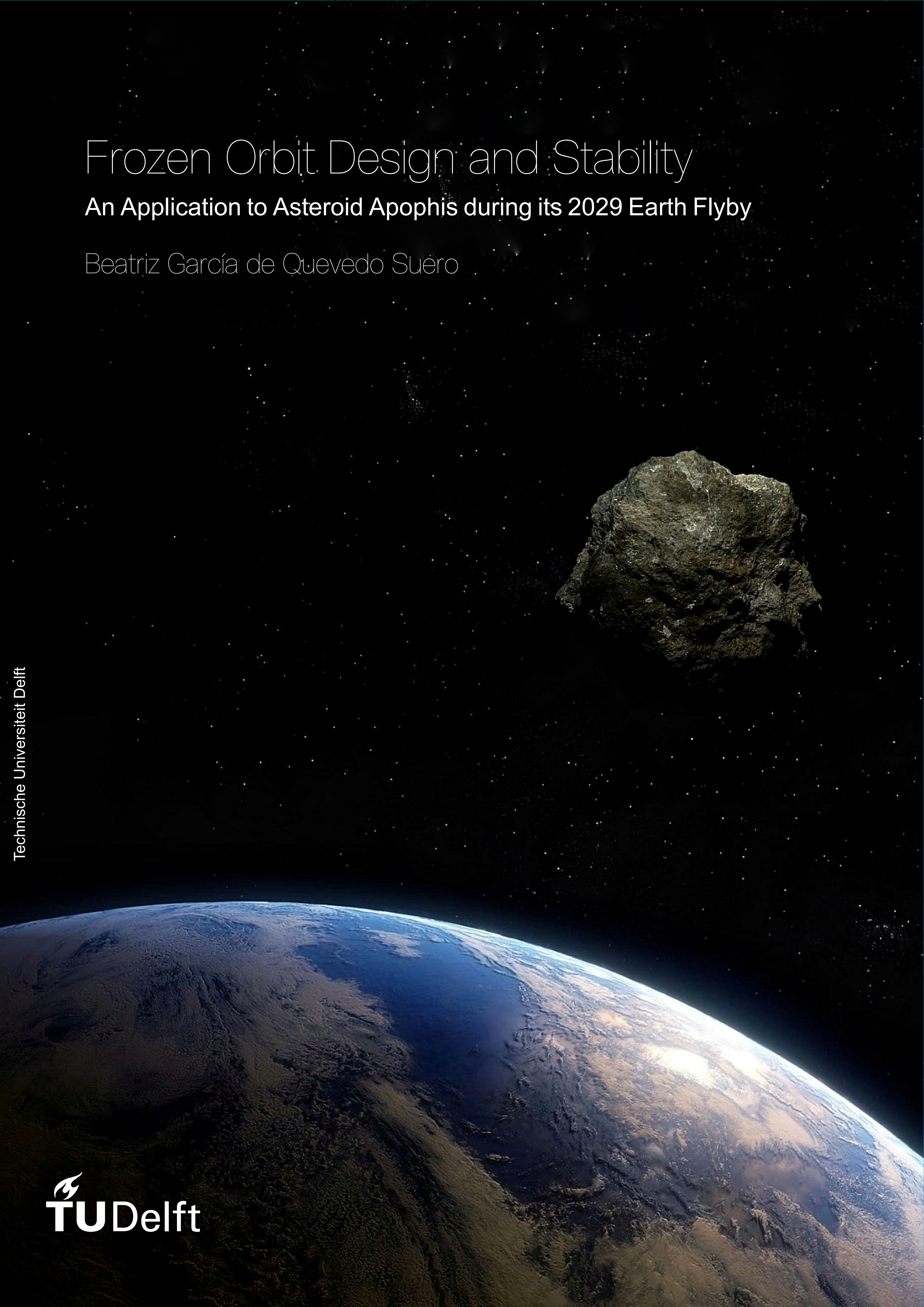

Frozen Orbit Design and Stability

An Application to Asteroid Apophis during its 2029 Earth Flyby

Beatriz García de Quevedo Suero

Technische Universiteit Delft

TU Delft

This page has been left blank intentionally.

Frozen Orbit Design and Stability

An Application to Asteroid Apophis during its 2029 Earth Flyby

by

Beatriz García de Quevedo Suero

to obtain the degree of

Master of Science Aerospace Engineering
at
Delft University of Technology

To be defended publicly on Friday the 7th of July, 2023 at 10:00 AM

Student number:	4678877	
Project duration:	24 October 2022 – 23 June 2023	
Thesis committee:	ir. R. Noomen	TU Delft, supervisor
	Dr. ir. E.J.O. Schrama	TU Delft, chair
	Dr. B.V.S. Jyoti	TU Delft, external examiner

Cover image: Artist's impression of an asteroid close to Earth. Credits: User urikyo33 via Pixabay.

This page has been left blank intentionally.

Preface

Before you lies the thesis 'Frozen Orbit Design and Stability: An Application to Asteroid Apophis during its 2029 Earth Flyby', the final work with which I am concluding my master's degree in Aerospace Engineering at the Delft University of Technology. This thesis delves into the topic of orbit design around asteroids, particularly the design of stable frozen orbits in the vicinity of asteroid Apophis around the time of its 2029 Earth flyby. Research in this area is of relevance not only to those investigating mission concepts to asteroid Apophis, such as the team behind NASA's OSIRIS-APEX mission but also to anyone studying the application of frozen orbits to other small bodies.

The road to obtaining a master's degree in aerospace engineering with a specialisation in space exploration has been as challenging as it has been rewarding. I can safely say that I could not have completed this degree without the support of the excellent professors who have accompanied me on this journey. First and foremost, I would like to thank my main supervisor ir. Ron Noomen for providing the perfect balance of guidance, support and freedom throughout this time. A special mention goes to ir. K.J. Cowan, Dr. ir. Erwin Mooij and Dr. ir. Dominic Dirkx for igniting my interest in the topic of numerical astrodynamics, propagation and optimisation, as well as for providing support with the use of the TU Delft Astrodynamics Toolbox. Additionally, I would like to extend my gratitude to the Aerospace Structures and Materials department members of the Faculty of Aerospace Engineering, specifically Dr. Calvin Rans and ir. Joris Melkert, for granting me the opportunity to work as a teaching assistant from November 2022 until May 2023.

I would also like to take this opportunity to thank the many people who have made my time in Delft an unforgettable experience. To all the amazing friends I have met on this journey, you will always hold a special place in my heart. A heartfelt thank you goes to my partner Neil for his unconditional love and support. To my sister, Coral, thank you for always being there for me. Last but not least, to my parents, Coral and David, thank you for always believing in me and giving me the courage to reach for the stars. I cannot thank you all enough.

Beatriz García de Quevedo Suero
Delft, June 2023

Abstract

Apophis, an Aten-type asteroid, was considered a significant threat to Earth upon its discovery due to its potential impact with Earth in 2029. Although the collision has now been ruled out, Apophis will still perform an exceptionally close flyby of Earth that same year at a distance of 32,000 km from the surface. This event presents a unique opportunity for the investigation of rotational changes due to tidal forces and post-encounter ephemerides for planetary defence purposes. In fact, the upcoming OSIRIS-APEX mission will enter orbit around Apophis shortly after the 2029 flyby. Even though orbits around near-Earth asteroids like Apophis face challenges due to the asteroid's low gravity and the strong perturbations induced by solar radiation pressure, frozen orbits – a specialised orbit with constant eccentricity and argument of periapsis on average – can achieve orbital stability in such a complex dynamical environment.

Frozen orbits were successfully employed for some of the mission phases of the OSIRIS-REx mission, and past research has greatly focused on the investigation of frozen orbits around Apophis and other small bodies through the use of analytical and numerical methods. However, no prior research has addressed the design of frozen orbits that can survive the close approach in 2029 without orbital correction manoeuvres. The aim of this research is thus to investigate the stability of control-free frozen orbits around Apophis during the 2029 Earth flyby.

To fulfil this goal, both analytical and numerical methods are employed. The analytical analysis involves averaging of Lagrange's Planetary Equations including perturbations from solar radiation pressure and Apophis' zonal gravity up to degree four in combination with a Lyapunov stability analysis and a comparison to numerical simulations. Assuming an argument of periapsis and longitude of the ascending node of $\pm 90^\circ$, the analytical method identifies two main solution families: near-equatorial heliotropic/anti-heliotropic orbits and near-polar Sun-terminator orbits. However, the stability analysis predicts only half of the sampled solutions to be stable. The comparison to numerical simulations shows that both analytical techniques fail to identify stable, frozen orbits. The stability index correctly identifies stability for 66.67% of the results that reach the end of a numerical propagation without surface impact or orbital escape. More significantly, 42% of the results are identified as false positives. The variations in eccentricity and argument of periapsis for the solutions that reach the end of a 28-day simulation are approximately 0.69 and 600° respectively for the near-equatorial solutions and, at best, 0.89 and 215° for the near-polar solutions, which are too large to be considered frozen orbits.

In the numerical analysis, the frozen orbit problem is defined as a multi-objective optimisation problem with two objectives: minimisation of the maximum variation in eccentricity and argument of periapsis. Trajectories with different orbital injection parameters are simulated to find the optimal initial state leading to a frozen orbit. First, the results are focused exclusively on the pre-flyby period with no constraint on surviving the flyby. The best solutions lead to a maximum variation in eccentricity and argument of periapsis of approximately 0.047 and 66° respectively over a 28-day period. However, these orbits all eventually collide with the asteroid at the time of the flyby. Imposing a constraint on survival increases the maximum variation in eccentricity and argument of periapsis to ranges of 0.08–0.21 and 103°–110.5° in the pre-flyby period. The behaviour post-flyby is stable for some of these solutions but no longer corresponds to the frozen configuration. In both cases, the solutions are categorised under the near-circular, near-polar, Sun-terminator frozen orbit family, the same type of orbit employed for the frozen orbit phases of the OSIRIS-REx mission. Despite the limitations of this work, the numerical pre-flyby results exhibit robustness against uncertainties in modelling parameters and orbital injection inaccuracies.

List of Abbreviations

AU	Astronomical Unit
CE	Close Encounter
DE	Differential Evolution
D/O	Degree/Order
ECLIPJ2000	J2000 Ecliptic reference frame
ERS	European Remote Sensing
ESA	European Space Agency
GEO	Geosynchronous Equatorial Orbit
JPL	Jet Propulsion Laboratory
LPEs	Lagrange’s Planetary Equations
LRO	Lunar Reconnaissance Orbiter
MOO	Multi-Objective Optimisation
MRO	Mars Reconnaissance Orbiter
NASA	National Aeronautics and Space Administration
NEAR	Near Earth Asteroid Rendezvous
NPA	Non-Principal Axis
NSGA-II	Non-dominated Sorting Genetic Algorithm
PaGMO	Parallel Global Multi-Objective Optimisation
PM	Point mass
PyGMO	Python Global Multi-Objective Optimiser
RK	Runge-Kutta
RKF	Runge-Kutta-Fehlberg
RKDP	Runge-Kutta Dormand-Prince
SAM	Short Axis Mode
SAM	Sun Anti-Momentum

SH	Spherical Harmonics
SRP	Solar Radiation Pressure
SSB	Solar System Barycentre
TDB	Barycentric Dynamical Time
TUDAT	TU Delft Astrodynamics Toolbox
UTC	Universal Time Coordinated
USM-EM	Unified State Model - Exponential Map

List of Symbols

Roman		
$\boldsymbol{a}$	Cartesian acceleration vector	m s^{-2}
$\boldsymbol{a}_p$	Perturbing accelerations vector	m s^{-2}
a	Semi-major axis	m
$C_{n,m}$	Unnormalised spherical harmonics cosine coefficient	-
$\bar{C}_{n,m}$	Normalised spherical harmonics cosine coefficient	-
C_r	Reflection coefficient	-
c	Speed of light	m s^{-1}
c	Differential equation solution constant	-
d	Asteroid-Sun distance	m
$\frac{d}{dt}$	Derivative with respect to time	s^{-1}
$\mathscr{E}$	Specific orbital energy	m^2 s^{-2}
e	Euler's number	-
e	Eccentricity	-
e_{max}	Maximum eccentricity	-
$\boldsymbol{f}(\boldsymbol{X})$	Lyapunov stability state vector time derivative	m s^{-1}, deg s^{-1}
$\mathbf{f}(\boldsymbol{x})$	Fitness function vector	-
f_e	Fitness function for e	-
$\mathrm{f}_n(\boldsymbol{x})$	Fitness function for objective n	-
f_ω	Fitness function for ω	
$\frac{\partial \boldsymbol{f}}{\partial \boldsymbol{X}}$	Jacobian matrix	-
G	Gravitational constant	m^3 kg^{-1} s^{-2}
g_0	Standard gravity	m/s^2
$\boldsymbol{H}$	Angular momentum vector	m^2 s^{-1}
h	Orbital altitude	m
h_{min}	Minimum orbital altitude	m
I_i	Moment of inertia of the intermediate axis	kg m^2
I_l	Moment of inertia of the long axis	kg m^2
I_s	Moment of inertia of the short axis	kg m^2
I_{sp}	Specific impulse	s
$Im(\lambda)$	Imaginary part of eigenvalue	-
i	Inclination	deg
i	Imaginary number	-
$\mathcal{J}$	Element of Jacobian matrix $\frac{\partial \boldsymbol{f}}{\partial \boldsymbol{X}}$	-
J_n	Zonal spherical harmonics coefficient of order n	-
$\mathcal{K}$	Lagrange Planetary Equation constant	deg s^{-1}

k	Order of interpolator	-
$\mathbf{lb}$	Lower bounds of decision vector	-
M	Mass of central body	kg
m	Spherical harmonics order	-
m_0	Initial mass	kg
m_{prop}	Propellant mass	kg
m_{sc}	Spacecraft mass	kg
N	Along-track direction	-
N	Asteroid mean motion	deg s^{-1}
n	Spacecraft mean motion	deg s^{-1}
n	Spherical harmonics degree	-
n_{obj}	Number of objectives	-
P	Luminosity of the Sun	W
P_{ast}	Asteroid orbital period	s
$P_{n,m}$	Unnormalised Legendre function of the first kind	-
$\bar{P}_{n,m}$	Normalised Legendre function of the first kind	-
P_{ϕ_s}	Average precession period of the short axis	s
P_{ϕ_l}	Average precession period of the long axis	s
P_{ψ}	Rotation period about the chosen rotation axis by convention	s
R	Radius	m
R_{max}	Maximum radius	m
$Re(\lambda)$	Real part of eigenvalue	-
$\boldsymbol{R}^{(B/A)}$	Rotation matrix from frame A to frame B	-
$\dot{\boldsymbol{R}}^{(B/A)}$	Time derivative of rotation matrix from frame A to frame B	-
$\boldsymbol{r}$	Cartesian position vector	m
$\dot{\boldsymbol{r}}$	Cartesian velocity vector	m s^{-1}
$\ddot{\boldsymbol{r}}$	Cartesian acceleration vector	m s^{-2}
r	Radial position	m
r_p	Periapsis radius	m
S	Radial direction	-
$S_{n,m}$	Unnormalised spherical harmonics sine coefficient	-
$\bar{S}_{n,m}$	Normalised spherical harmonics sine coefficient	-
S_{ref}	Spacecraft reference area	m^2
$\boldsymbol{s}$	Spherical state vector	m, deg, m s^{-1}
t	Time	s
t_0	Time of pericentre passage	s
U	Potential	m^2 s^{-2}
$\bar{U}$	Averaged potential	m^2 s^{-2}
$\mathbf{ub}$	Upper bounds of decision vector	-
V	Velocity	m s^{-1}
V_{esc}	Escape velocity	m s^{-1}
$\boldsymbol{v}$	Cartesian velocity vector	m s^{-1}
v_x	Cartesian velocity component along the X-axis	m s^{-1}

v_y	Cartesian velocity component along the Y-axis	m s^{-1}
v_z	Cartesian velocity component along the Z-axis	m s^{-1}
W	Cross-track direction	-
$\boldsymbol{X}$	Lyapunov stability state vector	m, deg
$\dot{\boldsymbol{X}}$	Lyapunov stability state vector time derivative	m s^{-1}, deg s^{-1}
$\boldsymbol{X}^*$	Lyapunov stability equilibrium solution	m, deg
$\boldsymbol{x}$	Decision vector	-
$\mathbf{x}$	Cartesian state vector	m, m s^{-1}
x	Cartesian position component along the X-axis	m
$\dot{x}$	Cartesian velocity component along the X-axis	m s^{-1}
y	Cartesian position component along the Y-axis	m
$\dot{y}$	Cartesian velocity component along the Y-axis	m s^{-1}
z	Cartesian position component along the Z-axis	m
$\dot{z}$	Cartesian velocity component along the Z-axis	m s^{-1}
	Greek	
α	Right ascension	deg
β	J2000 Ecliptic latitude	deg
γ	Flight path angle	deg
ΔV	Change in velocity	m/s
δ	Declination	deg
$\delta\boldsymbol{X}$	Lyapunov stability deviation from equilibrium solution	m, deg
δ_ε	Cosine of the obliquity	-
ε	Obliquity	deg
ζ	Stability index	-
Θ	Nutation angle	deg
θ	True anomaly	deg
$\boldsymbol{\kappa}$	Keplerian state vector	m, deg
Λ	Planetocentric longitude	deg
λ	J2000 Ecliptic longitude	deg
λ	Eigenvalue	-
μ	Gravitational parameter	m^3 s^{-2}
σ	Standard deviation	unit
ϕ	Planetocentric latitude	deg
Ψ	Flight path azimuth	deg
Ω	Longitude of the ascending node	deg
ω	Argument of periapsis	deg
	Other	
Υ	Vernal equinox	-
∇	Gradient with respect to position	-

Contents

1

Introduction

Upon its discovery on June 19, 2004, Aten-type asteroid Apophis was identified as one of the most dangerous near-Earth asteroids due to its high likelihood of impact with Earth in 2029. Even though the collision has now been ruled out with the help of additional optical and radar observations, it has been determined that Apophis will perform an incredibly close flyby in 2029, coming as close as 32,000 km from Earth [1]. This event presents a unique mission opportunity to investigate the asteroid's rotational changes due to the tidal forces present during the close encounter (CE), further ascertain the post-encounter orbit solutions for planetary defence purposes and deepen our knowledge on the formation and evolution of the Solar System [2, 3, 4].

Nevertheless, orbiter missions around near-Earth asteroids face a multitude of challenges. Due to the strongly perturbed environment caused by solar radiation pressure (SRP) and the asteroid's irregular shape, control-free orbits will usually impact or escape in the period of hours to days [4]. Achieving stable orbits in such an environment can be made possible using frozen orbits, which are designed such that the eccentricity and argument of periapsis remain constant over time, and are thus inherently stable [5, 6]. In fact, Sun-terminator frozen orbits were successfully applied for most of the proximity operations of OSIRIS-REx – a sample return mission sent to explore asteroid Bennu [7]. The OSIRIS-APEX mission, which will set out to enter orbit around Apophis shortly after the 2029 flyby, was approved in April 2022 as an extension of the OSIRIS-REx mission [8]. For this reason, a research opportunity arises to investigate frozen orbits for an orbiter mission around Apophis at the time of the CE.

Past research on the analysis of stable orbits around asteroids and other small bodies is extensive. However, few studies have focused on the investigation of frozen orbits, and even fewer on their application to Apophis specifically. Most proposed methods for finding frozen orbit solutions involve analytical approaches such as averaging the Lagrange Planetary Equations. This is exemplified by the work of Kikuchi, Oki, and Tsuda, which includes the effects of SRP and zonal gravity up to J_4 for the analysis of frozen orbits around asteroid Ryugu [5]. Lang, Chen, and Guo applied a similar method to find frozen orbits around Apophis, leading to two main orbit family solutions: near-equatorial heliotropic orbits and near-terminator orbits [9]. Although analytical methods can provide useful insights into orbital stability zones around small bodies, numerical methods are better suited for the modelling of complex perturbation environments [10]. Additional studies aimed at the investigation of stable orbits around Apophis include the work of Bellei, Cano, and Sánchez, who found terminator photo-gravitational stable orbits around Apophis for some of the possible spin-axis orientations, and of Ivashkin and Guo, who found long-lifetime orbits prior to the 2029 flyby by modelling Apophis as a homogeneous triaxial ellipsoid [10, 11]. Lang also investigated terminator orbits around Apophis, modelling the asteroid as a triaxial ellipsoid to calculate its gravity potential [12]. Finally, Aljbaae et al. investigated spacecraft behaviour around Apophis at the time of the 2029 Earth flyby by modelling the asteroid's gravity using a mascon-based method and implementing a control law for orbit maintenance [13].

Despite the significant contribution of these studies to the analysis of frozen orbits around Apophis, no past research has focused on the design of control-free frozen orbits that can survive the close approach in 2029. Another important consideration is that some of these studies were carried out before 2021, and are thus missing the most recent observational data of Apophis which further constrained the knowledge on its gravity and rotation state [14]. This thesis sets out to cover these research gaps by pursuing the following objectives:

- Using numerical optimisation to find frozen orbit solutions shortly before the 2029 close approach in a high-fidelity dynamical environment, including the asteroid's spherical harmonic gravity up to degree and order 4, solar radiation pressure and third-body gravity effects.
- Assessing the spacecraft behaviour in the frozen orbit solutions at the time of the close encounter.
- Finding solutions for control-free frozen orbits that remain bounded after the 2029 flyby.
- Investigating the robustness of the solutions to modelling assumptions and uncertainties.

1.1. Research Question

Based on the aforementioned objectives, the following research question has been formulated:

What is the feasibility of designing and maintaining stable control-free frozen orbits around asteroid Apophis before and during the 2029 Earth flyby?

In order to answer this question, the following sub-questions shall be answered:

- What is the solution space of initial orbital elements leading to frozen orbits around Apophis?
- Can a frozen orbit around Apophis survive the strong perturbations encountered during the 2029 flyby without orbital escape or surface impact?
- What is the sensitivity of the frozen orbit solutions around Apophis to practical elements like orbit injection inaccuracies and physical modelling uncertainties?

1.2. Outline

The report is divided into four main parts. Part I deals with the problem definition and contains Chapters 2 and 3. Chapter 2 summarises key background information on past missions and knowledge of the physical and dynamical parameters of Apophis. The assumed mission scenario, which outlines the requirements and spacecraft considerations, is also included in this chapter. Then, the orbital dynamics theory specific to the research problem is discussed in Chapter 3, where a first assessment of the perturbations acting on an Apophis-orbiting spacecraft is provided. Part II contains the analytical methodology and results, which are presented in Chapters 4 and 5 respectively. The next chapters comprise Part III, which focuses on the numerical method. The tools used are explained in Chapter 6. Following from this, the simulation and optimisation set-up is described in Chapters 7 and 8 respectively. The main results of this work are presented in Part IV. The numerical frozen orbit results are shown in Chapter 9. In Chapter 10, the sensitivity of the solutions to modelling uncertainties and orbital injection inaccuracies is determined. The verification and validation procedures performed to check the validity of the results are explained in Chapter 11. Finally, the conclusions and recommendations for future research are provided in Chapters 12 and 13 respectively.

I

Problem Definition

The first part of this work deals with the definition of the research problem. The relevant background, comprising details of similar missions, Apophis' dynamical and physical parameters, and the assumed mission scenario is provided in Chapter 2. The orbital dynamics theory associated with the research question is reviewed in Chapter 3.

2

Background

As an initial step in answering the research question, this chapter provides details of precedent missions, current knowledge of Apophis' dynamical and physical parameters, and a hypothetical mission proposal definition. First, the mission heritage is presented in Section 2.1. Here, past missions to other asteroids and missions employing a frozen configuration are examined. In Section 2.2, the current knowledge on asteroid Apophis is reviewed. Finally, the assumed mission scenario for the study case in question is documented in Section 2.3.

2.1. Heritage

A multitude of missions have taken advantage of frozen orbits since their first application to the SeaSat mission in 1978 [15]. Since then, frozen orbits have been exploited for remote sensing missions around Earth, the Moon and even Mars [16, 17, 18]. Past missions to asteroids, on the other hand, have been mostly limited to flybys which are incompatible with frozen orbit design [19]. The ongoing OSIRIS-REx mission is the only example of the application of frozen orbits to small-body exploration [7].

2.1.1. Frozen orbit missions

SeaSat, a satellite launched in 1978 to observe Earth's oceans, was the first mission to use the frozen orbit concept. The objective of this mission was to collect data on the ocean's topography, temperature and winds. Despite its short lifespan of 110 days, the satellite collected a large amount of information about the global oceans through its five sensors, including a synthetic aperture radar, a radar altimeter, a scatterometer system, a radiometer, and a microwave radiometer [15]. The satellite was launched into a nearly circular low Earth orbit at 775 x 799 km altitude with a 108° inclination, allowing it to cover 95% of the global oceans every 36 hours [15, 20]. Other Earth orbiters that have flown in a frozen orbit include the European Remote Sensing satellites (ERS-1 and ERS-2), Envisat and TOPEX/Poseidon, which all exceeded their nominal mission lifetime by several years [21].

The use of frozen orbits for observation missions extends beyond Earth satellites and has also been successful for lunar missions. A notable example is the Lunar Reconnaissance Orbiter (LRO). LRO is an active mission of the National Aeronautics and Space Administration (NASA) to map the Moon's surface, locate potential resources and landing sites, and measure radiation levels. Although the mission had a planned duration of just one year, it has been extended multiple times since its launch in 2009 [17]. In fact, the latest mission extension was approved in April 2022 with an additional three years of operations [8]. LRO was placed in a frozen orbit for two months during commissioning, saving propellant and allowing for instrument calibration [22, 21]. The frozen orbit design, with an eccentricity of 0.043, argument of periapsis of 270° and inclination of 90°, leads to a resulting variation in altitude and argument of periapsis of 30-45 km and 267-273° respectively [22]. The drift in argument of periapsis and eccentricity over a four-month period for this frozen orbit can be seen in Figure 2.1, with each colour representing a consecutive month [22].

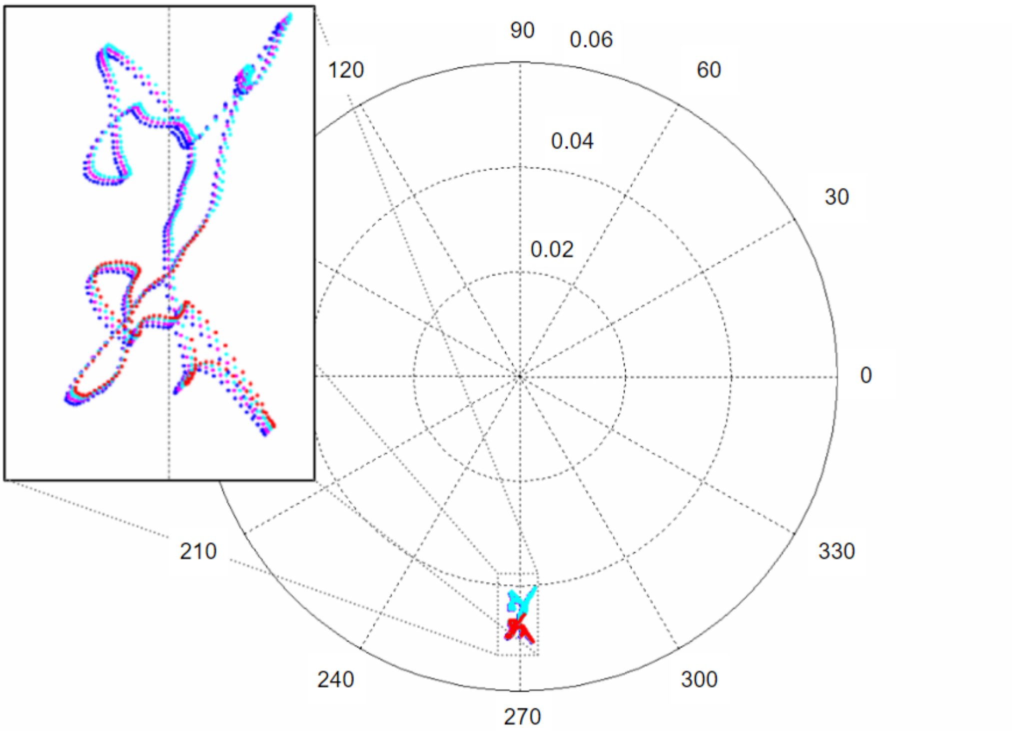

Figure 2.1: Polar plot showing drift of argument of periapsis and eccentricity over a period of four months for the Lunar Reconnaissance Orbiter frozen commissioning orbit [22].

Although the change in eccentricity and argument of periapsis seen in Figure 2.1 is not exactly zero, as per the definition of a frozen orbit, their values are essentially librating around the true frozen solution. In reality, true frozen orbits are impossible to achieve and thus these ”quasi-frozen” orbits will be referred to as frozen throughout this work [23].

A multitude of Martian orbiters have employed frozen orbits throughout their missions, such as the Mars Global Surveyor, Mars Odyssey and Mars Reconnaissance Orbiter [18]. The two latter missions are still active and were approved in April 2022 for an additional three-year mission extension [8]. The Mars Reconnaissance Orbiter (MRO), launched in 2005, had the primary objective to study the history of water on Mars [24]. During its primary science phase, which had a duration of two years, the spacecraft orbited in a near-polar, near-circular, Sun-synchronous frozen orbit. The frozen orbit offers a few operational advantages. Firstly, it simplifies payload design as the instruments are not affected by large changes in altitude and speed. Secondly, for the MRO mission scenario, the frozen configuration allows the lowest altitude over the Martian surface compared to other orbits. Nevertheless, non-frozen orbits are preferable for survey and mapping modes for faster access to diverse parts of the planet. For this reason, a requirement was set such that at least part of the orbit would have an altitude higher than 300 km [25]. The more recent ExoMars Trace Gas Orbiter, launched in 2016, used similar orbit design principles which limited the altitude variation over a single orbit to around 70 km [26, 27].

Overall, past applications of frozen orbits to space missions have proven successful in reducing propellant consumption, simplifying operations and extending the duration of said missions. The latter is also advantageous in increasing scientific output. For near-circular orbits, the near-constant altitude resulting from the frozen orbit design is advantageous for carrying out instrument calibration [21]. Furthermore, the near-constant altitude over a point on the central body’s surface characteristic of frozen orbits is useful for reconnaissance and altimetry [28]. The stability of an orbit in the frozen configuration is also beneficial to safely reach the extremely low orbital altitudes needed to obtain high-resolution imaging with a reduced risk of surface collision [29]. In general, the frozen configuration is chosen in combination with a Sun-synchronous, near-polar orbit, which offers additional advantages for science operations. For example, the constant illumination is beneficial for power generation [21].

2.1.2. Asteroid missions

Since the discovery of Ceres in 1801, optical observations carried out from Earth's surface have been the primary means of studying asteroids. Although these observations are important for a preliminary assessment of the asteroid's orbit and size, they have limitations when it comes to investigating the shape and rotational state of most asteroids. Thus, space missions are key to obtaining precise models for small bodies [30].

The first space-based observations of asteroids were made during incidental flybys of spacecraft en route to other targets [30]. The 1991 NASA Galileo mission to Jupiter was the first to produce detailed images of an asteroid, Gaspra, during a flyby at a distance of 1600 km. Two years later, it discovered Ida had a moon, Dactyl, after a second pass through the asteroid belt [19].

Compared to remote observations and flybys, rendezvous missions bring a more complete understanding of the asteroid's parameters by allowing extended periods of proximity observations. The first orbiter mission to an asteroid was the Near Earth Asteroid Rendezvous (NEAR) Shoemaker mission by NASA, sent to study asteroid Eros in 1996 [30]. After a 4-year journey, the NEAR Shoemaker spacecraft entered orbit around Eros and began its scientific operations. The orbital phase, which lasted a little over a year, involved 25 orbital correction manoeuvres including two low-altitude flyovers at distances of 5.4 km and 2.7 km [31]. For reference, Eros is 33 km long [32].

JAXA's Hayabusa mission was the first sample return mission to an asteroid, with asteroid Itokawa being the target [30]. The mission's science phase involved positioning the spacecraft in a hovering position, including a ”gate position” at 20 km altitude and a ”home position” at 7 km altitude [33]. A second sample return mission, Hayabusa-2, was launched in 2014 to explore asteroid Ryugu. This mission followed similar orbital operations – in this case a ”home position” at 20 km altitude – due to the asteroid's weak gravity field and limited reaction control system accuracy [34].

In 2007, the Dawn mission set off to explore two of the largest bodies in the main asteroid belt – Vesta and Ceres. At Vesta, four distinct orbital phases were included in the mission design, all involving near-polar circular orbits: Survey, High Altitude Mapping Orbit, Low Altitude Mapping Orbit, and High Altitude Mapping Orbit 2. The specific orbital parameters for each phase were chosen to meet coverage and resolution requirements [35]. The orbital phases at Ceres followed a similar structure [36].

As previously mentioned, OSIRIS-REx is the only asteroid mission to date to have incorporated frozen orbits into its orbital design [7]. OSIRIS-REx is a sample return mission to near-Earth asteroid Bennu launched in 2016 [37]. All orbital phases at Bennu, except one, used a Sun-terminator frozen orbit configuration to balance perturbations from the Sun and minimise variations in eccentricity and angular deviation. The use of frozen terminator orbits for the OSIRIS-REx mission proved beneficial from an operational standpoint but made it more difficult to estimate physical parameters such as gravity and solar radiation pressure. Improving the characterisation of these forces and the environment around Bennu could be achieved by incorporating additional orbital phases with non-frozen configurations [38]. Figure 2.2 shows the initial frozen orbit design for Orbital Phase A from two different views [7].

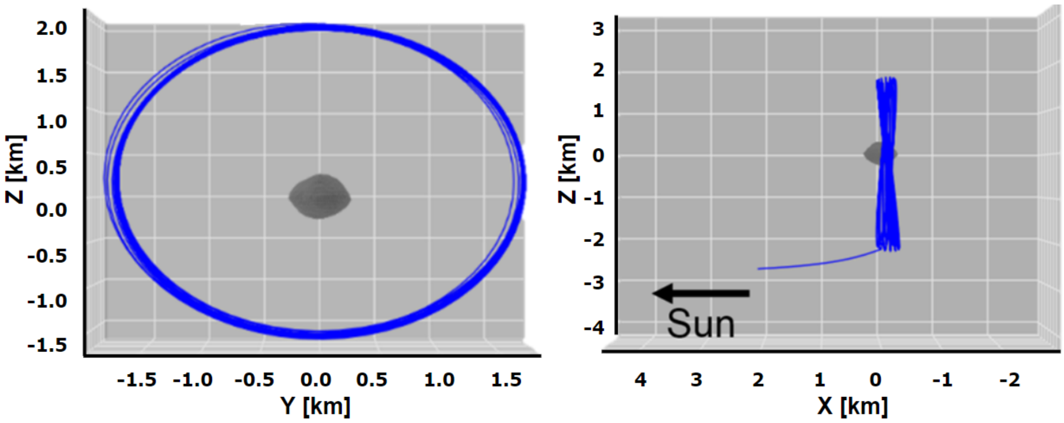

Figure 2.2: Target orbit for Orbital Phase A of the OSIRIS-REX mission with semi-major axis 1.75 km. Adapted from Wibben et al. [7].

2.2. Apophis

Upon its discovery in 2004, asteroid 99942 Apophis made headlines due to its statistically high chance of collision with Earth in 2029 [39]. Although a small impact probability was also estimated for 2036 and 2068, a series of recent optical and radar observations have confirmed that Apophis does not pose any risk to Earth for at least the next 100 years. Nevertheless, it is now known that during Apophis' 2029 flyby, the asteroid will come as close as 32,000 km from Earth's surface – closer than satellites in geosynchronous equatorial orbit (GEO) – thus providing a unique opportunity to study Apophis up close through a combination of space-based and ground-based measurements [1]. Apophis' trajectory around the time of the close encounter is visualised in Figure 2.3 [40].

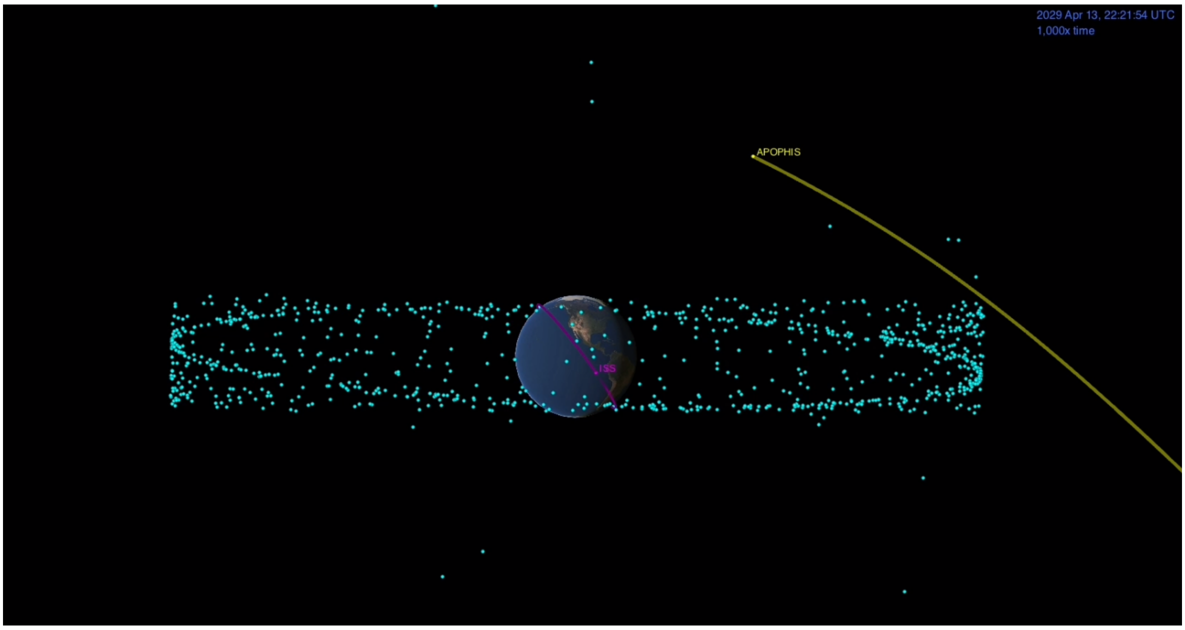

Figure 2.3: Trajectory and position of Apophis shortly before and after the close approach on April 13, 2029. GEO satellites are represented by cyan dots [40].

The design of a frozen orbit around a small asteroid requires a priori knowledge of the body's physical parameters, some of which are still largely unknown for Apophis. Since there have been no past missions to this asteroid, current knowledge is limited to that obtained via ground-based observations. The first optical measurements of Apophis were obtained during its discovery in June 2004, although the observations only lasted two nights. With the addition of a series of measurements obtained throughout December 2004, the 2029 impact probability increased up to 2.7%. Thankfully, pre-discovery data from March of the same year completely eliminated said possibility shortly after.

Additional observations and tracking throughout 2005 further improved the estimates on Apophis' orbit [41]. New polarimetric and photometric observations from 2006 were used to improve the estimates of Apophis' diameter and albedo, leading to updated values of 270 ± 60 m and 0.33 ± 0.08 respectively [42]. During a period of visibility in 2012/2013, the European Space Agency's (ESA) Gaia mission performed astrometric measurements to further reduce Apophis' orbit uncertainty [43]. During this same period, the Herschel Space Observatory obtained the first thermal measurements of the asteroid. This new data lead to improved predictions on the asteroid's shape, albedo, thermal inertia and mass [44]. Finally, astronomers used radar observations during a flyby of Apophis on March 5th, 2021, to refine its orbit around the Sun with high precision, resulting in the elimination of any impact risk in 2068 and beyond. These measurements were taken by the Goldstone observatory in Goldstone, California when the asteroid was 17 million km away from Earth [1]. Images obtained during this observation campaign are displayed in Figure 2.4 [14].

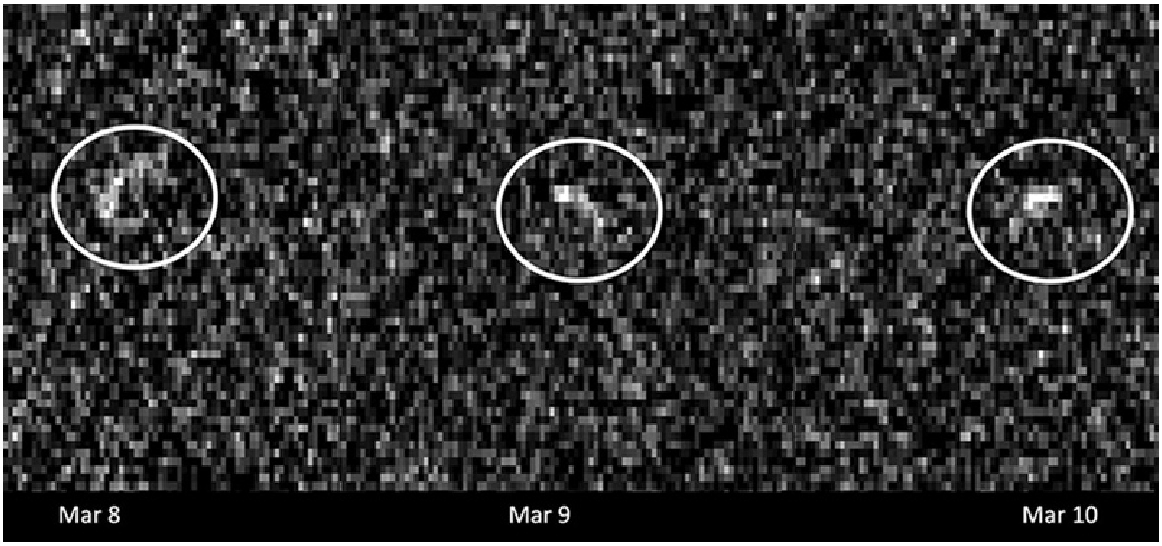

Figure 2.4: Radio images of Apophis with a resolution of 38.75 m/pixel captured in March 2021 [14].

2.2.1. Orbit

Apophis is an asteroid belonging to the Aten category, meaning its orbit crosses that of Earth with a semi-major axis smaller than 1 Astronomical Unit (AU) [1]. The close encounter with Earth in 2029 will cause Apophis' semi-major axis to increase from around 0.9 to 1.1 AU [3]. With this change, Apophis will be reclassified as an Apollo-type asteroid - its orbit will still cross Earth's orbit but with a semi-major axis larger than 1 AU [1]. Due to the nature of Apophis' orbit, there are repeated chances of close flybys with Earth and the Moon. Table 2.1 displays the Apophis-Earth distance for five of the closest future encounters, showing the 2029 flyby is by far the closest in the next ~100 years. The date is displayed using Barycentric Dynamical Time (TDB) [23].

Table 2.1: Minimal distance between Apophis and Earth for the five closest future encounters [45].

Date/Time [TDB]	Minimal Distance [AU]
2029-Apr-13 21:46	0.00025
2051-Apr-20 01:55	0.04146
2066-Sep-16 02:10	0.06956
2102-Sep-11 20:32	0.02343
2116-Apr-12 17:50	0.01946

The current osculating orbital elements of Apophis and their 1σ uncertainty are presented in Table 2.2. The data were obtained from a total of 7300 observations gathered between 2004 and 2021, including radar delay and Doppler measurements [45].

Table 2.2: Osculating orbital elements of Apophis at epoch 2460000.5 (2023-Feb-25.0) TDB [45].

Element	Value	Uncertainty (1σ)	Unit
a	0.922716	2.0453E-9	AU
e	0.191417	1.1454E-9	-
i	3.339273	1.1041E-7	deg
Ω	203.957515	3.7763E-6	deg
ω	126.605861	4.1783E-6	deg
t_p	2460072.030429	7.4583E-7	TDB

Figure 2.5 shows a visualisation of Apophis' orbit as of 13th January 2023 [46]. UTC is the Universal Time Coordinated standard of time [23].

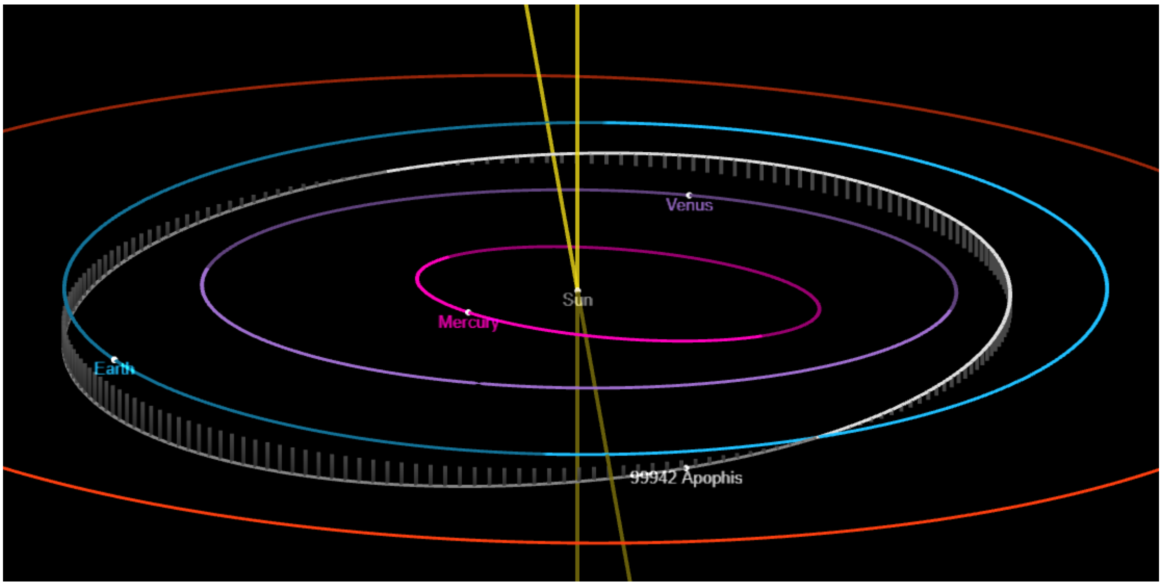

Figure 2.5: Orbit of Apophis as of 13th January 2023 00:00 UTC [46]. White vertical bars are perpendicular to the ecliptic plane.

2.2.2. Mass

The most recent estimate of Apophis' mass is that obtained by Müller et al. using Herschel Space Observatory measurements from 2014, leading to a value of $5.3 \pm 0.9 \times 10^{10}$ kg. The calculation was carried out using the bulk density of asteroid Itokawa or an average rock density of 3.2 g/cm^3 with 30-50% porosity [44].

2.2.3. Shape

The most recent study on the shape of Apophis is that of Aljbaae et al. [13]. This work improved past shape models by applying corrections to match the mass and diameter estimate from Müller et al. – $5.3 \pm 0.9 \times 10^{10}$ kg and 0.387 km respectively [47, 48, 44]. This new shape model has dimensions of $(-0.280, 0.259) \times (-0.184, 0.191) \times (-0.156, 0.169)$ km. The volume of the polyhedron shape, based on an assumed constant density of 1.75 g/cm^3, is 0.03034285 km^3. This corresponds to a spherical diameter equivalent of 0.387 km [13]. Figure 2.6 shows the shape derived from the work of Brozović et al. [48, 13].

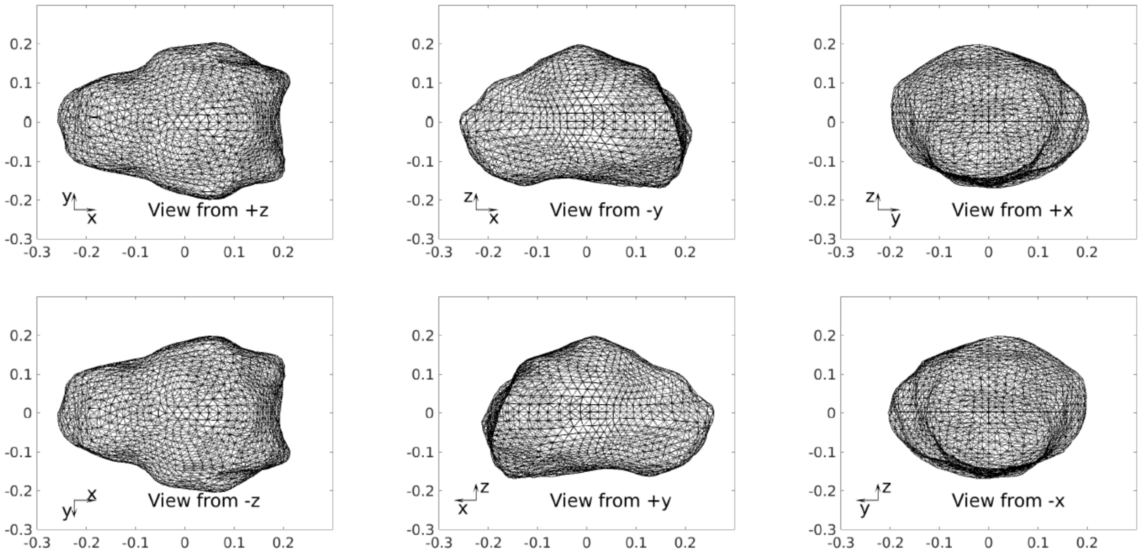

Figure 2.6: Polyhedral shape of Apophis using 2000 vertices and 3996 faces and rescaling using volume equivalent [48, 13]

Although Aljbaae et al. use an equivalent spherical diameter of 387 m for the derivation of their shape model, other values have been obtained by alternative studies. Müller et al. found a diameter range of 365-389 m [44]. Most recently, Reddy et al. found the diameter of Apophis to be between 290-390 m using radar observations from 2020 [49].

2.2.4. Rotational state

The first estimations of Apophis' rotational parameters were carried out by Pravec et al. using photometric observations from 2012-2013. They discovered that Apophis is a non-principal axis (NPA) rotator in the short-axis mode (SAM), which means the short axis is the one that circulates around the angular momentum vector [47, 50]. Furthermore, the orientation of the angular momentum vector indicates a retrograde rotation [47]. Radar observations obtained during the same observation period in 2012-2013 were used by Brozović et al. to update the values of Apophis' spin state parameters [48]. The latest study to characterise the asteroid's rotation was carried out by Lee et al. using the latest data obtained during the 2020-2021 flyby [51]. The spin state solutions obtained from these three studies are summarised in Table 2.3. The relatively large flyby distance during the 2012-2013 observation period meant that Brozović et al. were unable to reduce the uncertainties of the photometric solution from Pravec et al. The values from Brozović et al. are thus subject to similar uncertainties [52].

Table 2.3: Pre-flyby spin state solutions for Apophis with 3σ uncertainties [47, 48, 51, 52].

Model	P_{ϕ_s} [h]		P_{ϕ_l} [h]		P_{ψ}[h]		λ [deg]		β [deg]		I_l/I_s		I_i/I_s	
Pravec et al. (2014)	27.3800	± 0.0700	30.56	±0.01	263.00	±6.00	250	±27	-75	±14	0.61	+0.11 -0.08	0.965	+0.009 -0.015
Brozović et al. (2018)	27.4500		30.62		265.70		247		-59		0.73		0.950	
Lee et al. (2022)	27.3855	±0.0003	30.56		264.18	±0.03	278	+9 -8	-86	+5 -4	0.64	+0.02 -0.09	0.962	+0.023 -0.002

In Table 2.3, P_{ϕ_s} and P_{ϕ_l} represent the average precession period of the short and long axis respectively around the angular momentum vector $\boldsymbol{H}$. The short axis is the one with the maximum inertia, such that $I_l \leq I_i \leq I_s$, with I_l, I_i and I_s representing the moment of inertia around the long, intermediate and short axes. It can be more instinctual to use the long axis convention due to Apophis' elongated shape [52]. Then, P_{ψ} is the rotation period about the chosen rotation axis by convention. The orientation of the angular momentum vector $\boldsymbol{H}$ is defined in the J2000 ecliptic coordinate system by the longitude λ and latitude β [52]. In Figure 2.7, a visual representation of P_{ϕ_l}, P_{ψ}, $\boldsymbol{H}$ and Θ is provided. The nutation angle Θ is defined between the long axis and the angular momentum vector and is a function of time [52].

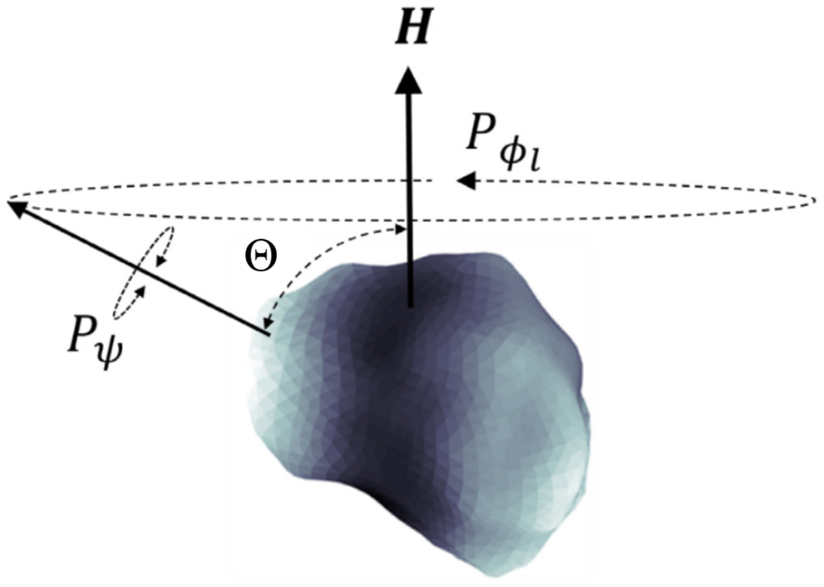

Figure 2.7: Definition of spin state parameters [52].

It is expected that the proximity of the 2029 flyby will lead to large changes in the spin state of Apophis [53, 54]. Even though the large uncertainty in the pre-flyby state hinders the assessment of the post-encounter parameters, Benson et al. have investigated the post-flyby direction of the angular momentum vector based on the pre-flyby solutions obtained by Pravec et al. and Brozović et al. [52, 47, 48]. Figure 2.8 shows the distribution of possible solutions for the post-flyby ecliptic longitude λ and latitude β of the angular momentum vector compared to the pre-flyby solutions [52].

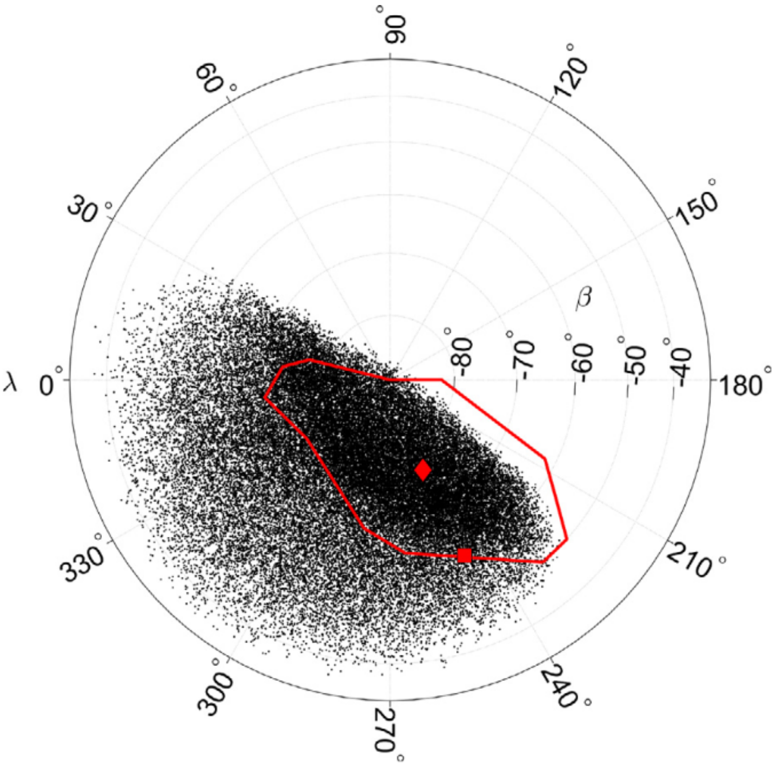

Figure 2.8: Post-flyby angular momentum orientation solution space shown in black dots. The red diamond and bounded red area represent the pre-flyby nominal solution and 3σ area from Pravec et al. respectively, while the red square denotes the nominal solution from Brozović et al. [52].

2.2.5. Gravity field

Methods to model the gravity field of irregular bodies such as asteroids have been extensively studied in literature, including but not limited to spherical harmonics and the polyhedron method [55].

The simplest way of representing the gravity field of a body is the point mass assumption, which only requires the total mass of the asteroid to be known [23]. The point mass assumption is generally only applicable between bodies positioned at large distances from each other, which is not the case for spacecraft orbiting a small body [44, 23]. An alternative approach demonstrated by Lang is to model the body as a triaxial ellipsoid to calculate the gravitational potential. For this method, only the gravitational parameter and the length of the three ellipsoid axes are required [12].

Spherical harmonics coefficients of Apophis up to degree and order 4 have been derived by Aljbaae et al. and Lang, Chen, and Guo [13, 9]. In both studies, the coefficients were computed from polyhedral shape models. However, these models differ largely in the assumed density, polyhedron volume, and number of vertices and faces, leading to different coefficients. The spherical harmonics coefficients from Aljbaae et al. are derived from the shape model previously shown in Figure 2.6, a non-convex shape model with a higher number of vertices and faces than the one from Lang, Chen, and Guo. It is thus assumed that the spherical harmonics coefficients from Aljbaae et al. have higher accuracy. The unnormalised spherical harmonics cosine and sine coefficients, $C_{n,m}$ and $S_{n,m}$ respectively, are presented in Table 2.4. The reference plane is the asteroid's equator, defined by the x-y plane shown in Figure 2.6 and perpendicular to the angular momentum vector $\boldsymbol{H}$ from Figure 2.7.

Table 2.4: Unnormalised spherical harmonics coefficients of Apophis up to degree and order 4 [13].

Degree	Order	C_{nm}	S_{nm}
0	0	1.0000000000	-
1	0	0.0000000000	-
1	1	0.0000000000	0.0000000000
2	0	-0.0783221323	-
2	1	0.0000000000	0.0000000000
2	2	0.0263789204	-0.0000000000
3	0	0.0448720700	-
3	1	0.0071441362	-0.0022479382
3	2	-0.0086800988	-0.0031712753
3	3	-0.0045154950	0.0001852096
4	0	0.0063633515	-
4	1	-0.0036166896	-0.0009014188
4	2	-0.0004122196	0.0002392422
4	3	0.0001533535	0.0002872799
4	4	0.0000804961	0.0000311549

In numerical applications, the spherical harmonics series is often truncated to reduce computational effort [56]. The resulting expression is then only an approximation of the exact gravitational potential, but it can often be assumed that the contribution of higher-order terms is negligible. Since convergence is not guaranteed within the circumscribing sphere, also called Brillouin sphere, extremely low-altitude orbits should be avoided when using this expression, especially for bodies with a highly irregular mass distribution such as asteroids [57]. However, since landing and ascent trajectories are not a part of this work, a constraint can be set on the minimum altitude of the spacecraft to avoid convergence issues. Furthermore, the $C_{n,m}$ and $S_{n,m}$ coefficients are often normalised to avoid numerical arithmetic involving a combination of very large and small numbers [23]. The normalised coefficients are represented by $\bar{C}_{n,m}$ and $\bar{S}_{n,m}$ respectively.

As opposed to the spherical harmonics model, the polyhedron model is valid on and close to the surface of the body, which is useful for the assessment of surface impact probability [57]. The polyhedron model requires the availability of a shape model and generally assumes a constant density when the asteroid's mass distribution is unknown. The accuracy of this method increases with the number of faces used at the cost of higher computational effort [55].

Finally, as seen in Subsection 2.2.2, the current knowledge on Apophis' mass has an uncertainty of $\pm 17\%$. Since all gravity models require knowledge of the asteroid's mass or the gravitational parameter, the sensitivity of the results to the mass uncertainty is analysed in Subsection 10.2.1.

2.3. Mission Scenario

A hypothetical mission scenario is defined based on similar asteroid mission proposals for the refinement of the study case of frozen orbits around Apophis at the time of the 2029 flyby. At this point in time, the only approved mission to Apophis is NASA's OSIRIS-APEX mission, an extension of the OSIRIS-REx mission [3]. The OSIRIS-REx spacecraft is currently on the last leg of its journey back to Earth with an expected return date of the sample capsule in September 2023 [58]. Following this Earth flyby, OSIRIS-REx will remain in a heliocentric orbit with a leftover ΔV capacity of 600 m/s and a fully operational payload compatible with the investigation of a similar-sized asteroid [59]. Sutter et al. investigated the trajectory design for this extended mission within the spacecraft's propellant limitations and found the spacecraft could reach Apophis by April 21, 2029 – just eight days after the CE – with a ΔV consumption of only 271 m/s [59]. However, since insertion prior to the CE would greatly improve scientific output, in this research a fictive mission scenario is proposed whereby an OSIRIS-REx-like spacecraft enters orbit around Apophis shortly prior to the 2029 flyby. Apart from this, the mission's requirements and spacecraft definition are heavily inspired by NASA's OSIRIS-APEX mission.

2.3.1. Requirements

The following fictive mission requirements are assumed to refine the mission scenario:

1. The spacecraft's orbital altitude shall not be lower than 100 m at any point in time.
2. The spacecraft's orbital altitude shall not be higher than 6 km at any point in time.
3. The spacecraft shall enter orbit around Apophis four weeks before the CE.
4. The spacecraft shall remain in orbit for at least four weeks.

The minimum orbital altitude requirement is necessary for several reasons. Firstly, it reduces the risk of surface impact. Secondly, it helps ensure convergence if one uses the spherical harmonics gravity model. Finally, although low altitudes are beneficial for high-resolution imaging, one must also consider that higher altitudes provide more coverage in less time. The maximum orbital altitude is set semi-arbitrarily to 6 km. This follows from the fact that below an orbital altitude of ~6 km, the accelerations from Apophis' gravity should always be larger than those of Earth during the flyby, which is expected to help with orbital stability [13]. Finally, although the orbital insertion date is assumed to be four weeks before the CE in this study to limit the computational effort, for practical reasons the spacecraft can be placed into orbit around Apophis prior to this date with the equivalent initial orbital elements leading to the same frozen orbit solution. The details of the orbital insertion strategy are assumed to be beyond the scope of this study.

2.3.2. Spacecraft

In order to model the perturbations acting on the spacecraft, its mass, dimensions and surface optical properties need to be known. These data are assumed equal to that of the OSIRIS-REx spacecraft and are shown in Table 2.5 [13].

Table 2.5: Assumed spacecraft physical properties [13].

Mass [kg]	Reflectance [-]	Reference area [m^2]
1500	0.4	25

The dry and wet mass of OSIRIS-REx is 880 kg and 2110 kg respectively [60]. Thus, taking the mass to be equal to 1500 kg is an accurate representation of the spacecraft's mass upon completion of the OSIRIS-REx mission, indicating a remaining propellant mass of 620 kg. Finally, the spacecraft is equipped with a suite of instruments, ranging from the OSIRIS-REx Laser Altimeter to the OSIRIS-REx Thermal Emission Spectrometer, which are assumed to be able to provide valuable scientific output when orbiting Apophis [60].

3

Orbital Dynamics

This chapter deals with the orbital dynamics in the vicinity of an asteroid and the mathematical expressions that are used to model the spacecraft behaviour. First, the relevant reference frames and coordinate systems are described in Sections 3.1 and 3.2. Subsequently, the equations of motion for the problem are introduced in Section 3.3. Finally, the main perturbations to be considered for the case of an asteroid-orbiting spacecraft are defined in Section 3.4.

3.1. Reference Frames

Reference frames are required to know the position and velocity of the spacecraft at any point in time [23]. Inertial reference frames are a special type of non-rotating frame which have a non-accelerating origin. The Solar System Barycentre (SSB) is considered to be the only inertial origin at the Solar System scale [61]. When analysing spacecraft orbits, usually a non-rotating reference frame is used with its point of origin located at the centre of the celestial body being orbited. For the case of an asteroid orbiter mission, there are several applicable reference frames [1] [23, 61]:

- **ECLIPJ2000 reference frame:** inertial reference frame defined as shown in Figure 3.1.

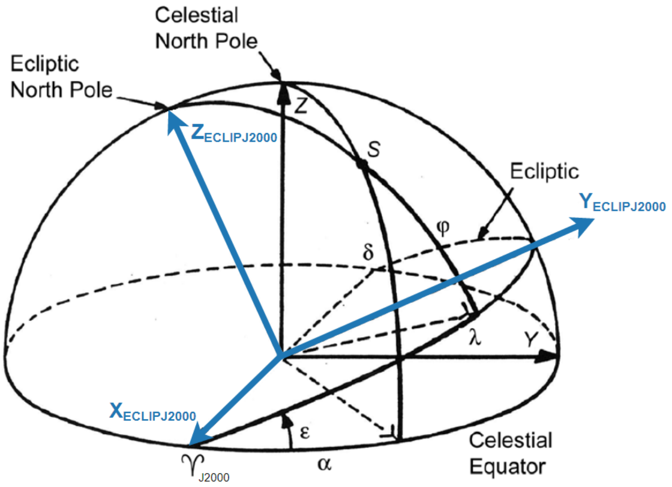

Figure 3.1: Definition of ECLIPJ2000 reference frame. Adapted from Wakker [23].

The X-axis points towards the position of the vernal equinox Υ at the J2000 epoch. The J2000 epoch refers to the 1st of January 2000 at 00:00 hours UTC and is generally used as a time reference. The J2000 vernal equinox Υ_{J2000} is thus defined as the intersection point between the

---

[1] All reference frames are orthogonal, right-handed frames.

ecliptic – the plane formed by the Earth's orbit around the Sun – and the celestial equator – the plane aligned with the Earth's equator – at this point in time. The Z-axis is perpendicular to the ecliptic plane at the J2000 epoch and is also referred to as the celestial north pole. The Y-axis completes the orthogonal, right-handed frame. The origin of the reference frame is the SSB.

- **Asteroid-centred, ECLIPJ2000 reference frame:** non-inertial, non-rotating reference frame. All axis orientations are parallel to the ECLIPJ2000 reference frame, but the reference frame origin is translated to the centre of mass of the asteroid. Note that, unless the obliquity of the asteroid is 0°, the reference frame axes are not aligned with the asteroid's rotation axis or equator. This is the reference frame used for numerical propagation, as explained in Section 7.1.
- **Asteroid-centred, polar-equatorial reference frame:** non-inertial, non-rotating reference frame centred at the centre of mass of the asteroid. The Z-axis is aligned with the asteroid's rotation axis, which is assumed to have a constant orientation. The remaining axes are parallel with the asteroid's equatorial plane. All orbital element time evolution results shown in this work are given with respect to this reference frame unless otherwise specified.

The implementation of the transformation between the asteroid-centred, ECLIPJ2000 reference frame and the asteroid-centred, polar-equatorial reference frame is described in further detail in Section 7.1. Furthermore, verification of this transformation is presented in Subsection 11.1.4.

3.2. Coordinate Systems

Different coordinate systems can be used to represent the location or motion of a satellite with respect to a reference frame [23]. The coordinate systems used in this work are rectangular coordinates, spherical coordinates and orbital elements.

3.2.1. Rectangular coordinates

Rectangular coordinates, also called Cartesian coordinates, describe the state of a satellite in terms of its position and velocity with respect to the origin of the chosen reference frame. The Cartesian state is thus defined by six parameters in three-dimensional space: the positions x, y, z, also denoted by the vector $\boldsymbol{r}$, and the velocities $\dot{x}, \dot{y}, \dot{z}$ or v_x, v_y, v_z, denoted by the vectors $\dot{\boldsymbol{r}}$ and $\boldsymbol{v}$ respectively. The Cartesian state vector is then defined by Equation 3.1.

$$\mathbf{x} = [x, y, z, \dot{x}, \dot{y}, \dot{z}]^T \tag{3.1}$$

The rectangular coordinate representation is useful for numerical integration procedures and can also be used, for example, to compute the energy of the orbit at any point in time [21].

3.2.2. Spherical coordinates

The spherical coordinates are made up of six parameters: the magnitude of the radial position vector r, right ascension α, declination δ, velocity V, flight path angle γ and flight path azimuth ψ. The spherical state vector is defined by Equation 3.2.

$$\boldsymbol{s} = [r, \alpha, \delta, V, \gamma, \psi]^T \tag{3.2}$$

The radial position, right ascension and declination, which make up the spherical position, are illustrated in Figure 3.2. If the spherical coordinates are calculated with respect to a reference frame whose XY plane is aligned with the equator of the asteroid, the right ascension and declination are similar to the longitude and latitude respectively. These can be useful for analysing the altitude over a given point on the asteroid's surface over consecutive passes.

3.2.3. Orbital elements

Orbital elements are essential for the design of frozen orbits, which involves analysing the variation of the eccentricity and argument of periapsis [21]. The Keplerian orbital elements are comprised of six parameters: the semi-major axis a, eccentricity e, inclination i, argument of periapsis ω, longitude of the ascending node Ω and true anomaly θ [23]. The Keplerian state vector is defined by Equation 3.3.

$$\boldsymbol{\kappa} = [a, e, i, \omega, \Omega, \theta]^T \tag{3.3}$$

When units are not provided, one can assume the orbital elements are given in metres and degrees. The semi-major axis and eccentricity define the size and shape of the orbit, while the inclination, longitude of the ascending node, and argument of periapsis are used to define the orientation of the orbital plane with respect to a non-rotating reference frame. Finally, the true anomaly describes the position of the orbiting body in this orbit. A number of these elements are shown in Figure 3.2.

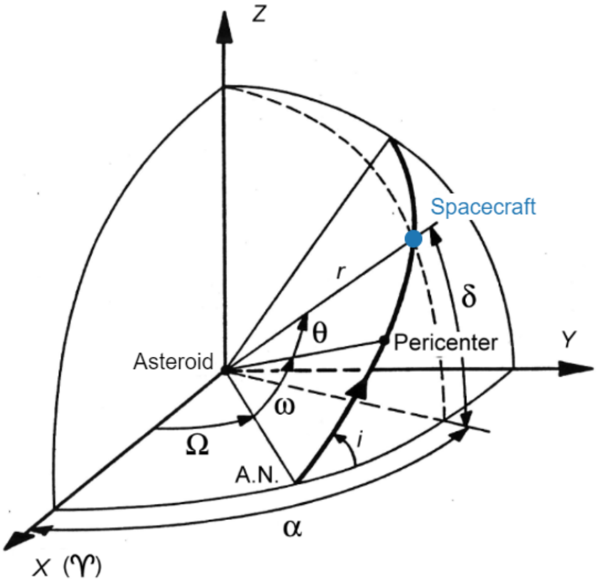

Figure 3.2: Definition of orbital elements: inclination i, argument of periapsis ω, longitude of the ascending node Ω and true anomaly θ; and spherical coordinates: radial position r, right ascension α and declination δ, with respect to an asteroid-centred, non-rotating reference frame. Adapted from Wakker [23].

3.3. Equations of Motion

The two-body problem is taken as the starting point for the derivation of the equations of motion for a spacecraft orbiting Apophis around the time of the 2029 Earth flyby. The two-body problem describes the motion of two point masses in free space, where the only acceleration present is the mutual gravitational pull between the two bodies. Under this assumption, the motion of a satellite A with respect to a non-rotating reference frame with body B at its origin is described by Equation 3.4 [23].

$$\ddot{\boldsymbol{r}}_{BA} = -G\frac{m_B + m_A}{r_{BA}^3}\boldsymbol{r}_{BA} \tag{3.4}$$

The vector $\boldsymbol{r}_{BA}$ is the position vector of spacecraft A with respect to asteroid B, while $\ddot{\boldsymbol{r}}_{BA}$ represents its second time derivative. The gravitational constant, with a value of 6.67384×10^{11} $\mathrm{m^3kg^{-1}s^{-2}}$, is denoted by the parameter G. Finally, m_A and m_B are the masses of bodies A and B respectively.

For the case of a spacecraft orbiting an asteroid, it can be further assumed that $m_B >> m_A$. Defining the central body mass as $M = m_B$, the gravitational parameter $\mu = GM$ is introduced. Further omitting the BA subscript from this point forward for simplification purposes leads to Equation 3.5.

$$\ddot{\boldsymbol{r}}_{BA} = -\frac{\mu}{r^3}\boldsymbol{r} \tag{3.5}$$

The usefulness of this equation comes from the fact that it can be solved analytically in closed form. Thus, an expression that mathematically describes the orbit as a conic section can be derived using the conservation laws of orbital energy and angular momentum, as shown in Equation 3.6.

$$r = \frac{a(1 - e^2)}{1 + e\cos\theta} \tag{3.6}$$

This equation is also referred to as the *orbital equation*. The type of conic section that describes the orbit is dependent on the eccentricity value. For $e = 0$, the orbit is represented by a circle and for $0 < e < 1$ by an ellipse. Parabolic and hyperbolic orbits, represented by $e = 1$ and $e > 1$ respectively, are not of interest for an orbiter mission [23].

3.4. Perturbations

Under the two-body assumption, which is only valid when the primary body's mass distribution is axially symmetric around its rotation axis, the motion of the orbiting body is said to be Keplerian and is described by Equation 3.6 [23]. Any additional forces, called perturbations, lead to deviations from this Keplerian orbit and can be added to Equation 3.5 to obtain Equation 3.7, where $\boldsymbol{a}_p$ represents the perturbing accelerations vector [62].

$$\ddot{\boldsymbol{r}} = -\frac{\mu}{r^3}\boldsymbol{r} + \boldsymbol{a}_p \tag{3.7}$$

The gravitational acceleration for a given perturbing potential U can generally be formulated using Equation 3.8 [56]. In this equation, $\nabla = \partial/\partial\boldsymbol{r}$ is the gradient with respect to the inertial position.

$$\boldsymbol{a}_p = -\nabla U(\boldsymbol{r}) \tag{3.8}$$

The largest perturbations acting on an asteroid-orbiting spacecraft originate from the asteroid's mass irregularities, the effect of SRP and the gravitational pull of nearby bodies [13]. A first analysis of the magnitude of the accelerations acting on an Apophis-orbiting spacecraft is carried out by propagating the state of OSIRIS-REx for 42 days, starting 28 days before the Earth flyby. The accelerations included are the spherical harmonics (SH) gravity of Apophis up to degree and order (D/O) four, SH of Earth up to D/O 50, SH of the Moon up to D/O 50, cannonball SRP, and the point mass (PM) gravity of the Sun and the remaining Solar System planets. Further details on the set-up of the simulation environment, such as the employed integrator and propagator, are provided in Chapter 7. Thus, the acceleration norms in Figure 3.3 are obtained. An initial Keplerian state vector $\boldsymbol{\kappa}_0 = [1206, 0.32, 76, 220, 134, 0]^T$ defined with respect to the Apophis-centred, polar-equatorial reference frame is used for all plots in this chapter as it is known to survive the Earth flyby without impact or escape.

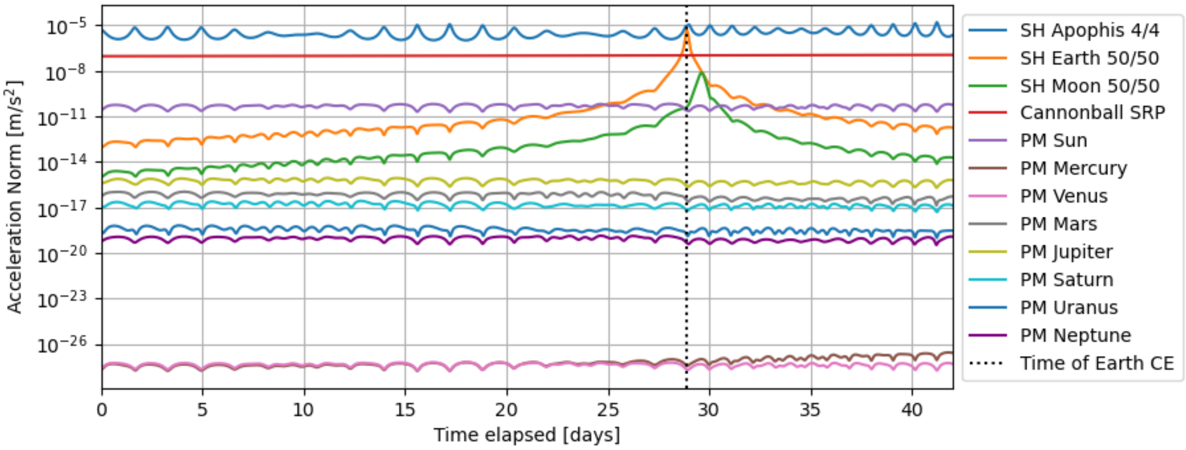

Figure 3.3: Acceleration norms of different perturbation sources for an initial Keplerian state vector $\boldsymbol{\kappa}_0 = [1206, 0.32, 76, 220, 134, 0]^T$ with a simulation start date of March 16, 2029.

It is confirmed that the main perturbations arise from the gravity of Apophis, SRP and the gravity from the Sun, Earth and Moon. The inverse square relation between acceleration and distance defined by Equation 3.5 is visible in the time evolution of the acceleration norms of the Earth and Moon due to the decreasing distance between the spacecraft and these bodies leading up to the close encounters. As expected, the acceleration norm corresponding to the Earth's PM gravity reaches its maximum value at the time of the Earth CE. For this initial Keplerian state and combination of accelerations, the propagation terminates upon reaching the end of the user-specified simulation time of 42 days.

It is also useful to look at the variation of some of the perturbations at different orbital altitudes. Figure 3.4 shows the acceleration norms for the zonal gravity of Apophis and SRP at different radial distances, obtained by varying the initial semi-major axis value. The acceleration norms are retrieved at the first time step of the simulation. The radial distance is measured from the centre of mass of the asteroid and the Brillouin sphere is defined at a radius of 280 m, following from the asteroid's maximum radius from the shape model of Aljbaae et al. presented in Subsection 2.2.3 [13].

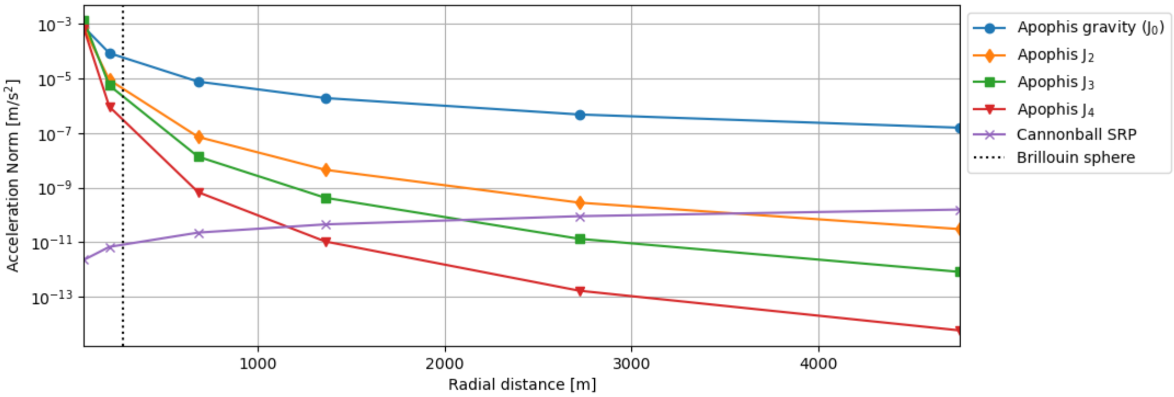

Figure 3.4: Acceleration norms of different perturbation sources at different radial distances, calculated for a Keplerian state vector $\boldsymbol{\kappa}_0 = [a, 0.32, 76, 220, 134, 0]^T$ on March 16, 2029.

The zonal coefficients are defined by $J_n = -C_{n,0}$. As expected, the magnitudes of the accelerations from Apophis' gravity decrease quadratically with increasing radial distance since the distance is computed from the asteroid's centre of mass, whereas the magnitude of SRP increases slightly with increasing radial distance. The latter can be attributed to the chosen initial Keplerian state vector, which represents an orbit slightly inclined towards the Sun at periapsis. Thus, increasing the radial distance by increasing the semi-major axis reduces the spacecraft-Sun distance. Furthermore, the order of magnitude of the accelerations due to zonal spherical harmonics coefficients matches the relative magnitudes of the coefficients shown in Table 2.4. Finally, it is noted that the SRP acceleration is lower than the shown zonal gravity terms for radial distances below 1200 m, suggesting that maintaining the spacecraft's altitude below 1000 m may help avoid orbital escape.

Apart from the accelerations shown in Figure 3.3, there are other accelerations acting on the spacecraft. For example, the *Poynting-Robertson* effect describes a phenomenon associated with SRP whereby a body is subjected to a drag-type force which causes it to lose angular momentum and slowly spiral towards the Sun. Nevertheless, even for small particles this process takes thousands to millions of years, so it can be assumed negligible for an asteroid-orbiting spacecraft with a limited mission duration in the order of months to years [23]. More relevant perturbations for this scenario are the spacecraft's thermal re-radiation and antenna pressure as well as the asteroid's thermal re-radiation. This was exemplified by the OSIRIS-REx mission around Bennu, where these perturbations had a magnitude of 10^{-8} and 10^{-10} m/s^2 respectively [63]. However, the modelling of these parameters is assumed to be beyond the scope of this study.

3.4.1. Spherical harmonics gravity

For a small body such as Apophis, where the irregularity of the shape and mass distribution is known to have a considerable effect on the spacecraft's orbital motion, the spherical harmonics model can be used to formulate the gravity potential. The gravitational potential expressed as a spherical harmonics series expansion is shown in Equation 3.9 [23].

$$U(\boldsymbol{r}) = \frac{\mu}{r}\left[\sum_{n=0}^{\infty}\sum_{m=0}^{n}\left(\frac{R}{r}\right)^{n} P_{n,m}(\sin\phi)\left\{\bar{C}_{n,m}\cos m\Lambda + \bar{S}_{n,m}\sin m\Lambda\right\}\right] \tag{3.9}$$

In this equation, the subscripts n and m represent the degree and order respectively. The reference radius of the central body – typically the equatorial radius – is given by R, while the $\bar{P}_{n,m}(\sin\phi)$ terms are normalised Legendre functions of the first kind. $\bar{C}_{n,m}$ and $\bar{S}_{n,m}$ are the normalised spherical harmonics coefficients. Finally, r, ϕ and Λ are the radial distance, latitude and longitude respectively [23].

If Equation 3.9 is truncated at $n = m = 0$, the expression simplifies to that of the point mass gravitational potential. Other combinations of n and m represent the variations in both north-south and east-west directions, as illustrated in Figure 3.5 [64].

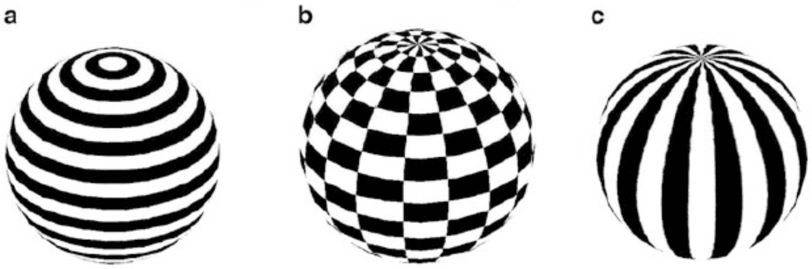

Figure 3.5: Illustration of spherical harmonics for a) zonal harmonics ($n \neq 0, m = 0$), b) tesseral harmonics ($m \neq n \neq 0$) and c) sectorial harmonics ($m = n \neq 0$) [64].

The effect on the orbital element evolution of the addition of Apophis' spherical harmonics gravity to the two-body, point mass solution is visible in Figure 3.6.

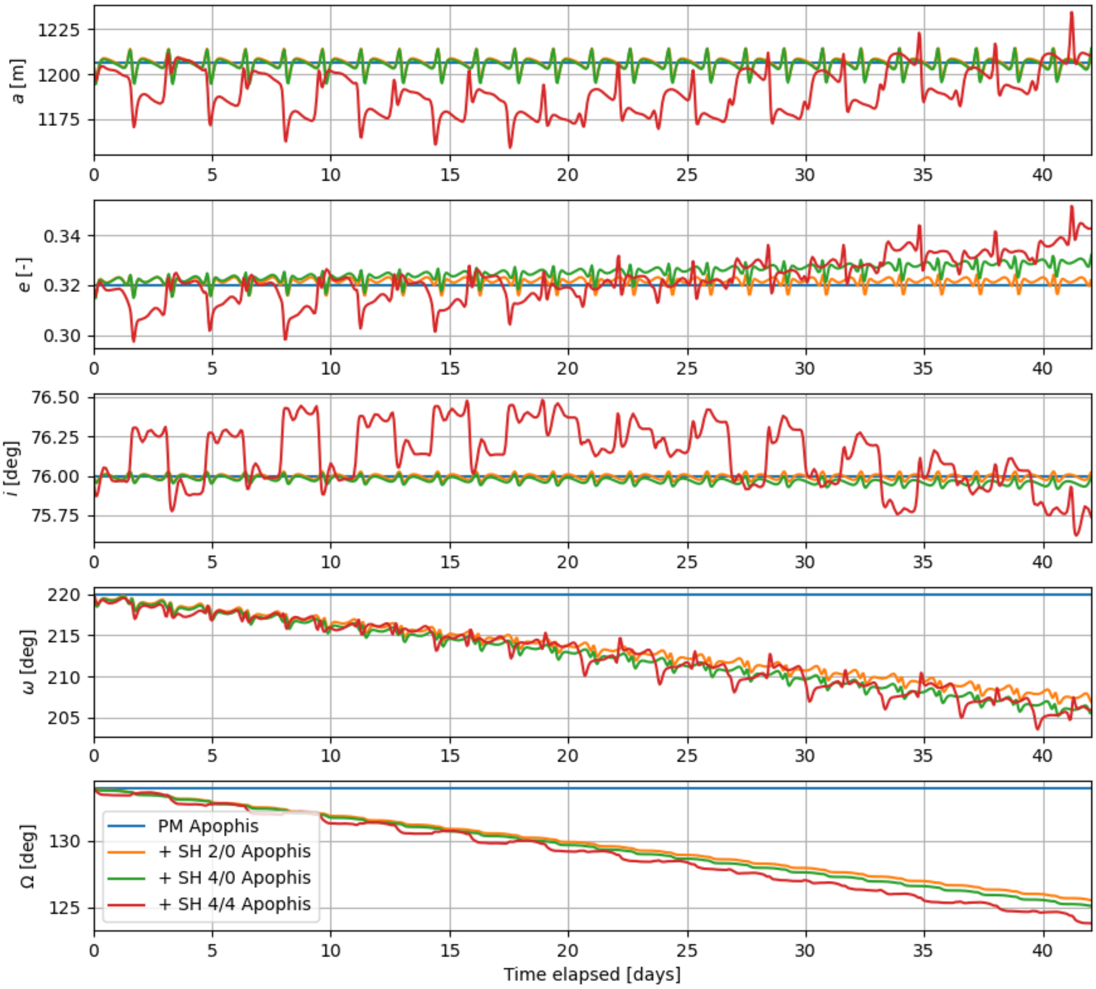

Figure 3.6: Orbital element evolution upon addition of Apophis' spherical harmonics gravity truncated at D/O 2/0, 4/0 and 4/4 for an initial Keplerian state vector $\boldsymbol{\kappa}_0 = [1206, 0.32, 76, 220, 134, 0]^T$ with a simulation start date of March 16, 2029.

It is first noted looking at Figure 3.6 that the orbital elements for the 'PM Apophis' solution are constant over time, which is in accordance with the two-body theory described in Section 3.3. The true anomaly has been omitted as it is known to vary periodically. For a semi-major axis of 1206 m, the orbital period is of approximately 1.6 days. The short-period effects in the order of one orbital period for the zonal gravity perturbations can be attributed to the fact that this is the time it takes for the spacecraft to go over the same latitude, a parameter associated with the definition of the SH gravitational potential as shown in Equation 3.9.

Furthermore, a secular effect is observed for the argument of periapsis and longitude of the ascending node. The secular variation in the longitude of the ascending node is a well-known effect referred to as nodal precession and is induced by the oblateness of the central body, as is the precession of the argument of periapsis [21]. The direction of the nodal precession depends on the inclination of the orbit. For an oblate body, the effect of the equatorial bulge on a prograde orbit will lead the longitude of the ascending node to drift westwards, i.e. the precession is negative [23]. This matches the behaviour observed in Figure 3.6 for the drift in the longitude of the ascending node, since the orbital inclination of $\sim 76^{\circ}$ corresponds to a prograde orbit.

The behaviour upon the addition of higher zonals and tesserals is harder to predict because the coefficients can have different signs, leading some periodic effects to cancel each other out. In fact, this is why the '+ SH 2/0' solution and the '+ SH 4/0' solution are almost the same although Apophis' J_3 and J_4 coefficients are only 1.75 and 12 times smaller than J_2 respectively. For reference, Earth's higher-order zonals are in the order of 1000 times smaller than J_2 [65]. Furthermore, Figure 3.6 suggests that the inclusion of the tesseral gravity terms is important as the full gravity model up to degree and order 4 leads to the largest orbital element variations. This is expected since, for example, the $C_{2,2}$ coefficient is only three times smaller than J_2 [13].

In terms of the magnitude of the periodic and secular variations induced by the degree and order 4 gravity field of Apophis, a maximum variation of approximately 74 m is observed for the semi-major axis, 0.05 for the eccentricity, 0.9° for the inclination, 16° for the argument of periapsis and 10° for the longitude of the ascending node. It is clear that the variation in the orbital elements upon the addition of the tesseral harmonics terms cannot be assumed to be negligible. It is thus concluded that the inclusion of the tesseral harmonics terms is required for the modelling of Apophis' gravity field.

3.4.2. Gravitational perturbation by other bodies

In reality, the presence of other celestial bodies, such as the Sun or nearby planets, can also cause large changes in the spacecraft's orbit. Although the spherical harmonics formulation can be used to define the accelerations induced by these bodies, the point mass assumption can be an accurate simplification for faraway bodies. The gravitational potential is then expressed as shown in Equation 3.10 [56].

$$U(\boldsymbol{r}) = \frac{\mu}{\|\boldsymbol{r}\|} = \frac{\mu}{r} \tag{3.10}$$

As expected, combining Equations 3.8 and 3.10 leads to the equation of motion of the two-body problem previously shown in Equation 3.5. For bodies in closer proximity, such as the Earth during the 2029 flyby, the spherical harmonics expansion can be used as defined in Equation 3.9.

In numerical simulations, the gravitational potential is defined in the same way for all bodies, regardless of them being central or third bodies. The software handles the computation of the perturbation as a third-body acceleration or central gravitational acceleration based on the definition by the user of the propagation origin, which is usually assigned to the central body. In this work, the propagation origin is assigned to the asteroid as described in Section 7.1. The acceleration due to a third-body perturbation is computed from Equation 3.11 when the central body is non-inertial, where A is the spacecraft, B is the third body, and C is the central body [56].

$$\ddot{\boldsymbol{r}} = \nabla U_B(\boldsymbol{r}_A) - \nabla U_B(\boldsymbol{r}_C) \tag{3.11}$$

For a preliminary analysis of the effect of third-body perturbations, the effect on the orbital element time evolution upon the addition of the point mass gravity of different third bodies compared to the two-body, point mass solution is assessed. Considering the acceleration magnitudes seen in Figure 3.3, only the effects of the Sun, Moon and Earth are investigated here. In Figure 3.7, the effects of the perturbations from the Sun and Moon on the orbital elements are shown.

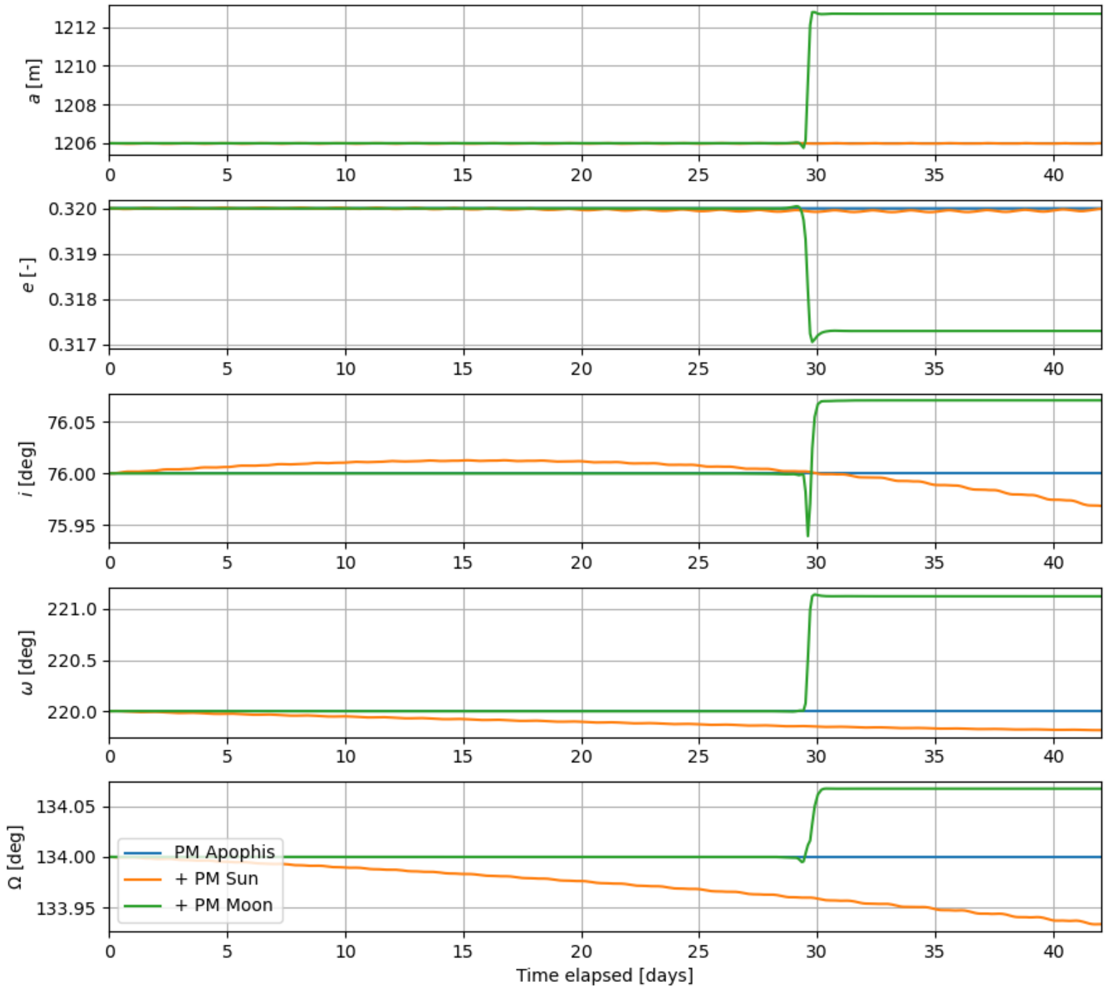

Figure 3.7: Orbital element evolution upon addition of the point mass gravity of the Sun and Moon for an initial Keplerian state vector $\boldsymbol{\kappa}_0 = [1206, 0.32, 76, 220, 134, 0]^T$ with a simulation start date of March 16, 2029.

Looking at the effect of including the perturbations due to the Moon's gravity, a negligible effect is observed until the time of the Moon flyby. The drift behaviour during this time is simply explained by Equation 3.10. The acceleration induced by the Moon increases as the spacecraft gets closer to it, i.e., as r becomes smaller, leading the orbital elements to change at the time of the flyby. Even then, the effect is still small, being in the order of 6.5 m for the semi-major axis, 0.003 for the eccentricity, and 1° or less for the inclination, argument of periapsis and longitude of the ascending node. The relatively small drift in the orbital elements is logical since the closest encounter with the Moon happens at a larger distance than that of the Earth, at around 96,000 and 37,000 km respectively, and the mass of the Moon is ~ 100 times smaller than that of the Earth [23, 45]. Furthermore, the orbital elements stabilise right after the Moon flyby, which can be attributed to the fact that the asteroid passes the Moon at very high speed and thus the Moon's gravitational perturbation is only at its peak for a short time.

For the Sun's contribution a more stable effect can be observed on the orbital element drift as the distance to the Sun is approximately constant. The short-term periodic effects, which can be linked to the small changes in the spacecraft-Sun distance over one orbital period, are especially small because, for the orbit shown, the orientation of the orbital plane is almost perpendicular to the Sun-asteroid position vector. This means the spacecraft's distance to the Sun is almost constant over one orbit and there are no eclipses from the asteroid itself. For an equatorial orbit, a much larger short-term periodic variation would be seen.

Similarly, the effect of the addition of the point mass gravity and spherical harmonics gravity up to D/O 2/0 of the Earth is presented in Figure 3.8.

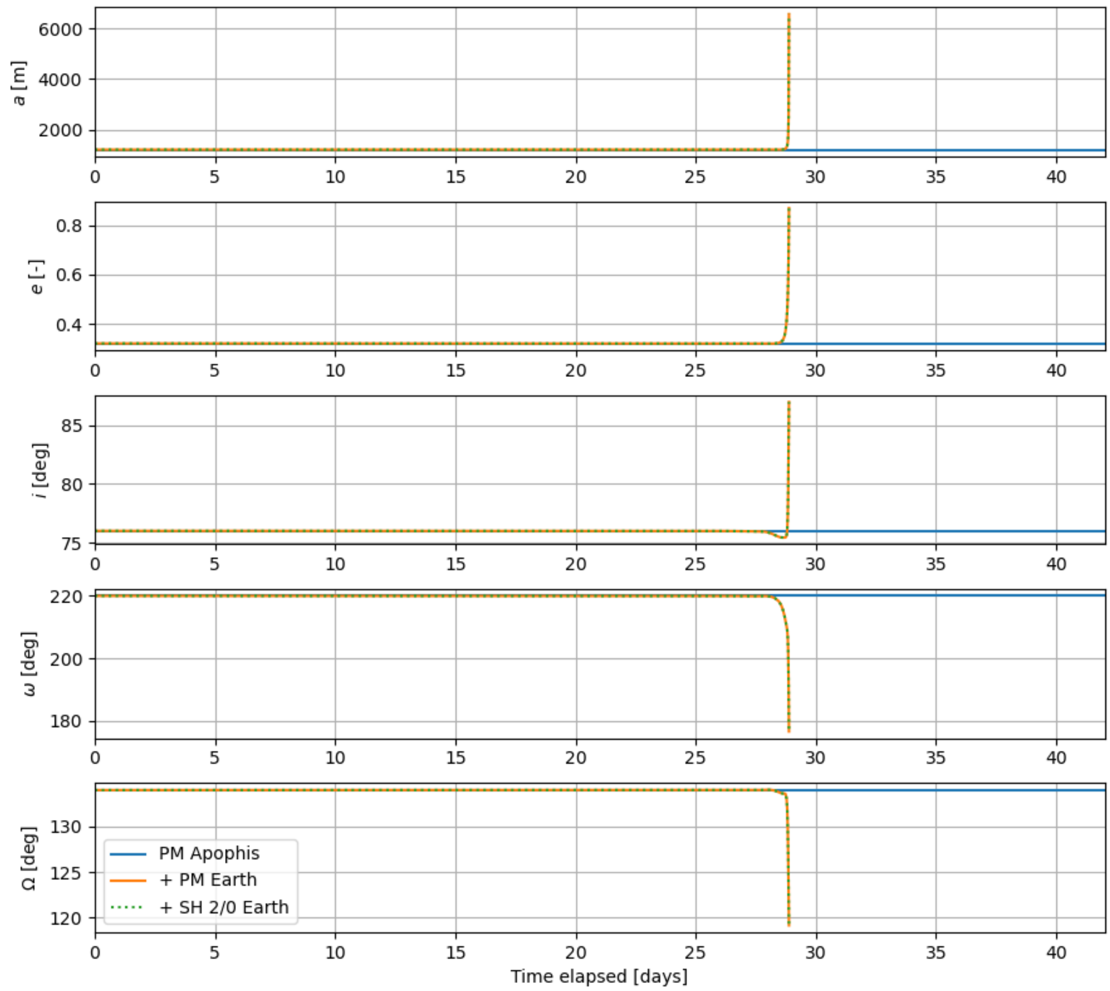

Figure 3.8: Orbital element evolution upon addition of the point mass gravity of the Earth and the spherical harmonics gravity up to D/O 2/0 for an initial Keplerian state vector $\boldsymbol{\kappa}_0 = [1206, 0.32, 76, 220, 134, 0]^T$ with a simulation start date of March 16, 2029.

Including the effect of Earth's gravity seems to have a negligible effect up until the time of the Earth flyby. In fact, the magnitude of the accelerations induced by the flyby leads to orbital escape, which is why the simulation ends at this time. This illustrates the importance of balancing the perturbations to obtain a stable orbit, since the chosen initial Keplerian state is known to survive the Earth flyby when all accelerations in Figure 3.3 are included. Although the addition of Earth's oblateness defined by the J_2 term seems to have a negligible effect in Figure 3.8, a more in-depth assessment of the contributions of different accelerations based on the difference in position when adding or removing accelerations is provided in Section 7.4.

3.4.3. Solar radiation pressure

As seen in Figure 3.3, SRP is the second-largest perturbation prior to the CE. One way of formulating the effect of SRP involves assuming the radiation stems from a source located at an infinite distance and the illuminated body is a perfect sphere, i.e. the cannonball model. Under these assumptions, the acceleration due to SRP is obtained from Equation 3.12 [56].

$$\ddot{\boldsymbol{r}} = \left(\frac{P}{4\pi c}\right)\left(\frac{C_r S_{ref}}{m_{sc}}\right)\frac{\boldsymbol{r}}{r^3} \tag{3.12}$$

Here, P is the total power or luminosity of the Sun, c is the speed of light, C_r is the reflection coefficient, S_{ref} is the reference area of the spacecraft and m_{sc} is the spacecraft mass. Thus, the SRP effect is dependent on the chosen spacecraft and the position vector. The effect of (partial) eclipses can be modelled by multiplying Equation 3.12 by a shadow function, which returns a value of 0 when the spacecraft is in umbra, a value between 0 and 1 when in penumbra, and a value of 1 when fully in sunlight [21].

The effect of the addition of SRP using the cannonball model is shown in Figure 3.9.

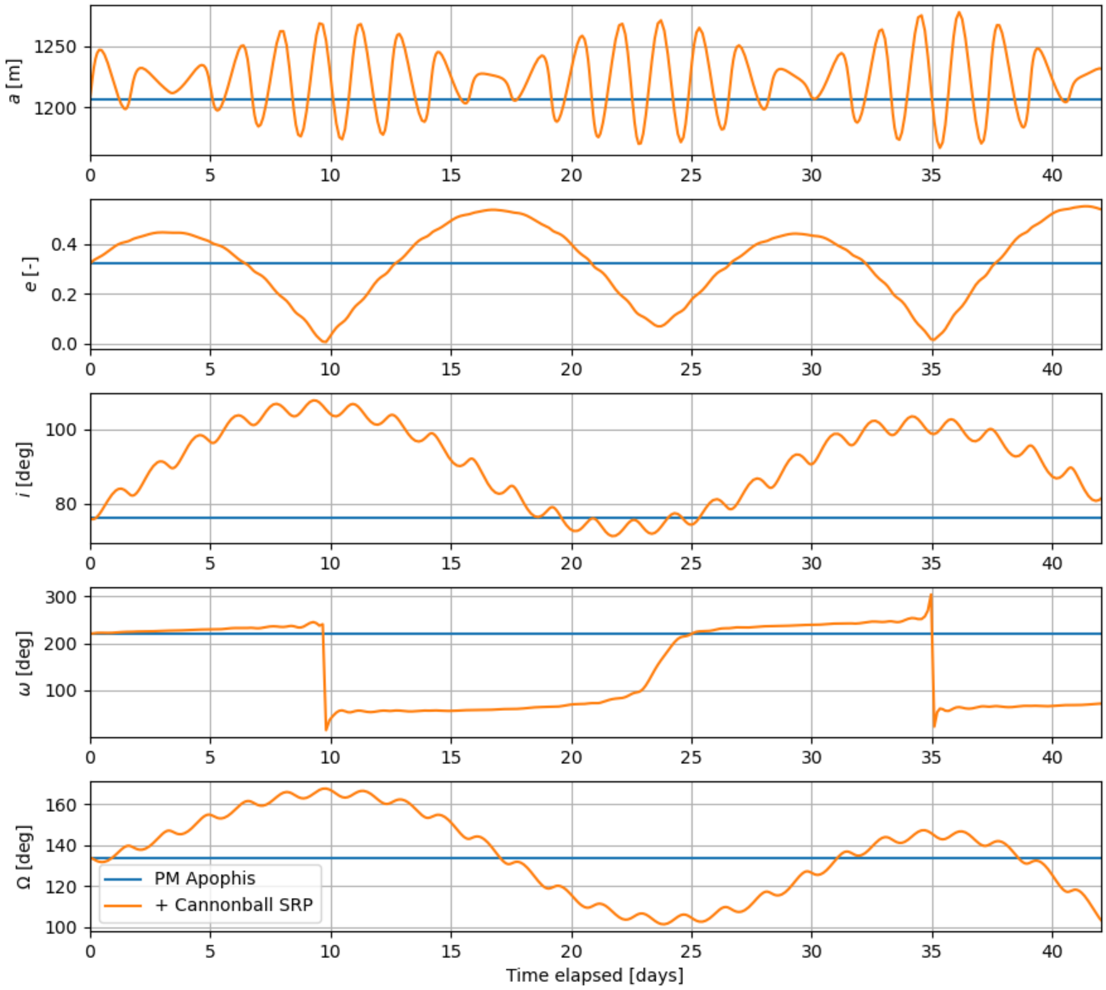

Figure 3.9: Orbital element evolution upon addition of the cannonball solar radiation pressure for an initial Keplerian state vector $\boldsymbol{\kappa}_0 = [1206, 0.32, 76, 220, 134, 0]^T$ with a simulation start date of March 16, 2029.

Compared to the other perturbations, SRP has the largest effect on the drift of the orbital elements, as expected by looking at the acceleration norms in Figure 3.3. The drift induced on the semi-major axis leads to variations of up to 100 m. The maximum change in eccentricity is around 0.54 and for the inclination it is around $37°$, leading the orbit to switch between prograde and retrograde rotation. The secular variation of ω leads to it going through all possible values, while Ω varies by up to $65°$.

In this chapter, the effects of the main perturbations have been analysed on an individual basis. The design of the frozen orbits will involve the balancing of these perturbations such that they cancel out to provide a stable orbit with quasi-constant eccentricity and argument of periapsis. Although all perturbations evaluated in this chapter have an effect on the orbital element evolution, an in-depth assessment of which perturbing accelerations are to be included in numerical simulations is provided in Section 7.4.

II

Analytical Analysis

An analytical analysis is carried out to investigate the solution space of frozen orbits around Apophis during the time of the flyby. The methodology is described in Chapter 4, while the analytical results and the comparison to numerical simulations are presented in Chapter 5.

4

Methodology

An analytical assessment of the frozen orbit solutions for an Apophis-orbiting spacecraft is carried out to gain initial insights into the solution space and, later on, have a point of reference for the numerical analysis and its results. As discussed in Chapter 1, several authors have undertaken the endeavour of deriving analytical equations for the analysis of frozen orbits around Apophis and other small bodies. For this work, the analytical solutions are obtained by following the method of Kikuchi, Oki, and Tsuda [5]. Due to the inclusion of the central body's zonal terms up to degree four and the effect of SRP, this formulation of Lagrange's Planetary Equations is considered to be the best approximation for this work available in literature. The frozen orbit definition of Kikuchi et al. involves setting the e, ω and Ω drift to zero, as the focus is on finding Sun-synchronous frozen orbits. In this work, the classical definition is assumed, which means the frozen orbit condition is defined by Equation 4.1.

$$\frac{d\omega}{dt} = \frac{de}{dt} = 0 \tag{4.1}$$

Under this condition, the altitude of the spacecraft above a given point on the asteroid's surface will be constant across consecutive passes [23]. Note that the frozen orbit definition is based on the long-term time derivative of the orbital element evolution rather than the instantaneous derivative. Thus, short-period variations, typically in the order of one orbital period, may still be present in a frozen orbit.

This chapter describes the methodology used for the analytical analysis, starting with the definition of the problem and its main assumptions in Section 4.1. Then, the derivation of the averaged potential functions is shown in Section 4.2. Lagrange's Planetary Equations are introduced in Section 4.3 to describe the time evolution of the orbital elements, while analytical formulations of the collision and escape conditions are given in Section 4.4. The method used to assess orbital stability is described in Section 4.5.

4.1. Problem Definition and Assumptions

The derivation of the time derivatives of the orbital elements is based on the averaging of Lagrange's Planetary Equations. The following assumptions and considerations are made:

- **Perpendicular-rotation assumption:** the asteroid orbital and equatorial planes are co-planar, with the consequence that the obliquity with respect to the ecliptic satisfies either $\varepsilon = 0°$ or $\varepsilon = 180°$. Equivalently, this means the asteroid's spin axis is assumed to be perpendicular to its orbital plane. The obliquity of Apophis' spin axis with respect to the ecliptic is 176°, so the assumption does not match the reality but is quite reasonable.
- **Acceleration assumption:** the only perturbations included are those due to the asteroid's J_2, J_3 and J_4 gravity and solar radiation pressure. Thus, tesseral terms and higher-order zonals are assumed to be negligible, as well as any other contribution such as third-body gravitational perturbations.

- **Full illumination assumption:** shadowing effects are not included in the formulation of solar radiation pressure. Thus, the spacecraft is assumed to be continuously in sunlight.

The Hill coordinate frame, which is the reference frame used to derive the analytical equations, is a rotating reference frame with its origin at the asteroid centre. In this frame, the x-axis points towards the anti-Sun direction and the z-axis is parallel to the angular velocity vector, i.e. perpendicular to the asteroid's orbital plane. The y-axis simply completes the right-handed orthogonal frame. The perpendicular-rotation assumption is necessary for this frame to be orthogonal. The definition of the frame and the orbital elements with respect to the asteroid's orbital and equatorial planes is shown in Figure 4.1.

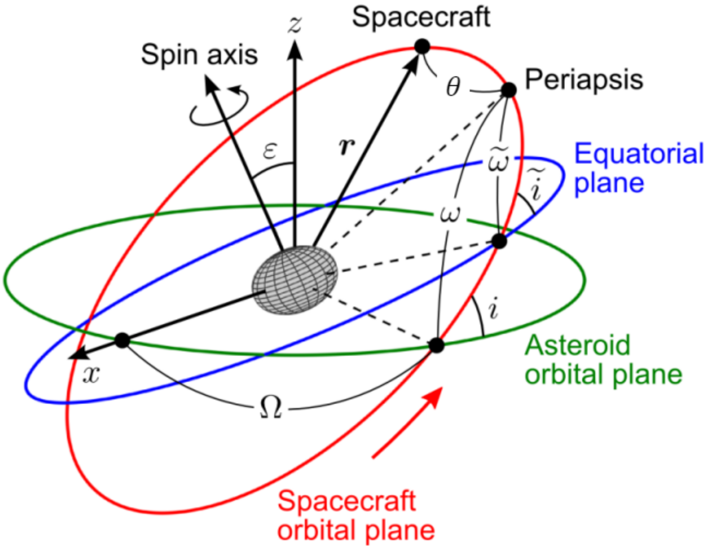

Figure 4.1: Reference frame and orbital element definition. Adapted from [5].

Here, i and ω are defined as the inclination and argument of periapsis with respect to the asteroid's orbital plane, while $\tilde{i}$ and $\tilde{\omega}$ are measured with respect to the asteroid's equatorial plane. The gravitational perturbations from the central body are typically measured with respect to the asteroid's equatorial plane while the SRP perturbation is more easily formulated with respect to the asteroid's orbital plane, as shown in Section 4.2.

4.2. Perturbation Functions

The perturbation potential functions for the zonal gravity up to degree four and SRP as a function of the orbital elements are given by Equation 4.2. For the full derivation, the reader is referred to the work of Kikuchi, Oki, and Tsuda [5].

$$\begin{aligned}
U_{J_2} &= -\frac{\mu J_2}{r}\left(\frac{R}{r}\right)^2 \times \frac{1}{2}\left\{3\sin^2\tilde{i}\sin^2(\tilde{\omega}+\theta)-1\right\} \\
U_{J_3} &= -\frac{\mu J_3}{r}\left(\frac{R}{r}\right)^3 \times \frac{1}{2}\left\{5\sin^3\tilde{i}\sin^3(\tilde{\omega}+\theta)-3\sin\tilde{i}\sin(\tilde{\omega}+\theta)\right\} \\
U_{J_4} &= -\frac{\mu J_4}{r}\left(\frac{R}{r}\right)^4 \times \frac{1}{8}\left\{35\sin^4\tilde{i}\sin^4(\tilde{\omega}+\theta)-30\sin^2\tilde{i}\sin^2(\tilde{\omega}+\theta)+3\right\} \\
U_{SRP} &= pr\left\{\cos\Omega\cos(\omega+\theta)-\cos i\sin\Omega\sin(\omega+\theta)\right\}
\end{aligned} \tag{4.2}$$

For the definition of the SRP potential, the constant p is introduced as defined by Equation 4.3, where d is the asteroid-Sun distance [5].

$$p \equiv \frac{C_r P S_{ref}}{c d^2 m_{sc}} \tag{4.3}$$

Formulating the perturbation potentials as a function of the orbital elements allows straight-forward averaging over one orbital period by integrating over the true anomaly θ as shown in Equation 4.4 [5]. In this way, short-period variations are removed.

$$\bar{U} = \frac{(1-e^2)^{\frac{3}{2}}}{2\pi} \int_0^{2\pi} \frac{U(\theta)}{(1+e\cos\theta)^2}\, d\theta \tag{4.4}$$

In order to write all perturbation functions using the same orbital elements, the parameter $\delta_\varepsilon = \cos\varepsilon$ is introduced, noting that for $\varepsilon = 0, 180°$, $\delta_\varepsilon = \pm 1$. Thus, the perpendicular-rotation assumption leads to the mathematical simplifications shown in Equation 4.5 [5].

$$\begin{array}{lcllcl} \sin\tilde{i} & = & \sin i & \cos\tilde{i} & = & \delta_\varepsilon \cos i \\ \sin\tilde{\omega} & = & \delta_\varepsilon \sin\omega & \cos\tilde{\omega} & = & \delta_\varepsilon \cos\omega \end{array} \tag{4.5}$$

Substituting Equation 4.5 into Equation 4.2 and performing the integral over one orbital period as shown in Equation 4.4 leads to the averaged perturbation potentials in Equation 4.6 [5].

$$\begin{array}{lcl} \bar{U}_{J_2} & = & \mu J_2 R^2 \times \dfrac{1}{4a^3(1-e^2)^{\frac{3}{2}}}(3\cos^2 i - 1) \\ \bar{U}_{J_3} & = & \mu J_3 R^3 \times \dfrac{3e}{8a^4(1-e^2)^{\frac{5}{2}}}(5\cos^2 i - 1)\delta_\varepsilon \sin\omega \\ \bar{U}_{J_4} & = & \mu J_4 R^4 \times \dfrac{3}{128a^5(1-e^2)^{\frac{7}{2}}}\{-10e^2 \sin^2 i(7\cos^2 i - 1)\cos 2\omega \\ & & \qquad - (2+3e^2)(35\cos^4 i - 30\cos^2 i + 3)\} \\ \bar{U}_{SRP} & = & -\dfrac{3}{2} pae(\cos\Omega\cos\omega - \cos i \sin\Omega \sin\omega) \end{array} \tag{4.6}$$

It is noted that δ_ε is only present in the averaged potential function for the J_3 zonal harmonics term. While the even zonal harmonics terms, i.e. J_2 and J_4, are symmetric about the equatorial plane, the odd zonals are not. Thus, the perturbation due to J_3 is dependent on the obliquity, and thus on δ_ε.

4.3. Lagrange's Planetary Equations

Lagrange's Planetary Equations (LPEs) are a set of six equations that mathematically define the evolution of the six orbital elements for a given perturbation potential U [21]. Using Lagrange's formulation, the time derivatives of e and ω can be estimated from Equation 4.7, where the averaged perturbation potential $\bar{U}$ is obtained from the summation of the potential functions in Equation 4.6 [5]. Because of the frozen orbit definition used in this work, the derivation of the time derivatives of the remaining orbital elements has been omitted.

$$\begin{aligned} \frac{de}{dt} &= \frac{1-e^2}{na^2e}\frac{\partial\bar{U}}{\partial\sigma} - \frac{\sqrt{1-e^2}}{na^2e}\frac{\partial\bar{U}}{\partial\omega} \\ \frac{d\omega}{dt} &= \frac{\sqrt{1-e^2}}{na^2e}\frac{\partial\bar{U}}{\partial e} - \frac{\cot i}{na^2\sqrt{1-e^2}}\frac{\partial\bar{U}}{\partial i} \end{aligned} \tag{4.7}$$

Here, σ is equal to $-Nt_0$, with N the mean motion of the asteroid around the Sun and t_0 the time of pericentre passage. The mean motion of the spacecraft around the asteroid is defined by $n = \sqrt{\mu/a^3}$, with μ being the gravitational parameter of the asteroid. Partial derivation of the averaged potentials presented in Equation 4.7 with respect to σ, ω, e and i leads to the final expressions for de/dt and $d\omega/dt$ in Equation 4.8 [5].

$$
\begin{aligned}
\frac{de}{dt} =& -\mathcal{K}_{SRP}\sqrt{1-e^2}(\cos\Omega\sin\omega+\cos i\sin\Omega\cos\omega)\\
&-\mathcal{K}_{J_3}\frac{1}{\left(1-e^2\right)^2}\sin i\left(5\cos^2 i-1\right)\cos\omega\\
&-\mathcal{K}_{J_4}\frac{e}{\left(1-e^2\right)^3}\sin^2 i\left(7\cos^2 i-1\right)\sin 2\omega\\
\frac{d\omega}{dt} =& -\mathcal{K}_{SRP}\frac{1}{e\sqrt{1-e^2}}\left\{\left(1-e^2\right)\cos\Omega\cos\omega-\cos i\sin\Omega\sin\omega\right\}\\
&+\mathcal{K}_{J_2}\frac{1}{2\left(1-e^2\right)^2}\left(5\cos^2 i-1\right)\\
&+\mathcal{K}_{J_3}\frac{1}{e\left(1-e^2\right)^3}\csc i\left\{e^2\left(35\sin^2 i\cos^2 i-4\right)\right.\\
&\left.+\sin^2 i\left(5\cos^2 i-1\right)\right\}\sin\omega\\
&+\mathcal{K}_{J_4}\frac{1}{4\left(1-e^2\right)^4}\left[2\left\{e^2\left(63\cos^4 i-56\cos^2 i+5\right)\right.\right.\\
&\left.-2\sin^2 i\left(7\cos^2 i-1\right)\right\}\cos 2\omega\\
&\left.-9e^2\left(21\cos^4 i-14\cos^2 i+1\right)-4\left(49\cos^4 i-36\cos^2 i+3\right)\right]
\end{aligned}
\tag{4.8}
$$

The parameters $\mathcal{K}_{SRP}$, $\mathcal{K}_{J_2}$, $\mathcal{K}_{J_3}$ and $\mathcal{K}_{J_4}$ are introduced to simplify the equations and are defined by Equation 4.9 [5]. For a given semi-major axis, these parameters are constants.

$$
\begin{aligned}
\mathcal{K}_{SRP}(a) &= \frac{3}{2}\frac{p}{na}\\
\mathcal{K}_{J_2}(a) &= \frac{3}{2}nJ_2\left(\frac{R}{a}\right)^2\\
\mathcal{K}_{J_3}(a) &= \frac{3}{8}n\delta_\varepsilon J_3\left(\frac{R}{a}\right)^3\\
\mathcal{K}_{J_4}(a) &= \frac{15}{32}nJ_4\left(\frac{R}{a}\right)^4
\end{aligned}
\tag{4.9}
$$

Assuming ω, $\Omega = \pm 90°$ in Equation 4.8 means $de/dt = 0$ for all a, e, i. Thus, the frozen orbit solutions can be obtained directly by finding the combinations of a, e and i that satisfy $d\omega/dt = 0$. In Equation 4.10, the simplified expression under this assumption is shown[1] [5].

$$
\begin{aligned}
\frac{d\omega}{dt} =& +\mathcal{K}_{\mathrm{SRP}}\frac{1}{e\sqrt{1-e^2}}\cos i\sin\Omega\sin\omega\\
&+\mathcal{K}_{J_2}\frac{1}{2\left(1-e^2\right)^2}\left(5\cos^2 i-1\right)\\
&+\mathcal{K}_{J_3}\frac{1}{e\left(1-e^2\right)^3}\csc i\left\{e^2\left(35\sin^2 i\cos^2 i-4\right)\right.\\
&\left.+\sin^2 i\left(5\cos^2 i-1\right)\right\}\sin\omega\\
&-\mathcal{K}_{J_4}\frac{1}{4\left(1-e^2\right)^4}\left\{e^2\left(315\cos^4 i-238\cos^2 i+19\right)\right.\\
&\left.+16\left(14\cos^4 i-11\cos^2 i+1\right)\right\}
\end{aligned}
\tag{4.10}
$$

The verification for the implementation of this method can be found in Subsection 11.1.1.

---

[1] Although all equations in this section are taken from Kikuchi, Oki, and Tsuda, a typo is present in their version of Equation 4.10 [5]. The sign of the $\mathcal{K}_{J_4}$ term in their work is positive when it should be negative. The corrected version is shown in this work.

4.4. Collision and Escape

Finding the solutions to $de/dt = d\omega/dt = 0$ from Equation 4.8 may lead to solutions which are invalid in real life. Collision and escape are two undesirable conditions for an orbiter spacecraft. Thus, analytical expressions are derived to identify the orbital element combinations at which they happen.

The derivation of the collision or impact condition follows straight-forwardly from the orbital equation in Equation 3.6. It is known that the smallest radial distance over one orbit occurs at periapsis r_p, which happens at $\theta = 0°$. This simplifies Equation 3.6 to $r_p = a(1-e)$, which is the equation for the pericentre distance. Thus, for a given a and e, surface impact with the asteroid occurs when $r_p = R_{max}$, with R_{max} being the maximum radius of the asteroid. This essentially places a constraint on the maximum eccentricity for a given semi-major axis, leading to the final expression for the collision condition expressed by Equation 4.11.

$$e_{max} = 1 - \frac{R_{max}}{a} \tag{4.11}$$

This expression can equivalently be used to place a lower limit on the minimum altitude h_{min} above the spacecraft's surface by substituting R_{max} for $R_{max} + h_{min}$. The impact condition is implemented in this way for the analytical results by placing a constraint by assuming $R_{max} = 280$ m. Furthermore, $h_{min} = 100$ m from the mission requirements presented in Subsection 2.3.1.

For the identification of the orbital escape condition, use is made of the *vis-viva equation*, which relates the specific orbital energy $\mathscr{E}$ to the orbit's semi-major axis a, position r and velocity V for any Keplerian orbit [23]. Note that V is the velocity with respect to a non-rotating reference frame. The relation is displayed in Equation 4.12.

$$\mathscr{E} = -\frac{\mu}{2a} = \frac{V^2}{2} - \frac{\mu}{r} \tag{4.12}$$

The specific orbital energy should be constant over time due to the energy conservation law for a Keplerian orbit. Orbital escape happens when $\mathscr{E} = 0$, which with some rearranging leads to Equation 4.13.

$$V_{esc} = \sqrt{\frac{2\mu}{r}} \tag{4.13}$$

Then, the escape condition is identified by Equation 4.14.

$$V \geq V_{esc} \tag{4.14}$$

Rearranging Equation 4.12 to make v the subject of the formula, substituting it into Equation 4.14, and simplifying leads to Equation 4.15.

$$a \leq 0 \tag{4.15}$$

According to the LPEs, even when including the perturbations from the central body's zonal gravity and SRP, $da/dt = 0$ after removing short-period variations in the order of one orbital period [5]. This means that as long as the semi-major axis input for the generation of the analytical results has a positive value, the escape condition will not be reached. Information on the implementation of the collision-escape conditions for the numerical analysis is provided in Section 7.2.

4.5. Lyapunov Stability

Characterising the stability of the found frozen orbit solutions is a critical aspect of this analysis, as the averaging of the perturbations over an orbital period and the approximation of including only zonal gravity terms can lead to unstable behaviour for a spacecraft in a real space environment. Analysis of the orbital stability can be carried out analytically via linearisation of the LPEs.

Defining $\boldsymbol{X} = [a, e, i, \Omega, \omega]^T$, the LPEs can be rewritten as $\dot{\boldsymbol{X}} = \boldsymbol{f}(\boldsymbol{X})$. Since frozen orbits are equilibrium points where the derivatives of the orbital elements are zero, $\dot{\boldsymbol{X}}$ can be linearised around the equilibrium state. For a frozen orbit solution $\boldsymbol{X}^*$, $\boldsymbol{f}(\boldsymbol{X}) = 0$ and $\delta\boldsymbol{X} = \boldsymbol{X} - \boldsymbol{X}^*$ is a small deviation from the equilibrium. Then, the variational equation is given by Equation 4.16 [5].

$$\delta\dot{\boldsymbol{X}} = \left.\frac{\partial\boldsymbol{f}}{\partial\boldsymbol{X}}\right|_{\boldsymbol{X}^*}\delta\boldsymbol{X} \tag{4.16}$$

The Jacobian matrix $\frac{\partial f}{\partial X}$ contains the partial derivatives with respect to the orbital elements of the time derivatives of the orbital elements. With the previous assumption that $\omega, \Omega = \pm 90°$, the Jacobian matrix simplifies to Equation 4.17 [5]:

$$\left.\frac{\partial\boldsymbol{f}}{\partial\boldsymbol{X}}\right|_{\boldsymbol{X}^*} = \begin{bmatrix} 0 & 0 & 0 & 0 & 0 \\ 0 & 0 & 0 & \mathcal{J}_A & \mathcal{J}_B \\ 0 & 0 & 0 & 0 & \mathcal{J}_C \\ \mathcal{J}_D & \mathcal{J}_E & \mathcal{J}_F & 0 & 0 \\ \mathcal{J}_G & \mathcal{J}_H & \mathcal{J}_I & 0 & 0 \end{bmatrix} \tag{4.17}$$

where $\mathcal{J}_A$, $\mathcal{J}_B$, $\mathcal{J}_C$, $\mathcal{J}_D$, $\mathcal{J}_E$, $\mathcal{J}_F$, $\mathcal{J}_G$, $\mathcal{J}_H$, $\mathcal{J}_I$ are given in Appendix A. The eigenvalues λ_k of the linearised system, where $k \in \{1, ..., 5\}$, determine the stability characteristics of the equilibrium point. The eigenvalues follow the form $\lambda = Re(\lambda) + Im(\lambda)i$, where $Re(\lambda)$ represents the real part, $Im(\lambda)$ the imaginary part and i is the imaginary number. Thus, the solution of the linearised equations of motion can be written as Equation 4.18. Note here that e is Euler's number and *not* the orbital eccentricity.

$$\delta\boldsymbol{X} = \sum_{k=1}^{5} c_k e^{\lambda_k} = \sum_{k=1}^{5} c_k e^{Re(\lambda_k)t}(\cos Im(\lambda_k)t + i\sin Im(\lambda_k)t) \tag{4.18}$$

From Equation 4.18, it is apparent that the real parts of the eigenvalues dictate the overall stability of the system while the imaginary parts only affect the oscillatory behaviour. The values of c_k are simply constants determined by the initial conditions. If all the eigenvalues have negative real parts, the equilibrium is said to be asymptotically stable, indicating that any small perturbation from the equilibrium will decay over time. On the other hand, if just one of the eigenvalues has a real positive part, even a small initial perturbation can lead to an exponential deviation from the equilibrium. Thus, Lyapunov stability is achieved when all the real parts of the eigenvalues are ≤ 0 [5]. Following from this definition, the stability index ζ in Equation 4.19 is introduced.

$$\zeta = max(Re(\lambda_k)) \tag{4.19}$$

Thus, stable orbits are characterised by $\zeta \leq 0$.

5

Results

With the methodology covered, the analytical frozen orbit results and their stability are presented in Section 5.1. The analytical results are then compared to numerical simulations in Section 5.2. Final conclusions on the strengths and limitations of the analytical method are provided in Section 5.3.

5.1. Analytical Results

The initial results are obtained by calculating $d\omega/dt$ over a grid of e and i values for a given a, for all combinations of ω and Ω. Then, the values of e and i at which $d\omega/dt = 0$ are found by locating the points at which the output of the $d\omega/dt$ function changes sign. This means the accuracy of the results is dependent on the $e - i$ grid resolution used in the numerical implementation to obtain the analytical solutions. The results for different values of a are displayed in Figure 5.1, with the impact condition implemented as defined in Section 4.4.

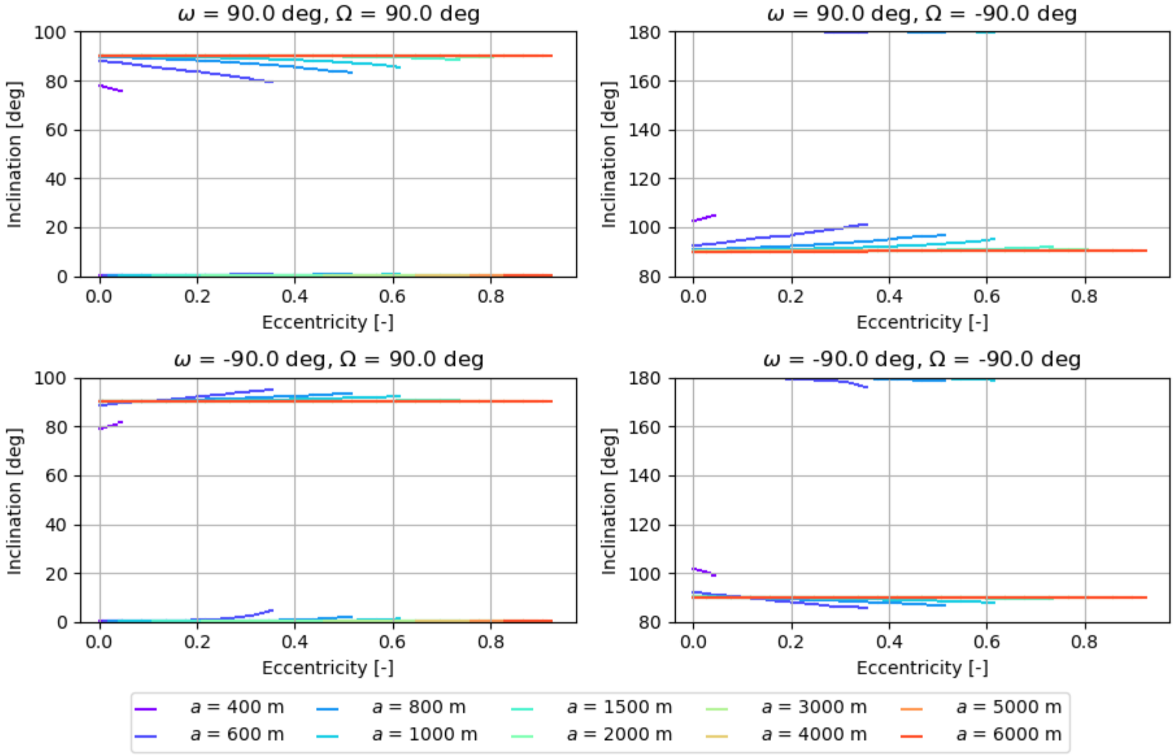

Figure 5.1: Frozen orbit solutions, corresponding to $d\omega/dt = de/dt = 0$, for different combinations of a,ω and Ω.

It is first noted that the solutions for lower a reach a lower maximum e than the ones with higher values of a. This follows from the constraint on surface impact with the additional requirement of having a minimum altitude above the surface of at least 100 m. For example, for a = 400 m, the maximum allowable eccentricity considering the minimum altitude requirement and the maximum radius of the asteroid of 280 m would be 0.05, as seen in the plots. Thus, this observation is independent from the frozen orbit condition.

The solutions can be divided into two main families: near-polar and near-equatorial orbits. The former group contains solutions ranging in inclination from 75° to 105°, while the latter ranges between 175° and 5°. This means in both groups there are both prograde and retrograde solutions. Furthermore, when Ω = 90° the near-equatorial solutions are all prograde orbits, whereas, for Ω = -90°, all orbits are retrograde.

For the near-polar solutions, symmetry in the inclination is observed for solutions with conjugate values of Ω and equal ω. Namely, for a given a, e and ω, if a frozen orbit solution exists for Ω = 90° at, e.g. i = 80°, the solution for the conjugate value of Ω = -90° will also be the conjugate of the inclination at 180 - 80 = 100°. Orbits with conjugate Ω and i have the same orientation but with the spacecraft orbiting in the reverse direction. Since only zonal gravity terms have been included, which are axially symmetric, and the orientation of these orbits with respect to the Sun is identical, meaning the perturbations from SRP are equal for either orbit, it is logical that this symmetry in the solution space is observed. It is expected that the inclusion of tesseral gravity terms would lead to non-symmetric solutions for conjugate pairs of Ω. Furthermore, a pattern is seen whereby orbits with lower semi-major axis exhibit frozen behaviour for inclinations deviating from 90°. At these inclinations, the effects of SRP and zonal gravity cancel out. For higher a, the zonal gravity terms are too weak to counteract the effects of SRP and thus the only solution is at exactly 90°, as it is at this inclination that the orbital plane is exactly perpendicular to the Sun-asteroid line and the SRP magnitude is constant over time. These orbits are generally referred to as Sun-terminator frozen orbits [5].

For near-equatorial orbits the latitude of the spacecraft is almost constant over time, meaning that the perturbations due to the central body's zonal gravity perturbations are also almost constant over time. The effect of SRP on this type of orbit in combination with zonal gravity perturbations is such that the precession of the orbit's argument of periapsis occurs at the same rate as the mean motion of the asteroid around the Sun. That is, the argument of periapsis is fixed with respect to the Sun-asteroid line, which stabilises the effects of SRP on the orbit. This type of orbit is referred to as a heliotropic or anti-heliotropic orbit depending on the location of the argument of periapsis. For ω = 90°, it is pointing towards the Sun and the orbit is anti-heliotropic, and vice versa for ω = -90°. This family of orbits is one of the typical solutions for frozen orbits around small bodies [5, 9].

At the time of writing, no previous studies have evaluated the Lyapunov stability of frozen orbits around Apophis. Here, the stability of the analytical frozen orbit solutions is assessed using the method described in Section 4.5 for all the discrete solutions shown in Figure 5.1. Since the analytical method is implemented numerically to obtain the results, a numerical rounding error is introduced in the process. The numerical precision for this work is 16 digits, so values of the stability index that are lower than 10^{-16} are rounded to zero to circumvent this issue. Furthermore, it is noted that for all cases, at least one of the eigenvalues has a real part that is greater than or equal to zero. This means there are no stable solutions with a negative stability index and all stable solutions correspond to a stability index of exactly zero after rounding.

First, the stability of the near-equatorial solutions with respect to the initial eccentricity and semi-major axis is shown in Figures 5.2 and 5.3.

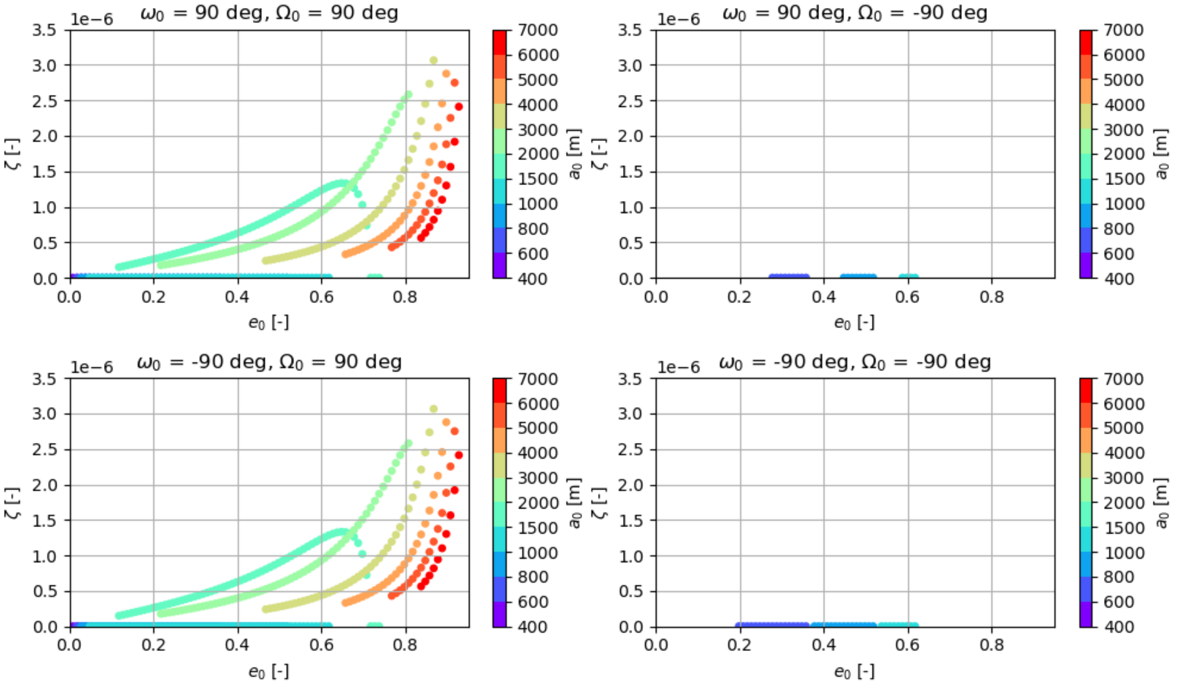

Figure 5.2: Stability index against initial eccentricity for near-equatorial analytical frozen orbit solutions.

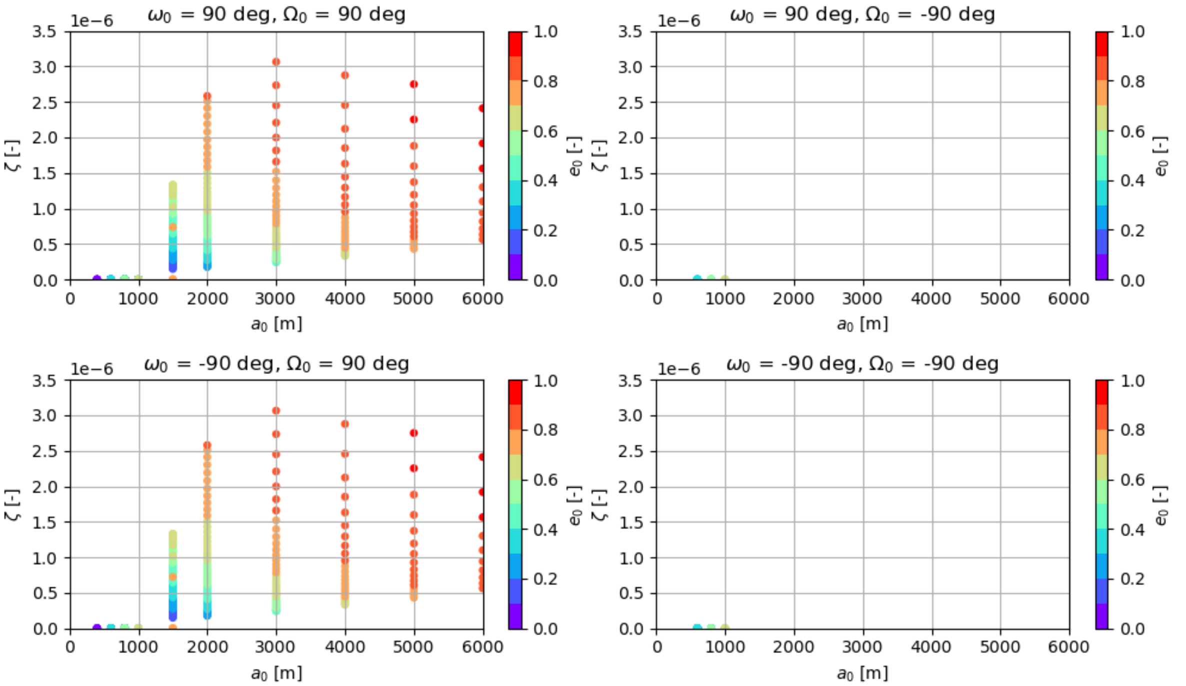

Figure 5.3: Stability index against initial semi-major axis for near-equatorial analytical frozen orbit solutions.

For Ω = 90°, there are no stable solutions for $e > 0.75$; for $e < 0.75$, ζ = 0 for all e when a = 400, 600, 800 and 1000 m and for $e \sim 0.73$ when a = 1500 m, indicating stable solutions. For Ω = -90°, all solutions have ζ = 0. It is also apparent that there are no stable solutions for $a > 1500$ m, indicating higher altitudes are inherently unstable for this case. There are seemingly only three solutions for Ω = -90° because, looking back at Figure 5.1, the near-equatorial solutions correspond to only three values of a. These results imply that a has a larger influence on the stability of the orbit than e.

The stability results for the near-polar solutions are given in Figures 5.4 and 5.5.

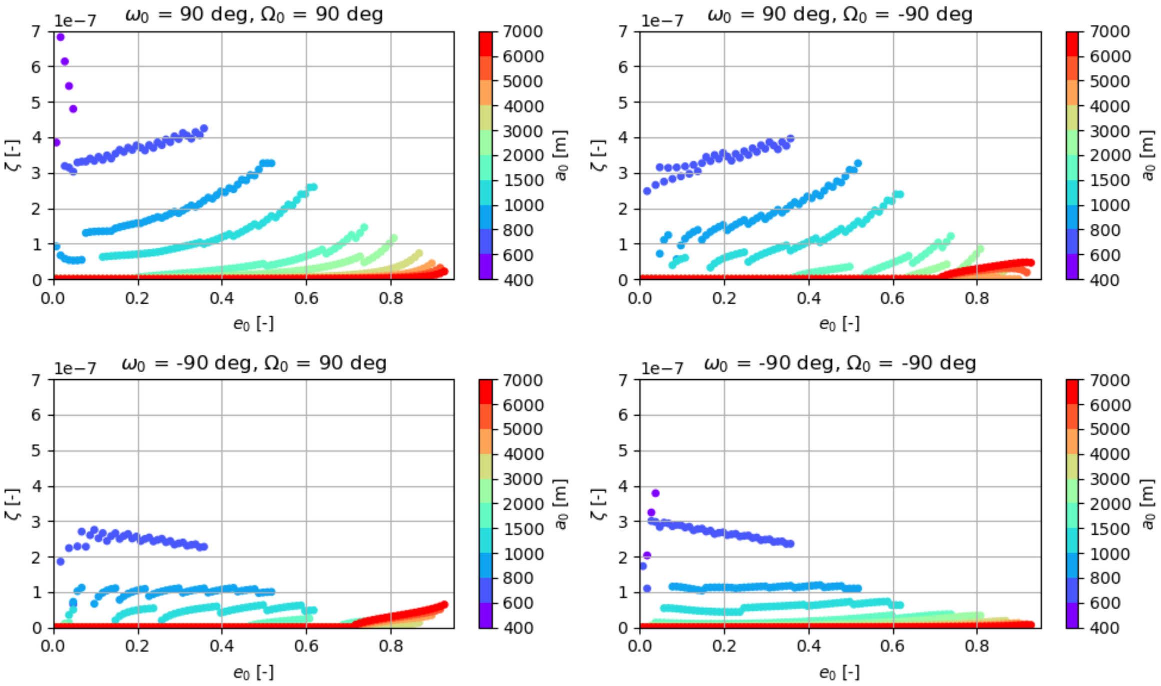

Figure 5.4: Stability index against initial eccentricity for near-polar analytical frozen orbit solutions.

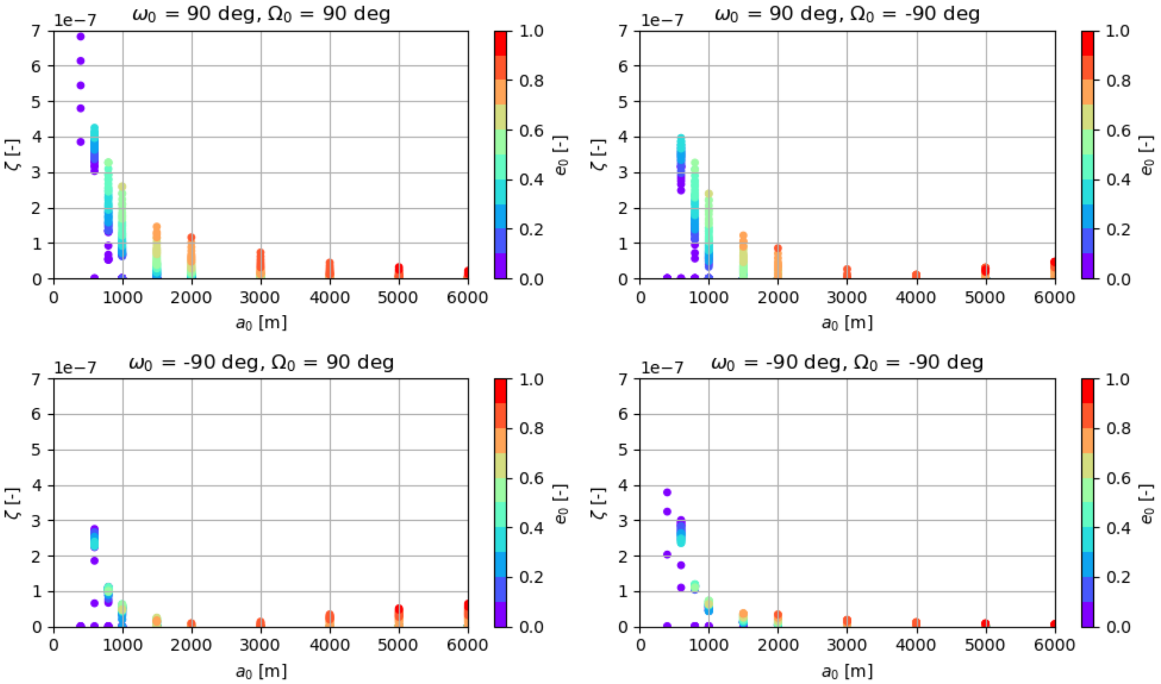

Figure 5.5: Stability index against initial semi-major axis for near-polar analytical frozen orbit solutions.

Stable orbits in the near-polar family are found at almost all values of eccentricity, showcasing the existence of both near-circular and high-eccentricity near-polar frozen orbits. With respect to the semi-major axis, stable orbits are also found at almost all sampled values of a, depending slightly on the combination of ω and Ω.

In conclusion, out of the 3476 discrete solutions shown in Figure 5.1, only 1503 have a stability index of 0. This means that more than half (56.8%) of the solutions found with the analytical method are unstable according to this parameter. Therefore, the frozen orbit solutions obtained from the derivation of the LPEs with SRP and zonal gravity up to degree four should be looked at critically.

5.2. Comparison with Numerical Simulations

To assess the quality of the analytical results, and look ahead at the numerical behaviour of frozen orbits presented in detail in Chapter 9, a comparison is made to the results obtained with numerical simulations. Since in the analytical method it has been assumed that the only perturbations are SRP and the zonal gravity perturbations of Apophis up to J_4, the same accelerations have been assumed in the numerical simulations. Furthermore, the rotation model of Apophis is defined such that the obliquity of the asteroid is 180° and the orbit of Apophis is assumed circular with a semi-major axis of 1 AU. Otherwise, the inputs described in Section 7.1 and the integrator selected in Section 7.3 have been used. Furthermore, the same termination conditions as described in Section 7.2 have been implemented, which include constraints on minimum altitude, maximum altitude and orbital escape.

5.2.1. Stability and termination time

The first part of the comparison with numerical results involves comparing the stability index to the termination time of the simulation. The 3476 discrete analytical frozen orbit solutions from Figure 5.1 are used as initial states for the simulation. Then, the state of the spacecraft is propagated for 28 days and the termination time is saved. If the simulation reaches one of the termination conditions, the simulation ends prematurely and the termination time is thus lower. If the stability index is a good indicator of stability, there should be a correlation between ζ and the termination time of the simulation.

Once again, the results have been divided into the near-polar and near-equatorial families. First, the stability index against termination time for the near-equatorial solutions is shown in Figure 5.6 with respect to the initial eccentricity, and in Figure 5.7 with respect to the initial semi-major axis.

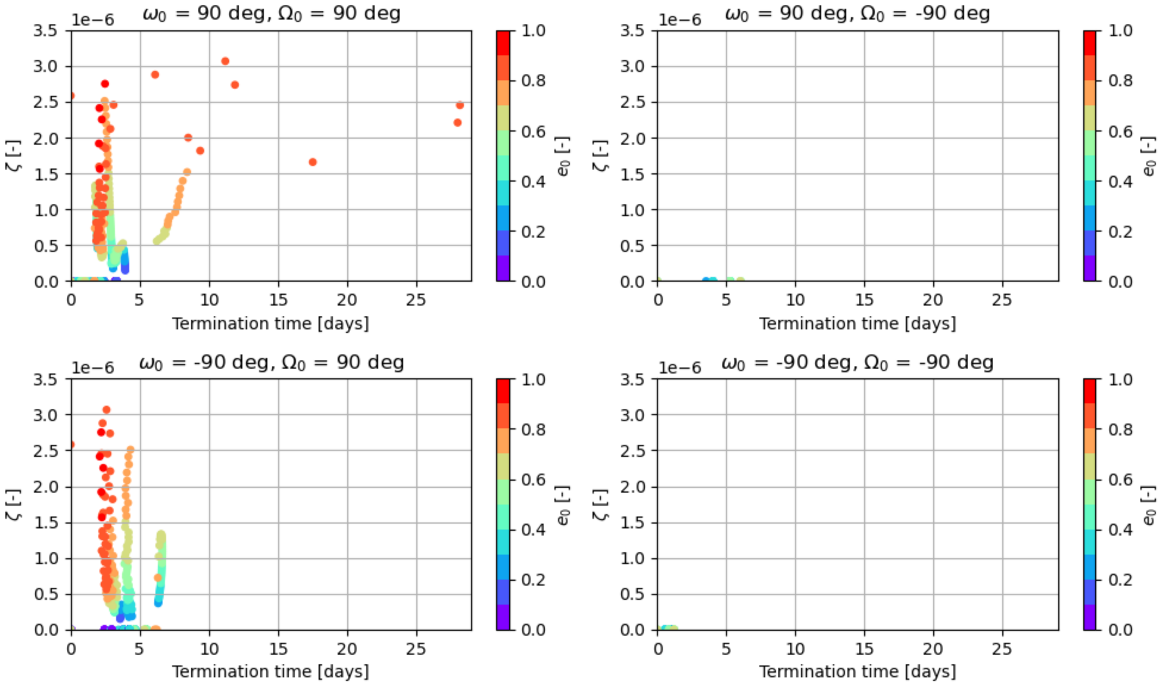

Figure 5.6: Stability index against propagation end time eccentricity for near-equatorial orbit solutions.

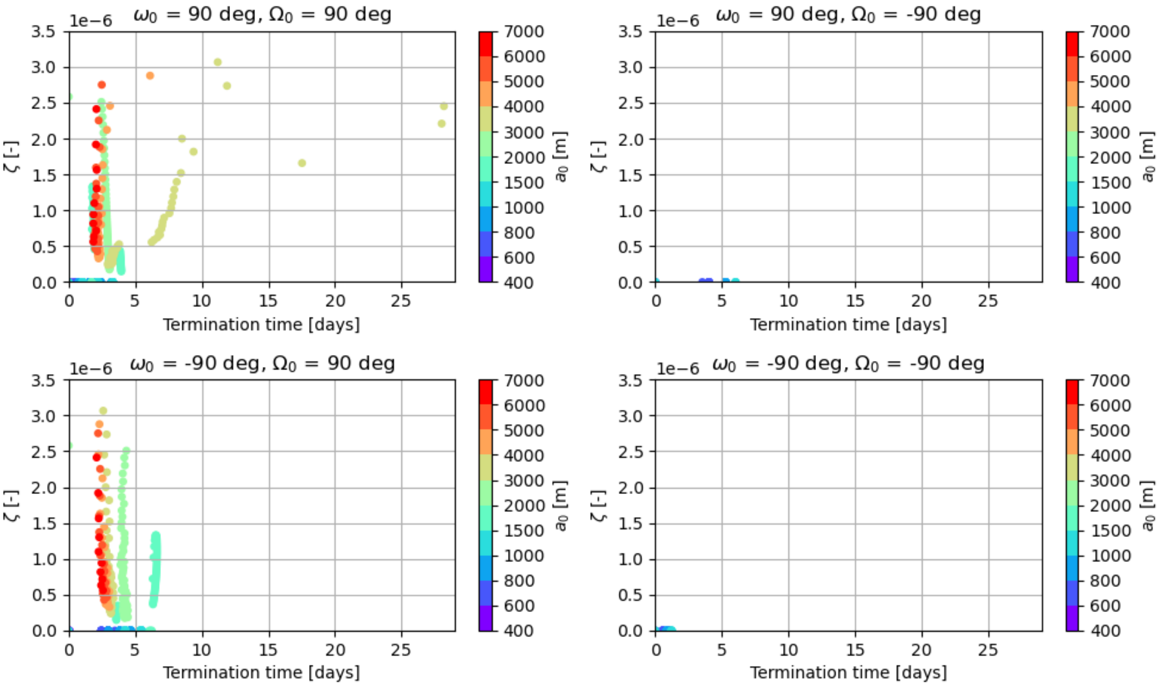

Figure 5.7: Stability index against propagation end time semi-major axis for near-equatorial orbit solutions.

For the near-equatorial solutions, the stability index does not seem to be a good indicator of stability. Most of the solutions from Figure 5.1 only remain in orbit for up to five days when used as initial state to the simulation, even when $\zeta = 0$. There are only two solutions that reach the end of the propagation, with a_0 = 3000 m and $e_0 \approx 0.8$, but with $\zeta > 0$. Thus, there seems to be no correlation between the stability index and the termination time of the simulations for the near-equatorial solutions.

For the near-polar analytical frozen orbit solutions, the stability index against termination time with respect to the initial eccentricity and initial semi-major axis is shown in Figures 5.6 and 5.7.

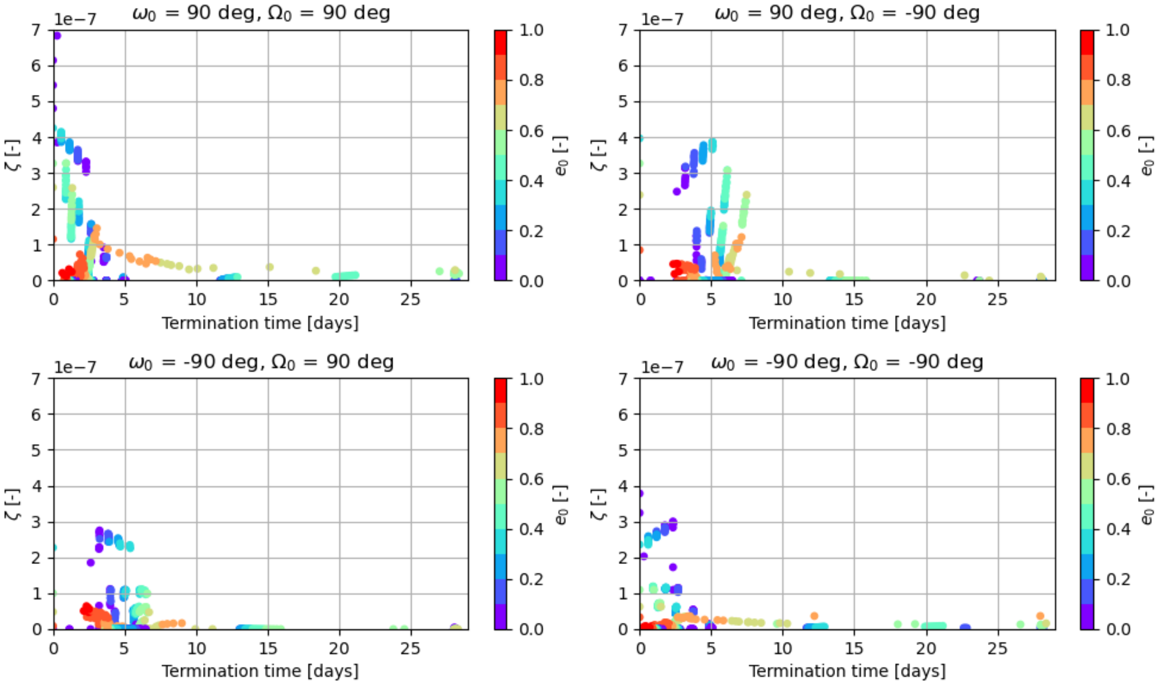

Figure 5.8: Stability index against propagation end time eccentricity for near-polar orbit solutions.

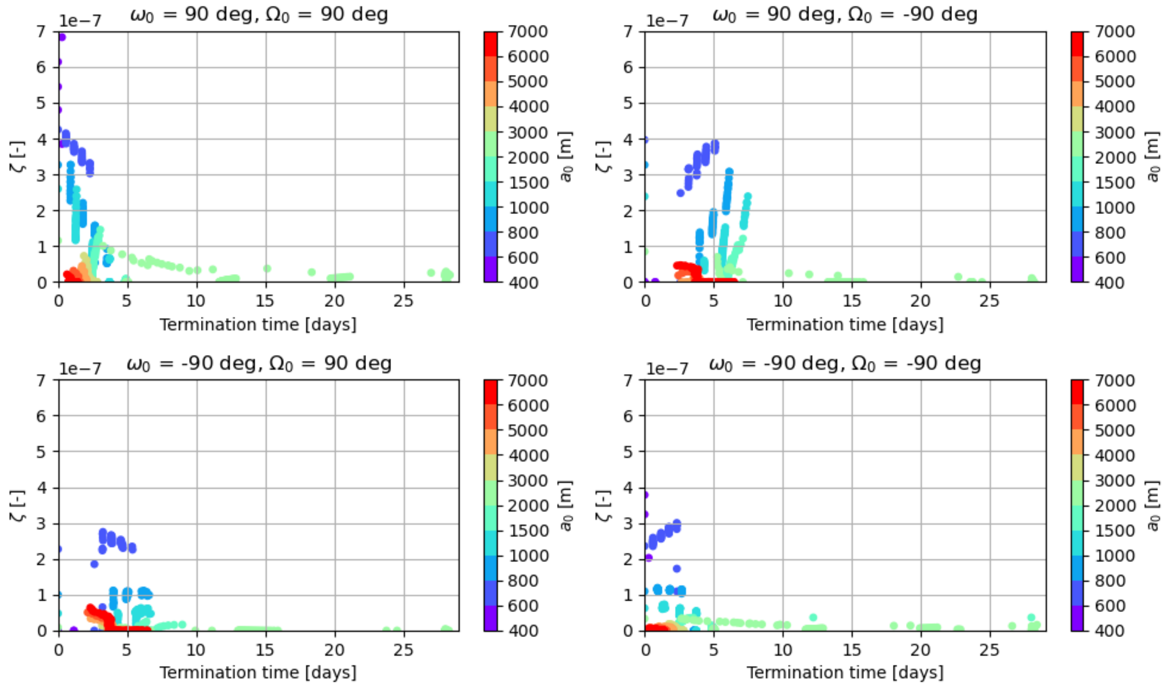

Figure 5.9: Stability index against propagation end time semi-major axis for near-polar orbit solutions.

For the near-polar family, there are slightly more solutions reaching longer termination times. It is interesting to see that all the solutions lasting longer than ~7 days have a_0 = 2000 m while still varying greatly in initial eccentricity. However, many solutions with ζ = 0 still terminate within the first seven days, showing the stability index is not a good measure for the assessment of orbital stability around Apophis.

The results of the comparison of the analytical stability index to the termination time of the numerical simulations are summarised in Table 5.1.

Table 5.1: Number of analytical frozen orbit solutions with ζ = 0 and that reach the end of the simulation.

	Termination time $\geq$ 28 days	Termination time $<$ 28 days	Total
$\zeta = 0$	58	1445	1503
$\zeta > 0$	29	1944	1973
Total	87	3389	3476

The stability index only correctly predicts stability for 1.7% of all solutions, an incredibly low proportion. However, it must be noted in the first place that out of the 3476 solutions, only 87 reach the end of the propagation. If the performance of the stability index is measured accounting only for these 87 solutions, it correctly predicts stability for 66.67% of solutions. On the other hand, there are many results that are identified as stable that do not reach the end of the propagation – 1445 solutions out of 3476 – so there is a large proportion of false positives. Thus, it is concluded that the stability index is not a reliable metric of long-duration frozen orbits around Apophis.

5.2.2. Orbital element drift

The second part of the comparison to numerical results involves checking whether the analytical frozen orbit solutions actually exhibit frozen behaviour. In order to assess this, the analytical frozen orbit solutions are again used as initial states to the simulation. In this case, only the solutions that reach the end of the 28-day simulation are included, i.e. 87 initial states. The quality of the frozen orbit solutions is then measured by computing the maximum difference in e and ω over the entire simulation period. For the computation of the maximum difference in ω the values are unwrapped such that, if ω oscillates around 0° or 360°, the calculation of the maximum difference is accurate.

The results for the near-equatorial orbits are shown first in Figure 5.10, noting it was already seen in Figure 5.7 that there are only two solutions for this case that reach the end of the propagation, both with a_0 = 3000 m, ω_0 = 90° and Ω_0 = 90°.

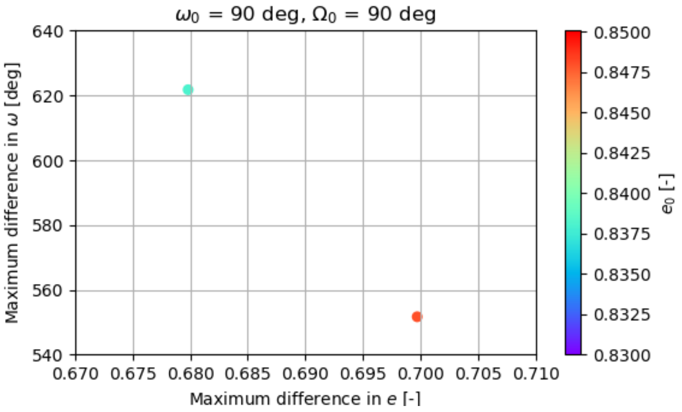

Figure 5.10: Maximum difference in e and ω for near-equatorial analytical frozen orbit solutions.

From Figure 5.10, it is apparent that both solutions lead to a similar maximum difference in e and ω. The maximum difference in ω is more than 360° for both solutions, showing that the drift in ω is secular for these cases instead of oscillating around a mean value. The maximum difference in e is around 0.7 for both solutions, which is large.

For the near-polar solutions, it was already seen in Figure 5.9 that all solutions with a termination time ≥ 28 days correspond to a_0 = 2000 m, but exist for all combinations of ω_0, Ω_0 = ±90°. The maximum difference in e and ω obtained from the numerical simulations for these cases is shown in Figure 5.11.

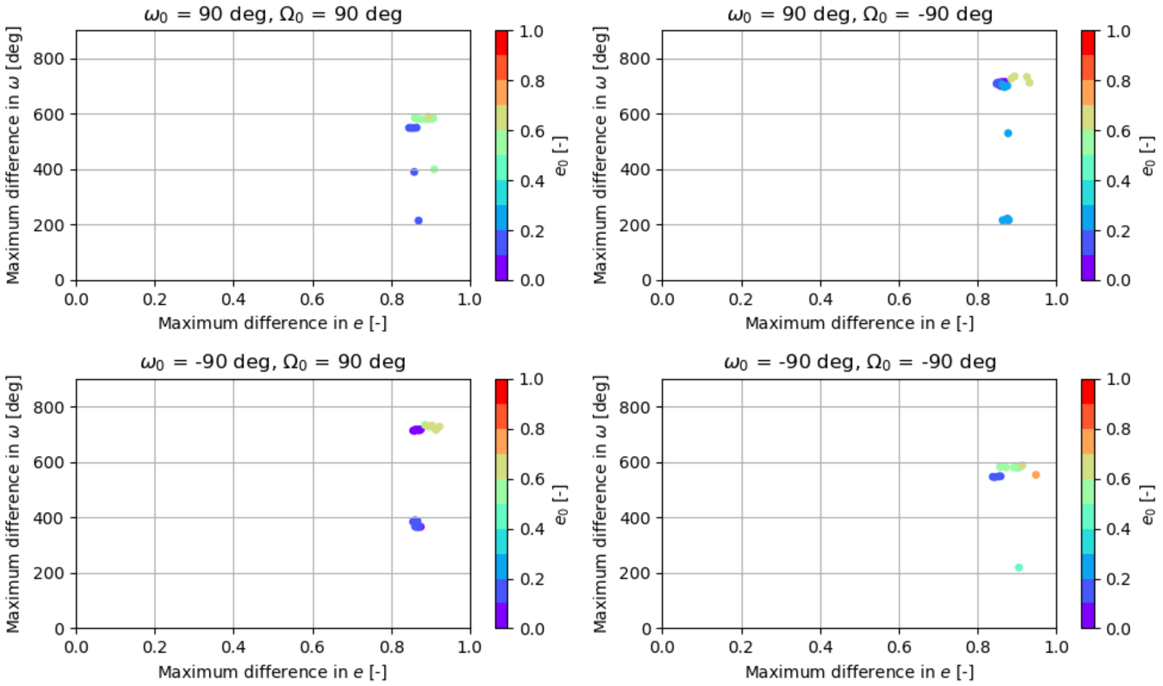

Figure 5.11: Maximum difference in e and ω for near-polar analytical frozen orbit solutions.

Here, the maximum difference in e is even higher than for the near-equatorial solutions, at around 0.9 on average. On the other hand, there are some solutions where the drift in ω is below 360°, but the variation in ω for these cases is still as high as 200°.

One of the near-polar analytical frozen orbit solutions with $\zeta = 0$ and termination time ≥ 28 days is analysed in more detail to see the behaviour of e and ω over time. The initial Keplerian state vector $\boldsymbol{\kappa}_0 = [2000, 0.148, 90.001, 90, 90, 0]$ is used, which results in a maximum difference in e of 0.87 and maximum difference in ω of 215°. A visualisation of the resulting orbit is displayed in Figure 5.12, where it is apparent that the rate of change of the orbital elements is nowhere near constant.

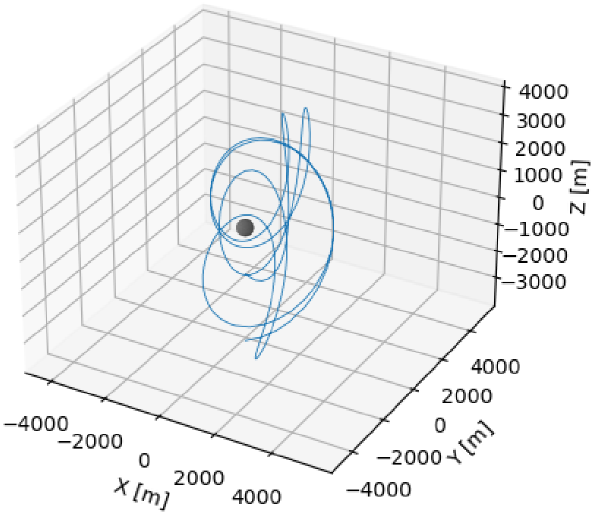

Figure 5.12: Orbit visualisation for an initial Keplerian state vector $\boldsymbol{\kappa}_0 = [2000, 0.148, 90.001, 90, 90, 0]$, including only accelerations due to SRP and Apophis' spherical harmonics zonal gravity up to degree four.

The drift in e and ω for this orbit is shown in Figure 5.13.

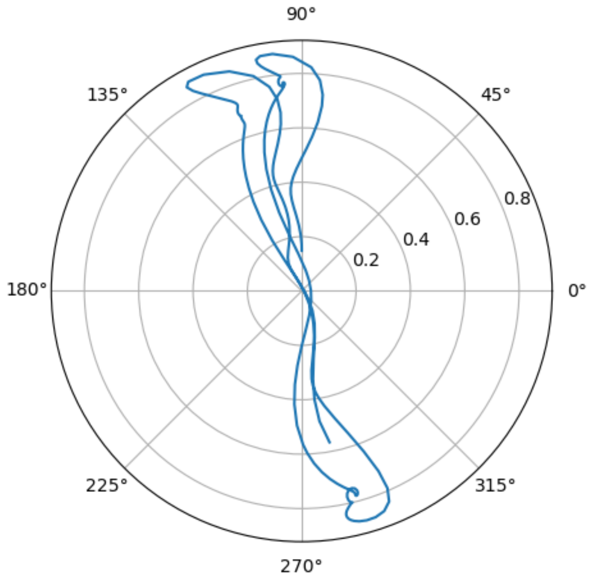

Figure 5.13: Polar plot of $e - \omega$ drift for an initial Keplerian state vector $\boldsymbol{\kappa}_0 = [2000, 0.148, 90.001, 90, 90, 0]$, including only accelerations due to SRP and Apophis' spherical harmonics zonal gravity up to degree four.

Although there is a somewhat periodic pattern, with the argument of periapsis switching by 180, there is still a slow precession in the anti-clockwise direction, i.e. a secular component of the ω drift. For a frozen orbit, there can be short-period variations in ω, but secular effects should not be present. For this example, the secular variation over a 28-day period is approximately 25° and it can be seen from the $e-\omega$ drift pattern that this value will keep increasing with time, which is not a characteristic of frozen orbits. Furthermore, e oscillates from 0 to almost 0.9 but in a constant periodic fashion. This behaviour is better explained by looking at the time evolution of the orbital elements separately.

The time evolution of all orbital elements for this solution is displayed in Figure 5.14.

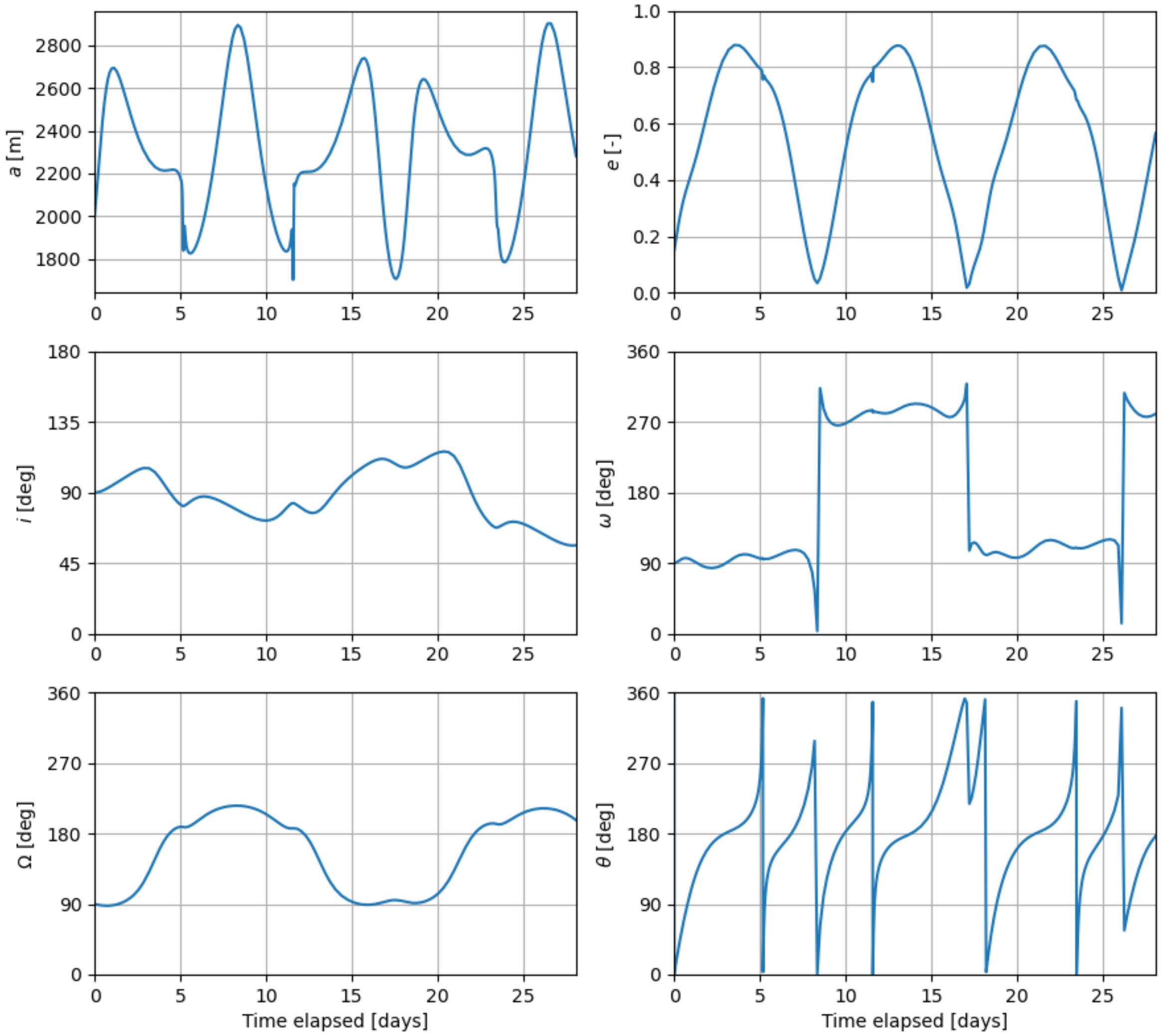

Figure 5.14: Orbital element time evolution for an initial Keplerian state vector $\boldsymbol{\kappa}_0$ = $[2000, 0.148, 90.001, 90, 90, 0]$, including only accelerations due to SRP and Apophis' spherical harmonics zonal gravity up to degree four.

The behaviour of ω is more or less constant in periods of approximately 8 days, with drastic switches to the conjugate value at the end of each period, i.e. the apoapsis and periapsis switch position. The points in time at which ω switches almost instantly coincide with the moments at which the osculating eccentricity goes close to zero. This is explained by the fact that ω is undefined for $e \approx 0$ [23]. Nevertheless, even if the switches in ω are overlooked, a secular variation is still present which does not align with the frozen orbit definition. From Figure 5.14, it is confirmed visually that the maximum e difference of 0.87 matches the maximum difference observed in the plot. For the maximum difference in ω, the calculation is carried out with the unwrapped values, so although it seems from the plot that the maximum difference is approximately 315 - 0 = 315°, the real value is actually much lower at 215°. Although it is not a necessary condition for a frozen orbit to have the drift of all orbital elements being zero on average, certain combinations of elements can help with maintaining orbital stability. The longitude of the ascending node for this example follows a clear periodic pattern which likely helps in balancing the strong SRP perturbations.

The altitude over Apophis' average radius is shown in Figure 5.15.

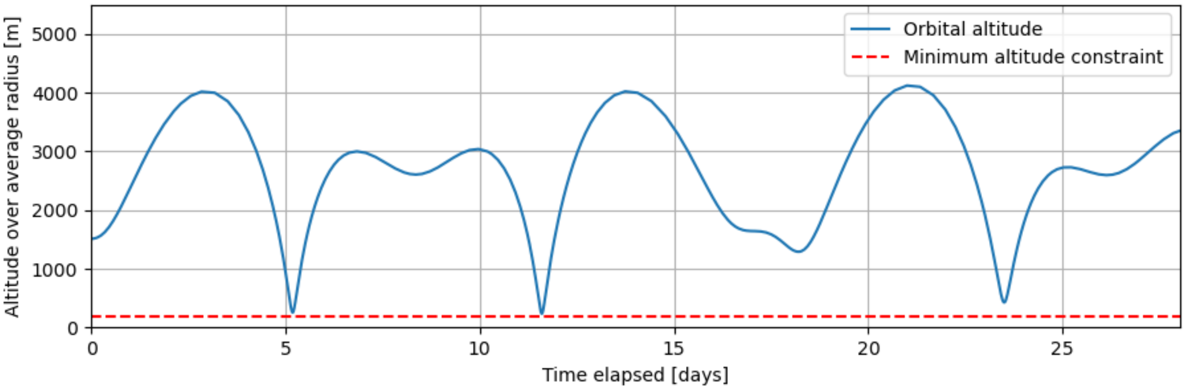

Figure 5.15: Altitude over average radius over time for an initial Keplerian state vector $\boldsymbol{\kappa}_0 = [2000, 0.148, 90.001, 90, 90, 0]$, including only accelerations due to SRP and Apophis' spherical harmonics zonal gravity up to degree four.

The variations in altitude over the 28-day period are extreme. At some points, the spacecraft comes as close as 66 m from the minimum altitude constraint, while reaching altitudes above 4000 m at other points in its orbit. Furthermore, the altitude variation shows no periodic pattern. This is because of the combination of osculating semi-major axis and eccentricity at a given point in time. For example, at around day five the osculating altitude is at a minimum. Looking back at Figure 5.14, this corresponds to a semi-major axis of around 1800 m, a large eccentricity of 0.8 and a true anomaly of 0°. The value of $\theta = 0°$ indicates the spacecraft is located at the periapsis, i.e. the point of the orbit closest to the central body, leading to a low altitude at this point in time. Alternatively, at around day eight the altitude reaches almost 3000 m. At this point in time, $a = 2900$ m, $e = 0.05$ and $\theta = 0°$. Although here the semi-major axis is larger, the eccentricity is much lower, resulting in a higher altitude than that of day five. For a frozen orbit, the altitude variation over one orbit is expected to be small and the altitude over a given point on the central body's surface should be more or less constant over time [21].

5.3. Conclusions

The analytical method based on Lagrange's Planetary Equations to find frozen orbits around Apophis identified two main families of orbits: heliotropic/anti-heliotropic near-equatorial orbits and near-polar Sun-terminator orbits. The Lyapunov stability analysis showed that only half of the sampled solutions were stable, marked by the stability index parameter ζ being equal to zero. Comparing these results to numerical simulations showed, firstly, that the stability index is not an accurate measure for the stability of orbits around Apophis even when the same assumptions on the accelerations, the spin-axis orientation and the asteroid's orbit are used. Secondly, the maximum difference in e and ω for both solution families is not characteristic of frozen behaviour, with variations of approximately 0.69 and 600° for the near-equatorial solutions and, at best, 0.89 and 215° for the near-polar solutions.

Besides the fact that the analytical method displays poor performance in finding orbits with small variations in e and ω, some of the assumptions used for the derivation of the equations have limitations when applied to a real-world scenario. Firstly, the perpendicular-rotation assumption is not true for Apophis, which has an ecliptic latitude of -86°, or equivalently, an obliquity with respect to the ecliptic of 176°. Nevertheless, Kikuchi, Oki, and Tsuda assessed the validity of this assumption for asteroids with similar obliquity and confirmed the assumption to be reasonable [5]. An assumption that is expected to have a larger influence on the case of Apophis is that of neglecting the perturbations due to the tesseral harmonics of the central body. It was already seen in Subsection 3.4.1 that including the perturbations from the spherical harmonics gravity of Apophis up to D/O 4/0 versus D/O 4/4 leads to large differences in the orbital element evolution. Finally, the full illumination assumption does not account for the fact that near-equatorial orbits will have abrupt changes in the accelerations induced by SRP due to the shadowing from the asteroid. This explains why most of the near-equatorial orbit solutions found analytically do not reach the end of the propagation.

Despite the limitations of the analytical method, some of the conclusions derived from this analysis, such as the existence of frozen orbits being limited to inclinations close to 0° or 90°, are useful for limiting the domain of the numerical simulations and verifying the numerical results.

III

Numerical Analysis

The numerical analysis involves a combination of simulation and optimisation procedures. First, the tools employed are outlined in Chapter 6. Then, the details of the simulation and optimisation set-up are provided in Chapters 7 and 8 respectively.

6

Tools

Assessing the behaviour of a spacecraft in the complex dynamical environment around Apophis at the time of the 2029 Earth flyby requires the use of software capable of solving the equations of motion for such a problem. A multitude of astrodynamics-oriented software packages have been developed in the past. The TU Delft Astrodynamics Toolbox (TUDAT) has been chosen as the main tool for this work due to its heritage in the field of space research and the availability of extensive documentation and direct support of staff and students from Delft University of Technology. Furthermore, since a part of this work involves the use of optimisation methods to find frozen orbit solutions, the use of TUDAT is convenient as it is compatible with the use of the Python Global Multi-Objective Optimiser (PyGMO) library, meaning the simulation and optimisation can be run within the same environment. The main functionalities of TUDAT and PyGMO are presented in Sections 6.1 and 6.2 respectively.

Although TUDAT includes ephemeris data of the Solar System planets and a selected number of moons and asteroids by default, data for smaller asteroids such as Apophis are not included. In Section 6.3, the use of NASA's Horizons System to extract the ephemeris of Apophis is explained. The use of NASA's SPICE Toolkit for auxiliary routines is described in Section 6.4. Additional information regarding the development platform used is presented in Section 6.5.

6.1. TU Delft Astrodynamics Toolbox

TUDAT is a set of libraries implemented in C++ equipped to solve a wide array of astrodynamics problems, ranging from perturbed satellite motion to gravity assist transfer trajectories. Its Python interface, called Tudatpy, offers the same functionality and is the selected tool for this work. The functionalities of TUDAT include flexible modelling of the dynamical environment via aerodynamic, gravity, ephemeris, shape, rotation and radiation pressure models, as well as the capability of creating and modifying planetary and spacecraft bodies. Various integrators and propagators are also available. Since the libraries are open-source, they can be modified wherever necessary to adapt to the problem at hand [66, 21].

The following TUDAT functionalities are employed in this work and are assumed to be verified:

- **Environment models:** Spherical shape model
- **Environment models:** Simple rotation model
- **Environment models:** Tabulated ephemeris
- **Environment models:** Radiation pressure interface
- **Acceleration models:** Spherical harmonics gravity acceleration
- **Acceleration models:** Point mass gravity acceleration
- **Acceleration models:** Cannonball solar radiation pressure acceleration

- **Numerical integrators:** Runge-Kutta fixed step-size (RK4)
- **Numerical integrators:** Runge-Kutta variable step-size (RKF4(5), RKF5(6), RKF7(8), RKDP8(7), RKF8(9))
- **Numerical propagators:** Cowell
- **Numerical propagators:** Unified State Model - Exponential Map
- **Element conversion:** Conversion between Keplerian elements and Cartesian coordinates
- **Time conversion:** Conversion between calendar date, Julian days, and seconds since epoch
- **Frame conversion:** Conversion between inertial and body-fixed frames

A number of standard kernels are automatically installed with TUDAT via SPICE, which include size, shape, orientation, rotation, mass and ephemerides data for a number of Solar System bodies. Whenever a default environment model is used, the data is extracted directly from SPICE as long as the body is available in the system. For bodies or parameters not included in the standard kernels, the additional required kernels can be loaded or even generated manually. The SPICE interface can also be used to compute the rotation matrix between two frames.

6.2. Python Global Multi-Objective Optimiser

PyGMO is a software tool for solving multi-objective optimisation problems. It is derived from its C++ counterpart, the Parallel Global Multi-objective Optimisation (PaGMO) library, which was developed by Biscani and Izzo for ESA [67]. Despite its name, PyGMO can be used to solve ”constrained, unconstrained, single objective, multiple objective, continuous and integer, stochastic and deterministic” optimisation problems [67].

The PyGMO optimisation algorithm employed in this work are:

- **Single-objective algorithms:** Differential Evolution Algorithm (DE)
- **Multi-objective algorithms:** Non-dominated Sorting Genetic Algorithm (NSGA-II)

6.3. Horizons System

The Horizons System is a Solar System data and ephemeris computation tool developed by NASA's Jet Propulsion Laboratory (JPL) [68]. The database includes more than a million asteroids, amongst which Apophis can be found. To make use of the Horizons System data, the `astroquery` package is used. This package contains a Horizons class which can be used to query the Horizons database directly so the process is fully automated. The output is a table of state vectors table that can then be easily input into TUDAT's `tabulated` ephemeris function.

6.4. SPICE

As previously mentioned, a number of SPICE kernels and wrapper functions are already included in TUDAT. However, external SPICE functionalities are also used in this work. Real flight data from the OSIRIS-REx mission, stored in kernels available in the SPICE system, are used as part of the validation process described in Section 11.2. The extraction and handling of this data is carried out with the help of the `spiceypy` package [69]. This package contains functions that allow loading of the kernel files containing the mission's orbit determination solutions, and subsequently, computation of the position and velocity of OSIRIS-REx for a specified time range. Frame kernels can also be downloaded to compute any necessary reference frame transformations.

The following `spiceypy` functions have been used in this work:

- `furnsh`: loads SPICE kernels
- `tparse`: converts time string to seconds past the J2000 epoch
- `spkezr`: computes the state of a target body relative to an observing body at a given epoch
- `sxform`: computes the state transformation matrix from one frame to another at a given epoch

6.5. Development Platform

All developed code was written in Jupyter Notebooks using Python 3.9 within the PyCharm Integrated Development Environment. The additional packages `matplotlib` and `numpy` were used for data visualisation and mathematical computing respectively. Furthermore, a private GitHub repository was used to safely back-up the work throughout the duration of the project. All simulations were carried out using a standard laptop with the specifications summarised in Table 6.1.

Table 6.1: Device specifications.

Model	HP ZBook Studio G4
OS	Windows 10
Processor	Intel(R) Core(TM) i7-7700HQ CPU @ 2.80GHz 2.81 GHz
RAM	8,00 GB (7,88 GB usable)

7

Simulation

The numerical simulation is used to predict the spacecraft behaviour in the vicinity of Apophis for a given initial Keplerian state vector input and a given time interval. First, the environment models need to be defined so that the dynamics are similar to that of physical reality. These include the shape, mass, ephemeris, rotation and gravity field of the included bodies, as well as the definition of the spacecraft body. The environment set-up is described in Section 7.1. Due to practical considerations, termination conditions are added so the simulation ends prematurely if the spacecraft reaches either the minimum altitude, maximum altitude or orbital escape conditions, as described in Section 7.2. The selection of an appropriate propagator and integrator, considering both accuracy and speed, is discussed in Section 7.3. Finally, tuning of the acceleration models to further alleviate the computational load in preparation for the optimisation is performed in Section 7.4.

7.1. Environment Set-up

Setting up a simulation requires a multitude of inputs which define the bodies and environment. The following simulation inputs are used to define the model:

- **Simulation epoch and duration:** input into the program following from the mission specification presented in Subsection 2.3.1. The start date of the simulation is set to four weeks before the CE, i.e. the 16th March 2029. For the assessment of the behaviour until right before the CE, the simulation duration is set to 28 days, whereas for the assessment of the post-flyby behaviour, the simulation duration is extended by two weeks and set to 42 days. It is expected that the control-free orbit solutions that survive the strong dynamics involved around the time of the CE and present a somewhat stable behaviour for at least two weeks after the CE will also survive for longer time periods without requiring any correction manoeuvres. Limiting the simulation duration is important for reducing the computational effort. The simulation ends after the specified simulation duration unless another termination condition is activated before, as explained in Section 7.2.
- **Global frame origin and orientation:** set to Apophis and ECLIPJ2000 respectively. Setting the central body as the global frame origin reduces numerical noise [70].
- **Propagation origin and propagated body:** set to Apophis such that the spacecraft's propagated state is given with respect to the asteroid's origin [70]. The propagated body is comparable to OSIRIS-REx.
- **Ephemerides:** loaded from Horizons System for Apophis using TUDAT's `tabulated` ephemeris function. The discrete state history data is extracted using a time step of one minute, which is generally much smaller than the time step of the integration – the reader is directed to Figure 7.7. When states between the provided time steps are required, the tabulated ephemeris is interpolated using a 6th-order Lagrange interpolator. At the edges, a cubic spline interpolator is used to reduce the effect of Runge's phenomenon [71]. For all other bodies, TUDAT's default is used.
- **Rotation:** defined for Apophis using TUDAT's `simple` rotation model function which takes the

pole declination, pole right ascension, meridian at epoch and rotation rate as inputs. Estimates of the pole's ecliptic longitude and latitude of 278 and -86 degrees respectively, taken from Lee et al., are transformed to the pole declination and right ascension using the NASA/IPAC Extragalactic Database online coordinate transformation calculator [72]. This calculator is verified as described in Subsection 11.1.3. Thus, for Apophis, the pole orientation is defined by $\alpha = 88.33°$ and $\delta = -70.51°$. The meridian at epoch is assumed to be $0°$. The rotation period P_{ast} is also taken from Lee et al. with a value of 30.56 hours [51]. For all other bodies, TUDAT's default is used.

- **Shape:** modelled using TUDAT's `spherical` shape model for Apophis with an average radius of 193 m [13]. For all other bodies, TUDAT's default is used. If the spacecraft altitude is retrieved from the simulation, it is computed with respect to this average radius and is thus not an accurate representation of the real altitude over the asteroid's surface. This is taken into account by setting a constraint on the minimum allowable spacecraft altitude as explained in Section 7.2.
- **Gravity field:** set to spherical harmonics gravity model up to D/O 4 for Apophis. The coefficients are obtained from the work of Aljbaae et al. [13]. TUDAT's `spherical_harmonics` function requires the spherical harmonics coefficients to be normalised. This is done using TUDAT's `normalize_spherical_harmonic_coefficients` function. The polyhedron model available on TUDAT is assumed to be too computationally intensive for this work, as the optimisation will require computation of $\sim 10^4$ propagations with a duration of up to 42 days per run [73]. TUDAT's default environment models include the gravity field definition up to a certain D/O for a number of Solar System bodies [74]. For the accelerations included in this work, no additional gravity field environments need to be defined other than the SH gravity model of Apophis.
- **Gravitational parameters:** input manually for Apophis based on its assumed mass. A value of 5.31×10^{10} kg is used [13]. For all other bodies, TUDAT's default is used. The gravitational parameters are needed for the transformation from Cartesian to Keplerian states and for the use of the point mass gravity acceleration model.
- **Solar radiation pressure interface:** defined for the cannonball radiation pressure model, which takes the spacecraft's mass, area and reflection coefficient as inputs. The spacecraft parameters for this model are taken from Table 2.5 [13]. The radiation pressure coefficient is set to 1.4 following from the spacecraft's reflectance. The occulting bodies included are Apophis, Earth and the Moon. Although the main shadows will be caused by Apophis itself, the Earth and Moon are added as occulting bodies in case the relative positions of these bodies during their respective flybys lead to eclipse periods for the spacecraft.

Currently, the only pre-defined inertial global frame orientations available in TUDAT are the J2000 and ECLIPJ2000 orientations, which are aligned with the celestial equator and ecliptic respectively [75]. Since the propagation is performed with respect to the Apophis-centred, ECLIPJ2000 reference frame, the initial Keplerian state input needs to be defined with respect to this reference frame. The output of the simulation is also given with respect to this reference frame. However, it is of interest for orbit analysis and design that both the initial Keplerian state input and the Keplerian element evolution output are defined with respect to the Apophis-centred, polar-equatorial reference frame described in Section 3.1. In this way, an orbit with a constant inclination of $90°$ defines a polar orbit and one with a constant inclination of $0°$ is a purely equatorial orbit.

First, the initial Keplerian state vector with respect to the Apophis-centred, polar-equatorial reference frame (as input by the user) is transformed to a Cartesian state vector. Then, the 3×3 rotation matrix $\boldsymbol{R}^{(I/B)}$ from body-fixed (B) to inertial reference frame (I) is extracted from the rotation model previously defined by the `simple` rotation model function. To extract this rotation matrix, the initial simulation epoch is used. For the transformation of a Cartesian state vector $\mathbf{x}$ from frame B to frame I, Equation 7.1 is used [56].

$$\mathbf{x}^{(I)} = \begin{pmatrix} \boldsymbol{R}^{(I/B)} & 0_{3\times 3} \\ \dot{\boldsymbol{R}}^{(I/B)} & \boldsymbol{R}^{(I/B)} \end{pmatrix} \mathbf{x}^{(B)} \tag{7.1}$$

Since the Apophis-centred, polar-equatorial reference frame is defined as a *non-rotating* reference frame, the rotation matrix time derivative $\dot{\boldsymbol{R}}^{(I/B)}$ can simply be set to zero. After this transformation, the Cartesian state vector with respect to the Apophis-centred, ECLIPJ2000 reference frame is ready to be input into the simulation. The reverse procedure is carried out on the output of the simulation to obtain the Cartesian and Keplerian state vectors with respect to the Apophis-centred, polar-equatorial reference frame. Because this frame is non-rotating, the transformation matrix only needs to be defined once and can be applied equally at all time steps. Furthermore, although the orbital elements in the Keplerian state change based on the used reference frame, the orbital element *drift* is assumed equal in both reference frames. Verification of this transformation is provided in Subsection 11.1.4. Note that for all results and figures presented in this work, the orbital elements are defined with respect to the Apophis-centred, polar-equatorial reference frame unless otherwise specified.

7.2. Termination Conditions

By default, the propagation terminates after reaching the end of the user-defined simulation duration. However, additional termination conditions can be included to directly remove undesirable results such as orbits that lead to surface collision or escape. Including these termination conditions is also useful for reduced computational effort during the optimisation phase.

Some of the termination conditions can be derived from the mission requirements presented in Subsection 2.3.1, such as the requirements on maximum and minimum orbital altitude. To meet the requirement on minimum altitude, set at 100 m, two considerations are made. The first is that the orbital altitude is defined numerically as the height above the radius of the spherically-modelled asteroid. Thus, the difference between the known maximum radius (280 m) and the spherical-equivalent radius (193 m) needs to be added to ensure the spacecraft is always at least 100 m above the surface in the real environment no matter the asteroid's orientation, i.e. 87 m [13]. The second consideration is the numerical accuracy of the chosen integration method. It is assumed already here that the position accuracy of the numerical results shall be in the order of at least 10 m, as will be confirmed in Sections 7.3 and 7.4. Thus, this position uncertainty is also added to the minimum altitude requirement of 100 m, leading to a total value of 100 + 87 + 10 = 197 m. This termination condition not only ensures that there is no surface collision but also prevents convergence issues upon the computation of the spherical harmonics gravity potential.

For the definition of the upper altitude termination, a similar argument is followed. In this case, the difference between the known minimum radius (156 m) and the spherical-equivalent radius (193 m), i.e. 37 m, and the numerical position uncertainty of 10 m both need to be subtracted from the mission requirement value of 6000 m, leading to a total value of 5953 m.

Finally, a termination condition is added for the orbital escape condition defined in Section 4.4. Although escape will eventually lead to an orbital altitude higher than that specified for the upper altitude termination condition, identifying escape prior to this may further reduce the computational effort by terminating the propagation earlier. Although the orbital escape condition is mathematically defined as $a \leq 0$, the condition is implemented using the apoapsis altitude rather than the semi-major axis, as the former parameter can be numerically extracted and used as a termination condition in a straightforward manner. Although according to theory the apoapsis radius should go to infinity during escape, in the numerical simulation the apoapsis altitude becomes negative for $a \leq 0$, so both parameters can be assumed equal under this consideration. This assumption is verified in Subsection 11.1.5.

Thus, the following termination conditions are implemented:

- **Time termination:** the propagation is terminated after reaching the specified simulation duration.
- **Lower altitude termination:** the propagation is terminated if the (numerical) orbital altitude is lower than 197 m.
- **Upper altitude termination:** the propagation is terminated if the (numerical) orbital altitude is higher than 5953 m.
- **Orbital escape termination:** the propagation is terminated if the orbit's apoapsis altitude becomes less than or equal to zero.

To limit the computational load, all termination conditions are set to *not* end on the exact condition.

7.3. Propagator and Integrator Selection

The propagator and integrator selection has a direct influence on the simulation accuracy as well as the computational effort. Since the optimisation will require a large number of simulations, it is important to achieve a reasonable trade-off between accuracy and speed.

The Cowell propagator is a translational propagator in which the propagated state is simply formulated as the Cartesian state [56]. Since TUDAT takes the Cartesian state with respect to the central body as initial state input independently from the chosen propagator, this means no transformations are required [76]. Another typical propagator used for astrodynamics problems uses Encke's formulation. In this method, the propagated state is the difference in Cartesian state with respect to a purely Keplerian reference orbit generated using the initial state [77]. Therefore, Encke's method is better suited for nearly Keplerian orbits with small perturbations [78]. Since large perturbations are expected for small-body orbiters, the Cowell propagator is chosen as the propagator for this work.

In terms of the integrator, a number of options are available in TUDAT which can be classified as multi-stage, multi-step and extrapolation-based integrators. Runge-Kutta integrators are multi-stage integrators, meaning several function evaluations are carried out for a single time step [56]. The Runge-Kutta (RK) 4th-order integrator is a fixed step-size integrator, which has the disadvantage of being computationally inefficient. For highly perturbed orbits, variable step-size multi-stage integrators are a better option. The step size is selected by the integrator at each time step based on the defined absolute and relative tolerance. Generally, a smaller step size is used for fast-changing dynamics, for example, close to periapsis, and vice versa. Runge-Kutta variable step-size integrators are considered the best choice for this work as they provide a good balance between accuracy and computational efficiency. Other integrators, such as the extrapolation-based Burlisch-Stoer integrator or the multi-step Adams-Bashforth-Moulton integrator, are considered to have too large and too small time steps for this problem respectively [79].

The tuning of the variable step-size integrator tolerance, which specifies the step size, has the biggest impact on the solution accuracy. Thus, the integrator selection is carried out by analysing the accuracy and computational efficiency of several Runge-Kutta integrators with different tolerances. The computational efficiency is measured directly using the total number of function evaluations. For unperturbed orbits, the true accuracy of an integrator can be assessed against analytical solutions. However, for the highly perturbed orbits considered in this study there are no direct analytical solutions, so a benchmark solution needs to be generated. This benchmark solution is assumed to be the highest accuracy solution against which the relative accuracy of the integrator can be measured.

In Section 7.2, a position accuracy of at least 10 m has been assumed. The asteroid has a radius of 193 m, so an accuracy of at least 10 m is considered a reasonable value for the size of the system. For practical purposes, the integrator selection is only carried out for one initial state. Therefore, an additional requirement is set such that the position accuracy of the selected integrator and accelerations with respect to the benchmark shall be one order of magnitude lower, at 1 m. Finally, the accuracy of the benchmark needs to be at least one order of magnitude lower than the integrator at 0.1 m.

7.3.1. Benchmark generation

In general, for the integrator selection, a high-fidelity model which includes the best approximation of the dynamical environment the spacecraft will be in is desired. The purpose of the benchmark and tuning cases is not to represent the spacecraft's trajectory to the highest accuracy but to assess the errors introduced by numerical methods in a similar dynamical environment. For practical purposes, the functionalities already included in TUDAT are employed to set up this high-fidelity model. Unless otherwise specified, the inputs described in Section 7.1 are used to define the environment. Furthermore, the following accelerations are included for the benchmark generation:

- **Apophis:** spherical harmonics central gravity, up to degree and order 4/4.
- **Earth, Moon:** spherical harmonics third-body gravity, up to degree and order 50/50.
- **Mercury, Venus, Mars, Jupiter, Saturn, Uranus, Neptune:** point mass third-body gravity.
- **Sun:** point mass third-body gravity, cannonball SRP.

The higher accuracy modelling of the Earth's and Moon's gravity is because of their proximity during the flyby. For the other third bodies the point mass gravity is assumed to be of sufficient accuracy as it has been shown in Section 3.4 that the magnitude of the accelerations induced by these bodies is several orders of magnitude smaller.

The Runge-Kutta-Fehlberg (RKF) integrator of order 8 with an embedded 7th order is chosen to generate the benchmark solution as it does not require a priori knowledge of the problem for the definition of the settings and it exhibits good performance for a large range of eccentricities [80]. The initial time step is set arbitrarily to a small number, in this case, 1 s. A very low relative and absolute error tolerance is selected as it leads to higher accuracy solutions. However, the tolerance value needs to be larger than the numerical precision, which is 16 digits in TUDAT. Thus, the tolerances are set to 10^{-15} [81]. Since very low tolerances are defined, the minimum and maximum step sizes are set to very low and high values respectively. The selected integrator settings are summarised in Table 7.1.

Table 7.1: Integrator settings used for the benchmark solution.

Parameter	Value
Initial time step [s]	1
Minimum step size [s]	10^{-12}
Maximum step size [s]	∞
Relative error tolerance [-]	10^{-15}
Absolute error tolerance [-]	10^{-15}

Finally, the initial state and simulation time need to be defined. Since the integration truncation error is known to increase with time, the benchmark solution is generated for the longer simulation duration of 42 days so that the accuracy requirements are assumed to be met directly also for the cases with a shorter simulation duration of 28 days [56]. The chosen initial Keplerian state vector is $\kappa_0 = [1206, 0.32, 76, 220, 134, 0]$, as it is known to reach the end of the 42-day simulation without activating any of the other termination conditions defined in Section 7.2. The visualisation of the orbit pertaining to the benchmark solution is shown in Figures 7.1 and 7.2 with respect to the Apophis-centred, polar-equatorial frame and Apophis-centred, ECLIPJ2000 frame respectively.

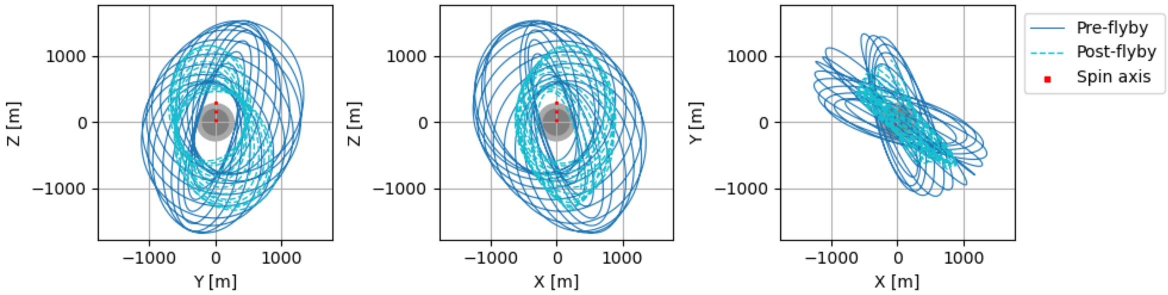

Figure 7.1: Benchmark solution orbit visualisation with respect to the Apophis-centred, polar-equatorial reference frame.

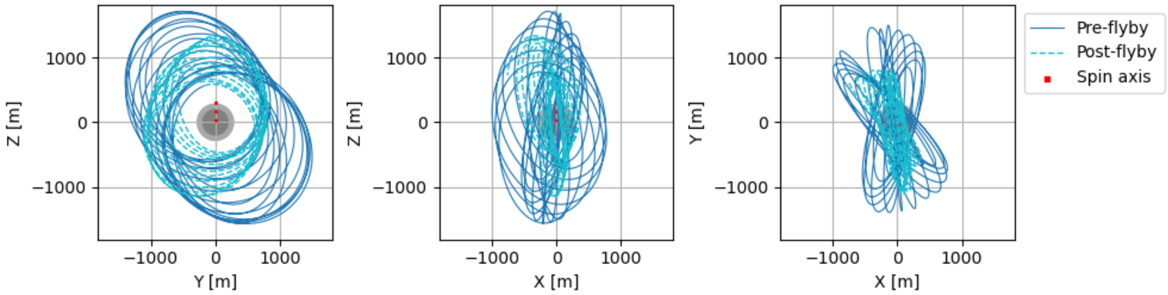

Figure 7.2: Benchmark solution orbit visualisation with respect to the Apophis-centred, ECLIPJ2000 reference frame.

The time evolution of the Kepler elements for the benchmark solution is presented in Figure 7.3.

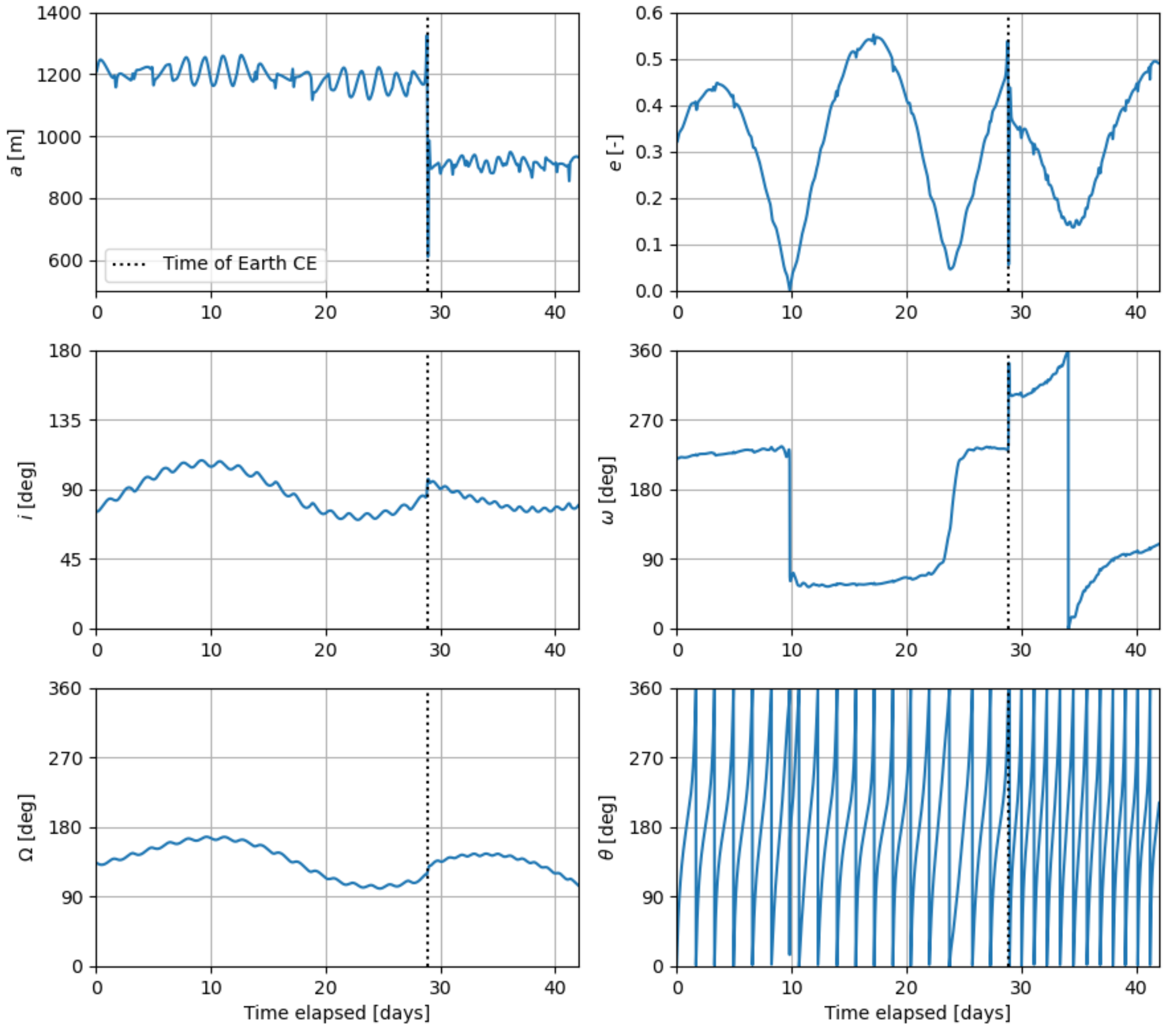

Figure 7.3: Benchmark solution orbital element time evolution with respect to the Apophis-centred, polar-equatorial reference frame.

A clear difference in the average orbital elements can be seen before and after the CE, especially for the semi-major axis, eccentricity and argument of periapsis. The semi-major axis changes from an average value of approximately 1200 m before the CE to around 900 m afterwards. The eccentricity value varies greatly, reaching as low as 0 and as high as 0.55. The large changes in the argument of periapsis correspond to the points in time at which the eccentricity goes very close to zero. This is expected since the argument of periapsis is undefined for circular orbits. It is interesting to see the inclination and longitude of the ascending node remain mostly unchanged both before and after the CE. The longitude of the ascending node of around 150° in the Apophis-centred, polar-equatorial frame corresponds to an orbital plane which is oriented perpendicular to the asteroid-Sun vector. Furthermore, the inclination oscillates around 90°. This combination of orbital elements defines a Sun-terminator orbit which is inherently stable. Since the benchmark solution has a large variation in the orbital elements, especially at the time of the CE, it is assumed that the accuracy of the chosen integrator and accelerations will be equal or better for the more stable dynamics of the optimised frozen orbit solutions.

Before proceeding to the integrator selection, the benchmark accuracy itself needs to be assessed. Since there is no analytical solution available, the accuracy is checked by generating two solutions that are thought to have similar accuracy. Then, the difference between the two solutions is computed. This difference is then assumed to be an estimate of the accuracy of the least accurate of the two [80].

Thus, two different checks are performed: the first one involves changing the tolerances to 10^{-14} and the second one changing the propagator to the Unified State Model - Exponential Map (USM-EM) propagator [78]. The results are shown in Figures 7.4a and 7.4b respectively. The position difference norm has been computed using the Apophis-centred, ECLIPJ2000 Cartesian state output of the simulator, as it is assumed that the position difference norm is equivalent in all frames. Furthermore, a 7th-order Lagrange interpolator has been used to compute the position difference as it is the highest accuracy interpolator available [82]. However, Lagrange interpolation is liable to introducing large errors for the first and last $(k-1)/2$ interpolation intervals, where k is the order of the interpolator. Thus, the last three time steps have been manually removed to avoid the interpolator error [56].

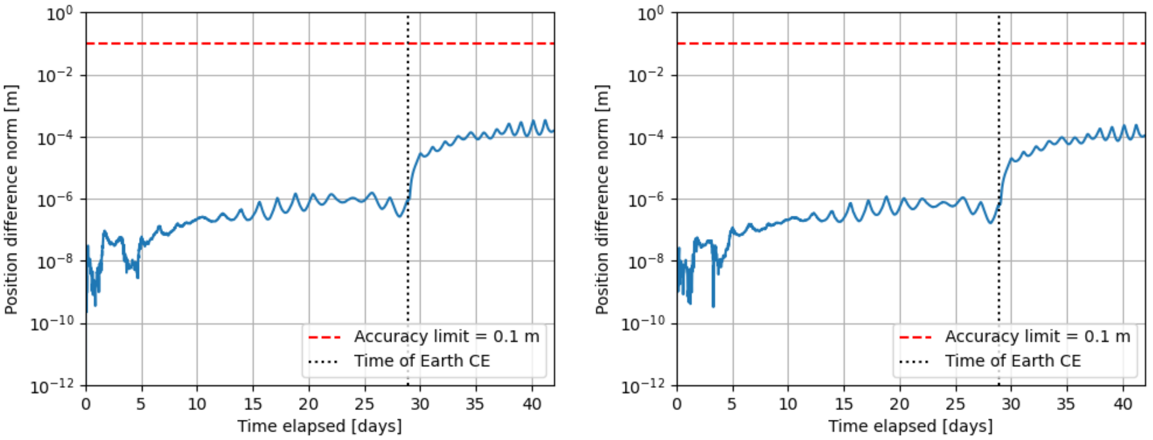

(a) With absolute and relative error tolerance changed to 10^{-14}

(b) With propagator changed to USM-EM

Figure 7.4: Benchmark accuracy checks.

It is first noted that the position difference norm in Figure 7.4 is well below the benchmark accuracy limit of 0.1 m for both checks. Thus, the benchmark solution reaches the position accuracy requirement. For the tolerance change, the maximum position difference norm is around 0.0003 m, while for the propagator change the maximum position difference norm is around 0.0002 m. Furthermore, the behaviour after day ~5 is relatively smooth, thus verifying that truncation error is dominant [80]. Looking back at Figure 7.3, the benchmark solution has an average semi-major axis of approximately 1200 m before the CE, corresponding to an orbital period of almost 39 hours. After the CE, the average semi-major axis is around 900 m, corresponding to an orbital period of 25 hours. The maximum time step used in the benchmark solution is approximately 0.55 hours, which is reasonably lower than the magnitude of the smallest orbital period. It is thus confirmed that the Runge-Kutta variable-step integrator provides a reasonable output density for the dynamics of this problem.

7.3.2. Results

A number of Runge-Kutta variable-step integrators are assessed by varying the absolute and relative error tolerance. The absolute and relative error tolerances are always set to the same value for a given run. All other integrator settings are kept the same as for the benchmark. Although the RK4 integrator is known to not be the most computationally efficient and is likely to not be chosen, it is included for reference. The following tolerances and step sizes are examined:

- **RK4:** step sizes of 10, 50, 100, 200 and 1000 s.
- **RKF4(5), RKF5(6), RKF7(8), RKF8(9), RKDP8(7):** absolute and relative error tolerances of 10^{-14}, 10^{-13}, 10^{-12}, 10^{-11}, 10^{-10} and 10^{-9}.

The maximum position difference norm against the total number of function evaluations is shown in Figure 7.5 for the different integrators and tolerances/step sizes described above.

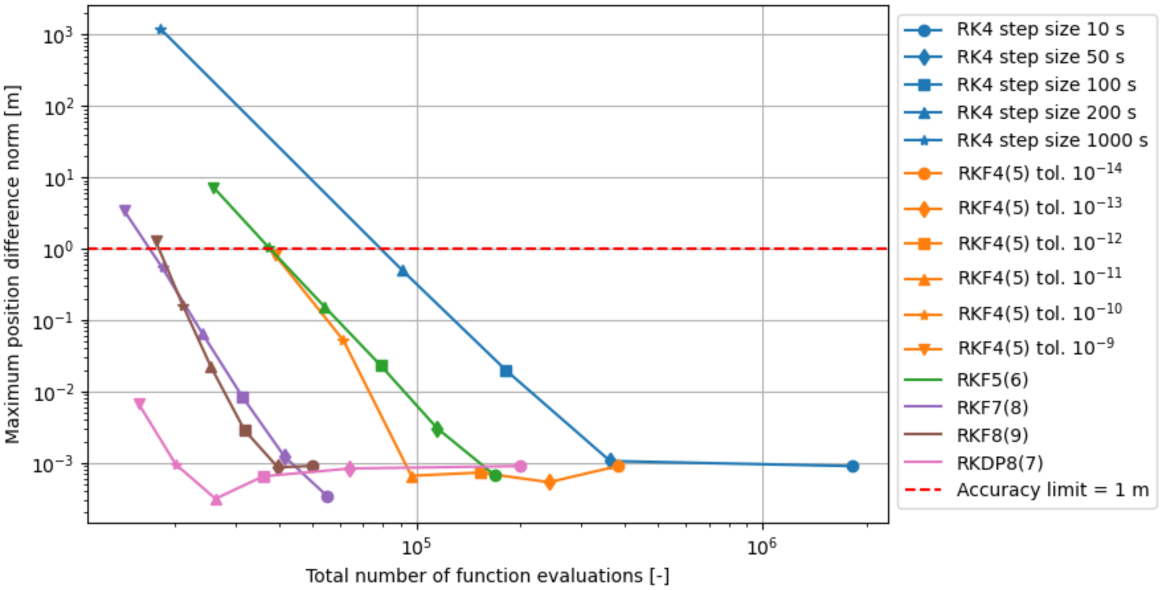

Figure 7.5: Total number of function evaluations against maximum position difference norm for different integrators and tolerances/step sizes.

A general trend can be observed for all integrators whereby a lower tolerance or step size leads to a lower maximum position difference norm at the expense of a larger number of function evaluations. For some integrators, further decreasing the tolerance after a certain point does not yield improvements in the maximum position error. This can be attributed to having dominant rounding error over truncation error for very small step sizes or tolerances. As expected, the fixed-step RK4 integrator has the worst performance of all, requiring a much higher number of function evaluations to reach a similar maximum position difference norm than the variable-step integrators. Since, as long as the maximum position error is below 1 m, there is greater importance given to speed than accuracy, the integrator with the lowest number of function evaluations below the accuracy limit is selected. This corresponds to the Runge-Kutta Dormand-Prince (RKDP) integrator of order 7 with an embedded 8th order, with an absolute and relative error tolerance of 10^{-9}, which has a total of 15732 function evaluations. Although a known drawback of this integrator is that it can get stuck when very low tolerances are used, it is assumed that for a tolerance of 10^{-9} it should have no issues [81].

The position difference norm over the 42-day integration period for the selected integrator and absolute and relative error tolerance is shown in Figure 7.6.

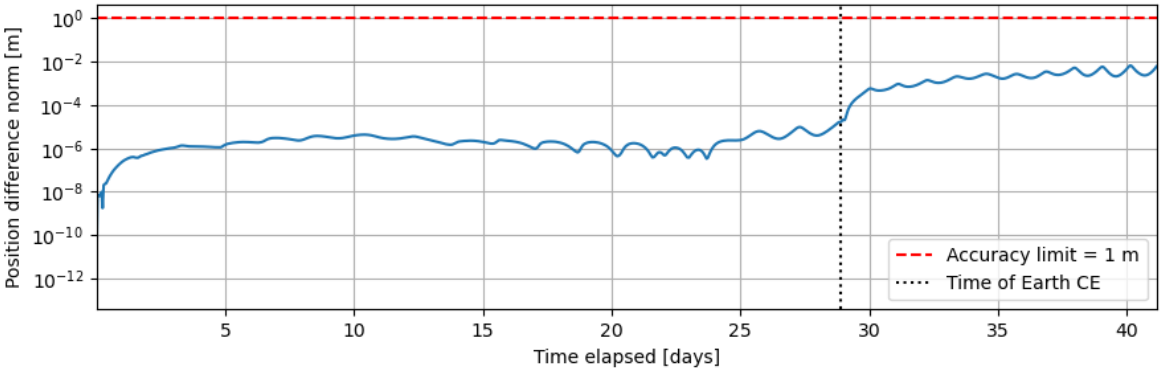

Figure 7.6: Position difference norm with respect to benchmark solution for RKDP8(7) integrator with absolute and relative error tolerance of 10^{-9}.

The behaviour is generally smooth, demonstrating the error source is due to truncation and not rounding. The position difference norm is around 10^{-8} m at the first time step and then proceeds to grow slowly over time. The maximum position difference norm corresponds to the last time step, as expected from the behaviour of truncation error, and is just below 10^{-2} m. Thus, the integrator accuracy requirement of 1 m is clearly met.

Finally, the step size used by the integrator at each step of the integration is shown in Figure 7.7.

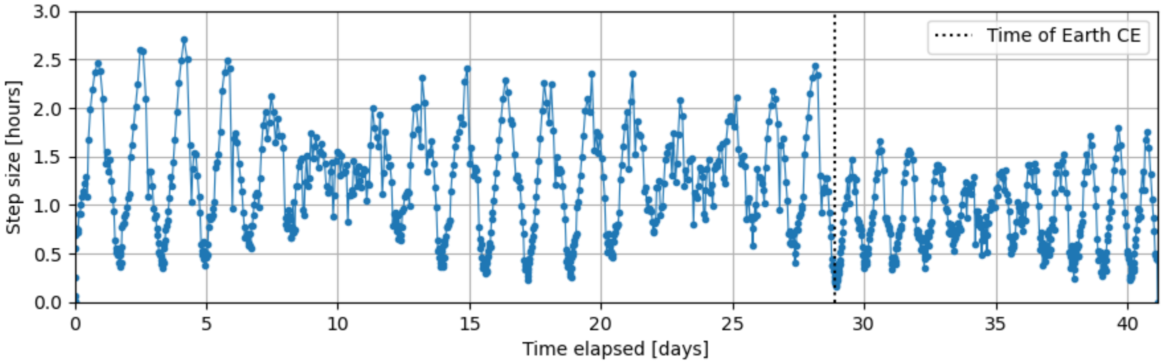

Figure 7.7: Step sizes used by RKDP8(7) integrator with absolute and relative error tolerance of 10^{-9} over time.

The periodic variations in the step size selected by the integrator correspond to the orbital motion of the spacecraft: smaller step sizes are used when the spacecraft is close to periapsis and has a higher velocity, whereas larger step sizes are employed for the slow dynamics around apoapsis. Since the benchmark solution has a relatively high eccentricity, the variation in step size between apoapsis and periapsis is relatively large. As previously stated for the benchmark solution, the used step size is considerably below the orbital period both before and after the CE. The maximum step size is 2.71 hours pre-flyby and 1.79 hours post-flyby. Furthermore, the average step size used is lower in the post-flyby section. This matches the fact that the orbit has a lower semi-major axis post-flyby and thus faster dynamics. Thus, the selected integrator does a good job of capturing the motion of a spacecraft in this environment.

7.4. Acceleration Tuning

Since the selected integrator has an accuracy well below 1 m, there is room for simplification of the acceleration models included in the simulation. When it comes to the optimisation phase later on, including fewer accelerations will reduce the required computational effort. However, the effect of removing accelerations on the final position accuracy needs to be assessed.

The tuning of the acceleration models is carried out in a similar manner to the integrator selection. The accelerations are changed, using the integrator and integrator settings specified in Section 7.3, and the state of the spacecraft at each time step is saved. Then, the position difference norm with respect to the benchmark is calculated. Note that by carrying out the acceleration tuning using the selected integrator, one can ensure the accuracy limit of 1 m is met for the simplified integrator and acceleration models combined.

Insights from Chapter 3 are used to simplify the acceleration tuning. It is expected that the point mass gravity of all Solar System bodies except the Earth, Moon and Sun can be neglected with little effect on the solution accuracy. Furthermore, the Moon's gravity is modelled using the point mass formulation instead of the SH up to D/O 50/50. Knowing the Earth's J_2 coefficient is many orders of magnitude larger than the higher order zonals, the Earth's gravity modelling is simplified from D/O 50/50 to D/O 2/0. Although one might think that modelling the Earth's gravity with the simple point mass formulation would provide sufficient accuracy, the maximum position difference norm goes from only 0.07 m to 9.45 m with this change. With these changes, the position difference norm with respect to the benchmark solution is as shown in Figure 7.8.

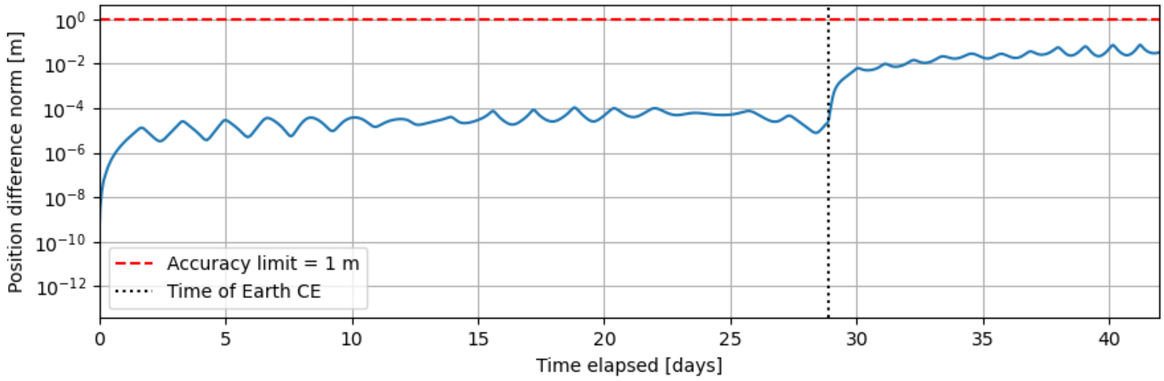

Figure 7.8: Position difference norm with respect to benchmark solution when including accelerations: SH Apophis 4/4, Earth SH 2/0, Sun and Moon PM gravity and cannonball SRP.

The maximum position difference norm is reached towards the end of the simulation and has a value of approximately 0.07 m. Therefore, the accuracy is below the requirement of 1 m. The final acceleration models to be included for the optimisation and results generation are as follows:

- **Apophis:** central body spherical harmonics gravity up to D/O 4/4.
- **Earth:** third-body spherical harmonics gravity up to D/O 2/0.
- **Moon:** third-body point mass gravity.
- **Sun:** third-body point mass gravity, cannonball SRP.

8

Optimisation

Optimisation is the method used for the numerical analysis of frozen orbits around Apophis. In PyGMO, optimisation problems are formulated as displayed in Equation 8.1 [67].

$$\text{find: } \mathbf{lb} \leq \boldsymbol{x} \leq \mathbf{ub} \qquad \text{to minimise: } \quad \mathbf{f}(\boldsymbol{x}) \in \mathbb{R}^{n_{obj}} \tag{8.1}$$

Here, $\boldsymbol{x}$ is the decision vector, $\mathbf{lb}$ and $\mathbf{ub}$ are the lower and upper bounds of $\boldsymbol{x}$, $\mathbf{f}(\boldsymbol{x})$ is the fitness function to be minimised and n_{obj} is the number of objectives [67]. In summary, an optimisation problem tries to find optimal values of the decision vector $\boldsymbol{x}$ within the range defined by the upper and lower bounds of each element in $\boldsymbol{x}$ which lead to the lowest output value of $\mathbf{f}(\boldsymbol{x})$. Problems with $n_{obj} > 1$ are referred to as multi-objective optimisation (MOO) problems.

To find a frozen orbit, the mathematical condition is $de/dt = d\omega/dt = 0$. Thus, the optimisation problem has $n_{obj} = 2$, and the fitness functions are defined as $\mathrm{f}_1(\boldsymbol{x}) = de/dt$ and $\mathrm{f}_2(\boldsymbol{x}) = d\omega/dt$ [23]. The fitness function used in this work is defined in Section 8.1. The decision vector $\boldsymbol{x}$, in this case, is the orbital injection vector, consisting of the time of injection and the six osculating orbital elements at this time. Thus, the problem has seven degrees of freedom. With insights into the dynamics of the problem, one can reduce the problem by fixing one or more of the design variables. In this work, the injection time has been directly assumed to be fixed and is set to the 16th March, 2029. The initial true anomaly θ_0 is also assumed equal to 0°, as it is essentially just another measure of time, equivalent to the phasing within the orbit. Further reduction of the problem is carried out by performing a design space exploration, as shown in Section 8.2. Finally, the algorithm choice and its settings are evaluated in Section 8.3.

8.1. Fitness Function

The fitness or objective function formulation for finding frozen orbits typically involves minimising the variation of the orbital elements averaged over one orbital period, since in this way short-period variations are removed and only secular effects remain. Semi-analytical methods for the averaging of the orbital elements have been employed in the past for the analysis of frozen orbits around Earth [83, 21]. However, these assume the central body's J_2 to be the largest perturbation source. For an Apophis-orbiting spacecraft, these methods fail to reconstruct the mean elements from osculating elements due to their exclusion of tesseral harmonics, SRP and third-body gravity. The reader is referred to Section A.2 for the results of the transformation from osculating to mean elements. To address this limitation, a straightforward approach is adopted: the objective function is defined as the maximum difference observed in e and ω over the entire simulation period.

The simulation method described in Chapter 7 is crucial for the definition of the fitness function. The decision vector, which consists of the six osculating orbital elements at the time of injection, is used as initial state to start the simulation. In this way, the time history of the osculating orbital elements is obtained. Then, the maximum difference in e and ω over the simulation duration is computed for that given initial state. For the latter, the time array of ω values is unwrapped before extracting the maximum and minimum value, as previously described in Section 5.2.

An important consideration concerning the fitness function definition is that for two orbits with similar secular variation in ω, if one orbit terminates before the other, the fitness function for ω, f_ω, will be smaller for the shorter orbit. For this reason, a penalty is introduced to ensure the optimiser converges towards solutions that reach the end of the full propagation. For a given decision vector, the resulting orbit is propagated and the termination time of the simulation is extracted. If the termination time is less than the user-specified simulation time, a penalty – a very large value – is added to f_e and f_ω.

An additional penalty is included to aid the convergence of the optimiser. If f_ω is larger than 360°, it means ω is varying secularly, which is undesirable to obtain the frozen orbit solution. Therefore, a similar penalty as for the termination time is included for decision vectors that lead to $f_\omega > 360°$.

8.2. Design Space Exploration

Design space exploration involves exploring the link between the design variable space and the objective space of an optimisation problem in an attempt to find patterns or regions with higher chances of containing optima. Reducing the search space of an optimisation problem by performing a design space exploration can greatly reduce the computational effort without removing the global optima.

A Monte Carlo analysis is chosen to perform the design space exploration due to its simplicity. This method works by generating random samples of design variables within specified ranges. The resulting fitness function(s) for the randomly generated design variables is calculated without optimisation. In this way, a potential correlation between a given design variable and objective can be identified. The design space exploration is initiated with 100,000 initial states within the ranges displayed in Table 8.1.

Table 8.1: Design variables before design space exploration.

Injection time	a [m]	e [-]	i [deg]	ω [deg]	Ω [deg]	θ [deg]
March 16, 2029	390 – 6146	0 – 0.95	0 – 180	0 – 360	0 – 360	0

The range for a is derived directly from the minimum and maximum altitude constraints in Section 7.2 together with the average radius of Apophis of 193 m [13]. The eccentricity range could go all the way up to 1, but an eccentricity higher than 0.95 is impractical for a real space mission in any case.

Out of 100,000 initial states, only 5615 (5.6%) reach the 28-day mark. The distribution of these solutions over the orbital elements is illustrated in Figure 8.1.

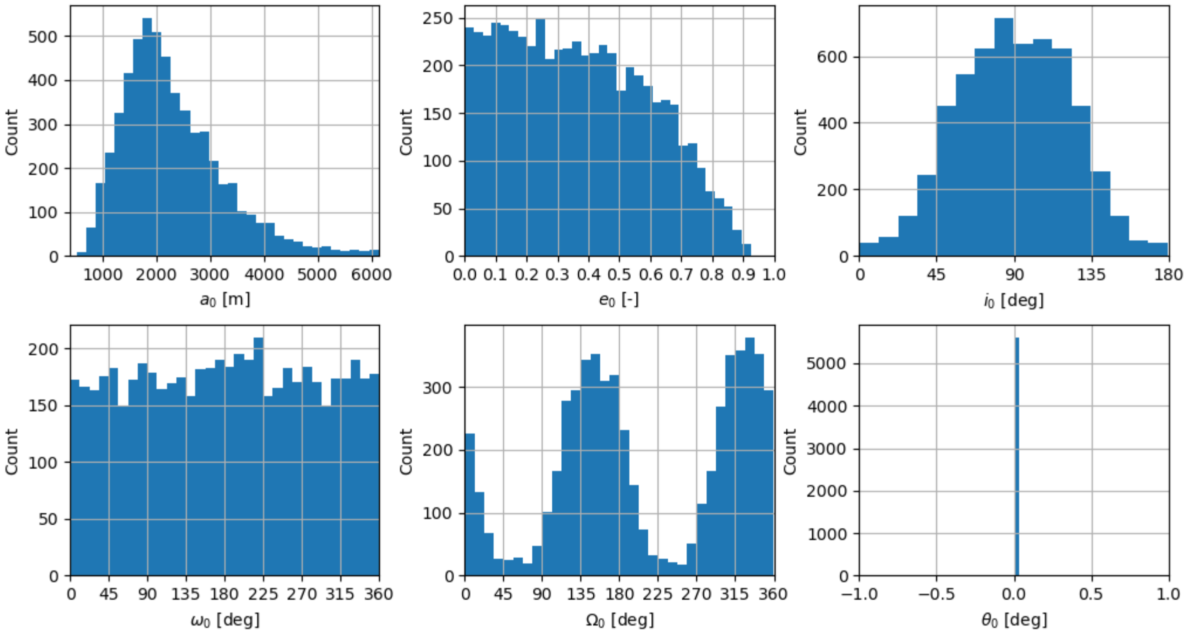

Figure 8.1: Histograms of initial orbital elements that reach the end of the propagation with θ_0 = 0°.

It is first noted that a single histogram bin is seen for θ_0 located at 0°. This confirms that the generation of random design variables to be used as input to the Monte Carlo simulation works correctly. For a_0 a skewed normal distribution is seen, centred at $a_0 \approx$ 1900 m. With regards to e_0, a lower number of solutions is present for higher e_0. A normal distribution is also observed for i_0, centred at 90°. While there are no clear patterns visible for ω_0, there are two clear optima for Ω_0 at around 150° and 330°. At the time of injection, these values of Ω_0 correspond to an orbit that is perpendicular to the Sun-asteroid line, which was already expected from the results of Section 5.2.

To investigate the link between the design variables and the fitness, the maximum difference in e and ω is plotted for the 5615 solutions that reach the end of the propagation. This is shown in Figure 8.2.

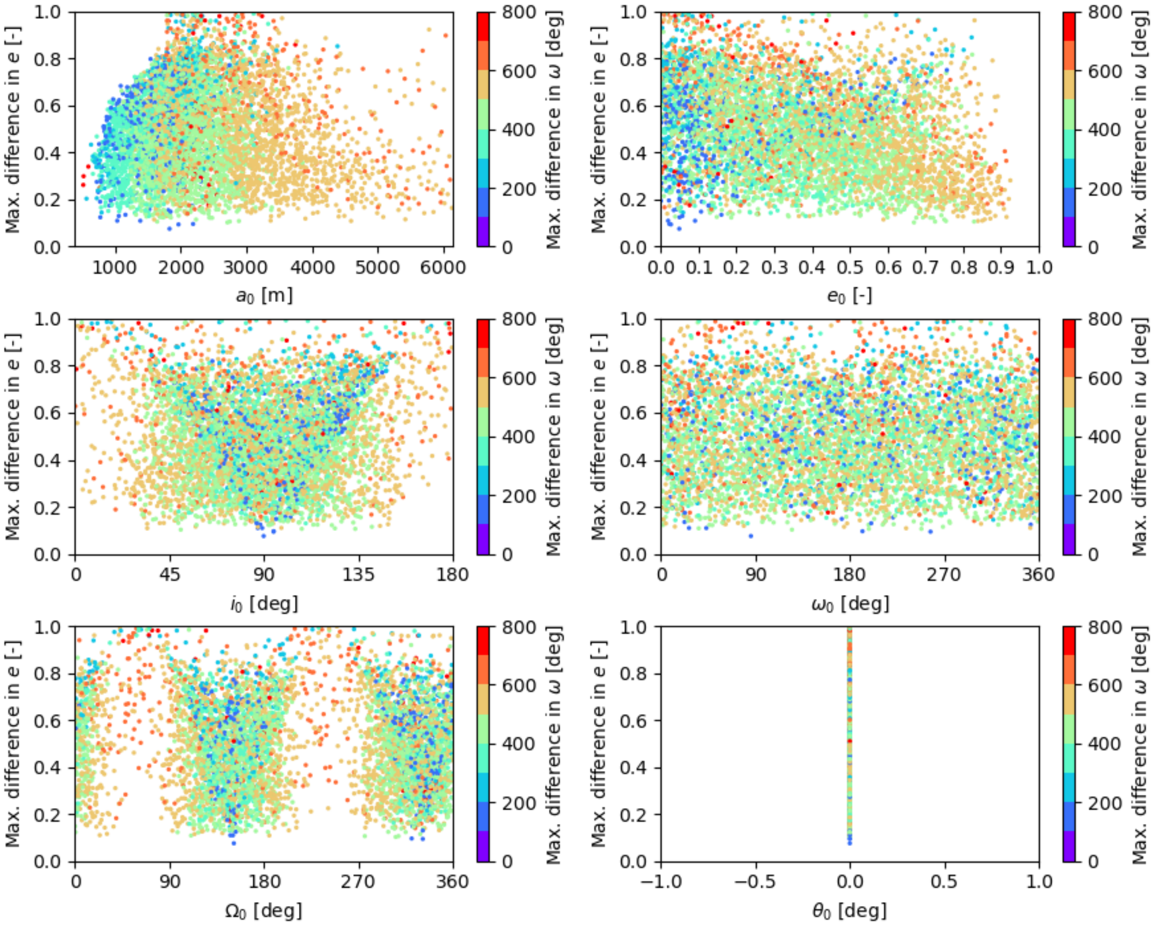

Figure 8.2: Fitness against design variables for θ_0 = 0°.

For the sampled decision vectors, there are solutions that reach a maximum difference in e as low as ~0.1 and a maximum difference in ω below 100°. Furthermore, the solutions with the lowest maximum difference in e appear to coincide with the lowest maximum difference in ω, showing the objectives are not necessarily competing. In terms of the correlation with the design variables, certain patterns can be observed. For a_0, there is a general trend showing that a larger a_0 leads to a larger maximum difference in ω. However, there are also a few solutions with a_0 < 500 m that lead to a secular variation of ω. The best solutions relative to a_0 appear to be located between 500 and 2000 m. For e_0, the maximum difference in ω is generally lower in the region of 0 to 0.15. A V-shaped pattern is visible in the plots of i_0 and Ω_0. The optimal solutions are centred at i_0 of 90°, as expected from the analytical results of Section 5.1. A similar difference in ω can be obtained moving away from 90° at the expense of a larger variation in e. A similar pattern is seen for Ω_0, where there are two local optima, one at 150° and the other at 330°. In the ECLIPJ2000 reference frame, these correspond to values of Ω_0 = ±90°, which matches the analytical results from Section 5.1. Furthermore, the similarities to the observations from

Figure 8.1 suggest that the design variables leading to lower maximum difference in e and ω represent orbits that are inherently more stable as there are more solutions that reach the end of the propagation for these initial conditions.

As previously explained, the values of Ω_0 leading to optimum solutions correspond to the Sun-terminator orbital family, which helps to stabilise the effects of SRP. Since the conjugate values of Ω_0 represent orbits of identical orientation, it is assumed that Ω_0 can be fixed at one of the two values. Thus, Ω_0 is fixed at 330°.

To check the interdependency between design variables, another Monte Carlo simulation is run with Ω_0 fixed at 330° in addition to the previous settings. This time, the simulation is initialised with 10,000 randomly generated decision vectors within the specified bounds. Again, only the results that reach the end of the propagation are displayed in Figure 8.3.

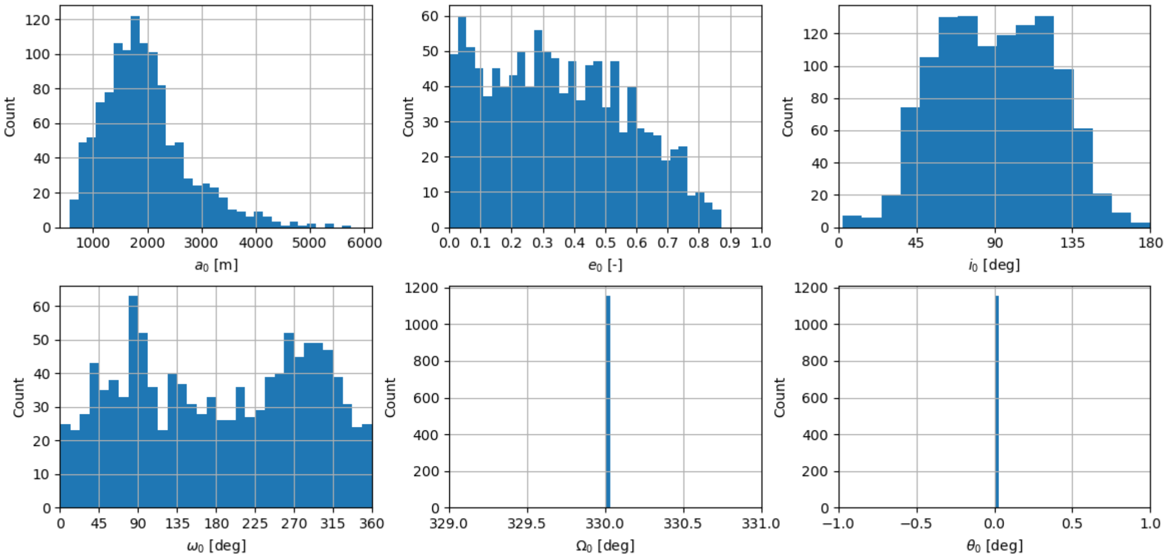

Figure 8.3: Histograms of initial orbital elements that reach the end of the propagation with θ_0 = 0° and Ω_0 = 330°.

This time, 1152 (11.52%) initial states reach the end of the simulation. Thus, the proportion of surviving orbits has more than doubled compared to when only θ_0 is fixed. Comparing Figure 8.3 to Figure 8.1, generally the same patterns are observed in the remaining design variables and there are no large solution space areas lost from fixing Ω_0 except from the solutions with e_0 > 0.87.

To further simplify the problem, i_0 is fixed at 90°. Apart from seeing this value leads to the best solutions looking at Figure 8.2, this inclination is also advantageous from a mission perspective as it allows maximum coverage up to the poles for mapping purposes [21]. A new Monte Carlo simulation is run with this additional constraint, using 10,000 randomly generated decision vectors. The results for the solutions that reach the end of the propagation are displayed in Figure 8.4.

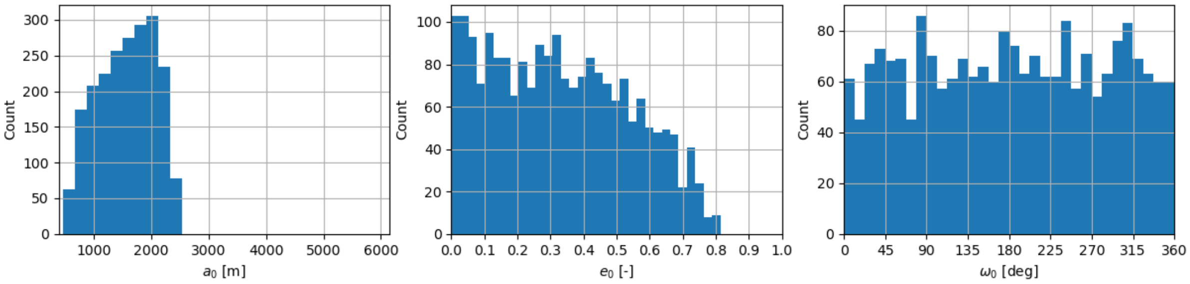

Figure 8.4: Histograms of initial orbital elements that reach the end of the propagation with θ_0 = 0°, Ω_0 = 330° and i_0 = 90°.

With these constraints on the design variables, 2110 (21.1%) solutions reach the end of the propagation. Although the constraint on i_0 removes all solutions with a_0 > 2500 m, it was already clear from Figure 8.2 that those solutions do not lead to optimal solutions in the objective space. On the other hand, there are still solutions that reach the end of the propagation for almost the entire range of e_0 and ω_0.

The correlation between the design space and objective space for the reduced problem is assessed with Figure 8.5.

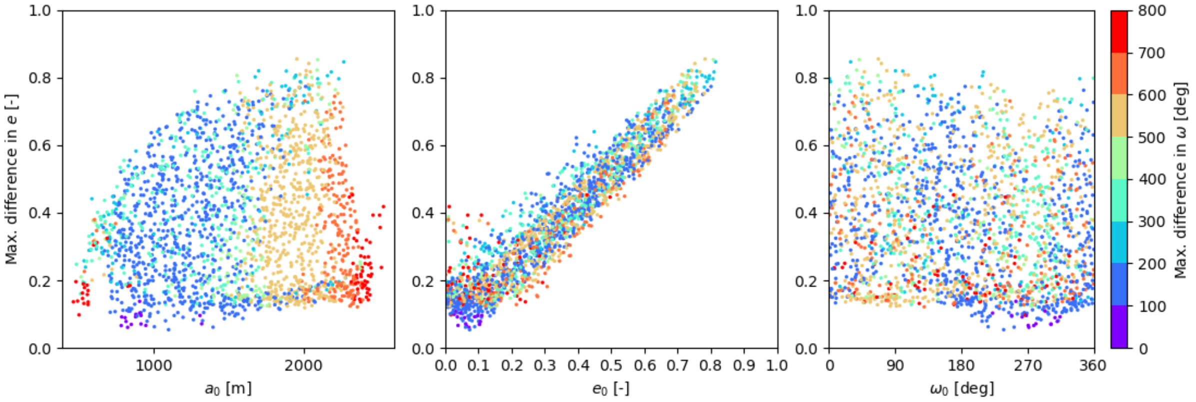

Figure 8.5: Fitness against design variables for θ_0 = 0°, Ω_0 = 330° and i_0 = 90°.

Looking at Figure 8.5, it is apparent that the optimal solutions correspond to a_0 values between ~600 and 1700 m. For reference, the OSIRIS-REx mission employed a semi-major axis of around 1850 and 1700 m respectively for the frozen orbits of the Orbital A and Orbital C phases [84, 85]. Since the characteristics of the OSIRIS-REx spacecraft have been assumed in this work, orbiting at a similar altitude above the surface of Apophis would mean the mapping instruments onboard the spacecraft would be able to provide images of similar resolution. Thus, translating the semi-major axis values to an equivalent orbital altitude for Apophis, a semi-major axis between 1800 and 1650 m respectively is obtained. Closer imaging of Bennu was carried out during the Orbital B phase, where the spacecraft was around 680 m above the asteroid's surface [86]. Translating this to Apophis would mean a semi-major axis of around 873 m. Since this a_0 value seems to correspond better to the optimal solutions in Figure 8.5 and would be a good choice of a for imaging in a real-life scenario, this value is selected.

Thanks to the design space exploration, the optimisation has been reduced from seven degrees of freedom to just two. By fixing all other design variables, the optimiser just needs to find the optimal combination of e_0 and ω_0 leading to the lowest f_e and f_ω. Even though these variables are left as free variables to be found by the optimisation algorithm, the search space can be reduced further from the results of Figure 8.5. Clearly, the optimal solutions in Figure 8.5 are distributed across an e_0 range of 0 to 0.15, and a range of ω_0 between 180° and 360°. The final design variables to be used in the optimisation and their values or ranges are thus provided as shown in Table 8.2.

Table 8.2: Design variables after design space exploration.

Injection time	a [m]	e [-]	i [deg]	ω [deg]	Ω [deg]	θ [deg]
16/03/2029	873	0 – 0.15	90	180 – 360	330	0

8.3. Algorithm Selection and Tuning

An optimisation algorithm is a numerical method designed to find the best possible solution to an optimisation problem. Different algorithms use different strategies to explore the search space. For practical purposes, the algorithm selection is limited to those available in PyGMO. The Non-dominated Sorting Genetic Algorithm (NSGA-II) and the Multi-Objective Evolutionary Algorithm by Decomposition (MOEA/D) are typical choices for astrodynamics problems. Although MOEA/D can be faster for some problems, NSGA-II generally obtains a better spread of solutions in the Pareto front [87, 88]. The Pareto front is the collection of solutions for which, for every individual in the front, it is not possible to further improve one objective without sacrificing the remaining objectives. Since the search space has already been greatly reduced, speed is not expected to be a limiting constraint. Thus, the NSGA-II algorithm is selected.

Genetic algorithms work by evolving an initially random population using crossover and mutation, where the most 'fit' individuals – the ones leading to the lowest fitness function values – are more likely to survive and reproduce [89]. The input parameters available for tuning the NSGA-II algorithm include the crossover and mutation probability, the crossover and mutation distribution index and the seed [90]. In this work, all the default values are assumed and the tuning is carried out on the population size and number of generations. A population size of 100 individuals with 100 generations is taken as a starting point.

For single-objective optimisation, the convergence of the algorithm can be checked in a straight-forward manner by confirming the fitness function value does not decrease further for an increased number of generations [21]. However, this is not possible for MOO as there is more than one fitness function and therefore there is not a single optimum but a Pareto front where all solutions can be considered optima. As an algorithm converges, the Pareto front for a minimisation problem will advance towards the lower left when considering two objectives. Therefore, tuning of the population size and number of generations is carried out by plotting the Pareto front at different generations. Convergence is identified when the Pareto front does not advance further with increased generations.

The progression of the Pareto front over different generations for a single run is shown in Figure 8.6.

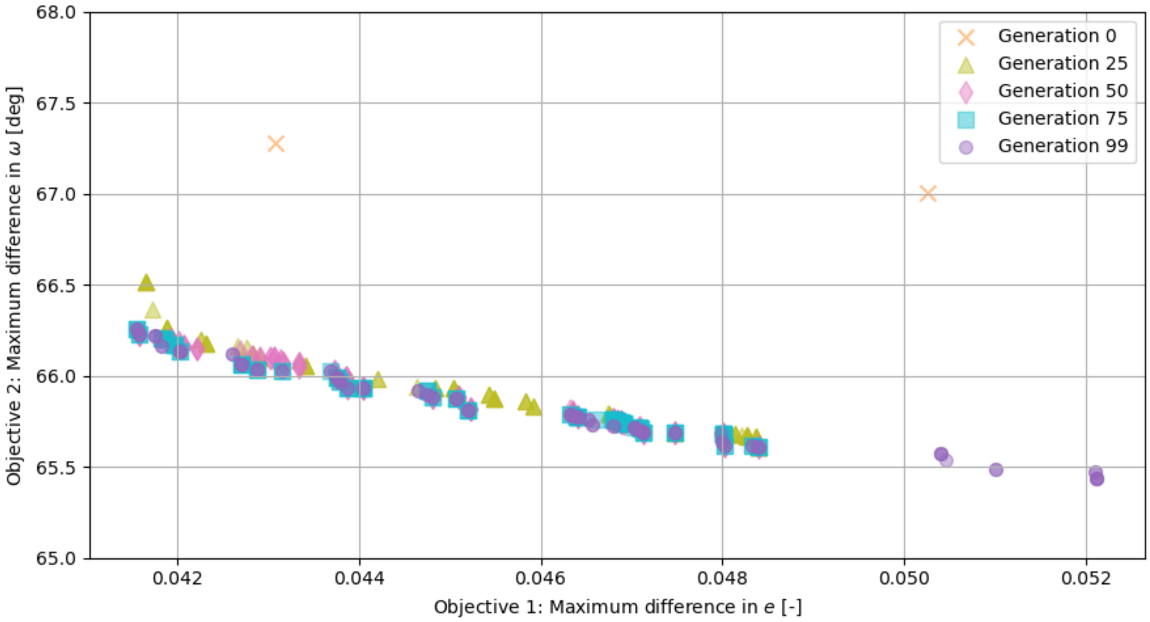

Figure 8.6: Pareto fronts at different generations for a population size of 100 individuals.

From generation 25 onwards, the Pareto front barely progresses further. Although the last generation manages to extend the Pareto front by finding solutions with an even lower maximum difference in ω, the remaining individuals are practically the same as for generation 75. Since there are still some additional solutions found for the last generation, the number of generations to be used for the generation of results is kept at 100 with a population size of 100. For the results shown in Figure 8.6, which are generated with a single run, the CPU time is approximately 40 minutes. Several runs are carried out with different seed numbers to increase the robustness of the final solutions shown in Chapter 9. If the solutions are robust, the Pareto front at the final generation should be more or less equal for any seed number, i.e. the solutions are not dependent on using a 'lucky' seed number. Since several runs are required for a single case, having a reasonable CPU time for a single run is important. Finally, if the final Pareto fronts for different seed numbers are similar, it can be confirmed that there is no need to tune the default parameters of the NSGA-II algorithm or the population size and number of generations.

IV

Results

The main results of this work are presented in the following chapters. First, the results obtained from the numerical analysis are presented in Chapter 9. Secondly, the results of the sensitivity analysis are shown in Chapter 10. Finally, the verification and validation procedures carried out to test the validity of the results are documented in Chapter 11.

9

Numerical Results

The aim of the numerical results is to answer the research question: what is the feasibility of designing and maintaining stable control-free frozen orbits around asteroid Apophis before and during the 2029 Earth flyby? Thus, the results are divided into two cases. In Section 9.1, the pre-flyby frozen orbit solutions are presented. Then, the results obtained with the added constraint of surviving until at least two weeks after the flyby – referred to as the post-flyby results – are shown in Section 9.2.

9.1. Pre-Flyby

The pre-flyby results are generated by setting up the simulation as described in Chapter 7. The simulation duration is set to 28 days with a start date of 16th March, 2029. With these inputs, the propagation terminates ~22 hours before the closest approach with Earth. When running the optimisation, there is a component of luck involved due to the random generation of the initial population. To account for this randomness, the optimisation is run three times with three different seeds. The Pareto front at the final generation is saved for each run and shown in Figure 9.1. For the pre-flyby case, each run took around 40 minutes of CPU time. This showcases the importance of the integrator selection, acceleration tuning and design space exploration carried out in Chapter 8 prior to the optimisation.

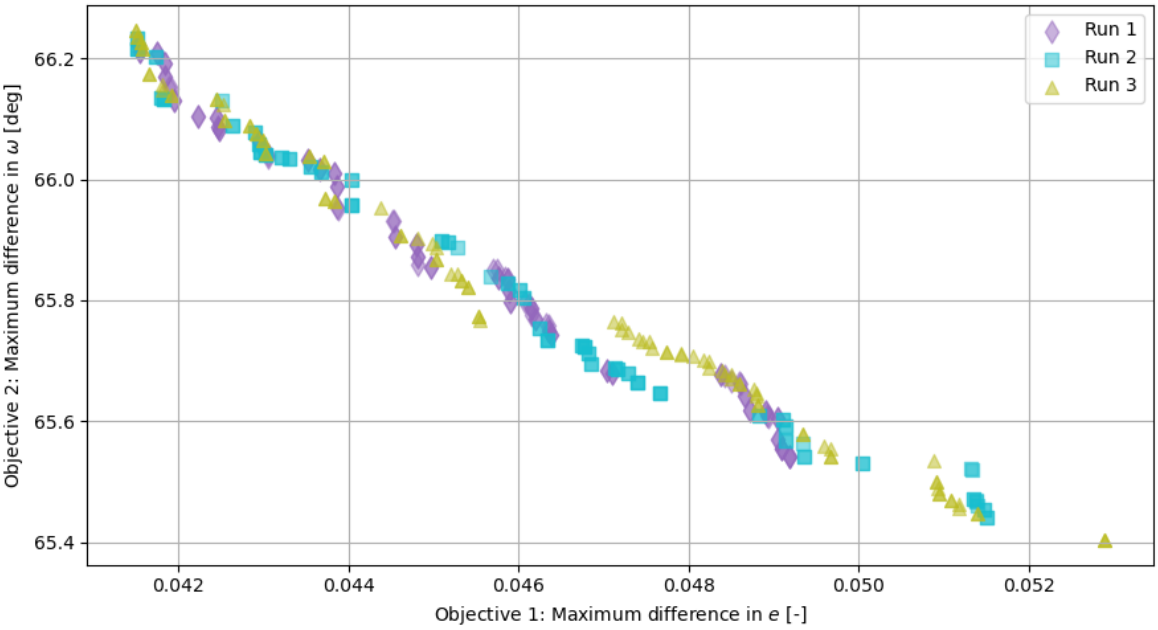

Figure 9.1: Pareto front at final generation of pre-flyby case for three different runs.

Figure 9.1 shows that a comparable Pareto front has been found by the optimiser for the three different runs. The maximum difference between these Pareto fronts is approximately 0.001 in e and below 0.1° in ω, demonstrating the convergence of the solutions. It is thus confirmed that the number of individuals and generations selected in Section 8.3 is appropriate for this problem.

In Figure 9.1, the final Pareto front obtained from combining the three runs is shown.

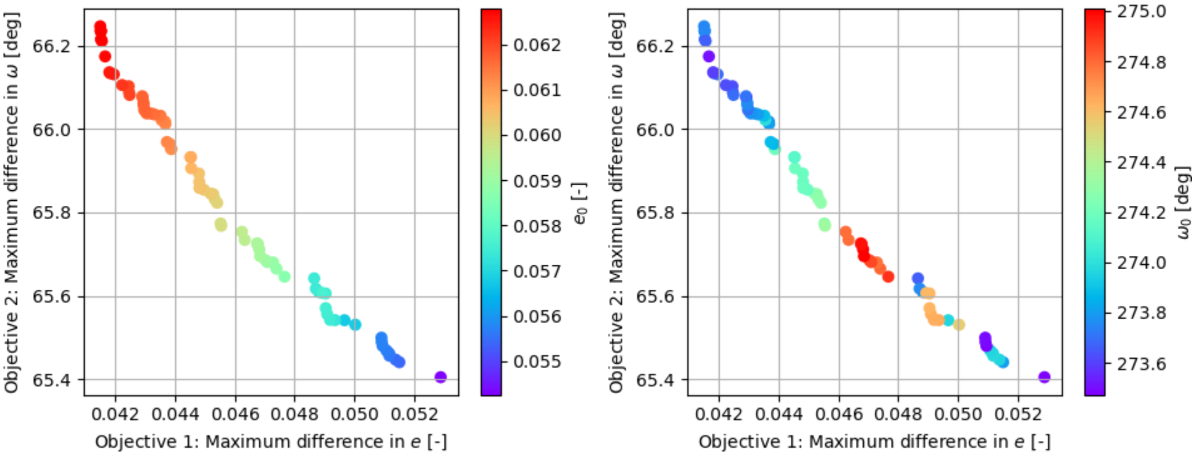

Figure 9.2: Final Pareto front against design variables for pre-flyby case.

The optimal solutions correspond to $e_0 \approx 0.06$ and $\omega_0 \approx 274°$. Within the small range of near-circular e_0 values, a smaller initial eccentricity increases the maximum difference in e and decreases the maximum difference in ω. On the other hand, a minimum-maximum-minimum pattern is observed for ω_0 for increasing e_0. Although the search space for ω_0 was constrained to values between 180° and 360°, it was already expected from Figure 8.5 that the optimal solutions would be close to 270°.

The spread of the design variables leading to the final Pareto front is of ~0.008 in e_0 and 1.5° in ω_0. Since the best orbit injection accuracy achieved during the OSIRIS-REx mission corresponded to 0.01 in e and 1.04° in ω, all the solutions can essentially be assumed equal to one optimum solution [7]. The small range in e_0 and ω_0 leading to this Pareto front also explains why the maximum difference in e and ω is spread over a small range – approximately 0.0115 for e and 0.85° for ω.

One of the solutions from the Pareto front is selected arbitrarily with the design variables e_0 = 0.06278 and ω_0 = 273.66°, consistent with the solutions from Figure 9.2. The remaining design variables are fixed to the values in Table 8.2. Although there are other solutions along the Pareto front, this solution is henceforth referred to as the pre-flyby result. The resulting orbit is illustrated in Figure 9.3 with respect to the Apophis-centred, polar-equatorial frame, and in Figure 9.4 with respect to the Apophis-centred, ECLIPJ2000 frame.

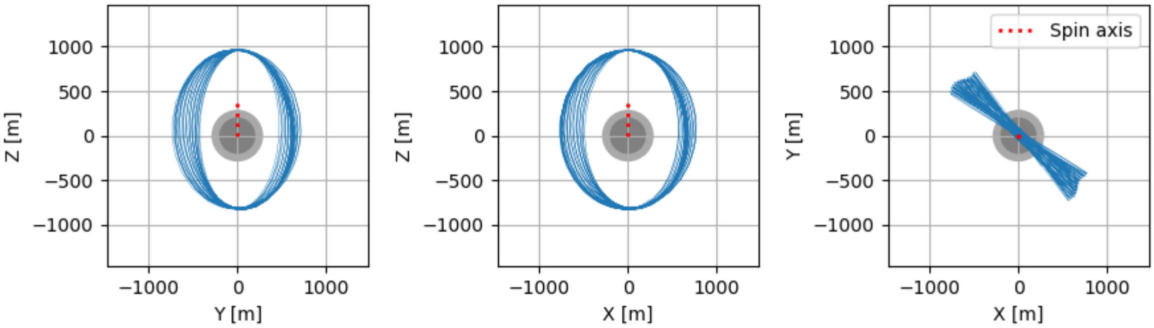

Figure 9.3: Orbit visualisation of pre-flyby result with respect to the Apophis-centred, polar-equatorial reference frame.

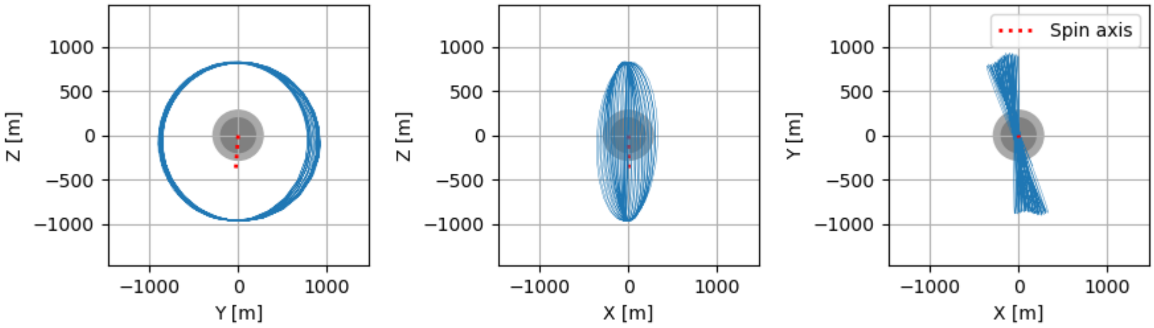

Figure 9.4: Orbit visualisation of pre-flyby result with respect to the Apophis-centred, ECLIPJ2000 reference frame.

From the orbit visualisation, the stability of the orbital elements is apparent. The solution corresponds to a near-circular, near-polar, Sun-terminator frozen orbit. This is the same type of frozen orbit employed in the Orbital A and Orbital C phases of the OSIRIS-REx mission [7].

The orbital element evolution for the pre-flyby case is then displayed in Figure 9.5.

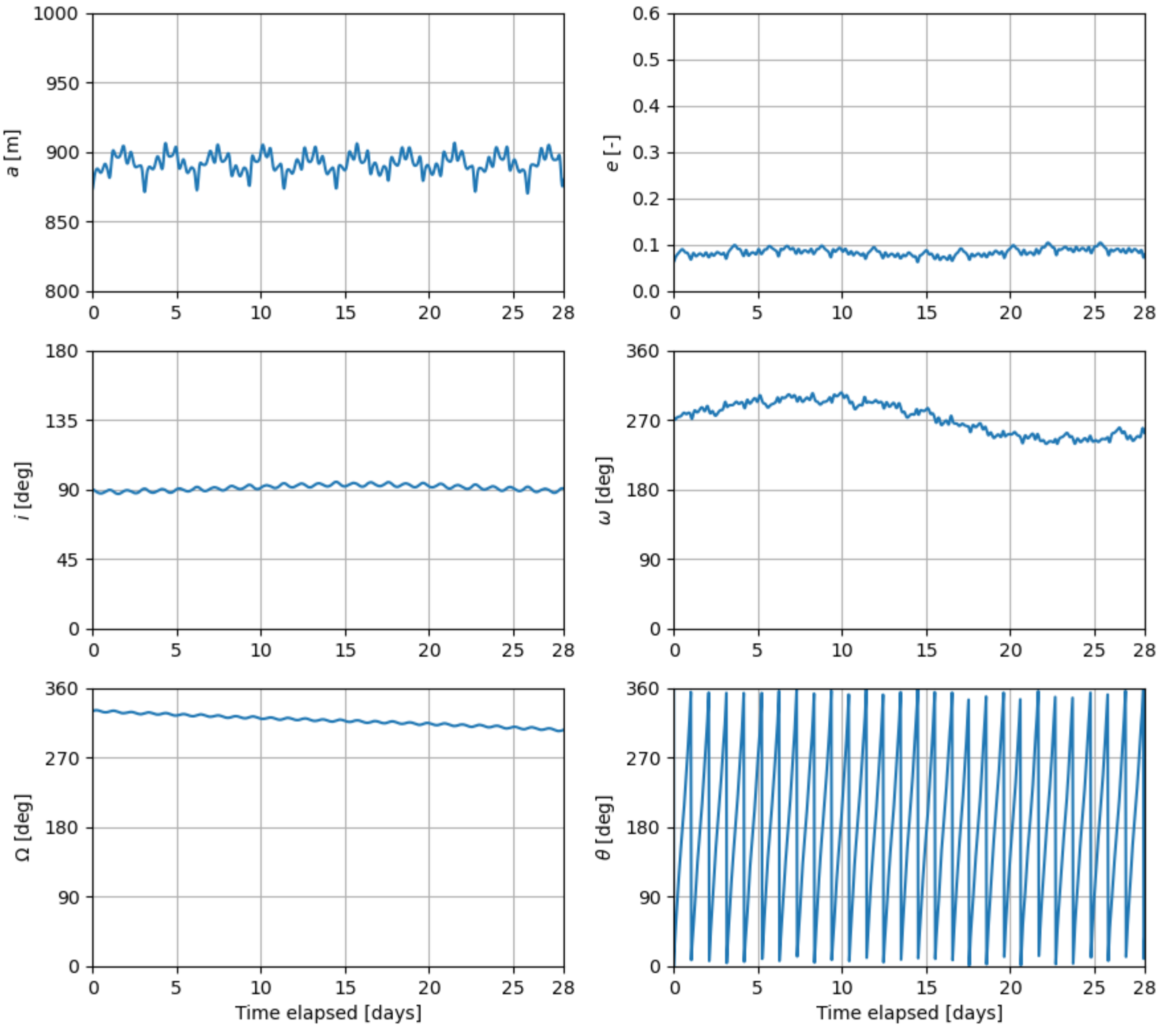

Figure 9.5: Orbital element time evolution for pre-flyby result.

A stable evolution is observed for all orbital elements. The maximum variation in the semi-major axis is ~35 m, the eccentricity varies between 0.06 and 0.1, and the inclination varies between 86° and 94°. A long-term periodic variation in ω is observed, leading to the maximum variation of approximately 66°. Furthermore, a secular variation in Ω is observed. The rate of change of Ω is approximately 0.9°/day. Knowing Apophis' semi-major axis at the time of the flyby is essentially 1 AU, which corresponds to a mean motion around the Sun of approximately 1°/day, it can be concluded that the secular variation of Ω leads to a Sun-synchronous orbit. Thus, the precession of Ω is such that the orientation of the orbital plane remains constant with respect to the Sun over time. Since the initial orientation of the orbit is perpendicular to the Sun-asteroid line, this also means the spacecraft is constantly illuminated.

The combined drift of e and ω can be visualised in Figure 9.6a, while the altitude at different sub-satellite locations is shown in Figure 9.6b.

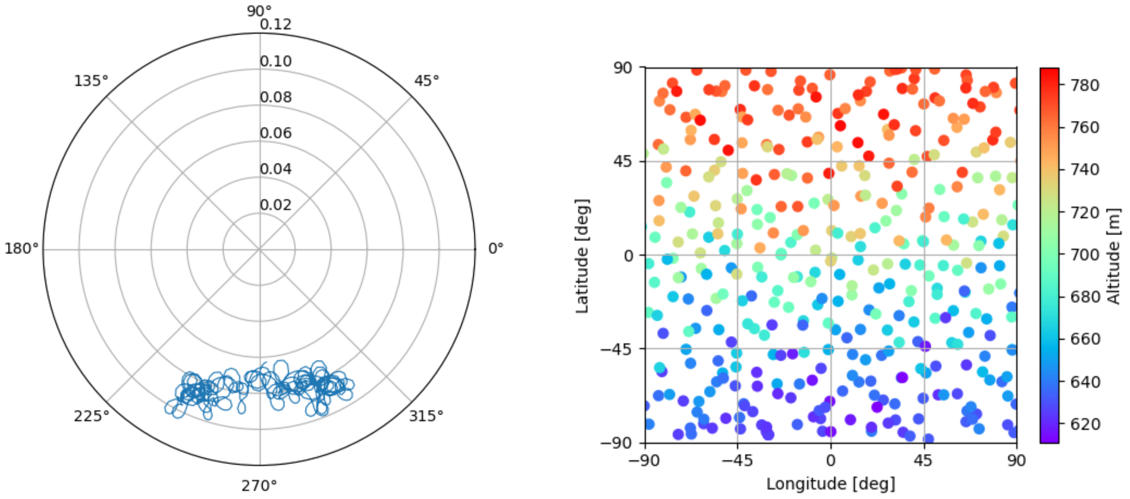

(a) Polar plot of $e - \omega$ drift.

(b) Orbital altitude variation over latitude and longitude.

Figure 9.6: Drift of e and ω and altitude variation over sub-satellite locations for pre-flyby result.

Although the $e - \omega$ drift appears to be somewhat chaotic, this is due to the fact that the osculating elements are plotted rather than the orbital-averaged elements, so the short-period variations are still present. Nevertheless, ω oscillates around the mean value of 270° in a periodic manner and the eccentricity oscillates between 0.06 and 0.10. From the definition of the frozen condition, the altitude over a given point on the surface of the central body should be approximately constant over consecutive passes [21]. Figure 9.6b shows the total altitude variation is around 180 m, reaching as low as 610 m and as high as 790 m. However, this is simply due to the fact that the orbit is not circular. The altitude at similar latitude and longitude appears to be somewhat constant, within $\approx$ 40 m, as expected from the frozen condition.

9.2. Post-Flyby

The post-flyby analysis focuses on finding frozen orbit solutions that survive the flyby and remain in orbit around Apophis for at least two weeks after. First, the solutions from the final Pareto front of the pre-flyby case are taken and the simulations are run with a simulation duration of 42 days rather than 28. All 77 unique design variable pairs obtained from Figure 9.2 terminate before day 42. In fact, all solutions terminate due to the surface impact condition. This is expected since the orbital altitude before the flyby is as low as 610 m and the minimum altitude condition is of 197 m and the perturbations during the flyby can easily lead to differences in altitude of more than 400 m. Given the size of the system, with Apophis' radius equal to 193 m, such drastic altitude changes signify a high risk of collision. Furthermore, the accelerations leading to these altitude changes can exert large stresses on the spacecraft structure, leading to partial or total failure.

Therefore, a new optimisation is carried out to find solutions that survive for at least two weeks post-flyby. The optimisation set-up is the same as for the pre-flyby case with the design variable inputs from

Table 8.2. The main difference is that the simulation duration is now set to 42 days and the maximum difference in e and ω is only calculated for the orbital elements up until the time of the flyby. Thus, the objective of the post-flyby optimisation case is to find the best frozen condition pre-flyby that survives the flyby and remains in orbit for two weeks after, even if the behaviour post-flyby does not correspond to a frozen orbit. In this case, the optimisation is run five times with five different seeds. The final Pareto front of each run is shown in Figure 9.7. Due to the longer propagation time, each run for the post-flyby case takes around 50 minutes of CPU time.

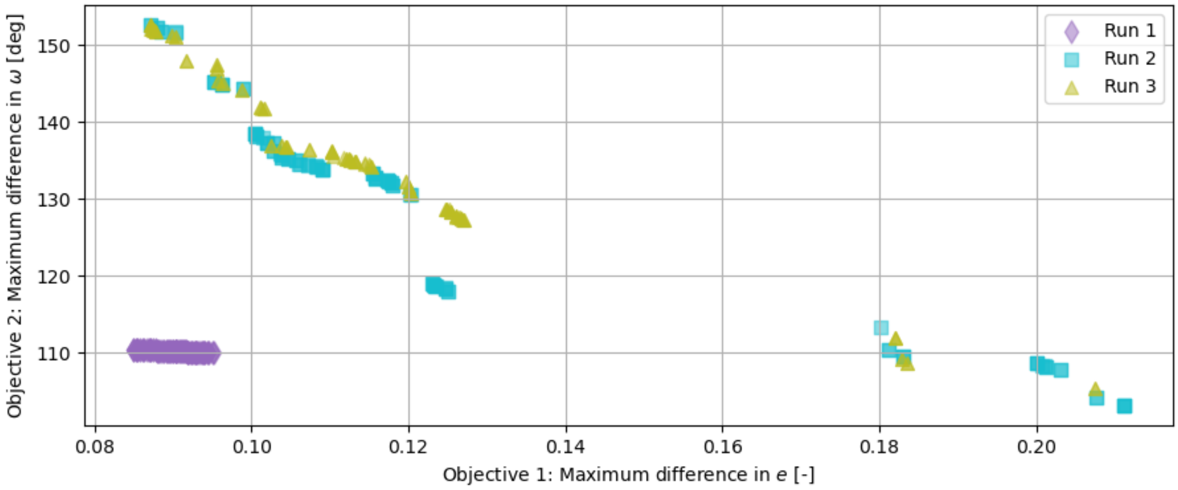

Figure 9.7: Pareto front at final generation of post-flyby case for five different runs.

For the post-flyby case, a larger difference between the three runs is observed than for the pre-flyby case. This illustrates the importance of performing multiple runs with different seeds. For run 1, the optimiser was 'lucky' to find a combination of design variables leading to a much lower maximum difference in ω than runs 1 and 2, at around 110° rather than 150° for the same maximum difference in e. This suggests that better convergence could be obtained with further tuning of the algorithm parameters or by performing a larger number of runs. However, these three runs are used for the final results due to time constraints. Furthermore, it is expected for the optimiser to display worse convergence for the post-flyby case as the dynamics involved are much more complex than for the pre-flyby scenario: the minimum achieved difference in e is around 0.085 and for ω it is 103°.

The final Pareto front of the post-flyby case, generated from the combination of the three runs in Figure 9.7, is displayed in Figure 9.8 together with the design variables e_0 and ω_0.

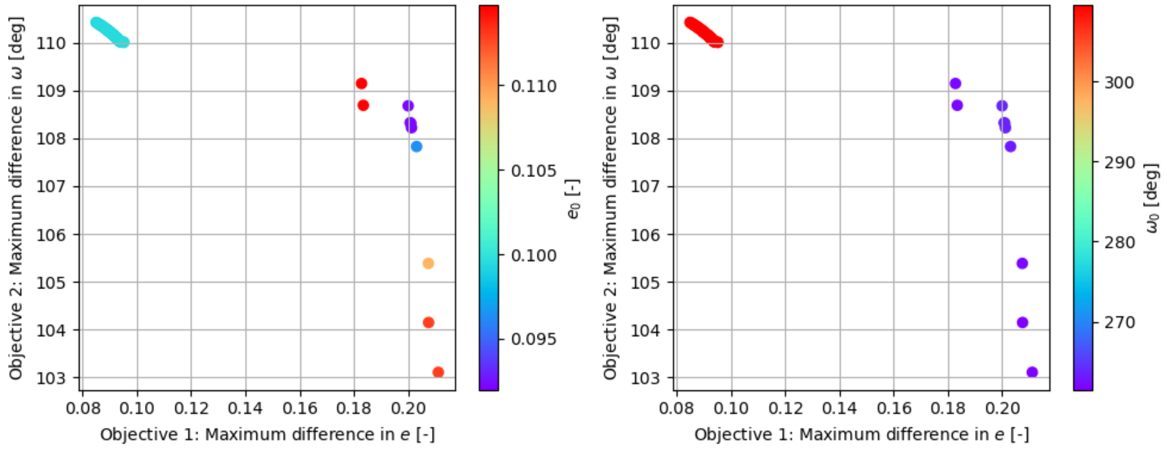

Figure 9.8: Final Pareto front against design variables for post-flyby case.

The range of e_0 leading to the final Pareto front is between 0.092 and 0.115. For the bundle of solutions on the top left edge of the Pareto front, $e_0 \approx 0.0994$. For ω_0 there are two main solutions, the solutions on the top left edge of the Pareto front correspond to $\omega_0 = 309.56^\circ$. The remaining solutions are obtained for ω_0 between 261.48° and 264°. The solutions with $\omega_0 \approx 263^\circ$ achieve a maximum difference in ω as low as 103° at the expense of more than doubling the maximum difference in e from 0.09 to 0.21.

For comparison, the Pareto fronts of the pre-flyby and post-flyby cases are shown in Figure 9.9.

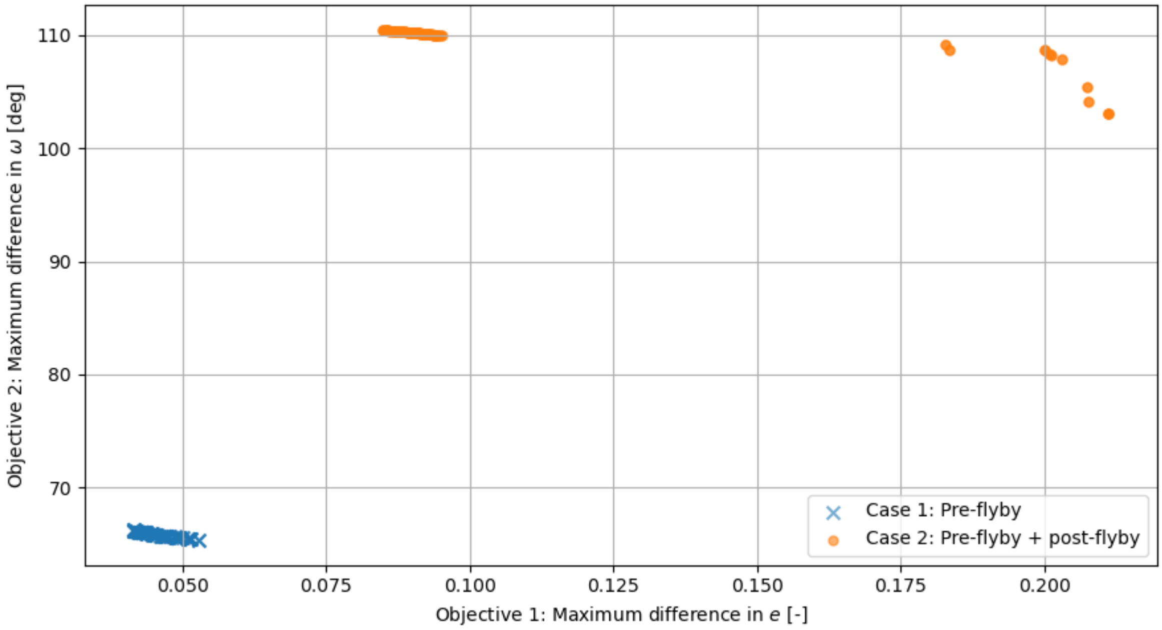

Figure 9.9: Final Pareto front against design variables for pre-flyby and post-flyby case.

As expected, the Pareto front for the post-flyby case is less optimal than for the pre-flyby case due to the constraint on reaching the end of the 42-day propagation and the strong perturbations acting on the spacecraft during the flyby. While the Pareto front for the pre-flyby case effectively represents just one orbit, there is greater variation in the post-flyby solutions.

One of the solutions from the final Pareto front of the post-flyby case is arbitrarily selected to take a closer look at the dynamic behaviour. The initial eccentricity for this result is 0.11473 and the initial argument of periapsis is 261.98°. This result is henceforth referred to as the post-flyby result, even though it includes the behaviour both before and after the flyby. The resulting orbit is shown in Figure 9.10 in the Apophis-centred, polar-equatorial frame and in Figure 9.11 in the Apophis-centred, ECLIPJ2000 reference frame.

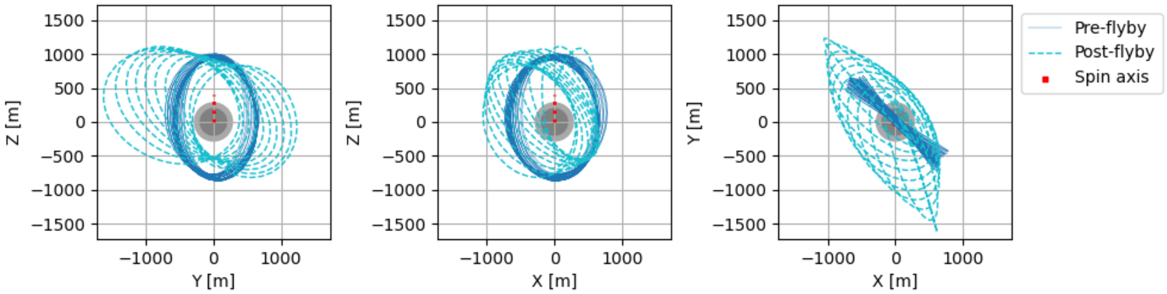

Figure 9.10: Orbit visualisation of post-flyby result with respect to the Apophis-centred, polar-equatorial reference frame.

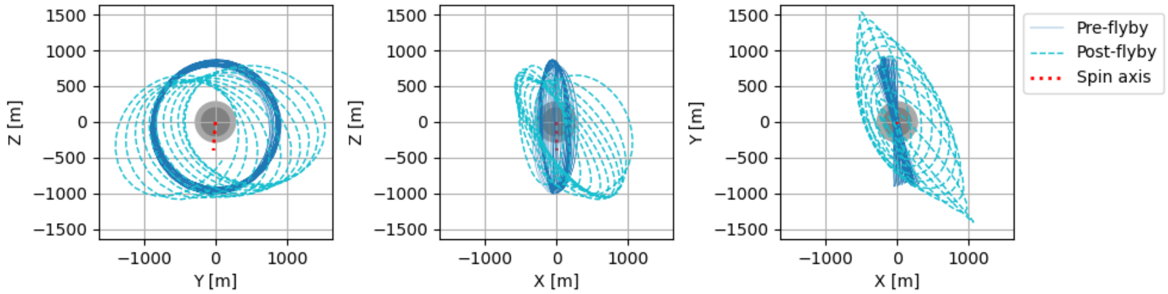

Figure 9.11: Orbit visualisation of post-flyby result with respect to the Apophis-centred, ECLIPJ2000 reference frame.

The pre-flyby portion of the orbit is very similar to the pre-flyby solution, i.e. a near-circular, near-polar, Sun-terminator frozen orbit. The destabilisation of the orbit induced by the flyby is apparent from the higher eccentricity and the precession of the argument of periapsis. Nevertheless, the orbit seems to maintain a constant orientation with respect to the Sun.

The orbital element evolution for the pre-flyby and post-flyby result is shown together in Figure 9.12.

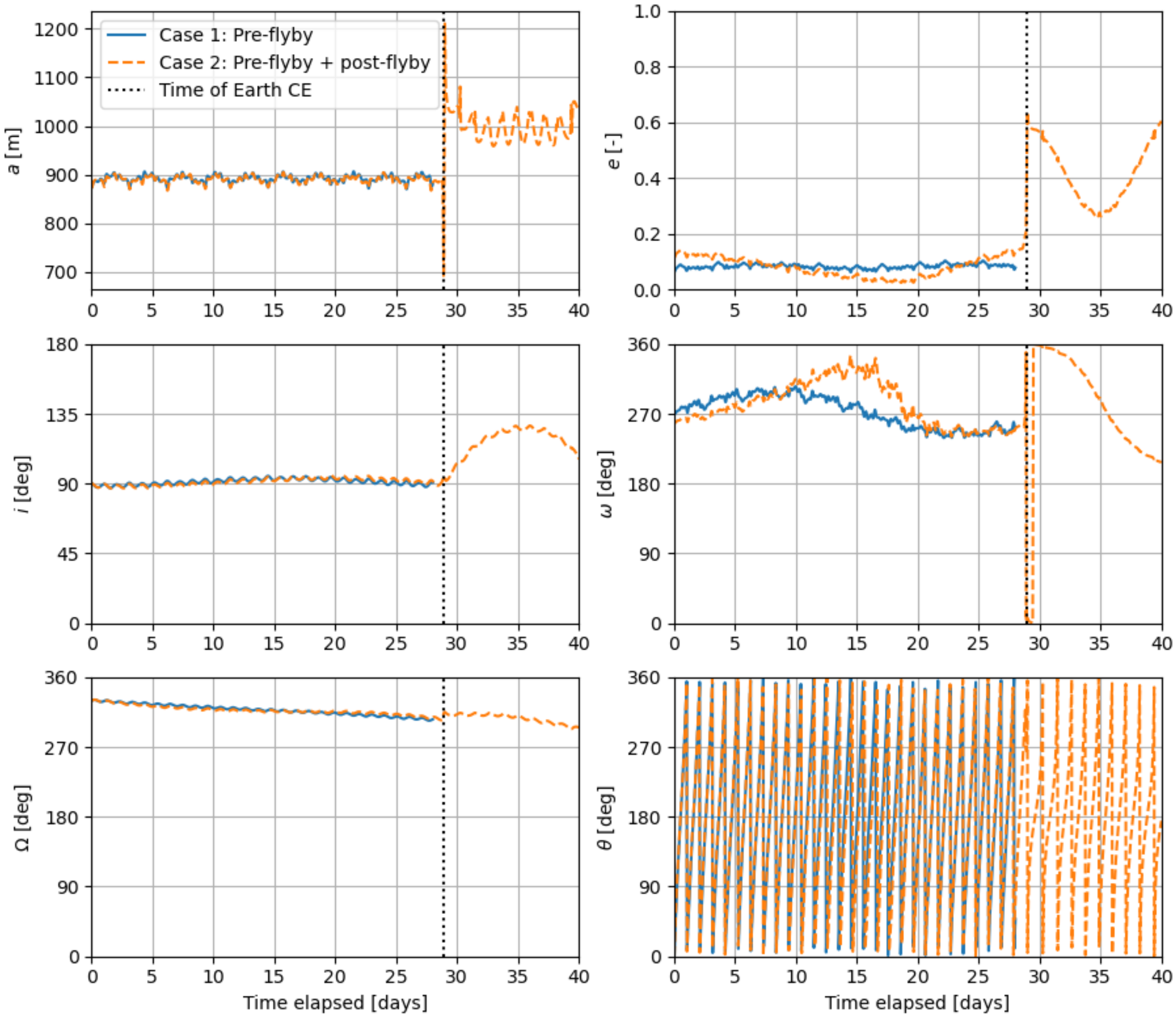

Figure 9.12: Orbital element time evolution for pre-flyby and post-flyby result.

Firstly, it is concluded that for the post-flyby result, the behaviour of e and ω does not correspond to a frozen orbit: the variations are too large. Nevertheless, the semi-major axis seems relatively stable even after the flyby with an average value of 1000 m. Although the eccentricity and argument of periapsis in the pre-flyby section do have a larger variation for the post-flyby result, the variation in a, i and Ω is almost identical for both results. The only orbital element that seems unchanged by the flyby is the longitude of the ascending node, which continues varying secularly with a rate corresponding to the Sun-synchronous condition. This result symbolises that the Sun-synchronous situation is the most important condition for the stability of the orbit around Apophis. This is consistent with the perturbation analysis carried out in Section 3.4, where it was seen that SRP leads to the largest variations in the orbital elements.

The drift in e and ω for both results is shown in Figure 9.13.

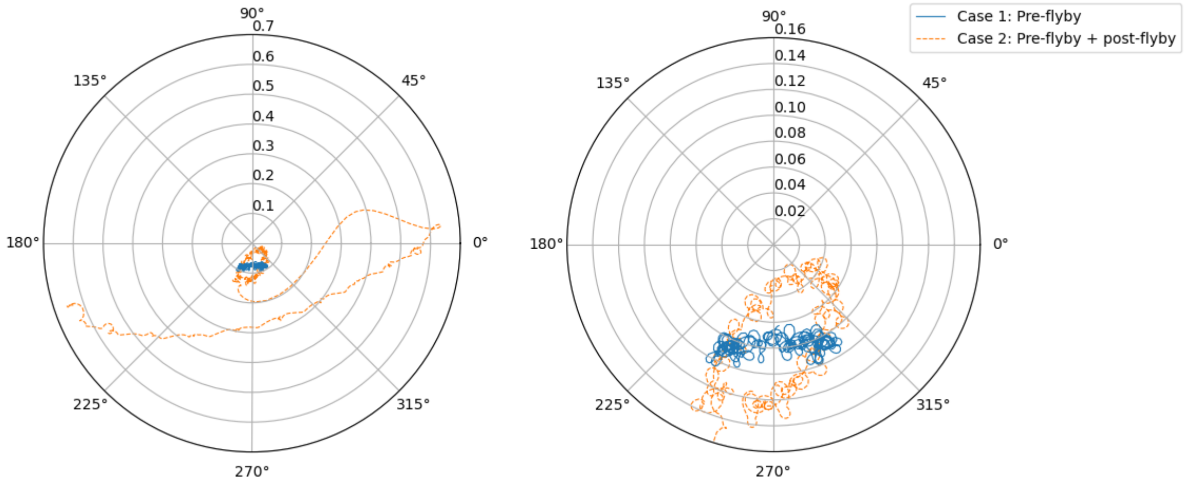

(a) Full 42-day propagation.

(b) Close-up of pre-flyby portion.

Figure 9.13: Polar plot of $e - \omega$ drift for pre-flyby and post-flyby result.

The drift in e and ω perfectly illustrates the change from a quasi-frozen orbit before the flyby to a non-frozen orbit after the flyby for the post-flyby result. In the close-up view of the $e - \omega$ drift, it is seen that both cases have a similar periodic variation in ω, but the drift of e is larger for the post-flyby case. If it were not for the disturbance of the flyby, the $e - \omega$ drift pattern suggests the orbital elements would continue to vary periodically.

Finally, the design variables and resulting fitness for the pre-flyby and post-flyby results are summarised in Table 9.1.

Table 9.1: Design variables and fitness of pre-flyby and post-flyby results.

Case	Design variable		Fitness	
	e_0 [-]	ω_0 [deg]	Max. difference in e [-]	Max. difference in ω [deg]
Pre-flyby	0.062785	273.66	0.04	66.21
Post-flyby	0.114734	261.98	0.18	109.15

It has been seen that e_0 and ω_0 describe a very similar orbit for the pre-flyby period for both cases: a near-circular, near-polar, Sun-terminator orbit. Nevertheless, the constraint set on surviving the flyby requires some sacrifice in the variations of e and ω in the pre-flyby part of the orbit. The similarity in design variables between the two cases illustrates how a relatively small error in injection could lead to vastly different behaviour during the flyby, since the pre-flyby case does not survive the flyby and the post-flyby case does. From a practical standpoint, it is evidently better to have a less optimal frozen orbit before the flyby with a longer mission duration, than an optimal frozen orbit pre-flyby that leads to impact at the time of the flyby.

Although this work focuses on control-free motion, performing an orbital correction manoeuvre shortly after the flyby to restore the orbit to the original quasi-frozen orbit design could be done in practice. As previously mentioned in Section 2.3, OSIRIS-REx will have a remaining ΔV capacity of 600 m/s after mission completion [59]. This value is taken as a reference to assess the feasibility of the required orbital correction.

Assuming the physical and dynamical parameters of Apophis are equal after the Earth flyby, a first-order assessment of the required ΔV for orbital correction may be carried out. The result shown in Figure 9.12 corresponds to an initial Keplerian state vector $\boldsymbol{\kappa}_0 = [873, 0.11473, 90, 261.98, 330, 0]$. Thus, it is assumed that the corrected orbit shall bring the inclination back to 90°, the argument of periapsis to approximately 270° and the eccentricity to around 0.115. From the design space exploration results shown in Figure 8.5, changes in a are deemed acceptable as long as the new a is in the range of 600 to 1700 m. The true anomaly is also considered a free variable. For a preliminary calculation, only purely tangential manoeuvres in the radial S, along-track N and cross-track W directions are considered here.

Looking at Figure 9.12, it is observed that at around day 35 the osculating argument of periapsis is around 270°. This point in time also corresponds to a relatively low eccentricity of 0.264. This is desirable since then the required change in eccentricity is smaller. Additionally, this point in time corresponds to θ = 90°, which means a minimum-ΔV impulsive manoeuvre in the N-direction can be carried out to change e without changing ω. The ΔV for such a manoeuvre is obtained from Equation 9.1 [23].

$$|\Delta V_N|_{min} = \frac{1}{2}\,|\Delta e|\sqrt{\frac{\mu}{a(1-e^2)}} \tag{9.1}$$

Thus, to bring the eccentricity from 0.264 to 0.115, the required ΔV_N is 0.00457 m/s. Nevertheless, this manoeuvre also causes a change in a, which can be calculated from Equation 9.2 [23].

$$\Delta a = 2\Delta V_N(1 + e\cos\theta)a\sqrt{\frac{a}{\mu(1-e^2)}} \tag{9.2}$$

Noting that it is assumed that θ = 90° for Equation 9.1, the corresponding Δa is 161 m, which brings the semi-major axis from 1008 to 1169 m. This is a very large increase considering that this is supposed to be an instantaneous manoeuvre, but for a preliminary calculation this is assumed reasonable. Furthermore, the new a value is still within the semi-major axis range of optimal solutions shown in Figure 8.5.

Although e is back to its original value, ω and i still need to be corrected, ideally without changing Ω as it is known this is the orbital element which represents the orientation of the orbit with respect to the Sun, thus balancing the SRP perturbations. For a change in ω and i an impulsive manoeuvre in the cross-track direction is required. At day 35 and θ = 90°, i = 125.7° and ω = 286.26°. It is noted that i and ω are unchanged from the first manoeuvre in N-direction. The required ΔV for a given change in i is given by Equation 9.3 [23].

$$\Delta V_W = \Delta i\sqrt{\frac{\mu}{a(1-e^2)}}\frac{1 + e\cos\theta}{\cos(\omega + \theta)} \tag{9.3}$$

Using the corrected values of e = 0.115 and a = 1169 m, and Δi = 90 - 125.7 = -35.7°, a value of ΔV_W = -0.03597 m/s is obtained. The change in ω is calculated using Equation 9.4 [23].

$$\Delta\omega = -\Delta V_W\sqrt{\frac{a(1-e^2)}{\mu}}\frac{\sin(\omega + \theta)}{\tan i(1 + e\cos\theta)} \tag{9.4}$$

Thus, $\Delta\omega$ = -7.48° and the corrected argument of periapsis is 278.78°. Looking at Figure 8.5, this value is assumed to also correspond to the frozen condition despite not being exactly equal to 270°.

The change in Ω for this manoeuvre is also important to consider and is calculated with Equation 9.5 [23].

$$\Delta\Omega = \Delta V_W \sqrt{\frac{a(1-e^2)}{\mu}} \frac{\sin(\omega+\theta)}{\sin i(1+e\cos\theta)} \tag{9.5}$$

This leads to $\Delta\Omega = -12.8°$ and a final value of $\Omega = 264.83°$.

With only two impulsive manoeuvres and a total ΔV of 0.0405 m/s, the orbit is brought back to almost the original frozen condition. Compared to the 600 m/s ΔV capacity, this value is considered more than reasonable.

A preliminary calculation of the required propellant mass for these orbital corrections can be carried out using Tsiolkovsky's rocket equation, which is rearranged as shown in Equation 9.6 to find the propellant mass [23].

$$m_{prop} = m_0(1 - e^{-\frac{\Delta V}{I_{sp}g_0}}) \tag{9.6}$$

Here, m_0 is the initial mass, m_{prop} is the propellant mass used to achieve a given ΔV, e is Euler's number, g_0 is the standard gravity and I_{sp} is the specific impulse of the rocket engine.

The calculation is carried out in two parts, first using ΔV_N. The initial spacecraft mass is assumed equal to 1500 kg and I_{sp} is taken to be 230 s, equal to that of the main thrusters of OSIRIS-REx [13, 91]. These values lead to m_{prop} = 0.00304 kg. Although this mass is almost negligible, for the second manoeuvre m_0 = 1500 - 0.003 = 1499.997 kg is used. Using ΔV_W this time and the new m_0, the required propellant mass for the second manoeuvre is 1 kg. Thus, a total propellant mass of 1.003 kg is required.

The validity of these preliminary calculations needs to be assessed further since the equations are obtained from the linearisation of Gauss' form of the LPEs and should only be used for small changes in the orbital elements. Due to time constraints, such work is left as a recommendation for future research.

10

Sensitivity

In this chapter, a sensitivity analysis is carried out to test the robustness of the solution to uncertainties in the modelling. Some of the parameters that are considered to be of biggest influence are examined. Before conducting the sensitivity analysis, the nominal result is generated with the high-fidelity model used to generate the benchmark solution in Subsection 7.3.1. This nominal result is presented in Section 10.1. Then, the sensitivity of this solution to the uncertainties in the physical parameters of Apophis, specifically its mass and spin-axis orientation, is analysed in Section 10.2. Following this, the sensitivity to different magnitudes of SRP is discussed in Section 10.3. Finally, the influence of orbit injection inaccuracies on the solution is analysed in Section 10.4.

10.1. Nominal Solution

The nominal solution is essentially the benchmark solution against which the sensitivity analysis is performed. The focus of the sensitivity analysis is only on the pre-flyby result since the uncertainty in the post-flyby parameters is unknown.

The initial state associated with the pre-flyby result presented in Section 9.1 is used in combination with the integration settings and acceleration models used for the benchmark generation in Subsection 7.3.1. This simulation includes more accelerations and a smaller integration time step and is thus assumed to be a high-fidelity solution.

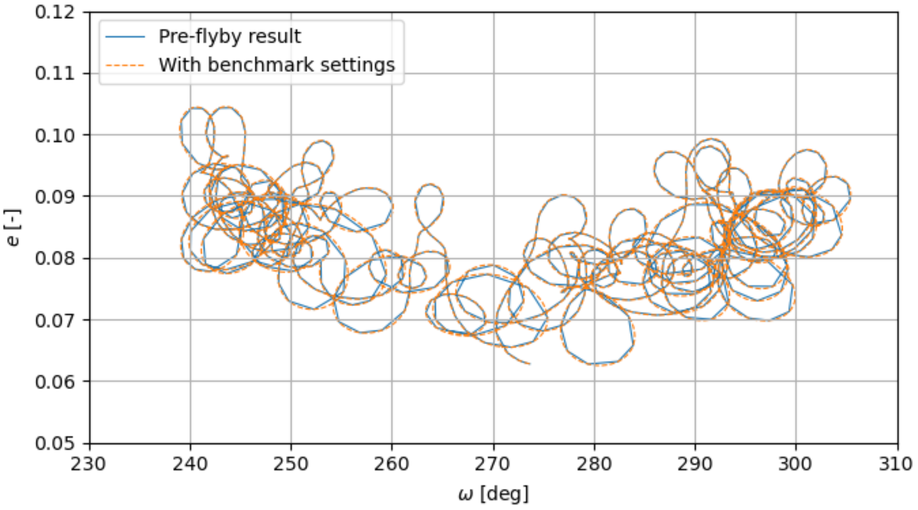

Figure 10.1: Drift in e and ω for pre-flyby result and that generated with benchmark settings.

The $e - \omega$ evolution is essentially the same. The result using benchmark settings appears to be smoother due to the smaller time step used. The final values for both cases are shown in Table 10.1.

Table 10.1: Final values of e and ω for pre-flyby result versus that generated with benchmark settings.

Case	e_{final} [-]	ω_{final} [deg]
Pre-flyby result	0.079334	253.000
With benchmark settings	0.078912	252.943
Difference	0.000422	0.057

Since both results employ variable-step integrators, the difference in the final e and ω can be attributed in part to the last time step used, since the propagation does not end exactly at the specified simulation time and an interpolator is not used. In any case, the difference between the two solutions is small enough to be considered negligible. Thus, it can be concluded and confirmed again that the assumptions made when simplifying the acceleration models and selecting a less accurate integrator were valid.

10.2. Apophis Parameters

As discussed in Section 2.2, many of the modelling parameters used to define the physical and dynamical properties of Apophis are not known to high accuracy. The asteroid's mass and spin-axis orientation uncertainty are expected to have the largest influence on the dynamics of an asteroid-orbiting spacecraft, so the sensitivity to these parameters is assessed.

10.2.1. Mass

It was seen in Subsection 2.2.2 that Apophis' mass has a value of $5.3 \pm 0.9 \times 10^{10}$ kg [44]. The effect of this uncertainty on the nominal results is displayed in Figure 10.2.

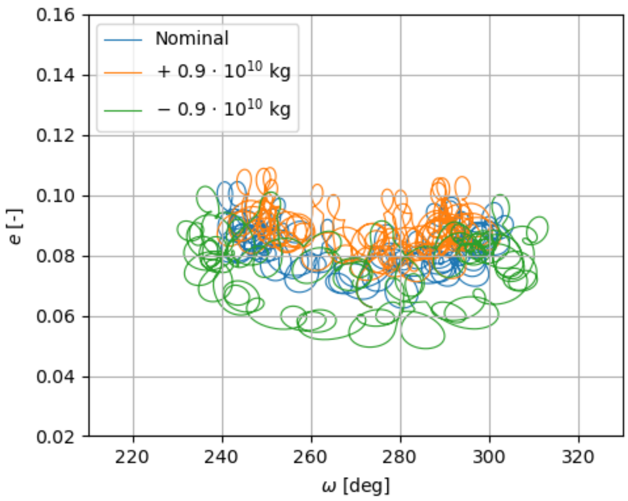

Figure 10.2: Drift in e and ω for uncertainty in the mass of Apophis compared to the nominal result.

Even though the uncertainty in the mass seems very large at ~17%, the pre-flyby result appears to be quite robust to variations in the mass. In fact, the $e - \omega$ drift improves for the case with higher mass. This is consistent with theory as a larger mass means the central body exerts a larger gravitational pull on the spacecraft, which provides greater stability against SRP.

10.2.2. Spin-axis orientation

The inaccuracy in the spin-axis orientation is taken directly from the work of Lee et al. [51]. The uncertainty in the ecliptic latitude and longitude is translated to the J2000 equatorial right ascension and declination, used as inputs to the simulation, using the NASA/IPAC Extragalactic Database online coordinate transformation calculator [72].

Table 10.2: Nominal values and 3sigma uncertainties for the spin-axis orientation definition [51].

Parameter	Nominal value	Uncertainty
λ [deg]	278	+9/-8
β [deg]	-86	+5/-4

The effect of the uncertainty in ecliptic latitude λ and ecliptic longitude β is shown in Figure 10.3.

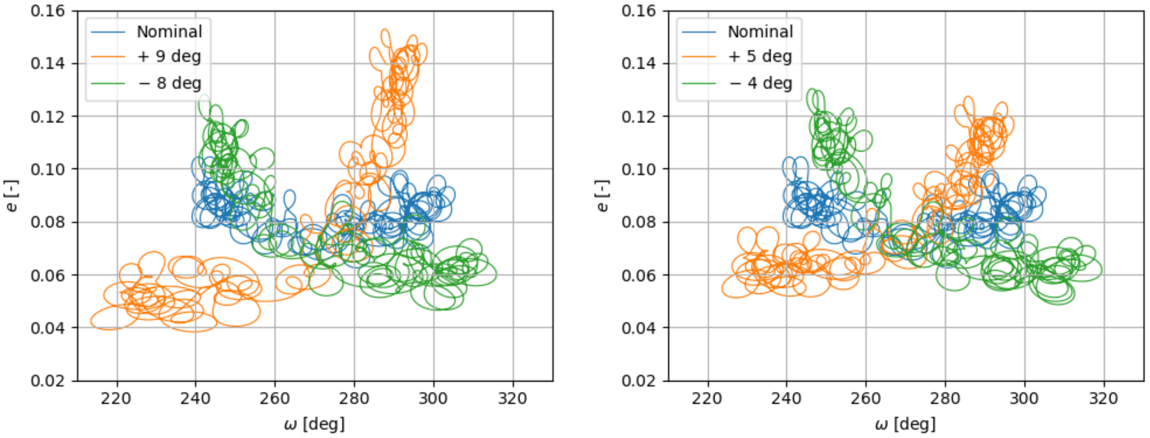

(a) Uncertainty in ecliptic latitude.

(b) Uncertainty in ecliptic longitude.

Figure 10.3: Drift in e and ω for uncertainty in spin-axis orientation parameters compared to the nominal result.

Although the uncertainty in λ and β leads to slightly larger variations in e and ω, the drift behaviour still presents the same periodic pattern. This suggests that the optimiser could converge towards equally optimal solutions for these different values of λ and β. In real life, the uncertainty in the spin-axis orientation can be reduced when approaching the asteroid prior to insertion into the frozen orbit. Thus, the optimal injection state can be recalculated during the mission based on updated data.

10.3. Solar Radiation Pressure

Since SRP is one of the perturbations with the largest magnitude, the sensitivity of the solution to this parameter is assessed by varying the spacecraft reference area by ±10% and ±50% of the nominal area. Although the spacecraft area is known to reasonable accuracy, this is established as a straightforward way of varying the magnitude of SRP, thus accounting for uncertainties in the spacecraft mass or reflection coefficient. The results are shown in Figure 10.4.

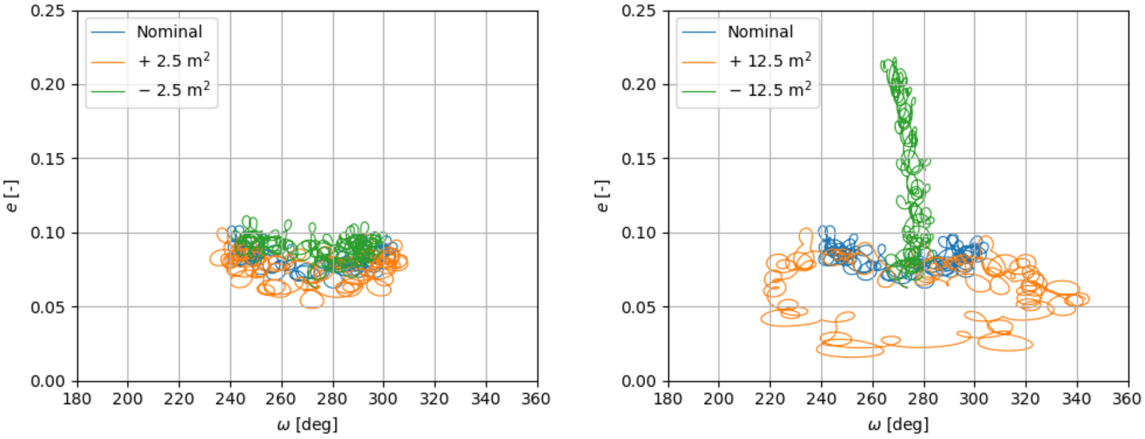

(a) Variation in reference area of ±10%.

(b) Variation in reference area of ±50%.

Figure 10.4: Drift in e and ω for different spacecraft reference areas compared to the nominal result.

When varying the spacecraft reference area by only ±10%, it is seen that a lower area leads to a slight improvement with respect to the nominal solution, while the opposite is seen for a larger area. This observation is consistent with the fact that SRP is one of the largest perturbations, and having a lower area leads to a lower SRP magnitude. However, when the area is decreased even further, looking at Figure 10.4b, the orbit is no longer frozen as the eccentricity is increasing secularly. This illustrates the importance of SRP in balancing the perturbations from the central body's irregularity.

10.4. Orbit Injection Accuracy

The orbit injection accuracy is taken from the difference between the target and achieved initial orbital elements achieved during the OSIRIS-REx mission. The data is shown in Table 10.3 [7].

Table 10.3: Target and final achieved initial orbital elements for OSIRIS-REx [7] .

Phase		a_0 [m]	e_0 [-]	i_0 [deg]	ω_0 [deg]	Ω_0 [deg]	θ_0 [deg]
Orbital B	Target	928.67	0.09	90.09	274.15	82.06	180.23
	Achieved	921.17	0.10	89.94	273.11	81.64	180.32
	Inaccuracy	2.50	0.01	0.15	1.04	0.42	0.09
Pre-TAG Trim	Target	884.82	0.18	90.05	94.44	269.51	207.41
	Achieved	905.33	0.16	89.82	89.98	269.80	213.67
	Inaccuracy	20.51	0.02	0.23	4.46	0.29	6.26

Since the magnitude of the initial orbital elements for the Orbital B and Pre-TAG Trim phases is similar to that of the pre-flyby initial state shown in Table 10.4, it is assumed that these inaccuracies can be taken as-is. For a worst-case sensitivity analysis, the inaccuracies of the Pre-TAG Trim Phase are used for all elements except for Ω_0, where the higher value from Orbital B Phase is used.

The nominal value and the inaccuracy assumed for each orbital element are displayed in Table 10.4.

Table 10.4: Nominal values and inaccuracies assumed for the sensitivity analysis of the orbit injection parameters [7].

Parameter	Nominal value	Inaccuracy
a_0 [m]	873	20.51
e_0 [-]	0.062785	0.02
i_0 [deg]	90	0.23
ω_0 [deg]	273.66	4.46
Ω_0 [deg]	330	0.42
θ_0 [deg]	0	6.26

First, the results for the injection inaccuracy in a_0 and e_0 are shown in Figures 10.5a and 10.5b.

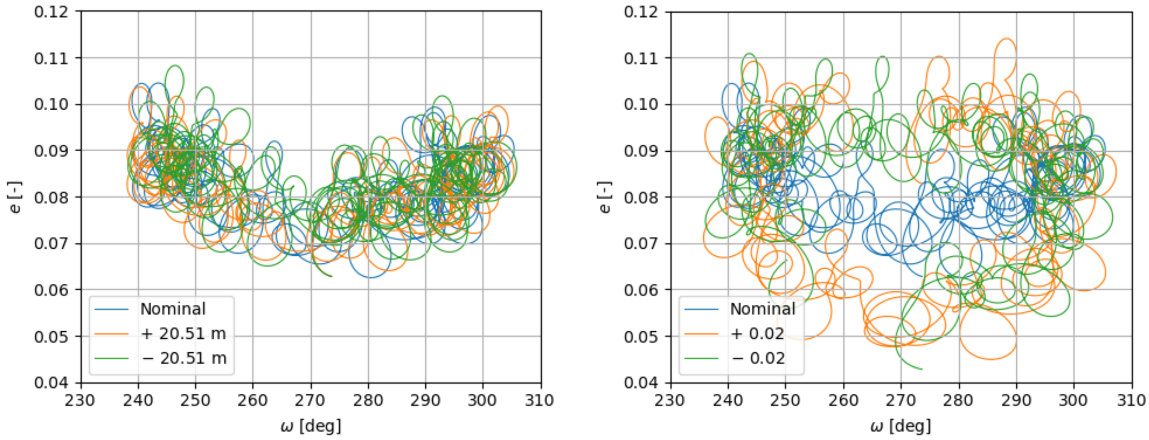

(a) Change in a_0.

(b) Change in e_0.

Figure 10.5: Drift in e and ω for orbit injection inaccuracy in a_0 and e_0 compared to the nominal result.

The variation in e and ω from the inaccuracy in a_0 is observed to be negligible. For the inaccuracy in e_0 the drift in ω remains similar but the drift in e increases by ± 0.03. This is expected from Figure 8.5.

The sensitivity to inaccuracies in i_0 and ω_0 is illustrated in Figures 10.6a and 10.6b respectively.

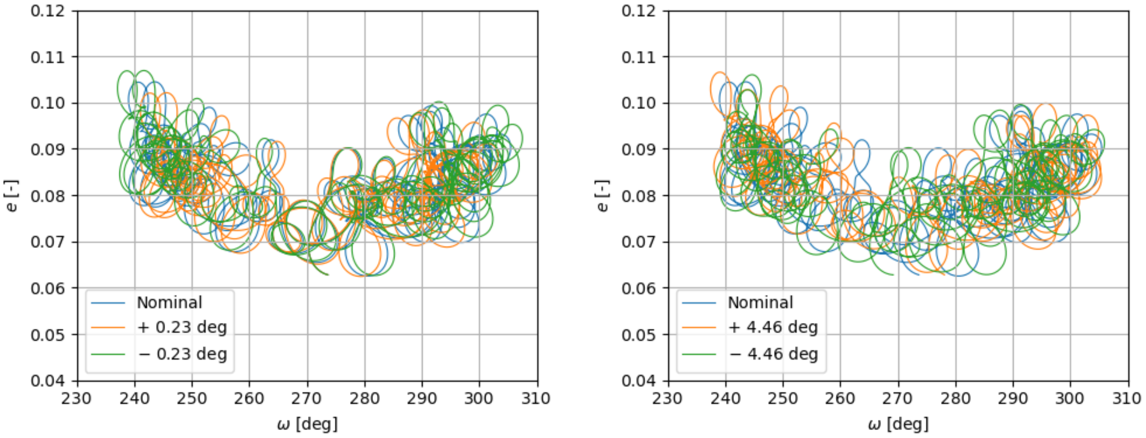

(a) Change in i_0.

(b) Change in ω_0.

Figure 10.6: Drift in e and ω for orbit injection inaccuracy in i_0 and ω_0 compared to the nominal result.

Again, the sensitivity to these parameters is negligible within these uncertainties.

Finally, the e–ω drifts for injection inaccuracies in Ω_0 and θ_0 are shown in Figures 10.7a and 10.7b.

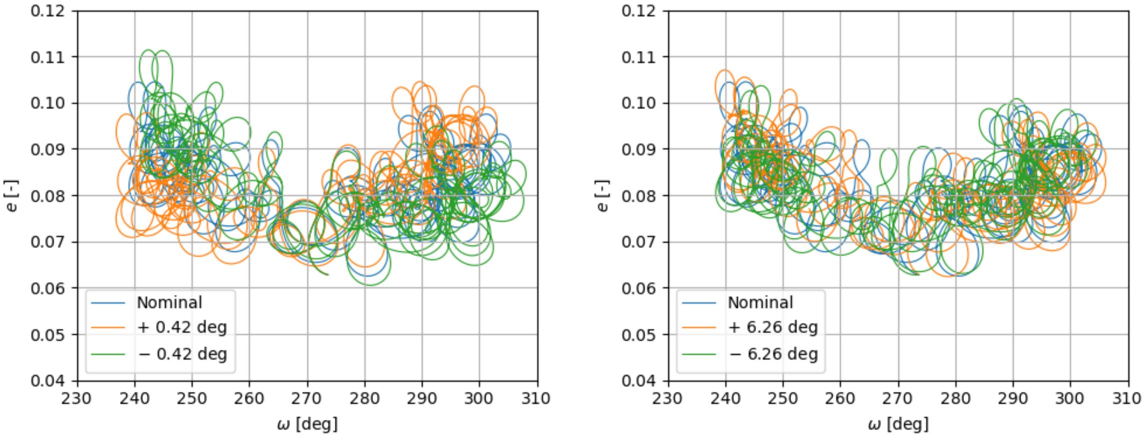

(a) Change in Ω_0.

(b) Change in θ_0.

Figure 10.7: Drift in e and ω for orbit injection inaccuracy in Ω_0 and θ_0 compared to the nominal result.

From this figure, it is concluded that the pre-flyby solution is also robust to the expected inaccuracies in Ω_0 and θ_0. Nevertheless, the change in $e-\omega$ drift is considerable for such a small uncertainty in Ω_0. It has been seen repeatedly in this work that the orientation of the orbit with respect to the Sun, which is mostly dependent on Ω, is one of the key parameters in maintaining a stable, frozen orbit.

Overall, most expected uncertainties lead to slightly larger $e-\omega$ drift but the orbit remains frozen. Improvements are observed for a larger central body mass and lower SRP magnitude, as expected from the theory explained in Chapter 3. SRP is the largest perturbation, so reducing it while having a stronger central body gravity can help stabilise the orbit. On the other hand, a too-small SRP magnitude can also lead to a deviation from the frozen condition, demonstrating SRP is still necessary to counteract the perturbations from the central body. The solution is also robust to the expected orbit injection inaccuracies of a real asteroid orbiter mission.

11

Verification and Validation

Verification deals with testing if the model is behaving as expected, whereas validation involves testing against the physical reality. The verification and validation procedures conducted for this work are presented in Sections 11.1 and 11.2 respectively.

11.1. Verification

When a functionality of TUDAT or PyGMO has been used without modifications, such as the environment and acceleration models, integrators, and propagators, the method is directly assumed to be verified as these functions have been extensively tested by students and staff of the Delft University of Technology [21]. Therefore, only the self-developed algorithms and scripts have to be verified.

11.1.1. Lagrange's planetary equations

The correct implementation of Lagrange's planetary equations including perturbations due to J_2, J_3, J_4 and SRP, which are used for the analytical analysis described in Chapter 4, is confirmed using the work of Kikuchi, Oki, and Tsuda [5]. The first part of the verification involves the recreation of Figure 6 from Kikuchi, Oki, and Tsuda [5]. Figures 11.1 and 11.2 correspond to the calculation of $d\Omega/dt$ and $d\omega/dt$ respectively, for $a = 1.4$ km, $\Omega = -90°$ and $\omega = +90°$.

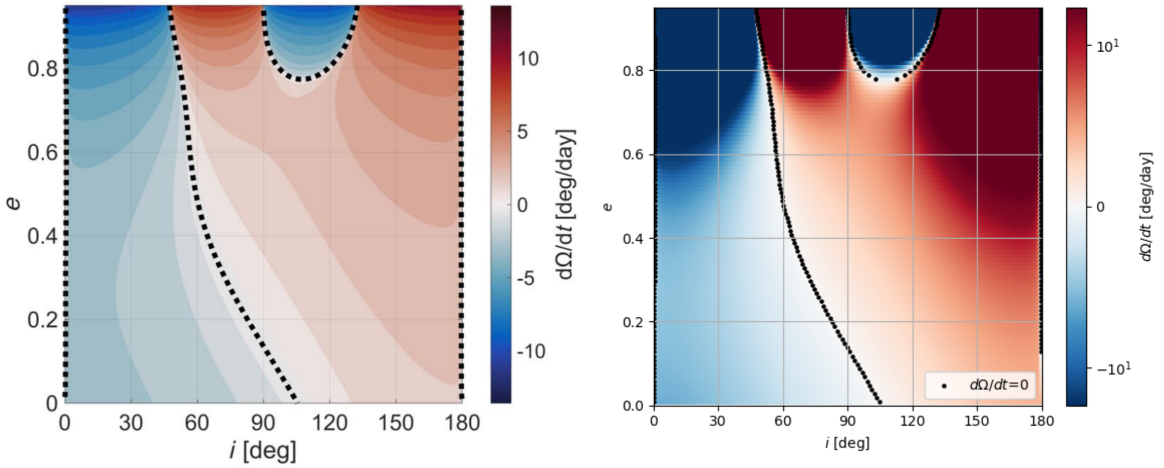

(a) Original plot

(b) Recreated plot

Figure 11.1: Verification of $d\Omega/dt$ plot shown in Figure 6 of Kikuchi, Oki, and Tsuda [5].

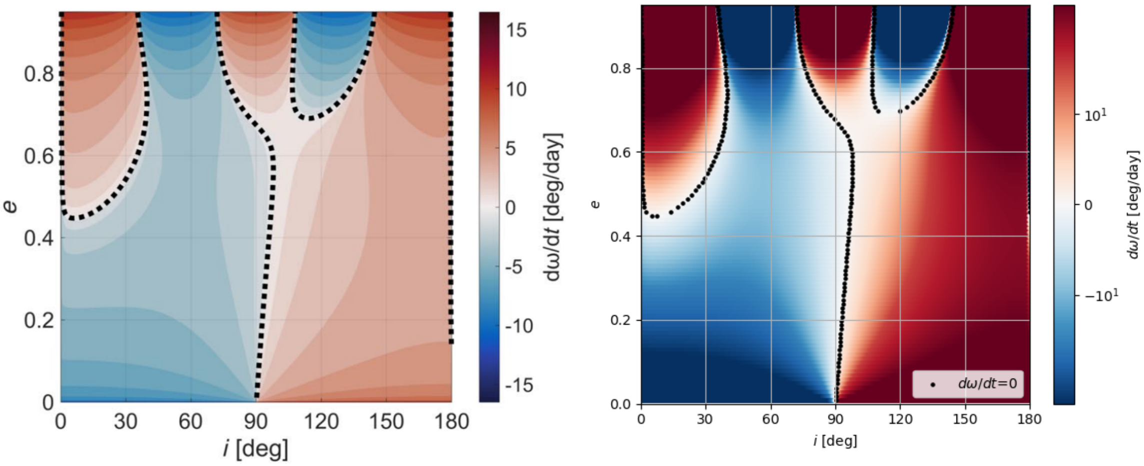

(a) Original plot

(b) Recreated plot

Figure 11.2: Verification of $d\omega/dt$ plot shown in Figure 6 of Kikuchi, Oki, and Tsuda [5].

A logarithmic scale has been used for the colour bar in the recreated plots to highlight the locations at which $d\Omega/dt$ and $d\omega/dt$ equal zero. It is confirmed that the solutions for $d\Omega/dt$ and $d\omega/dt$ in the recreated plots match the original plots from Kikuchi, Oki, and Tsuda [5].

For additional verification, the frozen orbit solutions for different a, ω, Ω as presented in Table 6 of Kikuchi, Oki, and Tsuda are recreated [5]. The reader is reminded that these frozen orbit solutions are obtained from setting $de/dt = d\omega/dt = d\Omega/dt = 0$ and that for $\omega, \Omega = \pm 90°$, de/dt is always zero. In order to find these solutions, use is made of the DE (single-objective) optimisation algorithm[1] with a fitness function definition that minimises the sum of the absolute values of $d\omega/dt$ and $d\Omega/dt$, which is equivalent to finding the closest solution to $d\omega/dt = d\Omega/dt = 0$. Although this method is still sensitive to rounding errors introduced by numerical arithmetic, it removes the issue of finding the minimum solution from a pre-defined mesh of e and i, which is quite computationally inefficient. However, since the DE algorithm is a global optimisation algorithm, it can miss local optima that happen to have a worse fitness value due to rounding. In fact, when using the algorithm to find the prograde ecliptic solutions, the optimiser always converged towards the optimum at $i \approx 90°$. For this reason, the search space was reduced from the full spectrum of i values to a range between 0 and $50°$ for these cases. In this way, all solutions were recreated and agreed to the resolution of the reference values. The verification results are shown in Table 11.1 [5].

Table 11.1: Verification of frozen orbit solutions with respect to Table 6 of Kikuchi, Oki, and Tsuda [5].

Orbit type	a [km]	e [-]		i [deg]	
		Reference	Verification	Reference	Verification
Northern terminator ω = - 90°, Ω = + 90°	0.72	0.248	0.24830	88.05	88.04885
	0.71	0.162	0.16207	90.57	90.56326
	1.00	0.090	0.08950	92.07	92.63960
	1.35	0.122	0.12185	91.68	91.67782
	3.00	0.093	0.09319	90.07	90.06886
Prograde ecliptic ω = + 90°, Ω = - 90°	1.00	0.260	0.25980	0.255	0.25510
	1.35	0.508	0.50795	0.545	0.54488
	1.80	0.682	0.68158	1.190	1.19060

11.1.2. Apophis ephemeris

As explained in Chapter 6, the ephemerides of a number of Solar System bodies are automatically loaded onto TUDAT from the SPICE database, but the ephemerides for Apophis have to be loaded

---

[1] Additional parameters: seed = 171015, population size = 100, number of generations = 100.

manually. The verification process for this part of the work is carried out in two parts. First, the trajectories of the terrestrial Solar System planets and of Apophis are extracted and plotted over a period of one year, starting on the 13th April, 2028 such that the end of the trajectory matches the day of the Earth flyby in 2029. All positions are retrieved with respect to the SSB with a time step of 20 minutes. The results are verified using NASA's Orbit Viewer tool and are presented in Figure 11.3 [46], where the yellow lines represent the ECLIPJ2000 reference frame axes.

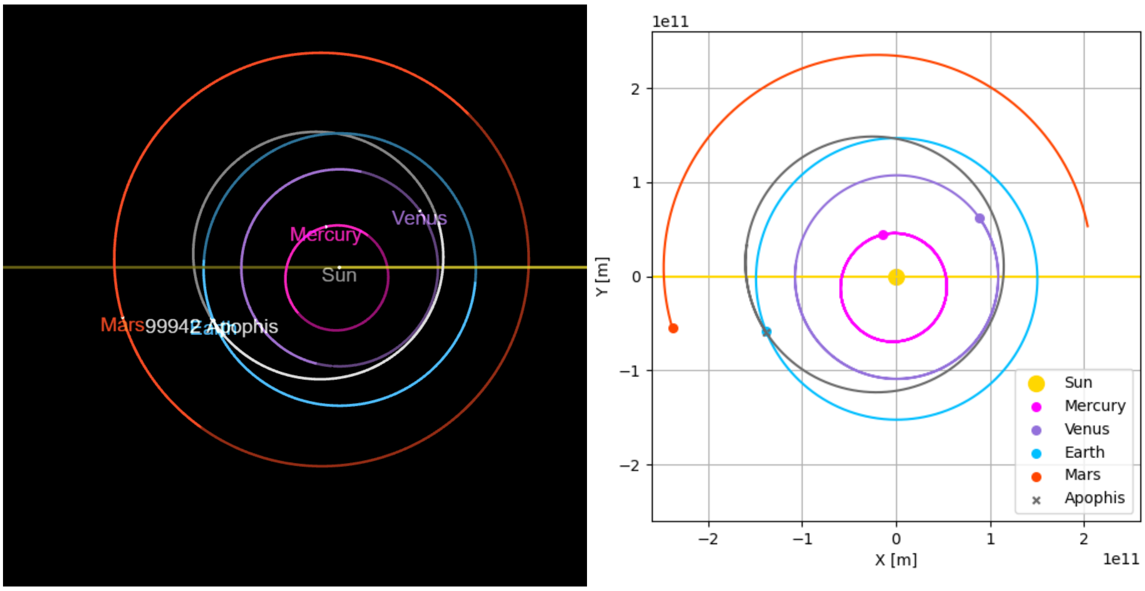

(a) Original plot

(b) Recreated plot

Figure 11.3: Verification of trajectories and positions of terrestrial Solar System planets and asteroid Apophis on the day of the Earth flyby (April 13th, 2029 at 00:00 UTC), viewed from above the ecliptic plane [46]. Sun, planets and asteroid not to scale.

Similarly, the trajectories and positions are compared when viewed from an angle to check the correct inclination of the orbit, as shown in Figure 11.4.

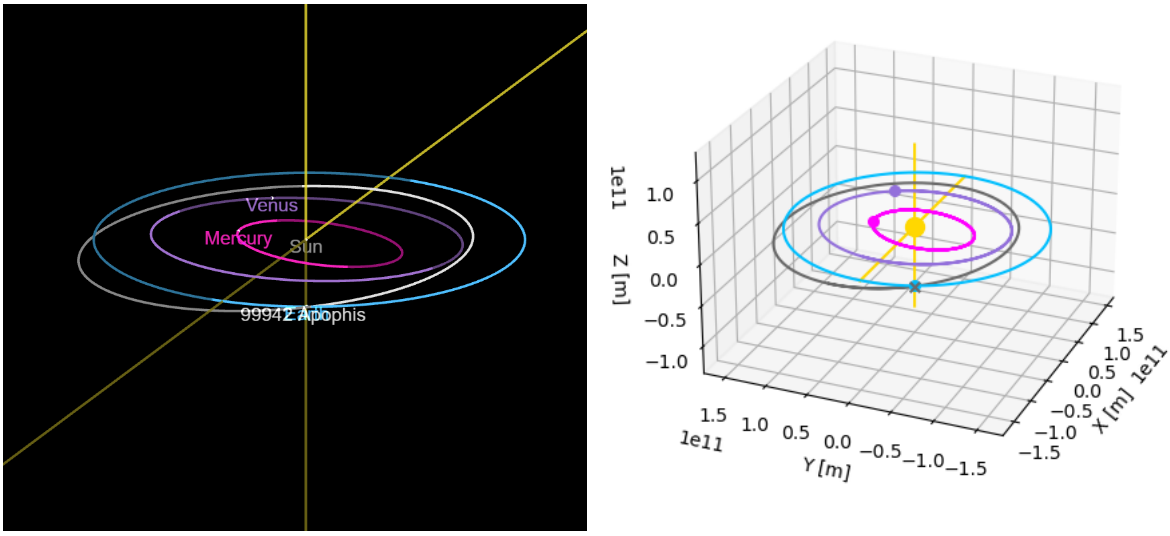

(a) Original plot

(b) Recreated plot

Figure 11.4: Verification of trajectories and positions of terrestrial Solar System planets and asteroid Apophis on the day of the Earth flyby (April 13th, 2029 at 00:00 UTC), viewed at an angle above the ecliptic plane [46]. Sun, planets and asteroid not to scale.

Figures 11.3 and 11.4 show that, generally, the correct data has been loaded. Nevertheless, since this is only a visual check, additional verification is carried out by computing the distance between the centre of mass of the Earth and Apophis from 13th April, 2029 at 00:00 UTC to 14th April, 2029 at 00:00 UTC, as it is known that the closest encounter should happen at 21:46 UTC [45]. In this case, a time step of 1 minute is used, which matches the time step used in the simulation and optimisation to generate the results in Chapter 9. The results are shown in Figure 11.5.

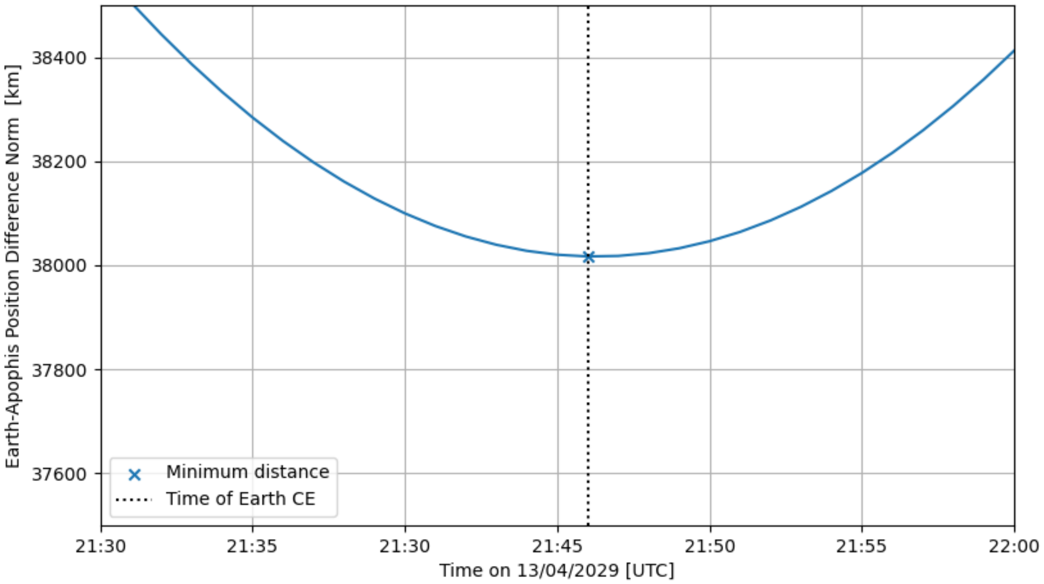

Figure 11.5: Earth-Apophis position difference norm during the time of the 2029 Earth flyby.

From Figure 11.5, it is confirmed that the smallest distance between the two bodies happens at the expected time of closest approach. The minimum distance has a value of 38,017 km at 21:46 UTC on 13th April, 2029. This is equivalent to 31,646 km above Earth's surface, which matches the value of ~32,000 km reported by NASA [1].

11.1.3. Spin-axis orientation transformation

The inputs to TUDAT's `simple` rotation model function are the pole declination δ and pole right ascension α, which are measured with respect to the J2000 Earth equatorial reference frame, whereas the spin-axis orientation obtained from Lee et al. is given in terms of the ecliptic longitude λ and ecliptic latitude β in the J2000 ecliptic reference frame [51]. Therefore, δ and α are obtained using the NASA/IPAC Extragalactic Database coordinate transformation calculator [72].

Verification of this calculator is performed using the work of Davies et al., where the pole orientation of asteroid Gaspra is given in terms of the ecliptic longitude and latitude with respect to the B1950 ecliptic frame and in terms of the right ascension and declination in J2000 Earth equatorial coordinates [92]. The verification results are presented in Table 11.2.

Table 11.2: Verification of the NASA/IPAC Extragalactic Database coordinate transformation calculator using data from Davies et al. [72, 92].

	λ	β	α [deg]		δ [deg]	
	[deg]	[deg]	Reference	Verification	Reference	Verification
Case 1	20	22	9.9	9.91	28.3	28.30
Case 2	15	24	4.2	4.22	28.1	28.13

From Table 11.2, it is confirmed that the calculator functions correctly, as the values match at least to the level of accuracy provided by Davies et al. [92].

11.1.4. Reference frame transformation

As explained in Section 7.1, a fundamental reference frame transformation is used on the simulation output to obtain the orbital element time evolution with respect to the Apophis-centred, polar-equatorial (non-rotating) reference frame. The correct implementation of this transformation is verified by propagating OSIRIS-REx's orbit around Apophis including only the point mass gravity of Apophis as acceleration. If the transformation is performed correctly, the latitude should remain constant at $0°$ when the initial Keplerian state input has an inclination of $0°$. The time evolution of the latitude for this case is provided in Figure 11.6.

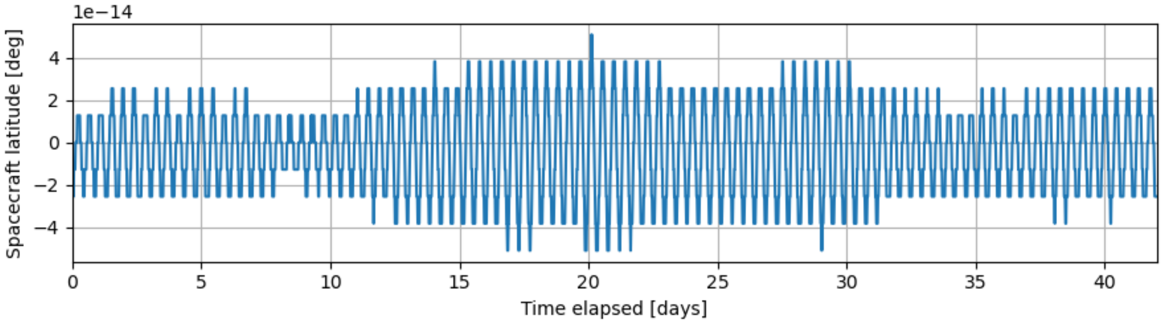

Figure 11.6: Spacecraft latitude time evolution with central point-mass gravity acceleration and $\boldsymbol{\kappa}_0 = [500, 0.01, 0, 90, 90, 0]^T$.

Although there is some degree of numerical error introduced by rounding, the latitude is essentially zero, which confirms the correct implementation of the reference frame transformation. The error increases slightly over time due to the accumulation of rounding errors at different time steps. Since the error is in the order of 10^{-14} degrees after 42 days, it is assumed to be negligible.

The orbit visualisation in both frames is shown in Figures 11.7 and 11.8 respectively. Here, the spin axis is represented by the red dotted line, while the dark and light grey circles represent the average and maximum asteroid radius respectively.

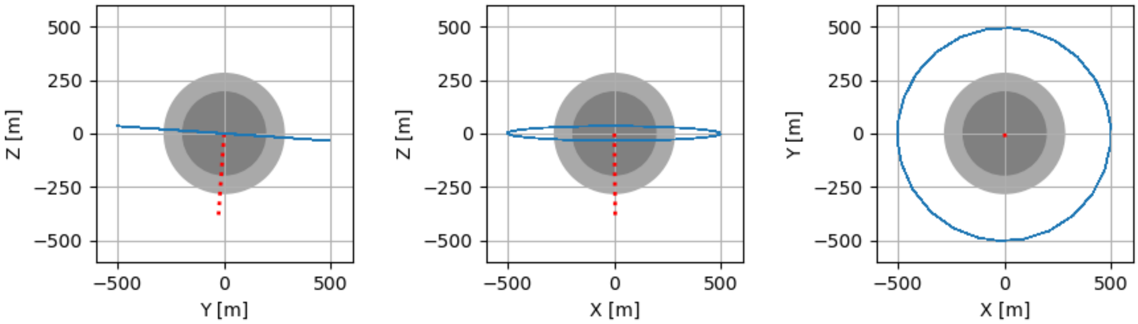

Figure 11.7: Orbit visualisation with central point-mass gravity acceleration and $\boldsymbol{\kappa}_0 = [500, 0.01, 0, 90, 90, 0]^T$ with respect to the Apophis-centred, ECLIPJ2000 reference frame.

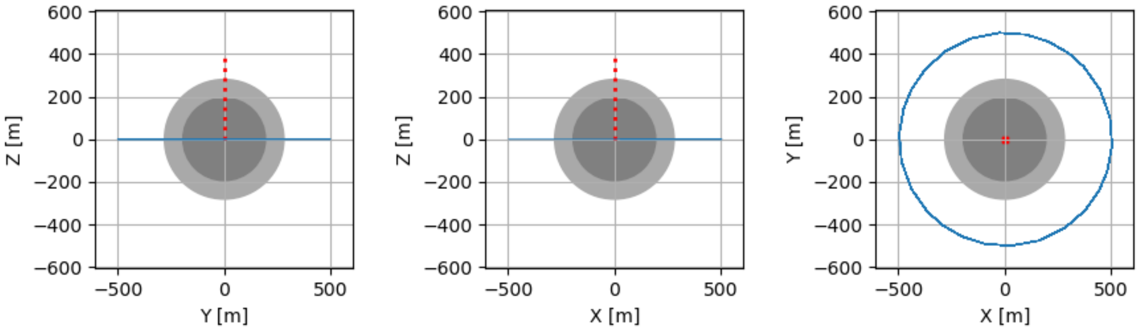

Figure 11.8: Orbit visualisation with central point-mass gravity acceleration and $\boldsymbol{\kappa}_0 = [500, 0.01, 0, 90, 90, 0]^T$ with respect to the Apophis-centred, polar-equatorial reference frame.

From Figure 11.7, the orientation of the asteroid's spin axis with respect to the ecliptic is apparent. Knowing the ecliptic latitude and longitude are defined equal to -86° and 278° respectively, one can visually confirm the orientation of the spin axis is as expected, pointing 'downwards' and almost perpendicular to the ecliptic XY-plane. Looking at Figure 11.8, one can confirm that the orbit is purely equatorial, as the plots from left to right essentially show the front, side and top view of the orbit.

The time evolution of the orbital elements with respect to their initial value is checked in both frames to assess whether the orbital element drift is equivalent. The results are presented in Figure 11.9.

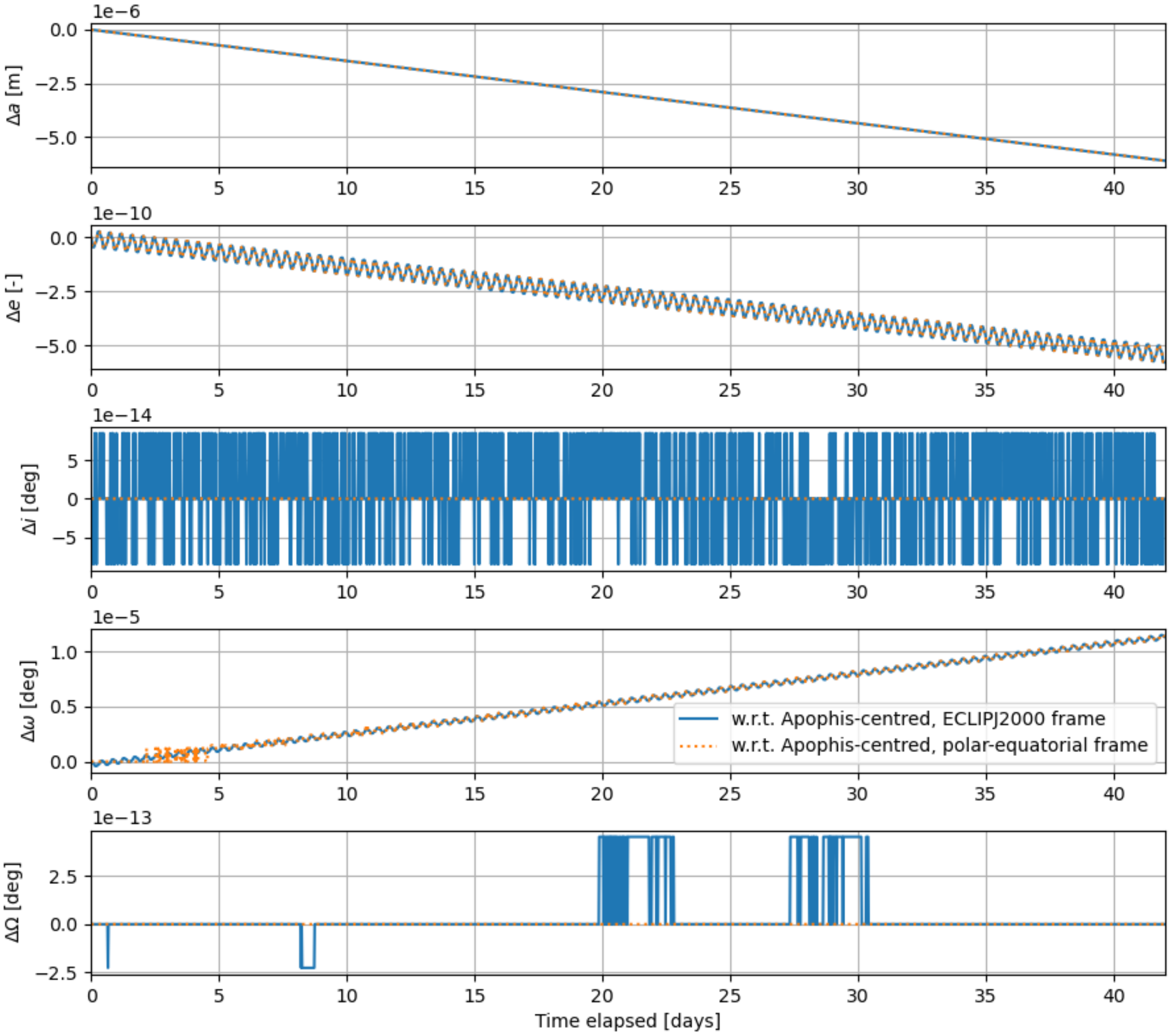

Figure 11.9: Orbital element time evolution with respect to initial value, with central point-mass gravity acceleration and $\boldsymbol{\kappa}_0 = [500, 0.01, 0, 90, 90, 0]^T$ and with respect to Apophis-centred, ECLIPJ2000 reference frame and Apophis-centred, polar-equatorial reference frame.

Since only the central point-mass gravity acceleration is included, the orbital element drift should be zero. However, Figure 11.9 shows the errors introduced by the numerical method. For the semi-major axis and eccentricity, the drift appears to be equal and is non-secular. The rounding errors in the order of 10^{-14} and 10^{-13} respectively for the inclination and longitude of the ascending node, apparent from the erratic behaviour, are assumed to be negligible. It is concluded that the reference frame transformation does not add any considerable errors to the Keplerian state solutions.

The same verification steps are carried out for an initial Keplerian state with an inclination of 90°. First, the latitude time evolution is shown in Figure 11.10.

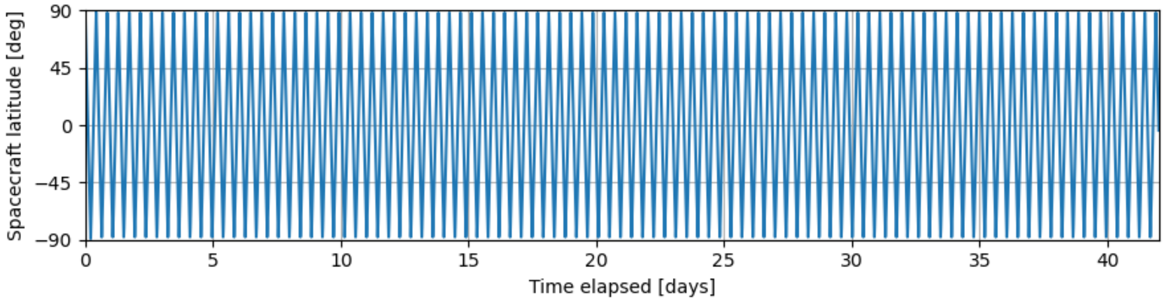

Figure 11.10: Spacecraft latitude time evolution with central point-mass gravity acceleration and $\boldsymbol{\kappa}_0 = [500, 0.01, 90, 90, 90, 0]^T$.

From Figure 11.10, it seems like the latitude reaches $+90°$ once per orbit as expected. Considering the orbital period for $a = 500$ m is 10.36 hours, that means a total of 11 peaks can be counted before day 5. Upon closer inspection, a maximum latitude of $\sim 88.0°$ is seen for some orbits. This is likely due to the use of large integration time steps which happen to skip the point at which the latitude is exactly $90°$. Upon running the same script with a smaller maximum integration time step, the maximum latitude across most orbits is seen to increase, confirming this is the source of the difference.

The orbit visualisation for the polar inclination in both frames is shown in Figures 11.11 and 11.12. Here, the spin axis is represented by the red dotted line, while the dark and light grey circles represent the average and maximum asteroid radius respectively.

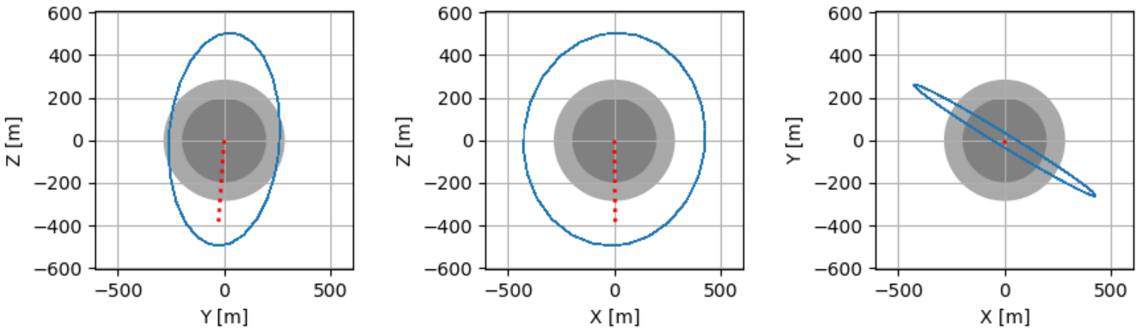

Figure 11.11: Orbit visualisation with central point-mass gravity acceleration and $\boldsymbol{\kappa}_0 = [500, 0.01, 90, 90, 90, 0]^T$ with respect to the Apophis-centred, ECLIPJ2000 reference frame.

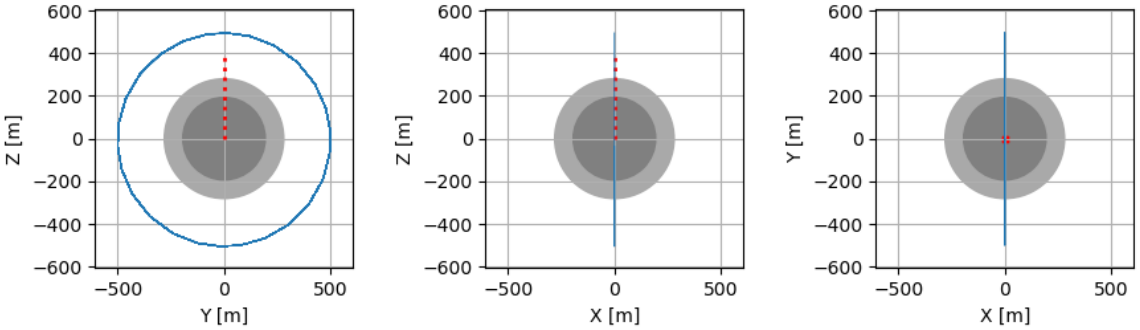

Figure 11.12: Orbit visualisation with central point-mass gravity acceleration and $\boldsymbol{\kappa}_0 = [500, 0.01, 90, 90, 90, 0]^T$ with respect to the Apophis-centred, polar-equatorial reference frame.

Here, the orientation of the orbit with respect to the spin axis is seen to match in both frames. As expected, the orbit is seen as a straight line when seen from the side (XZ) and top (XY) views in the Apophis-centred, polar-equatorial reference frame in Figure 11.12.

The time evolution of the orbital elements with respect to their initial value is shown in Figure 11.13, where the differences between the frames can be attributed to rounding errors due to the erratic pattern and magnitude in the order of 10^{-13} seen for i and Ω.

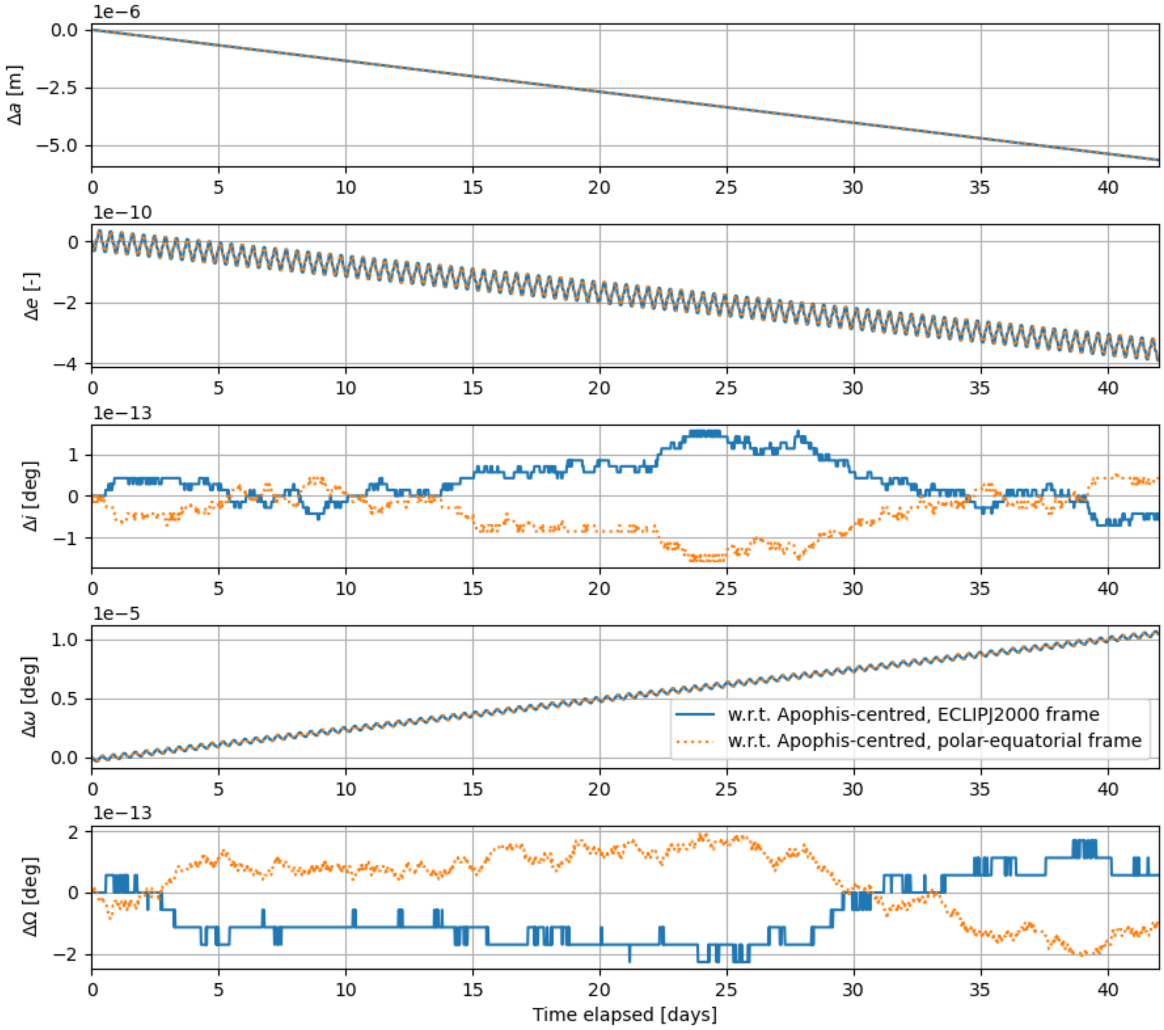

Figure 11.13: Orbital element time evolution with respect to initial value, with central point-mass gravity acceleration and $\boldsymbol{\kappa}_0 = [500, 0.01, 90, 90, 90, 0]^T$ and with respect to Apophis-centred, ECLIPJ2000 reference frame and Apophis-centred, polar-equatorial reference frame.

A final case is assessed for $i \neq 0, 90°$. This is done to check that for $i = [0 : 90]°$ the orbit is prograde, i.e. the spacecraft is orbiting the asteroid in the same direction as the asteroid's rotation, and vice versa for $i = [90 : 180]°$. This can be assessed by looking at the time evolution of the longitude, shown in Figure 11.14 for an inclination of $45°$ and Figure 11.15 for an inclination of $135°$.

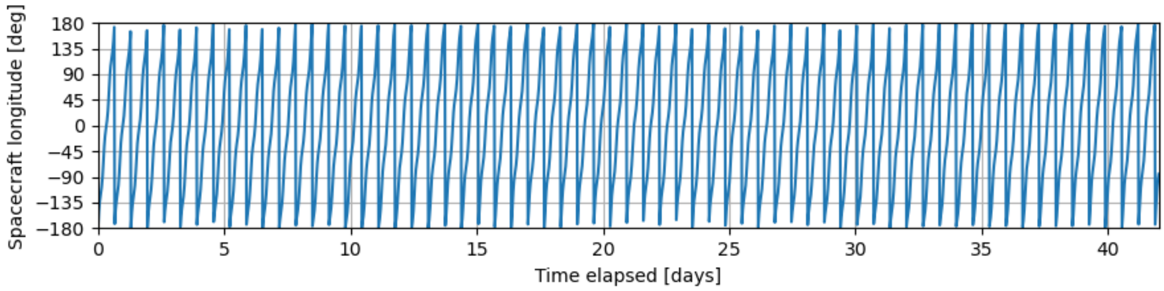

Figure 11.14: Spacecraft longitude time evolution with central point-mass gravity acceleration and $\boldsymbol{\kappa}_0 = [500, 0.01, 45, 90, 90, 0]^T$ (prograde orbit).

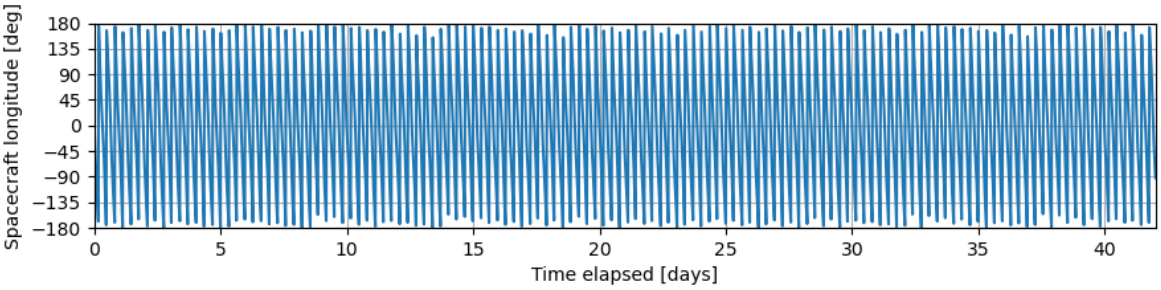

Figure 11.15: Spacecraft longitude time evolution with central point-mass gravity acceleration and $\boldsymbol{\kappa}_0 = [500, 0.01, 135, 90, 90, 0]^T$ (retrograde orbit).

The expected behaviour is confirmed by the figures: for a prograde orbit, the longitude should be increasing over time, whereas for a retrograde orbit, it should be decreasing [23]. It is also expected to see that the evolution of the longitude is faster for the prograde orbit, as the asteroid is moving backwards with respect to the forward motion of the spacecraft in its orbit. Although the longitude should go fully from $-180°$ to $+180°$, it is once again noted that the large integration time step leads to the behaviour shown in the figures. With this, the verification of the reference frame transformation is completed.

11.1.5. Orbital escape termination condition

Since the orbital escape termination condition implemented for the numerical simulations uses the apoapsis altitude instead of the semi-major axis value, it is verified that for a given orbit, both parameters result lead to termination at the same time step. Figure 11.16 shows the apoapsis altitude and semi-major axis in both frames for the last five times-steps of the simulation. The initial Keplerian state vector $\boldsymbol{\kappa}_0 = [1750, 0.228, 72, 274, 327, 0]^T$ is used for this verification procedure as it is known to reach the orbital escape condition.

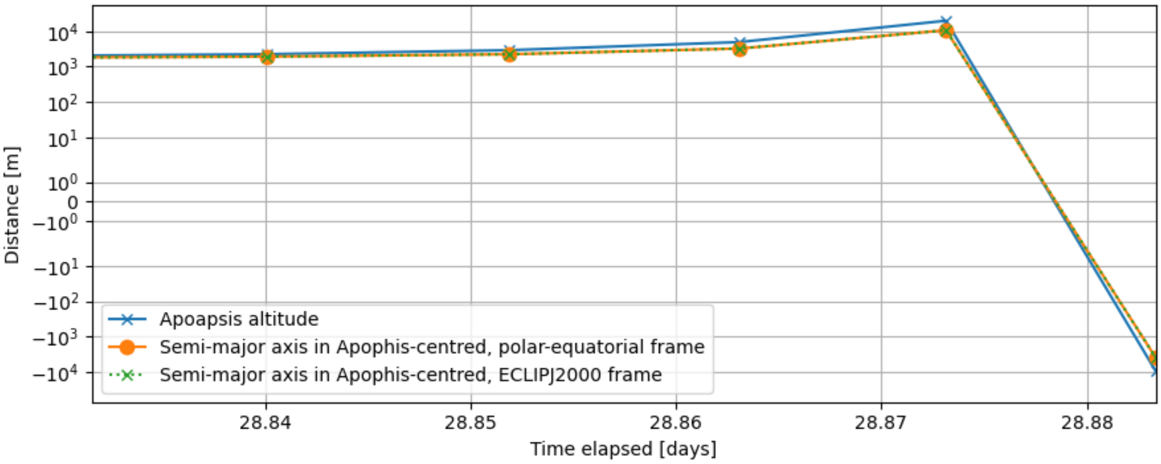

Figure 11.16: Semi-major axis and apoapsis altitude time evolution for an initial Keplerian state vector $\boldsymbol{\kappa}_0 = [1750, 0.228, 72, 274, 327, 0]^T$ with a simulation start date of 16/03/2029.

As explained previously in Section 7.2, it is known that the termination condition does not become active exactly on the final condition. This leads to the behaviour shown in Figure 11.16, where there is one time step with a semi-major axis lower than 0 m and that is where the propagation is terminated. For plots outside this section that terminate with the orbital escape condition, the last time step is removed for visualisation purposes. The semi-major axis is shown in both reference frames to show it is equivalent, since the apoapsis altitude extracted from the simulator is calculated with respect to the Apophis-centred, ECLIPJ2000 reference frame. Since the semi-major axis and eccentricity are the same in both frames, it can be assumed consequently that so is the apoapsis altitude.

11.2. Validation with OSIRIS-REx

Even when all models have been verified, it is important to check that they are actually representing the real physical situation under consideration. The OSIRIS-REx real flight data is used for this purpose, since it is considered to be the closest available representation of the real physical environment around Apophis and is the only mission around an asteroid to have employed frozen orbits for some of its mission phases [7]. Since there have been no missions to Apophis yet, it is assumed that the environments are similar enough for a first-order validation of the results. The spacecraft assumed in this work is OSIRIS-REx, so it is assumed the spacecraft parameters are equal and the differences stem from the physical dissimilarities between Apophis and Bennu. The main parameters of both asteroids are presented in Table 11.3 [93, 94, 95].

Table 11.3: Main physical parameters of Apophis and Bennu [93, 94, 95].

Parameters	Symbol	Apophis	Bennu	Unit
Mass and size	μ	3.54	4.89256	m^3/s^2
	M	5.31	7.33	10^{10} kg
	R_{mean}	193	244.89	m
	R_{max}	280	282.5	m
Spherical harmonics coefficients	$\bar{C}_{2,0}$	0.07832	0.01751	-
	$\bar{C}_{2,2}$	0.02638	0.00582	-
	$\bar{C}_{3,0}$	-0.04487	-0.00561	-
	$\bar{C}_{4,0}$	-0.00636	-0.01025	-
Rotational properties	λ	278	69.77	deg
	β	-86	-83.49	deg
	P_{ast}	30.56	4.297	hr

Despite having a similar size, Bennu has a higher mass than Apophis, which helps in keeping the spacecraft in orbit. Furthermore, the J_2 term for Bennu is more than four times lower than that of Apophis, showing Bennu's shape is quite regular compared to Apophis' elongated shape. The tesseral term $C_{2,2}$ is also much lower for Bennu. Nevertheless, the spherical harmonics coefficients are all similar in magnitude compared to those of larger bodies like Earth. In terms of the rotational properties, they both have similar retrograde rotation around the Sun with an ecliptic latitude of almost -90°, but the sidereal orbital period of Bennu is much lower than that of Apophis. These differences lead to the conclusion that it might be easier to achieve frozen orbits around Bennu than Apophis, but the solutions are still expected to resemble each other due to the similarities in size.

The orbit of each asteroid around the Sun is also of importance, as it has a direct influence on the magnitude and variation of SRP. The osculating orbital elements for each asteroid are given in Table 11.4. The elements of Apophis are from 25th February, 2023, while the ones for Bennu are from 30th March, 2019 [45, 95].

Table 11.4: Osculating orbital elements of Apophis and Bennu [45, 95].

Element	Apophis	Bennu	Unit
a	0.922716	1.1259	AU
e	0.191417	0.20372	-
i	3.339273	6.034	deg
Ω	203.957515	2.017	deg
ω	126.605861	66.304	deg

Both asteroids have similar orbits with semi-major axes close to 1 AU and eccentricities around 0.2. Overall, Bennu is at a larger distance from the Sun and thus the effect of SRP on a Bennu-orbiting spacecraft will be lower. However, this depends on the position of the asteroid along its orbit at the time of the mission, and around the time of the 2029 Earth flyby, Apophis' distance to the Sun is closer to 1 AU.

The OSIRIS-REx flight data that is used for the validation is extracted from SPICE kernels. To verify the method used to extract the flight data, Figure 4 from Wibben et al. is recreated [7]. The original figure is shown in Figure 11.17.

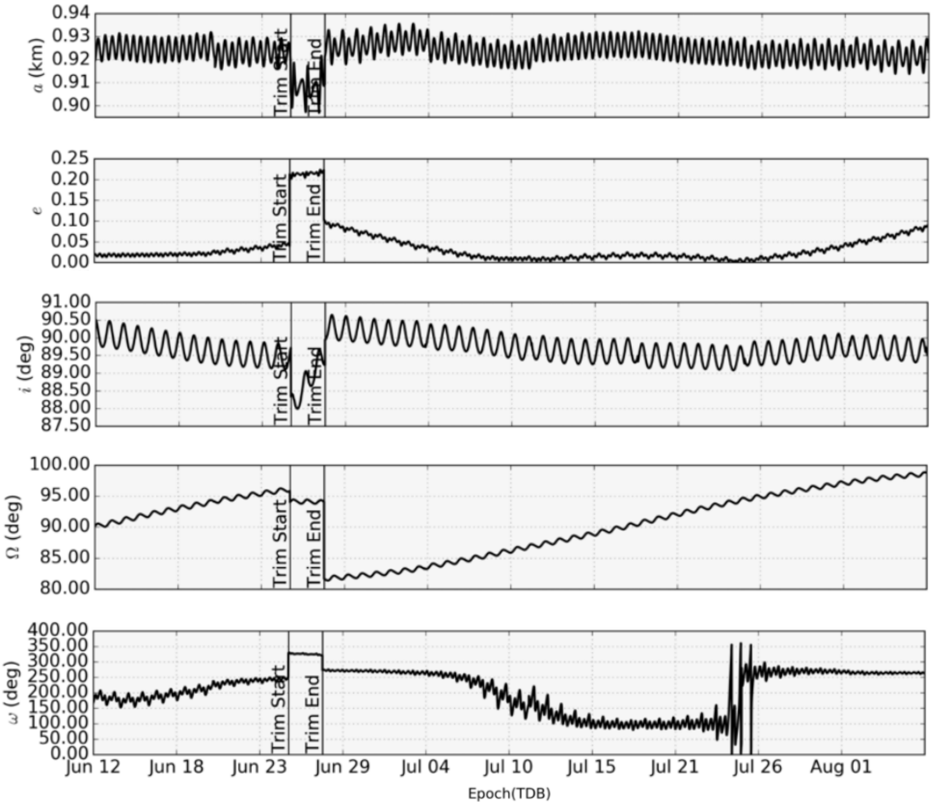

Figure 11.17: Orbital element time evolution during OSIRIS-REx Orbital B Phase. Figure 4 from Wibben et al. [7].

A number of orbit determination solutions for the OSIRIS-REx are available on SPICE [2]. The states for different orbital phases are simply extracted using knowledge on the approximate start and end date of each orbital phase. The dates displayed in Table 11.5 are used for each phase.

Table 11.5: Start and end date of different OSIRIS-REx orbital phases [7, 96].

Phase	Start date	End date
Orbital A	January 1, 2019	February 28, 2019
Orbital B	June 13, 2019	August 8, 2019
Orbital C	August 9, 2019	September 17, 2019

The `spiceypy` package previously described in Chapter 6 is used to load this data into TUDAT. The Cartesian state vectors are extracted using the `spkezr` function and then transformed to Keplerian elements using the gravitational parameter of Bennu of 4.89256 m^3/s^2 [93]. An additional step is carried out for the recreation of Figure 11.17. In the work of Wibben et al., the osculating orbital elements are defined with respect to the Sun Anti-Momentum (SAM) Frame, whereas the Cartesian states obtained using the `spkezr` function are defined with respect to the Bennu-centred, ECLIPJ2000 reference frame. Thus, the transformation between frames is carried out by loading the SPICE kernel which defines the SAM frame [3] and using the `sxform_c` function to get the state transformation matrix from the ECLIPJ2000 to the SAM frame. The final recreated plot is shown in Figure 11.18.

---

[2] https://naif.jpl.nasa.gov/pub/naif/pds/pds4/orex/orex_spice/spice_kernels/spk/

[3] https://naif.jpl.nasa.gov/pub/naif/pds/pds4/orex/orex_spice/spice_kernels/fk/orx_v14.tf

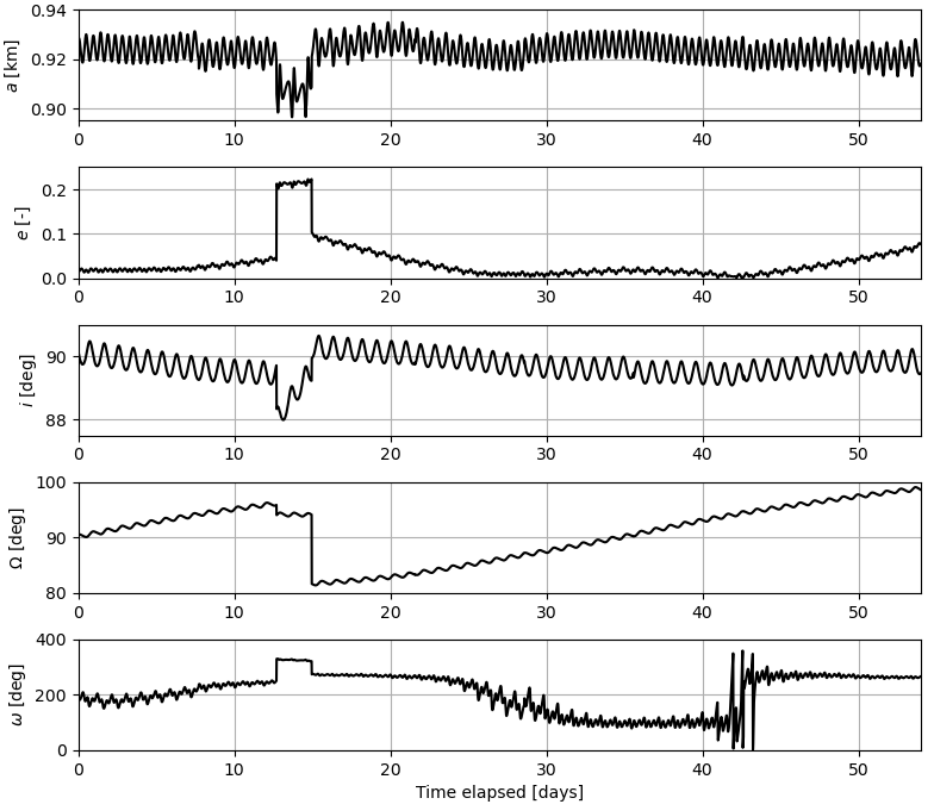

Figure 11.18: Orbital element time evolution during OSIRIS-REx Orbital B Phase. Recreation of Figure 4 from Wibben et al. [7].

From Figure 11.18, it is verified that the OSIRIS-REx data has been loaded correctly.

The validation is performed only on the pre-flyby result shown in Section 9.1 to ensure the dynamic environment of the two cases is similar since the OSIRIS-REx mission did not involve any flyby similar to Apophis' 2029 Earth flyby. Since Orbital A and Orbital C were the OSIRIS-REx phases employing frozen orbits, the comparison is made to these phases. The flight data for Orbital A and Orbital C is extracted using the start and end dates presented in Table 11.5. In this way, the initial osculating orbital elements are obtained. These are shown in Table 11.6 together with the initial Keplerian state vector corresponding to the pre-flyby result of Section 9.1. Note that these states are provided with respect to the asteroid-centred, ECLIPJ2000 reference frame.

Table 11.6: Orbital insertion parameters with respect to asteroid-centred, ECLIPJ2000 reference frame.

Case	Date	a_0 [m]	e_0 [-]	i_0 [deg]	ω_0 [deg]	Ω_0 [deg]	θ_0 [deg]
OSIRIS-REx Orbital A	January 1, 2019	1827	0.1557	97.52	84.60	326.87	7.87
OSIRIS-REx Orbital C	August 9, 2019	1751	0.1139	83.46	92.75	153.54	342.89
Pre-flyby result	March 16, 2029	873	0.0628	90.02	89.71	88.65	0.00

Both the OSIRIS-REx and the Apophis pre-flyby result correspond to the near-polar Sun-terminator family: the inclination is close to 90° and the value of Ω is such that the spacecraft's orbital plane is perpendicular to the Sun-asteroid line. The values do not necessarily match between cases because the value of Ω leading to this condition depends on the position of the asteroid in its orbit around the Sun when measured in the ECLIPJ2000 frame. For example, the values of Ω for both OSIRIS-REx phases are almost conjugate because approximately half a year passes between the start of each phase. Since the semi-major axis of Bennu's orbit is close to 1 AU, it takes approximately one year to orbit the Sun. This means the orientation to the Sun is the same for Orbital A and Orbital C.

Although a value of a = 873 m was chosen to generate the pre-flyby result, it was seen in Figure 8.5

that optimal solutions could be found for semi-major axis values ranging from 600 m to 1700 m, which is closer to the semi-major axis used for the OSIRIS-REx frozen orbits.

Finally, from frozen orbit theory, typical values of ω for frozen orbits are 90° or 270° depending on the sign of J_2 and J_3 [97, 25]. The argument of periapsis should be 270°, i.e. above the central body's south pole, if the signs of J_2 and J_3 are different. This is the case for Apophis and Bennu, looking at Table 11.3. For the cases in Table 11.6, ω is close to 90° for all. However, since this is measured using the ECLIPJ2000 orientation, and both Apophis and Bennu have an ecliptic latitude close to -90°, this means the argument of periapsis is located above the south pole for both asteroids.

The variation in e and ω for OSIRIS-REx Orbital A and C is shown in a polar plot in Figure 11.19 together with the $e - \omega$ drift of the Apophis pre-flyby result. Again, the orbital elements are shown with respect to the asteroid-centred, ECLIPJ2000 frame.

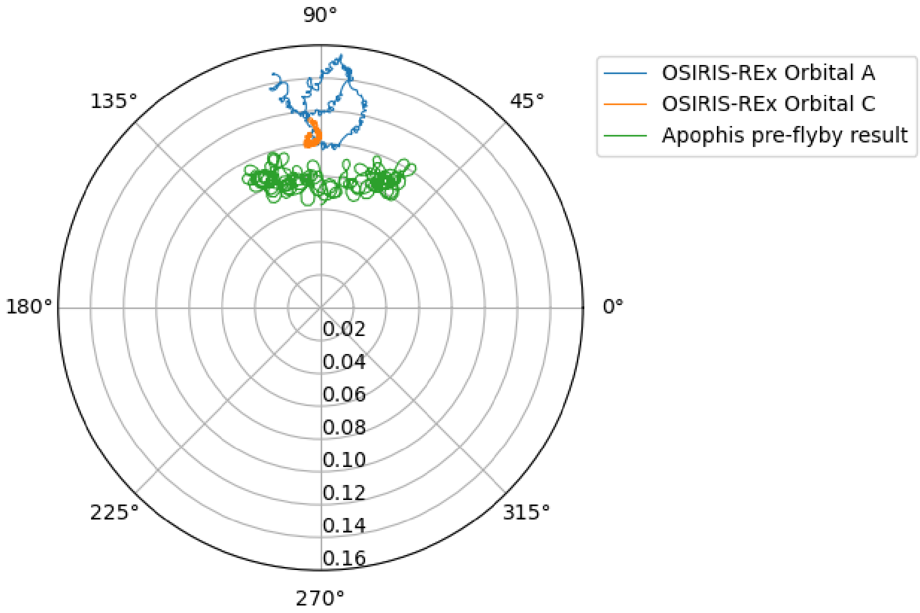

Figure 11.19: Polar plot of $e - \omega$ drift with respect to asteroid-centred, ECLIPJ2000 reference frame.

Although the frozen orbits of the OSIRIS-REx mission exhibit a smaller drift in e and ω than the solution for Apophis, the solutions are quite similar with ω varying within the 45°–135° quadrant.

The maximum difference in e and ω for all three cases is presented in Table 11.7.

Table 11.7: Maximum difference in e and ω for OSIRIS-REx Orbital A and C, and Apophis pre-flyby result.

Case	Maximum difference in e [-]	Maximum difference in ω [deg]
OSIRIS-REx Orbital A	0.05860	26.12
OSIRIS-REx Orbital C	0.01749	6.03
Apophis pre-flyby result	0.04155	66.21

Orbital C clearly achieves the smallest drift in e and ω, and both OSIRIS-REx cases attain a smaller maximum difference in ω than the Apophis pre-flyby result. Nevertheless, the drift in e for the Apophis result is lower than that of Orbital A. Although the pre-flyby result does not reach the flyby itself, the perturbations from the Earth and Moon in close proximity are still present. For the OSIRIS-REx mission, this was not an issue. Thus, it is expected that a frozen orbit with smaller drift in e and ω could be achieved around Apophis for a mission carried out further away from the time of the 2029 Earth flyby. Considering this key difference in the dynamic environments of each case, the frozen orbit result for Apophis is assumed to be validated.

12

Conclusions

This work focuses on the investigation of spacecraft dynamics in the vicinity of asteroid Apophis around the time of the 2029 Earth flyby. The research objectives sub-questions first presented in Chapter 1 are repeated here:

- What is the solution space of initial orbital elements leading to frozen orbits around Apophis?
- Can a frozen orbit around Apophis survive the strong perturbations encountered during the 2029 flyby without orbital escape or surface impact?
- What is the sensitivity of the frozen orbit solutions around Apophis to practical elements like orbit injection inaccuracies and physical modelling uncertainties?

With regards to the solution space, initial insights are obtained from the analytical analysis. Two main solution families are identified: near-equatorial heliotropic/anti-heliotropic orbits and near-polar Sun-terminator orbits. However, from the comparison with numerical simulations, the assumptions employed in the analytical method are found to be too limiting for this problem. The resulting orbits are not frozen and mostly escape or impact after only five days. On the other hand, the numerical method identifies several quasi-frozen orbit solutions in the near-polar Sun-terminator family that remain in orbit for at least 28 days before the flyby. It is thus concluded that the near-equatorial heliotropic family is not part of the solution space of frozen orbits around Apophis. This is attributed to the weak gravitational field of the asteroid and the large perturbations due to both the zonal and tesseral terms of the spherical harmonics gravity field since the analytical method omits the effects of tesseral harmonics gravity. An additional conclusion is made that numerical methods are necessary for the investigation of frozen orbits around highly irregular asteroids such as Apophis, especially with the addition of the perturbations induced by the flyby which are not captured by the analytical formulation.

The second sub-question has also been answered. Since all the optimal pre-flyby frozen orbit solutions lead to surface impact at the time of the flyby, it is concluded that the frozen orbit condition needs to be relaxed in order to achieve an orbit that can survive the flyby with no orbital correction manoeuvres. If an additional variation in e and ω of approximately 0.04 and 40° respectively is considered acceptable, some solutions are found that survive the flyby without escape or impact. Although the post-flyby portion of the orbit diverges from the frozen configuration for all solutions, it remains stable for at least two weeks after the flyby. The main conclusion of this work is that pursuing an optimal frozen orbit is not recommended during the time of the flyby, since slightly alleviating the frozen constraint allows survival during the flyby for a long-duration mission with larger scientific output.

The sensitivity to modelling uncertainties and orbit injection inaccuracies has been assessed for the frozen orbit solution referred to as the pre-flyby result. Even for a mass uncertainty for Apophis of 17%, the solution remains stable, with only a slight increase in the e and ω variation for a lower central body mass. The uncertainty in the spin-axis orientation has a larger influence on the $e-\omega$ drift, the argument of periapsis still oscillates within the same quadrant and the orbit remains bounded. Variations in the SRP magnitude only lead to non-frozen behaviour when the reference spacecraft area is assumed to be 50% lower than the nominal value. When it is 50% larger, the variations in e and ω increase but the behaviour is still periodic. When assuming the orbit injection inaccuracies of the OSIRIS-REx mission, most parameters can be assumed to have a negligible effect except the inaccuracy in initial eccentricity, which leads to an increase in the maximum variation in eccentricity of around 0.03.

Finally, the main research question is answered:

What is the feasibility of designing and maintaining stable control-free frozen orbits around asteroid Apophis before and during the 2029 Earth flyby?

From the pre-flyby results, it is concluded that it is feasible to design a stable control-free frozen orbit around Apophis before the 2029 flyby. Although a small variation in eccentricity around 0.047 is achieved, the optimal solutions still present a variation in the osculating argument of periapsis of up to 66° due to the Earth's third-body gravity perturbations leading up to the flyby. All the solutions that survive the flyby are less frozen in the pre-flyby period and fully non-frozen post-flyby. For both cases, the optimal solutions correspond to a Sun-terminator frozen orbit.

13

Recommendations

Several recommendations for future research are proposed which can help address the limitations of this work and further enhance the understanding of spacecraft dynamics around Apophis. Although some limitations are inherent due to factors beyond the scope of this work, such as limited data on the asteroid's physical parameters, there are still areas of improvement worth pursuing.

- **Gravity modelling:** For improved fidelity, it is suggested to investigate the polyhedron-mascon gravitational model formulation to describe the gravity field of Apophis [13]. Although this method generally requires higher computational effort, it is expected to yield higher accuracy results.
- **Rotation modelling:** To capture the asteroid's true dynamics accurately, it is important to account for its tumbling spin state [47]. The tumbling behaviour may quickly destabilise the frozen orbit solutions due to the high irregularity of Apophis.
- **Solar Radiation Pressure modelling:** It is recommended to explore the use of the boxes-and-wings panelled spacecraft model, with a focus on the orientation of the spacecraft and its variation over time [98].
- **Empirical accelerations:** While this study has primarily focused on SRP and the asteroid's irregularity as the major perturbations, it is known from the OSIRIS-REx mission that other accelerations are present. These include the asteroid thermal radiation pressure and the spacecraft thermal radiation pressure, as well as stochastic accelerations specific to the real environment [99]. Similar accelerations could be modelled for the investigation of orbital motion around Apophis.
- **Sensitivity analysis:** While some sensitivity analysis has been performed in this study, the uncertainties in the parameters have only been evaluated individually. It is recommended to conduct additional sensitivity analysis to also evaluate the combined effects. Furthermore, the sensitivity of the post-flyby solution has not been assessed in this work.
- **Rotational changes during the flyby:** For the generation of post-flyby results in this work, it has been assumed that the asteroid's rotational parameters after the flyby are equivalent to those before the flyby. However, the flyby is expected to cause large changes in the orientation of Apophis' spin axis [53]. The sensitivity of the solutions to these rotational changes could be assessed as part of a future study.
- **Orbital maintenance manoeuvres:** While the current study focuses on uncontrolled motion, it would be interesting to explore optimal solutions that bring the spacecraft's post-flyby orbit back to the pre-flyby optimal solution with minimal ΔV.

Bibliography

[1] NASA Science Solar System Exploration. *Apophis*. https://solarsystem.nasa.gov/asteroids-comets-and-meteors/asteroids/apophis/in-depth/ [Accessed on: 13/01/2023].

[2] NASA. *Final Report Package: 2022 NASA Planetary Mission Senior Review (PMSR22)*. https://science.nasa.gov/science-red/s3fs-public/atoms/files/PMSR22%20Final%20Report%20Package.pdf [Accessed on: 10/02/2023]. Apr. 2022.

[3] D.S. Lauretta et al. "OSIRIS-REx at Apophis: Opportunity for an Extended Mission". In: *LPI Contributions* 2242 (Nov. 2020), p. 2008. URL: https://www.hou.usra.edu/meetings/apophis2020/pdf/2008.pdf.

[4] D.J. Scheeres. "Orbital mechanics about small bodies". In: *Acta Astronautica* 72 (Mar. 2012), pp. 1–14. ISSN: 0094-5765. DOI: 10.1016/j.actaastro.2011.10.021. URL: https://doi.org/10.1016/j.actaastro.2011.10.021.

[5] Shota Kikuchi, Yusuke Oki, and Yuichi Tsuda. "Frozen Orbits Under Radiation Pressure and Zonal Gravity Perturbations". In: *Journal of Guidance, Control, and Dynamics* 44.11 (Sept. 2021), pp. 1924–1946. ISSN: 1533-3884. DOI: 10.2514/1.G005564. URL: https://doi.org/10.2514/1.G005564.

[6] Shota Kikuchi et al. "Orbit-attitude coupled motion around small bodies: Sun-synchronous orbits with Sun-tracking attitude motion". In: *Acta Astronautica* 140 (Nov. 2017), pp. 34–48. ISSN: 0094-5765. DOI: 10.1016/j.actaastro.2017.07.043. URL: https://doi.org/10.1016/j.actaastro.2017.07.043.

[7] Daniel R. Wibben et al. "Maneuver strategy for OSIRIS-REx proximity operations". In: *GNC 2017: International ESA Conference on Guidance, Navigation & Control Systems*. GSFC-E-DAA-TN43065. Salzburg, Austria, May 2017. URL: https://ntrs.nasa.gov/citations/20170011465.

[8] NASA. *Update: NASA Extends Exploration for 8 Planetary Science Missions*. https://www.nasa.gov/feature/update-nasa-extends-exploration-for-8-planetary-science-missions [Accessed on: 30/01/2023].

[9] Anqi Lang, Gang Chen, and Peng Guo. "Heliotropic orbits at asteroid 99942 Apophis: Considering solar radiation pressure and zonal gravity perturbations". In: *Acta Astronautica* 198 (Sept. 2022), pp. 454–470. ISSN: 0094-5765. DOI: 10.1016/j.actaastro.2022.06.030. URL: https://doi.org/10.1016/j.actaastro.2022.06.030.

[10] Gabriele Bellei, Juan Luis Cano, and Mariano Sánchez. "Operational orbiting strategies about minor bodies". In: *21st International Symposium on Space Flight Dynamics ISSFD*. 2009. URL: https://issfd.org/ISSFD_2009/InterMissionDesignI/Cano.pdf.

[11] V.V. Ivashkin and Peng Guo. "Analysis of the possibility of creating a stable satellite of the asteroid apophis as a homogeneous triaxial ellipsoid". In: *Doklady Physics*. Vol. 64. Springer. Nov. 2019, pp. 418–423. DOI: 10.1134/S1028335819110016. URL: https://doi.org/10.1134/S1028335819110016.

[12] Anqi Lang. "Spacecraft orbital stability zones around asteroid 99942 Apophis". In: *Acta Astronautica* 182 (May 2021), pp. 251–263. ISSN: 0094-5765. DOI: 10.1016/j.actaastro.2021.02.013. URL: https://doi.org/10.1016/j.actaastro.2021.02.013.

[13] Safwan Aljbaae et al. "First approximation for spacecraft motion relative to (99942) Apophis". In: *Romanian Astronomical Journal* 31.3 (Nov. 2021), pp. 241–263. URL: https://arxiv.org/abs/2012.06781.

[14] NASA. *NASA Analysis: Earth Is Safe From Asteroid Apophis for 100-Plus Years*. https://www.nasa.gov/feature/jpl/nasa-analysis-earth-is-safe-from-asteroid-apophis-for-100-plus-years [Accessed on: 24/01/2023].

[15] G. H. Born, J. A. Dunne, and D. B. Lame. “Seasat Mission Overview”. In: *Science* 204.4400 (June 1979), pp. 1405–1406. ISSN: 0036-8075. DOI: 10.1126/science.204.4400.1405. URL: https://www.science.org/doi/abs/10.1126/science.204.4400.1405.

[16] European Space Agency. *TOPEX/Poseidon*. https://www.eoportal.org/satellite-missions/topex-poseidon [Accessed on: 17/01/2023].

[17] European Space Agency. *LRO (Lunar Reconnaissance Orbiter) + LCROSS*. https://www.eoportal.org/satellite-missions/lro#lro-lunar-reconnaissance-orbiter--lcross [Accessed on: 14/06/2023].

[18] R.H. Tolson et al. “Application of accelerometer data to atmospheric modeling during Mars aerobraking operations”. In: *Journal of Spacecraft and Rockets* 44.6 (Nov. 2007), pp. 1172–1179. DOI: 10.2514/1.28472. URL: https://doi.org/10.2514/1.28472.

[19] Wesley T. Huntress. “Missions to Comets and Asteroids”. In: *Composition and Origin of Cometary Materials*. Ed. by K. Altwegg et al. Dordrecht: Springer Netherlands, 1999, pp. 329–340. ISBN: 978-94-011-4211-3. DOI: 10.1007/978-94-011-4211-3_30. URL: https://doi.org/10.1007/978-94-011-4211-3_30.

[20] European Space Agency. *SeaSat*. https://www.eoportal.org/satellite-missions/seasat [Accessed on: 17/01/2023].

[21] Jan Hoogland. “Earth frozen orbits: Design, injection and stability”. MA thesis. Delft, The Netherlands: Delft University of Technology, 2016. URL: https://repository.tudelft.nl/islandora/object/uuid%5C%3Afc0a57ce-33df-4cd2-a61b-66e702cc9cf8?collection=education.

[22] Mark Beckman. “Mission design for the lunar reconnaissance orbiter”. In: *29th Annual AAS Guidance and Control Conference*. AAS-07-057. Breckenridge, CO, U.S.A., Feb. 2006. URL: https://lunar.gsfc.nasa.gov/library/LRO_AAS_Paper_07-057.pdf.

[23] Karel F. Wakker. *Fundamentals of Astrodynamics*. Delft, The Netherlands: Institutional Repository, Library Delft University of Technology, 2015. ISBN: 978-94-6168-419-2. URL: https://repository.tudelft.nl/islandora/object/uuid:3fc91471-8e47-4215-af43-718740e6694e?collection=research.

[24] NASA. *Mars Reconnaissance Orbiter: MRO Overview*. https://www.nasa.gov/mission_pages/MRO/mission/index.html [Accessed on: 31/01/2023].

[25] A.L. Bowes et al. “Primary science orbit design for the Mars Reconnaissance Orbiter mission”. In: *13th AAS/AIAA Space Flight Mechanics Meeting*. AAS 03-212. Ponce, Puerto Rico, Feb. 2003. URL: http://hdl.handle.net/2014/6427.

[26] NASA Science Solar System Exploration. *ExoMars Trace Gas Orbiter / Schiaparelli*. https://solarsystem.nasa.gov/missions/exomars-trace-gas-orbiter-schiaparelli/in-depth/ [Accessed on: 31/01/2023].

[27] Stacia Long et al. “ExoMars/TGO science orbit design”. In: *AIAA/AAS Astrodynamics Specialist Conference* 4881 (Sept. 2012). DOI: 10.2514/6.2012-4881. URL: https://doi.org/10.2514/6.2012-4881.

[28] Antonio Elipe and Martin Lara. “Frozen orbits about the moon”. In: *Journal of Guidance, Control, and Dynamics* 26.2 (Mar. 2003), pp. 238–243. DOI: 10.2514/2.5064. URL: https://doi.org/10.2514/2.5064.

[29] Sandeep Kumar Singh et al. “Feasibility of quasi-frozen, near-polar and extremely low-altitude lunar orbits”. In: *Acta Astronautica* 166 (Jan. 2020), pp. 450–468. ISSN: 0094-5765. DOI: 10.1016/j.actaastro.2019.10.037. URL: https://doi.org/10.1016/j.actaastro.2019.10.037.

[30] Marco Giancotti. “Stable Orbits in the Proximity of an Asteroid: Solutions for the Hayabusa 2 Mission”. PhD thesis. Rome, Italy: Sapienza Università di Roma, Jan. 2014. URL: https://core.ac.uk/download/pdf/74323432.pdf.

[31] Mark E. Holdridge. “NEAR shoemaker spacecraft mission operations”. In: *Johns Hopkins APL technical digest* 23.1 (Jan. 2002), pp. 58–70. URL: https://secwww.jhuapl.edu/techdigest/content/techdigest/pdf/V23-N01/23-01-Holdridge.pdf.

[32] NASA. *433 Eros*. https://solarsystem.nasa.gov/asteroids-comets-and-meteors/asteroids/433-eros/in-depth/ [Accessed on: 14/06/2023].

[33] Hitoshi Ikeda et al. “Orbit analysis of hayabusa around asteroid Itokawa”. In: *57th International Astronautical Congress*. Vol. 6. 5. AIAA, Oct. 2006, p. 9. DOI: 10.2514/6.IAC-06-C1.5.09. URL: https://doi.org/10.2514/6.IAC-06-C1.5.09.

[34] Tomohiro Yamaguchi et al. “Hayabusa2-Ryugu proximity operation planning and landing site selection”. In: *Acta Astronautica* 151 (Oct. 2018), pp. 217–227. ISSN: 0094-5765. DOI: 10.1016/j.actaastro.2018.05.032. URL: https://doi.org/10.1016/j.actaastro.2018.05.032.

[35] Dongsuk Han. *Orbit transfers for Dawn’s Vesta operations: navigation and mission design experience*. https://ntrs.nasa.gov/citations/20150004630 [Accessed on: 13/12/2022]. 2012.

[36] Dongsuk Han et al. “Orbit Transfers for Dawn’s Ceres Operations: Navigation and Mission Design Experience at a Dwarf Planet”. In: *14th International Conference on Space Operations*. 2427. May 2016. DOI: 10.2514/6.2016-2427. URL: https://doi.org/10.2514/6.2016-2427.

[37] NASA. *OSIRIS-REx Overview*. https://www.nasa.gov/content/osiris-rex-overview [Accessed on: 17/01/2023].

[38] Kenneth M. Getzandanner et al. “Small Body Proximity Operations & TAG: Navigation Experiences & Lessons Learned from the OSIRIS-REx Mission”. In: *AIAA SCITECH 2022 Forum*. 2387. Jan. 2022. DOI: 10.2514/6.2022-2387. URL: https://doi.org/10.2514/6.2022-2387.

[39] European Space Agency. *Herschel intercepts asteroid Apophis*. https://www.esa.int/Science_Exploration/Space_Science/Herschel_intercepts_asteroid_Apophis [Accessed on: 24/01/2023].

[40] NASA Jet Propulsion Laboratory. *Image: Asteroid Apophis*. https://www.jpl.nasa.gov/images/pia23195-asteroid-apophis [Accessed on: 14/06/2023].

[41] Steven R. Chesley. “Potential impact detection for near-Earth asteroids: The case of 99942 Apophis (2004 MN4)”. In: *Proceedings of the International Astronomical Union* 1.S229 (Aug. 2005), pp. 215–228. DOI: 10.1017/S1743921305006769. URL: https://doi.org/10.1017/S1743921305006769.

[42] M. Delbo, A. Cellino, and E.F. Tedesco. “Albedo and size determination of potentially hazardous asteroids:(99942) Apophis”. In: *Icarus* 188.1 (May 2007), pp. 266–269. ISSN: 0019-1035. DOI: 10.1016/j.icarus.2006.12.024. URL: https://doi.org/10.1016/j.icarus.2006.12.024.

[43] W. Thuillot et al. “The astrometric Gaia-FUN-SSO observation campaign of 99942 Apophis”. In: *Astronomy & Astrophysics* 583.A59 (Nov. 2015), p. 12. DOI: 10.1051/0004-6361/201425603. URL: https://doi.org/10.1051/0004-6361/201425603.

[44] T.G. Müller et al. “Thermal infrared observations of asteroid (99942) Apophis with Herschel”. In: *Astronomy & Astrophysics* 566.A22 (June 2014), p. 10. ISSN: 0004-6361 (print), 1432-0746 (online). DOI: 10.1051/0004-6361/201423841. URL: https://doi.org/10.1051/0004-6361/201423841.

[45] NASA Jet Propulsion Laboratory. *Small-Body Database Lookup*. https://ssd.jpl.nasa.gov/tools/sbdb_lookup.html#/?sstr=apophis [Accessed on: 27/01/2023].

[46] NASA Jet Propulsion Laboratory. *Orbit Viewer*. https://ssd.jpl.nasa.gov/tools/orbit_viewer.html [Accessed on: 13/01/2023].

[47] P. Pravec et al. “The tumbling spin state of (99942) Apophis”. In: *Icarus* 233 (May 2014), pp. 48–60. ISSN: 0019-1035. DOI: 10.1016/j.icarus.2014.01.026. URL: https://doi.org/10.1016/j.icarus.2014.01.026.

[48] Marina Brozović et al. “Goldstone and Arecibo radar observations of (99942) Apophis in 2012–2013”. In: *Icarus* 300 (Jan. 2018), pp. 115–128. ISSN: 0019-1035. DOI: 10.1016/j.icarus.2017.08.032. URL: https://doi.org/10.1016/j.icarus.2017.08.032.

[49] Vishnu Reddy et al. “Apophis Planetary Defense Campaign”. In: *The Planetary Science Journal* 3.5 (2022), p. 123. DOI: 10.3847/PSJ/ac66eb. URL: https://doi.org/10.3847/PSJ/ac66eb.

[50] Nalin H. Samarasinha and Beatrice E.A. Mueller. “Component periods of non-principal-axis rotation and their manifestations in the lightcurves of asteroids and bare cometary nuclei”. In: *Icarus* 248 (Mar. 2015), pp. 347–356. DOI: 10.1016/j.icarus.2014.10.036. URL: https://doi.org/10.1016%5C%2Fj.icarus.2014.10.036.

[51] H.-J. Lee et al. “Refinement of the convex shape model and tumbling spin state of (99942) Apophis using the 2020–2021 apparition data”. In: *Astronomy & Astrophysics* 661.L3 (May 2022). DOI: 10.1051/0004-6361/202243442. URL: https://doi.org/10.1051%5C%2F0004-6361%5C%2F202243442.

[52] Conor J. Benson et al. “Spin state evolution of (99942) Apophis during its 2029 Earth encounter”. In: *Icarus* 390.115324 (Nov. 2023). ISSN: 0019-1035. DOI: 10.1016/j.icarus.2022.115324. URL: https://doi.org/10.1016/j.icarus.2022.115324.

[53] S. Aljbaae et al. “Influence of Apophis’ spin axis variations on a spacecraft during the 2029 close approach with Earth”. In: *arXiv* (2021). DOI: 10.48550/arXiv.2105.14001. URL: https://arxiv.org/abs/2105.14001.

[54] Jean Souchay et al. “Changes of spin axis and rate of the asteroid (99942) Apophis during the 2029 close encounter with Earth: A constrained model”. In: *Astronomy & Astrophysics* 617.A74 (Sept. 2018), p. 11. ISSN: 0004-6361 (print), 1432-0746 (online). DOI: 10.1051/0004-6361/201832914. URL: https://doi.org/10.1051/0004-6361/201832914.

[55] Juan Garcia-Bonilla, Pablo Machuca, and Manuel Sanjurjo-Rivo. “Small-body Gravitational Modeling for On-board Operations and Mass Distribution Estimation: Trade-off Analysis and Novel Approach”. In: *2021 IAF International Astronautical Congress*. IAC-21/C1/6 Paper #66505. Oct. 2021. URL: https://iafastro.directory/iac/paper/id/66505/summary/.

[56] Dominic Dirkx. *Tudat mathematical model definition*. https://docs.tudat.space/en/v0.3.1/_src_about/technical_docs.html [Accessed on: 12/05/2023]. Jan. 2022.

[57] Robert A. Werner and Daniel J. Scheeres. “Exterior gravitation of a polyhedron derived and compared with harmonic and mascon gravitation representations of asteroid 4769 Castalia”. In: *Celestial Mechanics and Dynamical Astronomy* 65.3 (Sept. 1996), pp. 313–344. DOI: 10.1007/BF00053511. URL: https://doi.org/10.1007/BF00053511.

[58] NASA. *1st NASA Asteroid Sample Return Mission on Track for Fall ’23 Delivery*. https://www.nasa.gov/feature/goddard/2022/1st-nasa-asteroid-sample-return-mission-on-track-for-fall-23-delivery [Accessed on: 11/01/2023].

[59] Brian Sutter et al. “OSIRIS-REx Extended Mission Trajectory Design & Target Search”. In: *AIAA SCITECH 2022 Forum*. 2469. Jan. 2022. DOI: 10.2514/6.2022-2469. URL: https://doi.org/10.2514/6.2022-2469.

[60] NASA. *NASA’s OSIRIS-REx Asteroid Sample Return Mission*. https://www.nasa.gov/sites/default/files/atoms/files/osiris_rex_factsheet5-25.pdf [Accessed on: 08/03/2023].

[61] Tudat Team. *TudatPy API Reference: Frame Conversion*. https://py.api.tudat.space/en/latest/frame_conversion.html [Accessed on: 14/05/2023].

[62] Vladimir A. Chobotov. *Orbital mechanics*. 3rd ed. American Institute of Aeronautics and Astronautics, Inc., Jan. 2002. ISBN: 978-1-56347-537-5 (print), 978-1-60086-225-0 (online). DOI: 10.2514/4.862250. URL: https://doi.org/10.2514/4.862250.

[63] Jason M. Leonard et al. “OSIRIS-REx orbit determination performance during the navigation campaign”. In: *2019 AAS/AIAA Astrodynamics Specialist Conference*. Vol. 19. 714. Aug. 2019. URL: https://ntrs.nasa.gov/api/citations/20190029121/downloads/20190029121.pdf.

[64] F. Landis Markley and John L. Crassidis. *Fundamentals of spacecraft attitude determination and control*. 1st ed. Springer New York, NY, 2014. DOI: 10.1007/978-1-4939-0802-8. URL: https://doi.org/10.1007/978-1-4939-0802-8.

[65] Ron Noomen. *Flight and Orbital Mechanics: Lecture slides*. https://ocw.tudelft.nl/wp-content/uploads/AE2104-Orbital-Mechanics-Slides_8.pdf [Accessed on: 22/05/2023]. Oct. 2012.

[66] Tudat Team. *Tudat Space*. https://docs.tudat.space/en/stable/ [Accessed on: 31/05/2023].

[67] Francesco Biscani and Dario Izzo. “A parallel global multiobjective framework for optimization: pagmo”. In: *Journal of Open Source Software* 5.53 (Sept. 2020), p. 2338. ISSN: 2475-9066. DOI: 10.21105/joss.02338. URL: https://doi.org/10.21105/joss.02338.

[68] NASA Jet Propulsion Laboratory. *Horizons System*. https://ssd.jpl.nasa.gov/horizons/app.html#/ [Accessed on: 30/03/2023].

[69] SpiceyPy. *SpicePy package*. https://spiceypy.readthedocs.io/en/v2.3.1/documentation.html [Accessed on: 31/05/2023].

[70] Tudat Space. *Frames in the Environment*. https://docs.tudat.space/en/stable/_src_user_guide/state_propagation/environment_setup/architecture/frames_in_environment.html [Accessed on: 17/05/2023].

[71] Tudat Team. *TudatPy API Reference: Ephemeris*. https://py.api.tudat.space/en/latest/ephemeris.html [Accessed on: 17/05/2023].

[72] NASA/IPAC Extragalactic Database. *Coordinate Transformation & Galactic Extinction Calculator*. https://ned.ipac.caltech.edu/forms/calculator.html [Accessed on: 17/05/2022].

[73] Tudat Space. *Environment models*. https://docs.tudat.space/en/stable/_src_user_guide/state_propagation/environment_setup/create_bodies/environment_models.html [Accessed on: 17/05/2023].

[74] Tudat Space. *Default environment models*. https://docs.tudat.space/en/stable/_src_user_guide/state_propagation/environment_setup/create_bodies/default_env_models.html [Accessed on: 19/05/2023].

[75] Tudat Space. *Available State Definitions and Conversions*. https://docs.tudat.space/en/stable/_src_user_guide/state_propagation/environment_setup/architecture/available_state_definitions_conversions.html [Accessed on: 19/05/2023].

[76] Tudat Space. *Translational Dynamics*. https://docs.tudat.space/en/stable/_src_user_guide/state_propagation/propagation_setup/dynamics_types/translational.html [Accessed on: 31/05/2023].

[77] Tudat Team. *TudatPy API Reference: Propagator*. https://py.api.tudat.space/en/latest/propagator.html [Accessed on: 31/05/2023].

[78] Paul Torrente. “Uncontrolled Motion for Asteroid Missions: An Application to the Binary Asteroid 1999 KW4”. MA thesis. Delft, The Netherlands: Delft University of Technology, 2021. URL: https://repository.tudelft.nl/islandora/object/uuid%5C%3Ac09037d8-dd44-4ce8-9d6a-201749b5be0b.

[79] Tudat Space. *Integration Setup*. https://docs.tudat.space/en/stable/_src_user_guide/state_propagation/propagation_setup/integration_setup.html [Accessed on: 31/05/2023].

[80] Dominic Dirkx and Kevin Cowan. *AE4868 – Numerical Astrodynamics: Numerical Integration - Method Selection*. https://brightspace.tudelft.nl/d2l/le/content/278334/viewContent/2050583/View [Accessed on: 31/05/2023].

[81] Dominic Dirkx and Kevin Cowan. *AE4868 – Numerical Astrodynamics: Numerical Integration*. https://brightspace.tudelft.nl/d2l/le/content/278334/viewContent/2046280/View [Accessed on: 31/05/2023].

[82] Tudat Team. *TudatPy API Reference: Interpolators*. https://py.api.tudat.space/en/latest/interpolators.html [Accessed on: 31/05/2023].

[83] Sofya Spiridonova, Michael Kirschner, and Urs Hugentobler. “Precise mean orbital elements determination for LEO monitoring and maintenance”. In: *24th International Symposium on Space Flight Dynamics*. Laurel, MD, U.S.A., May 2014. URL: https://issfd.org/ISSFD_2014/ISSFD24_Paper_S8-2_Spiridonova.pdf.

[84] OSIRIS-REx. *Orbital A Phase*. https://www.asteroidmission.org/orbital-a-phase/ [Accessed on: 29/05/2022].

[85] OSIRIS-REx. *Orbital C Phase*. https://www.asteroidmission.org/orbital-c-phase/ [Accessed on: 29/05/2022].

[86] OSIRIS-REx. *Orbital B Phase*. https://www.asteroidmission.org/orbital-b-phase/ [Accessed on: 29/05/2022].

[87] Kalyanmoy Deb et al. “A fast and elitist multiobjective genetic algorithm: NSGA-II”. In: *IEEE transactions on evolutionary computation* 6.2 (2002), pp. 182–197. DOI: 10.1109/4235.996017. URL: https://doi.org/10.1109/4235.996017.

[88] Jesper Spillenaar Bilgen. “Global Ascent Trajectory Optimization of a Space Plane”. MA thesis. Delft, The Netherlands: Delft University of Technology, 2017. URL: https://repository.tudelft.nl/islandora/object/uuid%5C%3A64683ba4-50b4-485f-be74-22ec766cbf0d?collection=education.

[89] Thomas Weise. *Global Optimization Algorithms - Theory and Application*. https://citeseerx.ist.psu.edu/document?repid=rep1&type=pdf&doi=09686d3a65fa5b0fe595e8fe7405d068204f9803 [Accessed on: 17/05/2023]. June 2009.

[90] Pagmo 2.19.0 documentation. *Non dominated sorting genetic algorithm (NSGA-II)*. https://esa.github.io/pagmo2/docs/cpp/algorithms/nsga2.html [Accessed on: 04/06/2023].

[91] Spaceflight101. *OSIRIS-REx Spacecraft*. https://spaceflight101.com/osiris-rex/osiris-rex-spacecraft-overview/ [Accessed on: 10/06/2023].

[92] Merton E. Davies et al. "The direction of the north pole and the control network of asteroid 951 Gaspra". In: *Icarus* 107.1 (1994), pp. 18–22. DOI: 10.1006/icar.1994.1003. URL: https://doi.org/10.1006/icar.1994.1003.

[93] Sander Goossens et al. "Mass and shape determination of (101955) bennu using differenced data from multiple OSIRIS-REx mission phases". In: *The Planetary Science Journal* 2.6 (Nov. 2021), p. 219. DOI: 10.3847/PSJ/ac26c4. URL: https://doi.org/10.3847/PSJ/ac26c4.

[94] D.S. Lauretta et al. "The OSIRIS-REx target asteroid (101955) Bennu: Constraints on its physical, geological, and dynamical nature from astronomical observations". In: *Meteoritics & Planetary Science* 50.4 (Apr. 2015), pp. 834–849. DOI: 10.1111/maps.12353. URL: https://doi.org/10.1111/maps.12353.

[95] J.W. McMahon et al. "The OSIRIS-REx radio science experiment at Bennu". In: *Space Science Reviews* 214.43 (Feb. 2018), pp. 1–41. DOI: 10.1007/s11214-018-0480-y. URL: https://doi.org/10.1007/s11214-018-0480-y.

[96] NASA. *OSIRIS-REx: Mission Status*. https://www.asteroidmission.org/status-updates/ [Accessed on: 12/05/2023].

[97] Kyoung-Min Roh et al. "Investigating suitable orbits for the Swarm constellation mission–The frozen orbit". In: *Aerospace Science and Technology* 13.1 (Jan. 2009), pp. 49–58. ISSN: 1270-9638. DOI: 10.1016/j.ast.2008.03.001. URL: https://doi.org/10.1016/j.ast.2008.03.001.

[98] Siamak G. Hesar et al. "Precise model for small-body thermal radiation pressure acting on spacecraft". In: *Journal of Guidance, Control, and Dynamics* 40.10 (Oct. 2017), pp. 2432–2441. ISSN: 0731-5090 (print), 1533-3884 (online). DOI: 10.2514/1.G002566. URL: https://doi.org/10.2514/1.G002566.

[99] Peter G. Antresian et al. "Comparing Pre-Launch Assumptions to In-Flight Navigation Performance of OSIRIS-REx". In: *44th Annual AAS Guidance, Navigation and Control (GN&C) Conference*. Vol. 22. 167. Feb. 2022. URL: https://ntrs.nasa.gov/api/citations/20220001855/downloads/OSIRIS_REx_Comparing_Pre_Launch_Assumptions_to_In_Flight_Navigation_Performance.pdf.

A

Appendix

In this appendix, additional equations and results are provided for completeness. In Section A.1, the equations for the computation of the elements in the Jacobian matrix for the stability analysis described in Section 4.5 are provided. Section A.2 presents the equations and results of the mean-osculating element transformation using the method of Spiridonova, Kirschner, and Hugentobler [83].

A.1. Jacobian Matrix Elements

The equations for $\mathcal{J}_A$, $\mathcal{J}_B$, $\mathcal{J}_C$, $\mathcal{J}_D$, $\mathcal{J}_E$, $\mathcal{J}_F$, $\mathcal{J}_G$, $\mathcal{J}_H$ and $\mathcal{J}_I$, taken from the work of Kikuchi, Oki, and Tsuda, are provided here [5].

$$\mathcal{J}_A = \mathcal{K}_{\text{SRP}}\sqrt{1-e^2}\,\delta_\Omega\delta_\omega \tag{A.1}$$

$$\begin{aligned}\mathcal{J}_B =& \mathcal{K}_{\text{SRP}}\sqrt{1-e^2}\cos i\cdot\delta_\Omega\delta_\omega \\ &+ \mathcal{K}_{J_3}\frac{1}{\left(1-e^2\right)^2}\sin i\left(5\cos^2 i-1\right)\delta_\omega \\ &+ \mathcal{K}_{J_4}\frac{2e}{\left(1-e^2\right)^3}\sin^2 i\left(7\cos^2 i-1\right)\end{aligned} \tag{A.2}$$

$$\begin{aligned}\mathcal{J}_C =& \mathcal{K}_{\text{SRP}}\frac{e}{\sqrt{1-e^2}}\sin i\cdot\delta_\Omega\delta_\omega \\ &- \mathcal{K}_{J_3}\frac{e}{\left(1-e^2\right)^3}\cos i\left(5\cos^2 i-1\right)\delta_\omega \\ &- \mathcal{K}_{J_4}\frac{2e^2}{\left(1-e^2\right)^4}\sin i\cos i\left(7\cos^2 i-1\right)\end{aligned} \tag{A.3}$$

$$\begin{aligned}\mathcal{J}_D =& -\mathcal{K}_{\text{SRP}}\frac{e}{2a\sqrt{1-e^2}}\delta_\Omega\delta_\omega \\ &+ \mathcal{K}_{J_2}\frac{7}{2a\left(1-e^2\right)^2}\cos i \\ &- \mathcal{K}_{J_3}\frac{9e}{2a\left(1-e^2\right)^3}\cot i\left(15\cos^2 i-11\right)\delta_\omega \\ &- \mathcal{K}_{J_4}\frac{11}{2a\left(1-e^2\right)^4}\cos i\left\{e^2\left(35\cos^2 i-17\right)\right. \\ &\left.+2\left(7\cos^2 i-3\right)\right\}\end{aligned} \tag{A.4}$$

$$\begin{aligned}\mathcal{J}_E =& -\mathcal{K}_{\text{SRP}}\frac{1}{\left(1-e^2\right)^{\frac{3}{2}}}\delta_\Omega\delta_\omega-\mathcal{K}_{J_2}\frac{4e}{\left(1-e^2\right)^3}\cos i\\&+\mathcal{K}_{J_3}\frac{1+5e^2}{\left(1-e^2\right)^4}\cot i\left(15\cos^2 i-11\right)\delta_\omega\\&+\mathcal{K}_{J_4}\frac{2e}{\left(1-e^2\right)^5}\cos i\left\{3e^2\left(35\cos^2 i-17\right)+91\cos^2 i-41\right\}\end{aligned}\tag{A.5}$$

$$\begin{aligned}\mathcal{J}_F =&\mathcal{K}_{J_2}\frac{1}{\left(1-e^2\right)^2}\sin i-\mathcal{K}_{J_3}\frac{e}{\left(1-e^2\right)^3}\left(4\csc^2 i+15\cos 2i\right)\delta_\omega\\&-\mathcal{K}_{J_4}\frac{1}{\left(1-e^2\right)^4}\sin i\left\{e^2\left(105\cos^2 i-17\right)+6\left(7\cos^2 i-1\right)\right\}\end{aligned}\tag{A.6}$$

$$\begin{aligned}\mathcal{J}_G =&\mathcal{K}_{\text{SRP}}\frac{1}{2ae\sqrt{1-e^2}}\cos i\cdot\delta_\Omega\delta_\omega-\mathcal{K}_{J_2}\frac{7}{4a\left(1-e^2\right)^2}\left(5\cos^2 i-1\right)\\&-\mathcal{K}_{J_3}\frac{9}{2ae\left(1-e^2\right)^3}\csc i\Big\{e^2\Big(35\sin^2 i\cos^2 i-4\Big)\\&+\sin^2 i\left(5\cos^2 i-1\right)\Big\}\delta_\omega\\&+\mathcal{K}_{J_4}\frac{11}{8a\left(1-e^2\right)^4}\left\{e^2\left(315\cos^4 i-238\cos^2 i+19\right)\right.\\&\left.+16\left(14\cos^4 i-11\cos^2 i+1\right)\right\}\end{aligned}\tag{A.7}$$

$$\begin{aligned}\mathcal{J}_H =& -\mathcal{K}_{\text{SRP}}\frac{1-2e^2}{e^2\left(1-e^2\right)^{\frac{3}{2}}}\cos i\cdot\delta_\Omega\delta_\omega+\mathcal{K}_{J_2}\frac{2e}{\left(1-e^2\right)^3}\left(5\cos^2 i-1\right)\\&+\mathcal{K}_{J_3}\frac{1}{e^2\left(1-e^2\right)^4}\csc i\Big\{5e^4\Big(35\sin^2 i\cos^2 i-4\Big)\\&+e^2\Big(70\sin^2 i\cos^2 i+7\cos^2 i-11\Big)-\sin^2 i\left(5\cos^2 i-1\right)\Big\}\delta_\omega\\&-\mathcal{K}_{J_4}\frac{e}{2\left(1-e^2\right)^5}\left\{3e^2\left(315\cos^4 i-238\cos^2 i+19\right)\right.\\&\left.+1211\cos^4 i-942\cos^2 i+83\right\}\end{aligned}\tag{A.8}$$

$$\begin{aligned}\mathcal{J}_I =& -\mathcal{K}_{\text{SRP}}\frac{1}{e\sqrt{1-e^2}}\sin i\cdot\delta_\Omega\delta_\omega-\mathcal{K}_{J_2}\frac{5}{\left(1-e^2\right)^2}\sin i\cos i\\&-\mathcal{K}_{J_3}\frac{1}{e\left(1-e^2\right)^3}\cot i\csc i\left\{e^2\left(105\cos^4 i-175\cos^2 i+66\right)\right.\\&\left.-\sin^2 i\left(15\cos^2 i-11\right)\right\}\delta_\omega\\&+\mathcal{K}_{J_4}\frac{1}{\left(1-e^2\right)^4}\sin i\cos i\left\{7e^2\left(45\cos^2 i-17\right)\right.\\&\left.+8\left(28\cos^2 i-11\right)\right\}\end{aligned}\tag{A.9}$$

A.2. Mean-Osculating Element Transformation

The computation of mean elements from osculating orbital elements has been successfully carried out for Earth orbiters as exemplified by the work of Spiridonova, Kirschner, and Hugentobler [83]. Here, the equations and main outline of this method are presented. First, the change in the orbital elements is formulated based on Lagrange's Planetary Equations including first and second-order J_2 perturbations. However, Eckstein-Ustinov theory is used to redefine the orbital elements into a set of non-singular elements $a, h, l, i, \Omega, \lambda$, called Eckstein-Ustinov elements. This removes the eccentricity from the denominator of the equations to avoid singularities at e = 0. The new elements h, l and λ are defined as shown in Equation A.10 , where M is the mean anomaly [83].

$$\begin{aligned} h &= e \sin \omega \\ l &= e \cos \omega \\ \lambda &= \omega + M \end{aligned} \tag{A.10}$$

The final formulation for the change in Eckstein-Ustinov elements is presented in Equation A.11 [83].

$$\begin{aligned}
\Delta a = &-\frac{3a_0}{2\lambda'} G_{20} \left[\left(2 - \frac{7}{2}\beta_0^2\right) l_0 \cos \lambda_0 + \left(2 - \frac{5}{2}\beta_0^2\right) h_0 \sin \lambda_0 \right. \\
&\left. + \beta_0^2 \cos 2\lambda_0 + \frac{7}{2}\beta_0^2 \left(l_0 \cos 3\lambda_0 + h_0 \sin 3\lambda_0\right) \right] \\
&+ \frac{3a_0}{4} G_{20}^2 \beta_0^2 \left[7\left(2 - 3\beta_0^2\right) \cos 2\lambda_0 + \beta_0^2 \cos 4\lambda_0\right] \\
\Delta h = &-\frac{3}{2\lambda'} G_{20} \left[\left(1 - \frac{7}{4}\beta_0^2\right) \sin \lambda_0 + \left(1 - 3\beta_0^2\right) l_0 \sin 2\lambda_0 \right. \\
&\left. + \left(-\frac{3}{2} + 2\beta_0^2\right) h_0 \cos 2\lambda_0 + \frac{7}{12}\beta_0^2 \sin 3\lambda_0 + \frac{17}{8}\beta_0^2 \left(l_0 \sin 4\lambda_0 - h_0 \cos 4\lambda_0\right) \right] \\
\Delta l = &-\frac{3}{2\lambda'} G_{20} \left[\left(1 - \frac{5}{4}\beta_0^2\right) \cos \lambda_0 + \frac{1}{2}\left(3 - 5\beta_0^2\right) l_0 \cos 2\lambda_0 \right. \\
&\left. + \left(2 - \frac{3}{2}\beta_0^2\right) h_0 \sin 2\lambda_0 + \frac{7}{12}\beta_0^2 \cos 3\lambda_0 + \frac{17}{8}\beta_0^2 \left(l_0 \cos 4\lambda_0 + h_0 \sin 4\lambda_0\right) \right] \\
\Delta i = &-\frac{3}{4\lambda'} G_{20} \beta_0 \sqrt{1 - \beta_0^2} \left[-l_0 \cos \lambda_0 + h_0 \sin \lambda_0 \right. \\
&\left. + \cos 2\lambda_0 + \frac{7}{3}\left(l_0 \cos 3\lambda_0 + h_0 \sin 3\lambda_0\right) \right] \\
\Delta \Omega = &\frac{3}{2\lambda'} G_{20} \sqrt{1 - \beta_0^2} \left[\frac{7}{2} l_0 \sin \lambda_0 - \frac{5}{2} h_0 \cos \lambda_0 - \frac{1}{2} \sin 2\lambda_0 \right. \\
&\left. - \frac{7}{6} l_0 \sin 3\lambda_0 + \frac{7}{6} h_0 \cos 3\lambda_0 \right] \\
\Delta \lambda = &-\frac{3}{2\lambda'} G_{20} \left[\left(10 - \frac{119}{8}\beta_0^2\right) l_0 \sin \lambda_0 + \left(\frac{85}{8}\beta_0^2 - 9\right) h_0 \cos \lambda_0 \right. \\
&+ \left(2\beta_0^2 - \frac{1}{2}\right) \sin 2\lambda_0 + \left(-\frac{7}{6} + \frac{119}{24}\beta_0^2\right) \left(l_0 \sin 3\lambda_0 - h_0 \cos 3\lambda_0\right) \\
&- \left(3 - \frac{21}{4}\beta_0^2\right) l_0 \sin \lambda_0 + \left(3 - \frac{15}{4}\beta_0^2\right) h_0 \cos \lambda_0 \\
&\left. - \frac{3}{4}\beta_0^2 \sin 2\lambda_0 - \frac{21}{12}\beta_0^2 \left(l_0 \sin 3\lambda_0 - h_0 \cos 3\lambda_0\right) \right]
\end{aligned} \tag{A.11}$$

where:

$$\begin{aligned} \lambda' &= 1 - \frac{3}{2} G_{20} \left(3 - 4\beta_0\right) \\ \beta_0 &= \sin i_0 \\ G_{20} &= -J_2 \left(\frac{a_e}{a}\right)^2 \end{aligned}$$

Here, a_e is the central body's equatorial radius and the Eckstein-Ustinov elements with subscript 0 on the right-hand side of the equations represent the J_2-mean elements at a given point in time.

With Equation A.11, the osculating elements can be calculated from a set of mean elements in a straightforward manner using Equation A.12, where $\tilde{a}$ represents the mean semi-major axis and likewise for the remaining elements [83].

$$\begin{aligned}
a &= \tilde{a} + \Delta a \\
e &= \sqrt{l^2 + h^2} \quad \text{where} \quad l = \tilde{l} + \Delta l \quad \text{and} \quad h = \tilde{h} + \Delta h \\
i &= \tilde{i} + \Delta i \\
\omega &= \operatorname{atan2}\left(\frac{h}{\sqrt{h^2 + l^2}}, \frac{l}{\sqrt{h^2 + l^2}}\right) \\
\Omega &= \tilde{\Omega} + \Delta\Omega \\
M &= \tilde{\lambda} + \Delta\lambda - \omega
\end{aligned} \tag{A.12}$$

However, the transformation from osculating to mean elements, which is the desired transformation for finding frozen orbits, requires an iterative procedure. In a numerical simulation, the starting point is an osculating Cartesian state vector. This state vector is transformed into an osculating Keplerian state vector. The method involves an initial assumption whereby the osculating elements at a given point in time are assumed to be the mean elements. The osculating elements associated with these ’mean’ elements are computed with Equations A.11 and A.12 and then transformed back into a Cartesian state vector. Then, the difference between the two Cartesian state vectors is calculated and the difference is added to the initial osculating Cartesian state vector such that it is updated as an input for the next iteration. The number of iterations depends on the user-specified convergence, which can be defined by the difference between Cartesian state vectors being smaller than a given value.

Verification of the method is carried out prior to implementation for the transformation of elements for an Apophis orbiter. The original plots showing the osculating and mean elements of TOPEX/Poseidon from Spiridonova, Kirschner, and Hugentobler are shown in Figure A.1 [83].

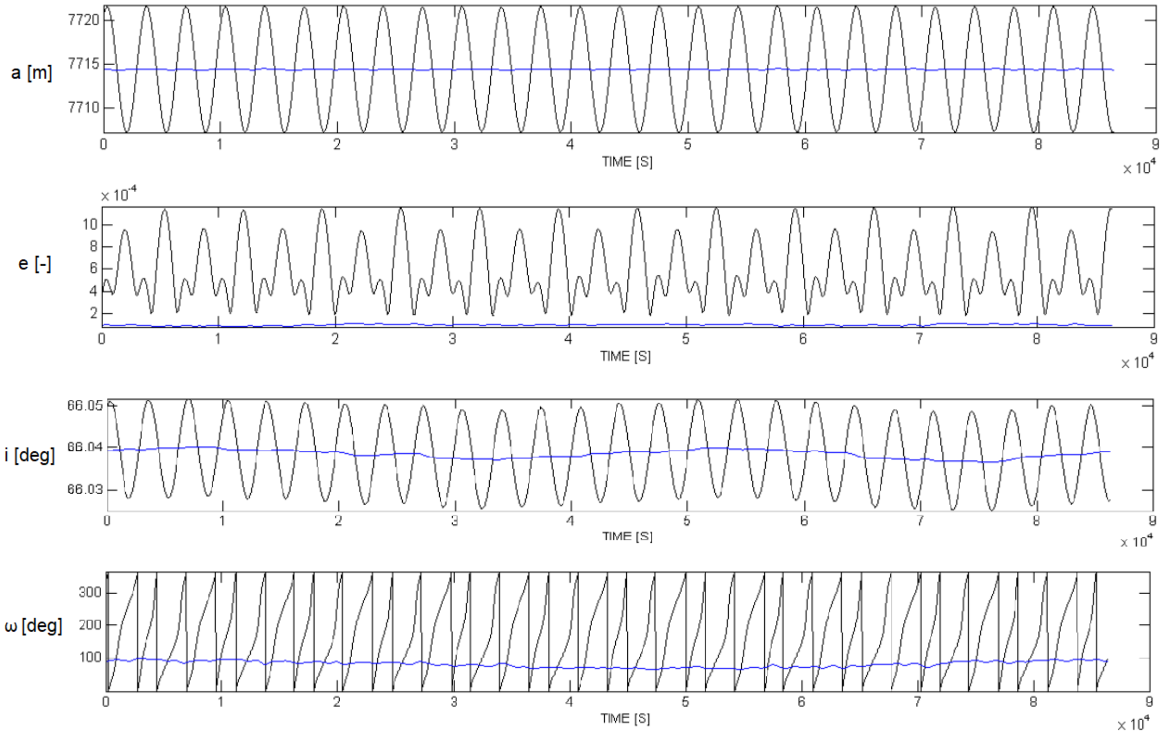

Figure A.1: Original plots of osculating and mean elements from Spiridonova, Kirschner, and Hugentobler [83]. The black lines represent the osculating elements while the blue lines are the reconstructed mean elements.

The recreation of these plots is shown in Figure A.2.

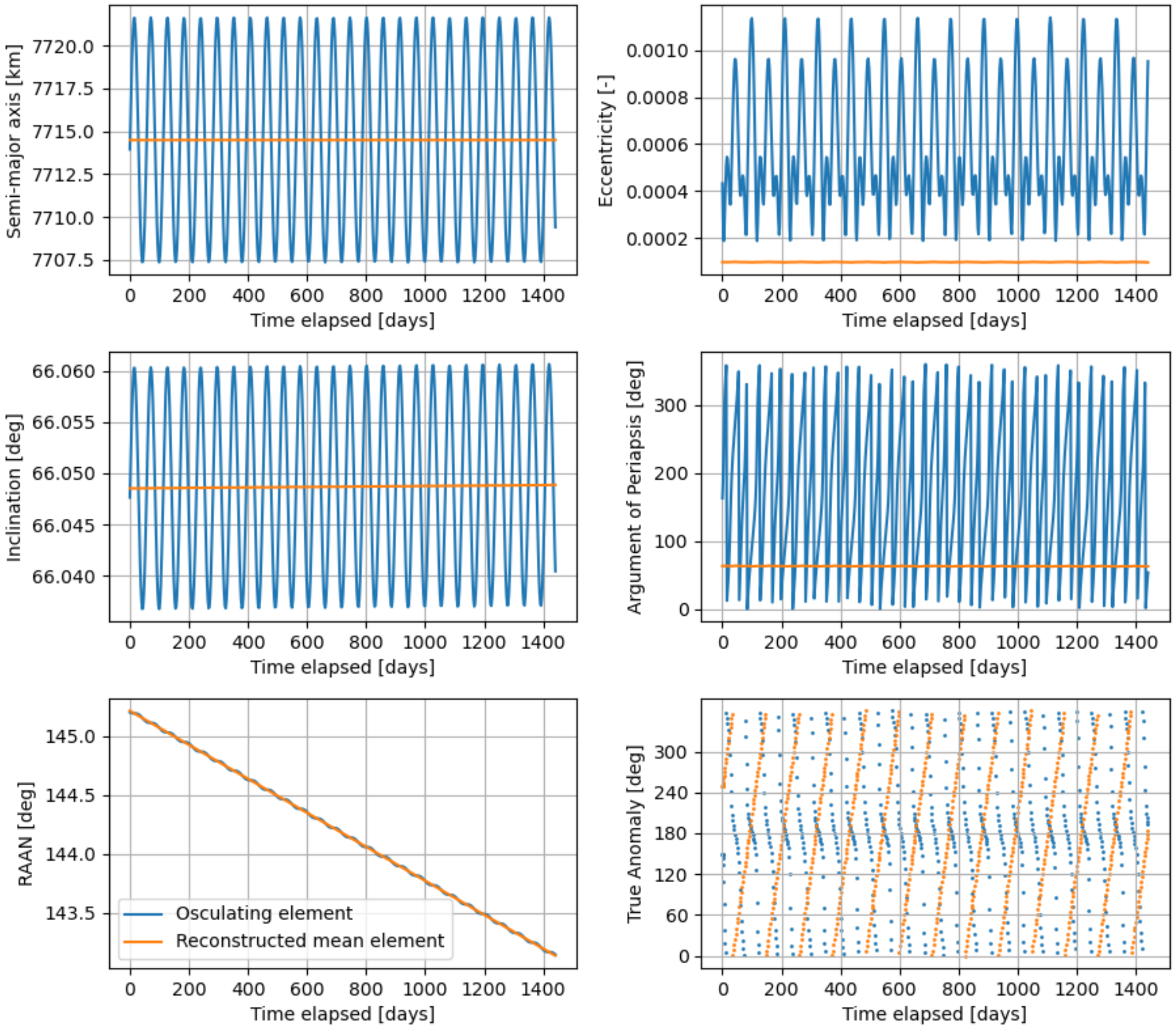

Figure A.2: Recreated plots of osculating and mean elements from Spiridonova, Kirschner, and Hugentobler [83].

The plots have been recreated to a reasonable level of accuracy and thus the implementation of the method is assumed to be correct. With the method verified, the same methodology is applied to an arbitrary orbit around Apophis by simply replacing the constants associated with the central body – mass, gravitational parameter and spherical harmonics coefficients.

The reconstructed mean elements from the osculating elements can be seen in Figure A.3. Here, it can be seen that the method is insufficient for the averaging of the osculating orbital elements for an Apophis-orbiting spacecraft. Even with different definitions of convergence, the results do not improve further. This is expected since, although the implementation is correct, it has been seen in Chapter 3 that there are other major perturbations in this system acting on this system. Thus, assuming perturbations due to J_2 only means the variation in the elements from all other perturbations, such as SRP and higher degree and order spherical harmonics terms, is neglected.

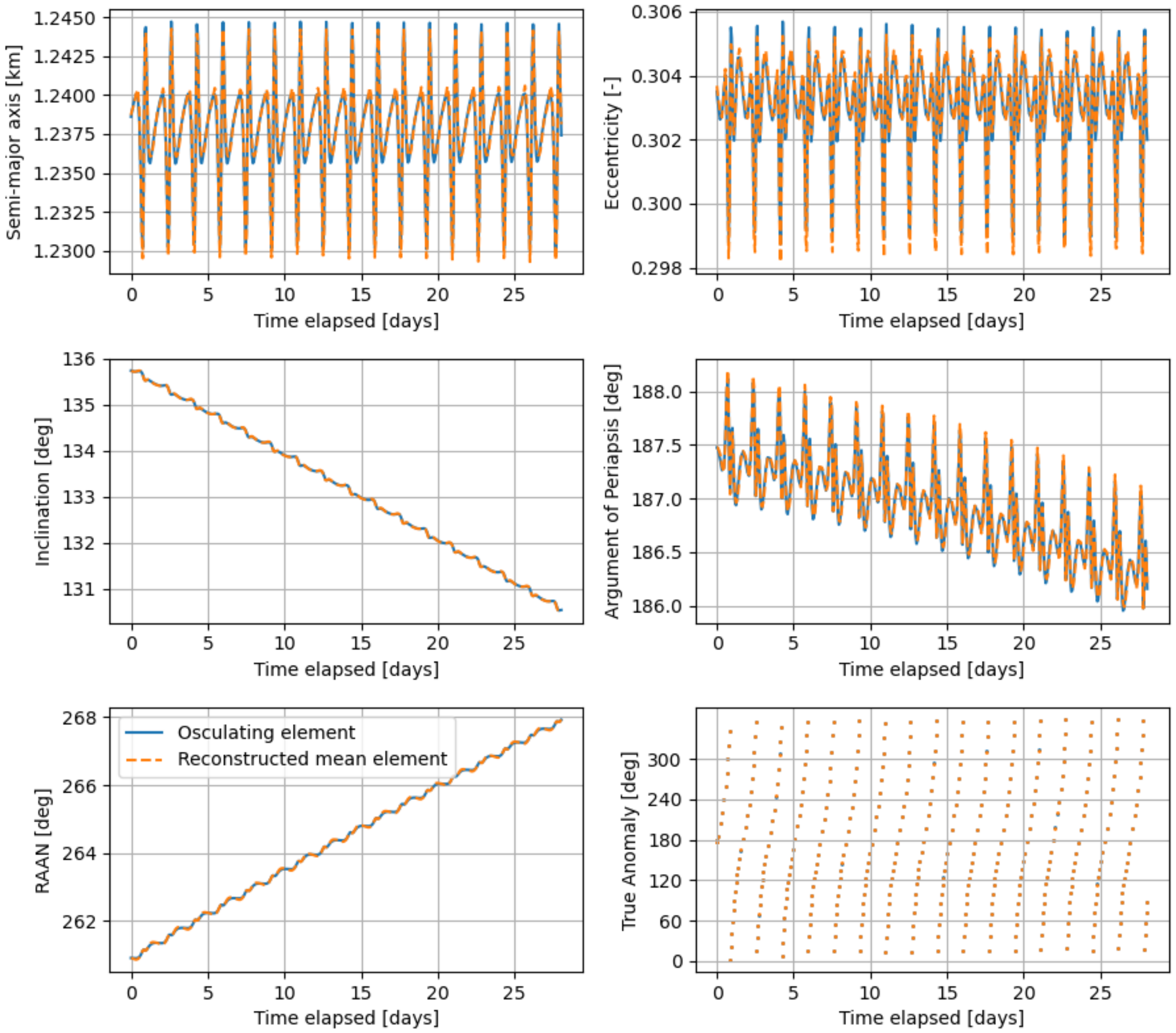

Figure A.3: Reconstruction of mean elements from osculating elements for an Apophis orbiter using the Eckstein-Ustinov method described in Spiridonova, Kirschner, and Hugentobler [83].

From these results, it is concluded that the method is inapplicable to the study case of an Apophis-orbiting spacecraft. Therefore, the alternative definition of the fitness function in Section 8.1 is used in this work.

This page has been left blank intentionally.